EUSKAL HERRIKO UNIBERTSITATEA/
UNIVERSIDAD DEL PAÍS VASCO

Dpto. de Bioquímica y Biología Molecular
Instituto Biofisika UPV-EHU/CSIC

Mechanisms of MPER helix binding at membrane interfaces and implications for the broad neutralization of HIV by antibodies

Edurne Rujas Diez

Leioa, 2016

A mi familia y amigos,

especialmente a ti, papá

Acknowledgements

The present thesis has been performed at the “Instituto Biofisika” (UPV-EHU/CSIC) under the supervision of Prof. José Luis Nieva Escandón and Prof. Jose Manuel Martinez Caaveiro to whom I would like to express my sincerest gratitude for their supervision and guidance.

This work has been supported by the National Institutes of Health, Grant R01 AI097051; the Basque Government, Grant IT838-13; the Canadian Institutes of Health Research, Grant MOP-114941 and the Japan Society for the Promotion of Science, Kakenhi A 25249115 and Kakenhi C 15K06962 grants. The author was recipient of a pre-doctoral fellowship from the government of the Basque Country.

Index

ABBREVIATIONS

6-HB	6-helix bundle
ΔH	Enthalpy change
ΔS	Entropy
ΔG	Gibb's free energy change
ΔG_{iwu}	Free energy change of partitioning from membrane in water
ΔG_{obs}	Observed partitioning free energy change
λ	Wavelength
σ_{ext}	Extintion coefficient
AIDS	Acquired Immune Deficiency Syndrome
AZT	Zidovudin
BCA	Bicinchoninic acid microassay
BCR	B-cell receptor
bNAbs	Broadly neutralizing antibodies
BSA	Buried surface area
CD4bs	CD4-binding site
CDR	Complementarity determining region
C_H	Constant heavy
Chol	Cholesterol
C_L	Constant light
CTL	Control
DEAE	Diethylaminoethyl-dextran hydrochloride
DHPC	Dihexanoyl-phosphocholine
DMSO	Dimethylsulfoxide
DOPC	1,2-dioleoyl-*sn*-glycero-3-phosphatidylcholine
DOPE	1,2-dioleoyl-*sn*-glycero-3-phosphatidylethanolamine
DOPS	1,2-dioleoyl-*sn*-glycero-3- phosphatidylserine
DPC	n-dodecylphosphocholine
DSC	Differential scanning calorimetry

EDTA	Ethylenediaminetetraacetic acid
ELISA	Enzyme linked immunosorbent assay
Env	Envelope protein
ER	Endoplasmic reticulum
F/F_0	Fluorescence intensity/Initial fluorescence intensity
Fab	Fragment, antigen-binding
FACS	Fluorescence-activated cell sorting
FCS	Fetal calf serum
FDA	Food and Drug Administration
FDC	Follicular dentritic cell
FP	Fusion peptide
Fv	Variable fragment
FWR	Framework regions
GC	Germinal centre
GFP	Green fluorescent protein
Grx	Glutaredoxin
HAART	Highly active antiretroviral therapy
HC	Heavy chain
HEPES	4-(2-hydroxyethyl)piperazine-1-ethanesulfonic acid
HIV-1	Human immunodeficiency virus type 1
HOMO	Highest occupied molecular orbital
HPLC	High performance liquid chromatography
HR	Heptad repeated region
HRP	Horseradish peroxidase
IC_{50}	50 % inhibitory concentration
IEC	Ion exchange chromatography
Ig	Immunoglobulin
IPTG	Isopropyl-D-thiogalactopyranoside
ITC	Isothermal titration calorimetry
K_a	Binding affinity constant
K_D	Dissociation constant
Kn	Kanamycin

k_{off}	Dissociation rate
k_{on}	Association rate
K_x	Molar fraction partition coefficient
LC	Light chain
LUMO	Lowest occupied molecular orbital
LUVs	Large unilamellar vesicles
MAb	Monoclonal antibodies
MALDI-TOF	Matrix-assisted laser desorption/ionization time-of-flight
MCS	Multiple cloning site
MDS	Molecular dynamics simulation
MHC	Major histocompatibility complex
MLV	Multilamellar vesicles
MPER	Membrane-proximal external region
n	Stoichiometry
NBD	7-nitro-1,2,3-benzoxadiazole
Ni-NTA	Nickel-nitrilotriacetic acid
OD	Optical density
o/n	Overnight
*p*BPA	p-benzoylphenylalanine
PDGFR	Platelet-derived growth-factor receptor
PG	Phosphatidylglycerol
PI(4,5)P2	Phosphatidylinositol-(4,5)-bisphosphate
PNGS	Potential N-glycosylation sites
POPC	1-palmitoyl-2-oleoyl-sn-glycero-3-phosphocholine
PS	Phosphatidylserine
PsV	Pseudovirus
Rbs	Ribosome binding site
Rho	Lissamine rhodamine B sulfonyl chloride
RLU	Relative luminescence units
Rmsd	Root-mean square deviation
RSCC	Real-space correlation coefficient

RT^1	Reverse transcription
RT^2	Room temperature
RU	Response units (in surface plasmon resonance)
S_0	Ground state
S_1	Excited state
Sc	Shape-complementarity coefficient
scFv	Single-chain variable fragment
SDS	Sodium dodecyl sulfate
SDS-PAGE	Sodium dodecyl sulfate polyacrylamide gel electrophoresis
SHIV	Simian-human immunodeficiency virus
SHM	Somatic hypermutation
SIV	Simian immunodeficiency virus
SM	Sphingomyelin
SPR	Surface plasmon resonance
TEV	Tobacco Etch Virus
T_M	Melting temperature
TMD	Transmembrane domain
Trp	Tryptophan
Trx	Thioredoxin
Tween 20	Polyethyleneglycol sorbitan monolaurate
V_H	Variable heavy
V_L	Variable light
VL	Virus-like
VSV-G	Vesicular stomatitis virus glycoprotein
WB	Western blot
WW	Wimley and White hydropathy-at-interface scale

PUBLICATIONS

I. Schlegel, S., **Rujas, E.**, Ytterberg, A.J., Zubarev, R.A., Luirink, J., and de Gier, J.W. (2013). Optimizing heterologous protein production in the periplasm of E. coli by regulating gene expression levels. Microb Cell Fact 12, 24.

II. Serrano, S., Araujo, A., Apellaniz, B., Bryson, S., Carravilla, P., de la Arada, I., Huarte, N., **Rujas, E**., Pai, E.F., Arrondo, J.L., et al. (2014). Structure and immunogenicity of a peptide vaccine, including the complete HIV-1 gp41 2F5 epitope: implications for antibody recognition mechanism and immunogen design. J Biol Chem 289, 6565-6580.

III. Apellaniz, B., **Rujas, E.**, Carravilla, P., Requejo-Isidro, J., Huarte, N., Domene, C., and Nieva, J.L. (2014). Cholesterol-dependent membrane fusion induced by the gp41 membrane-proximal external region-transmembrane domain connection suggests a mechanism for broad HIV-1 neutralization. J Virol 88, 13367-13377.

IV. Apellaniz, B., **Rujas, E.**, Serrano, S., Morante, K., Tsumoto, K., Caaveiro, J.M., Jimenez, M.A., and Nieva, J.L. (2015). The Atomic Structure of the HIV-1 gp41 Transmembrane Domain and Its Connection to the Immunogenic Membrane-proximal External Region. J Biol Chem 290, 12999-13015.

V. **Rujas, E.**, Gulzar, N., Morante, K., Tsumoto, K., Scott, J.K., Nieva, J.L., and Caaveiro, J.M. (2015). Structural and Thermodynamic Basis of Epitope Binding by Neutralizing and Nonneutralizing Forms of the Anti-HIV-1 Antibody 4E10. J Virol 89, 11975-11989.

VI. **Rujas, E.**, Gulzar, N., Morante, K., Tsumoto, K., Scott, J.K., Nieva, J.L., and Caaveiro, J.M. (2016). Reply to "The Broadly Neutralizing, Anti-HIV Antibody 4E10: an Open and Shut Case?". J Virol 90, 3276-3277.

VII. **Rujas E**., Caaveiro, J.M., Partida-Hanon A., Gulzar N., Morante K., Apellániz B., García-Porras M., Bruix M., Tsumoto K., Scott J.K., Jiménez M.A., and Nieva J.L. (2016). Structural basis for broad neutralization of HIV-1 through the molecular recognition of 10E8 helical epitope at the membrane interface. Sci Rep. *In press*.

VIII. Hjelm A., **Rujas E**., Zhe Z.; Alexandros K.; David V.; Dirk S. and de Gier, J.W. (2016). Tailoring Escherichia coli for the rhamnose PBAD promoter-based production of membrane and secretory proteins. ACS Synthetic Biology. *Submitted*

RESUMEN

Mecanismos de unión a la hélice MPER en la interfase de membrana por anticuerpos anti-VIH y su implicación para la neutralización del virus

Introducción

El VIH (virus de la inmunodeficiencia humana) es el agente causante del SIDA (síndrome de inmunodeficiencia adquirida). Fue aislado por primera vez en 1983 y, a pesar de los innumerables avances en el campo de la virología y farmacología, a día de hoy se desconoce un tratamiento antiretroviral que cure o una vacuna efectiva que prevenga la enfermedad. Esto ha conllevado a que el VIH se haya convertido en un problema de salud mundial con aproximadamente 36.7 millones de personas infectadas a finales de 2015 según los datos recogidos por la organización mundial de la salud (Informe de 2016).

El diseño de una vacuna constituye una de las estrategias con mayor potencial para la lucha contra el VIH. La diana para el desarrollo de dicha vacuna es la proteína de envoltura (Env) denominada gp160 que se localiza en la superficie de la membrana viral. Cada unidad funcional de gp160 está constituida por un trímero de heterodímeros, formados a su vez por las glicoproteínas gp120 y gp41 (Wyatt and Sodroski, 1998). La subunidad gp41 está constituída por varios dominios que incluyen un péptido de fusión (FP), los dominios helicoidales (NHR y CHR), una región externa próxima a la membrana (MPER), un dominio transmembrana (TMD) que actúa de anclaje de cada monómero a la membrana del virus y un dominio citoplasmático (CTD) (FIG 21A).

El proceso de infección comienza con el reconocimiento de la célula diana mediante la unión de la subunidad soluble gp120 al receptor CD4/ co-receptores CXCR4/CCR5 de los linfocitos T (Klatzmann et al., 1984). Dicho proceso desencadena una serie de cambios conformacionales que culminan con la inserción del FP en la membrana celular. La posterior reorganización de las regiones HR1 y HR2 en una estructura de 6 hélices de bajo contenido energético (Melikyan, 2008) provoca el acercamiento de las membranas (Blumenthal et al., 2012; Melikyan, 2011). FP y MPER desestabilizan la membrana celular (Apellaniz et al., 2014a) y viral (Apellaniz et al., 2014b; Suarez et al., 2000; Vishwanathan and Hunter, 2008), respectivamente, contribuyendo a su fusión y, por tanto, a la liberación del material genético del virus en el citoplasma de la célula diana.

A pesar del esfuerzo realizado en el desarrollo de una vacuna en los últimos años, únicamente se ha logrado alcanzar un 31 % de protección frente a la infección por el VIH (Haynes et al., 2012a; Rerks-Ngarm et al., 2009). El escaso éxito en la búsqueda de una vacuna anti-HIV se debe en cierta medida a los mecanismos de evasión que ha desarrollado el virus (Johnson and Desrosiers, 2002). La hipervariabilidad genética del virus provocada por la falta de actividad exonucleasa de la polimerasa del VIH (Parvin et al., 1986) constituye uno de los factores mas importantes en la habilidad del virus para evadir el sistema inmunitario. Sin embargo, la secuencia MPER presenta un alto grado de conservación debido a su importante función como agente promotor de la fusión requerida para la entrada del virus en la célula diana (Apellaniz et al., 2011; Apellaniz et al., 2014b; Salzwedel et al., 1999). Como consecuencia, los anticuerpos dirigidos contra esta región son denominados anticuerpos de alto espectro ya a que son capaces de neutralizar una gran variedad de cepas y aislados clínicos del virus (Binley et al., 2004; Huang et al., 2012; Kwong and Mascola, 2012; Stiegler et al., 2001).

Entre los anticuerpos anti-MPER de mayor espectro descritos actualmente se encuentran los anticuerpos 4E10 y 10E8. La actividad neutralizante de estos anticuerpos es dependiente de residuos hidrofóbicos localizados en el extremo de la región determinante de complementariedad de

la cadena pesada 3 (CDR-H3) (Alam et al., 2007; Cardoso et al., 2005; Huang et al., 2012; Sanchez-Martinez et al., 2006a; Scherer et al., 2010). Dichos residuos no están implicados en la interacción directa con el epítopo. Sin embargo, y debido al carácter anfipático del MPER que localiza esta región en la interfase de la membrane del virus, son imprescindibles para mediar la unión del anticuerpo al MPER en el contexto de una membrana lipídica (capítulos 3-6). Como consecuencia, el anticuerpos 4E10 presentan cierto grado de auto/polireactividad como demuestra su capacidad para interaccionar directamente con membranas celulares (Alam et al., 2007; Alam et al., 2009; Scherer et al., 2010). Sin embargo, y a pesar de reconocen secuencias solapadas de MPER, el anticuerpo 10E8 no es capaz de reconocer membranas lipídicas (Huang et al., 2012) sugiriendo mecanismos distintos en el bloqueo del virus.

Resultados y discusión

En esta tesis, se ha llevado a cabo un estudio detallado de la función que desempeña el lazo CDR-H3 de los anticuerpos 4E10 y 10E8 en la unión y neutralización del VIH, así como de la contribución de la unión directa a lípidos en el mecanismo de neutralización del anticuerpo 4E10. Por ello, uno de los objetivos de esta tesis ha consistido en poner a punto la expresión de Fab-s recombinantes en *E. coli*. La expresión en bacterias facilita la manipulación genética de estos especímenes para su uso en cristalografía, y ha permitido la realización de diferentes ensayos biofísicos que requieren altas concentraciones de material y marcajes con amino ácidos no-naturales o moléculas fluorescentes.

Por otra parte, el diseño racional de un inmunógeno capaz de inducir la producción de anticuerpos funcionales similares al 4E10 y 10E8 constituye un aspecto fundamental en el desarrollo de vacunas anti-MPER. Estudios estructurales recientes sobre la estructura del dominio MPER-N-TMD (^{671}NWFDITNWLWYIK^{683}-^{684}LFIMIVGGLV$^{693)}$ por resonancia magnética nuclear (RMN) (Apellaniz et al., 2015) revelan la existencia de una hélice continua

delimitada por dos regiones flexibles (subrayados). Estos datos cuestionan el modelo actual que propone que la hélice MPER se dispone de forma paralela la membrana hasta la Lys-683, que presuntamente marca el inicio de la TMD, o dominio de anclaje de la proteína a la membrana del virus, el cual adoptaría una orientación perpendicular a ésta. Por lo tanto, este modelo implica un giro en la hélice de aproximadamente 90º y un ángulo de aproximación de los anticuerpos al MPER perpendicular a la membrana. En el capítulo 3 se comparó la afinidad del anticuerpo 4E10 por un péptido que abarca la hélice ininterrumpida MPER-N-TMD ($MPER_{(671-693)}$) con la de un péptido truncado en posición Lys-683 ($MPER_{(656-683)}$). Los datos revelaron que preservar la hélice MPER-N-TMD no solo favorece la unión del anticuerpo 4E10 a su epítopo sino que inhabilita su reconocimiento por anticuerpos no neutralizantes (desprovistos del extremo del CDR-H3) cuando éste es presentado en un contexto de membrana.

Con el objetivo de establecer las bases moleculares que expliquen aspectos funcionales del anticuerpo 4E10 como su unión al virus y mecanismo de neutralización, en primer lugar se investigó el papel que desempeña el lazo CDR-H3 en dichos procesos (capítulo 4). Para ello se llevó a cabo un estudio comparativo del anticuerpo neutralizante 4E10 en presencia y ausencia del péptido $MPER_{(671-683)}$ y así como de dos versiones no neutralizantes del mismo (W/D-W/D y Δloop). Los datos revelan que la unión de dichos anticuerpos al péptido $MPER_{(671-683)}$ en solución es indistinguible desde un punto de vista estructural y energético. Por lo tanto, la diferencia entre el anticuerpo neutralizante y los no neutralizantes está relacionada con la capacidad de reconocer la gp41 en el contexto de la proteína nativa inserta en membranas biológicas.

La información extraída de los resultados cristalográficos en presencia y ausencia de ligando, revela que la unión al péptido supone una menor disminución de la flexibilidad el lazo CDR-H3 en comparación con el resto de lazos implicados en la unión. Esta observación, indica la posible existencia de interacciones adicionales entre el CDR-H3 y el antígeno que no están satisfechas en la unión al péptido $MPER_{(671-683)}$. En línea con esta hipótesis en

los capítulos 5 y 6 se han identificado interacciones específicas no covalentes entre el Trp100b$_{HC}$ del CDR-H3 de los anticuerpos 4E10 y 10E8 con la TMD. Además se ha establecido una correlación entre la formación de dichas interacciones en la interfase de la membrana y la capacidad neutralizante de ambos anticuerpos. Estos datos sugieren la formación de un complejo péptido-lípido-anticuerpo de alta estabilidad capaz de fijar la conformación del MPER de modo que inhabilite su función desestabilizadora de la membrana viral interrumpiendo así con el proceso de fusión.

Es probable que la potencia del anticuerpo dependa en parte del estadío de la fusión en el cual cada anticuerpo sea capaz de unirse. Se ha descrito previamente que el anticuerpo 10E8 es capaz de unirse a viriones en un estado prefusogénico (Huang et al., 2012) mientras que el 4E10 reconoce un intermediario de fusión (Frey et al., 2008) tras el reconocimiento de los receptores/correceptores en la célula diana (Binley et al., 2003; Dimitrov et al., 2007). La estructura del complejo 10E8-MPER$_{(664-690)}$ resuelta por rayos X en el capítulo 5 demuestra la capacidad del anticuerpo 10E8 de rotar su dominio constante disminuyendo así los impedimentos estéricos ejercidos por la subunidad gp120 y facilitando así su unión a la Env en estado prefusogénico. Además, la orientación de la región C-terminal del péptido MPER$_{(664-690)}$ en dicha estructura sugiere que el anticuerpo adquiere una posición paralela al plano de la membrana al unirse a la gp41, consistente con la estructura obtenida por Cryo-EM de la Env native unida al 10E8. Por lo tanto, estos datos refuerzan la existencia de una hélice ininterrumpida que engloba el MPER y la parte N terminal de la TMD, la cual penetraría en la membrana con un grado de inclinación.

A diferencia del 10E8, el 4E10 no es capaz de unirse a viriones en el estado prefusogénico y por consiguiente, una vez producida la activación, dispone de un intervalo de tiempo limitado para unirse a su epítopo (Binley et al., 2003; Dimitrov et al., 2007). El estudio llevado a cabo en el capítulo 7 sugiere que el anticuerpo 4E10 se comporta como una proteína periférica de membrane. Así, este anticuerpo habría adquirido la habilidad de interaccionar con membranas cargadas negativamente (membrana viral) para maximizar la

eficiencia de unión del anticuerpo a su epítopo en el corto intervalo de tiempo que dura el proceso de fusión. Los datos sugieren que dicha capacidad incrementa la velocidad del anticuerpo 4E10 de unirse a su epítopo presentado en la membrane del virus.

En conclusión, los datos obtenidos en esta tesis aportan información relevante para el diseño racional de vacunas anti-MPER capaces de generar anticuerpos con características similares al 4E10 y el 10E8.

Chapter 1

GENERAL INTRODUCTION

In 1983, the human retrovirus that was ultimately termed Human Immunodeficiency Virus type 1 (HIV-1) (Coffin et al., 1986) was isolated for the first time (Barre-Sinoussi et al., 1983; Gallo et al., 1984; Levy et al., 1984). This virus constitutes the causative agent of the Acquired Immune Deficiency Syndrome (AIDS), one of the current leading global health problems. Despite of the innumerable advances in virology, pharmacology and clinical fields throughout these years, 36.7 million people remained infected by HIV by the end of 2015 (WHO, 2016), turning AIDS into a worldwide pandemic.

Zidovudin (AZT) was the first anti-HIV drug approved by the U.S. Food and Drug Administration (FDA) in 1987. However, it was not until the mid-1990 when antiretroviral therapy (ART) based on protease inhibitors allowed a sustained control of viral replication, resulting in a sharp decrease in morbidity and mortality caused by HIV infection (Palella et al., 1998). Since then, 23 additional antiretroviral agents inhibiting different steps of the viral life-cycle have been identified. Combination of different ART agents gave rise to the standard treatment known today as “Highly Active Antiretroviral Therapy” (HAART) that progressively turned HIV infection into a chronic controllable disease. Hence, HAART provides a long-term therapy, favoring immune system recovery, reducing the risk of transmission and, hence, hampering virus spread. However, HAART is unable to eradicate HIV infection. Moreover, exposure to long-term medication often causes undesirable side-effects in the treated patients. These shortcomings strengthen the need of developing a protective vaccine. In this regard, RV144 constitutes to date the most successful vaccine trial, which provided a modest protection (31 %) against HIV infection (Haynes et al., 2012a; Rerks-Ngarm et al., 2009).

In addition, the passive administration of broadly neutralizing antibodies (bNAbs) has been proposed as a plausible alternative for infection treatment. These antibodies can act antivirally by targeting conserved regions on the surface envelope protein (Env). As a proof-of-concept, bNAb-based therapies have been proven effective against the chimeric simian-human

immunodeficiency virus (SHIV) in macaques (Barouch et al., 2013; Moldt et al., 2012; Shingai et al., 2013) and against HIV-1 in humanized rodent models (Balazs et al., 2012; Gruell et al., 2013; Halper-Stromberg et al., 2014; Klein et al., 2012b; Veselinovic et al., 2012). Moreover, transient viral control has also been observed in humans passively administrated with bNAbs in a phase 1 study (Caskey et al., 2015). Besides, viral suppression can be achieved after medication interruption (Scheid et al., 2016) further supporting the efficacy of bNAbs-based therapies.

1.1. NEW TECHNIQUES FOR HUMAN MONOCLONAL ANTIBODY ISOLATION

Isolation of monoclonal antibodies (mAb) that arise from an effective immune response might constitute the starting point for the so-called “structural vaccinology” methodology. This approach proposes the use of isolated bNAbs for structural definition of antigens that can guide vaccine design as has been succesfully demonstrated for the respiratory syncytial virus (McLellan et al., 2013). Until recently, a mayor bottleneck in the field was the absence of high-throughput methods for the selection of specimens. Antibody production was limited by the use of immortalized B-cell lines (Kohler and Milstein, 1975; Lanzavecchia et al., 2007; Steinitz et al., 1977). The yield of this methodology is remarkably low and time consuming. Besides, only a fraction of the B-cell population becomes immortalized resulting in the loss of a vast amount of relevant antibodies.

Another method for mAb isolation is based on the phage display technology (Barbas et al., 1991; McCafferty et al., 1990) (FIG 1). This method requires the generation of cDNA libraries of variable heavy (V_H) and variable light (V_L) chain fragments. For that, mRNA encoding both chains is isolated from a pool of B-cells, converted into cDNA by reverse transcription (RT)-PCR and subsequently cloned into the M13 phage vector. Either the V_H or the V_L gene is fused to the structural protein PIII gene and the resulting plasmid used

to transform *E. coli* in the presence of a helper phage (Schofield et al., 2007). The phages secreted from *E.coli* display on their surface a fusion protein consisting on the phage PIII protein and a specific antibody properly paired in the periplasm of the bacteria through a disulfide bond (FIG 1). Surface exposure of the antibody in the bacteriophage coat allows the specific selection in a subsequently antigen-binding screening, an enrichment step known as "panning". Bound phages can be amplified by *E. coli* reinfection and the selected V_H and V_L sequences isolated and further sequenced. However, since chain pairing occurs *in vitro* in a random fashion, the resulting antibodies do not necessarily represent the natural antibody repertory. Besides, phage selection is based on binding screenings, limiting the use of this technology to the isolation of antibodies targeting known epitopes, but missing those targeting new, undefined ones.

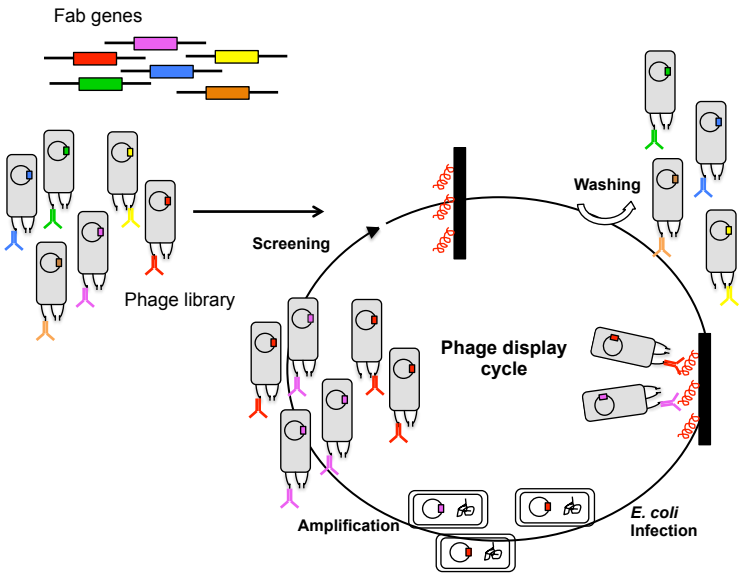

FIG 1. Phage display methodology for antibody selection. This technology is used for the generation of DNA libraries encoding the heavy and light chains of the antibodies generated by a B-cell population. The cDNA is inserted into filamentous phage genes codifying for phage coat protein. The antibody is expressed as a fusion protein displayed in the phage surface. Specific monoclonal antibodies (mAbs) selection is performed by repetitive cycle of screening, bacteria infection and amplification.

In the last few years, several methodologies for the rapid and efficient generation of human mAbs have been developed. Single-cell sorting coupled to RT-PCR represents an important advance in this field (Tiller et al., 2008). This method uses specific cell-surface markers of B-cell subtypes as baits for the identification of a desired B-cells population. Targeting of such markers with a fluorescent antibody enables isolation of specific single B-cells by using fluorescence-activated cell sorting (FACS). In addition, immunogens based on protein scaffolds can also be used as baits in this procedure (Scheid et al., 2009). Antigenic positive cells are placed on individual wells for amplification by RT-PCR, allowing further sequencing of the cDNA encoding the antibody chain segments produced by a particular B-lymphocyte. (Li et al., 2010). Moreover, improved methods for B-cell culturing and activation based on cytokine-secreting feeder cells, together with high-throughput binding and functional screening (Smith et al., 2009) have also contributed to the discovery of new generations of human mAbs with a broad spectrum of biological activity.

1.2. THE HIV-ENVELOPE SPIKE: A TARGET FOR BROADLY NEUTRALIZING ANTIBODIES

HIV-1 genome is composed of 9 genes organized in 3 open reading frames that encode all viral proteins. Among them, *gag*, *pol* and *env* are the most important viral genes of HIV. *Gag* and *pol* encode the structural and enzymatic proteins necessary for viral assembly and replication, respectively (Freed, 2015). *Env* encodes the envelope spike responsible for viral entry into host cells. The precursor polyprotein termed gp160, undergoes oligomerization (mainly trimers) (Earl et al., 1990; Schawaller et al., 1989) and several posttranslational modifications in the endoplasmic reticulum (ER) and Golgi, in its route to the plasma membrane, from where nascent virions bud (FIG 2).

Posttranslational modifications involve massive glycosylation (50 % of the final mass) (Doores et al., 2010) and protein cleavage by furin-like proteases (Hallenberger et al., 1992). Protease cleavage renders the soluble

gp120 and the membrane-bound gp41 subunits that remain linked through non-covalent interactions (see section 1.2.1). Hence, the HIV-1 envelope glycoprotein (Env) exposed on the surface of the virus, is comprised by trimers of non-covalently associated heterodimers. Furthermore, Env trimeric spikes incorporate at very low density into virions (8-14 spikes/virion) (Zanetti et al., 2006; Zhu et al., 2006). This is supposed to hamper B-cell activation since the wide spacing between spikes disfavors B-cell receptor cross-linking. Consequently, B-cell activation as an initial step in the generation of antibodies capable of blocking the virus becomes very challenging and not trivial.

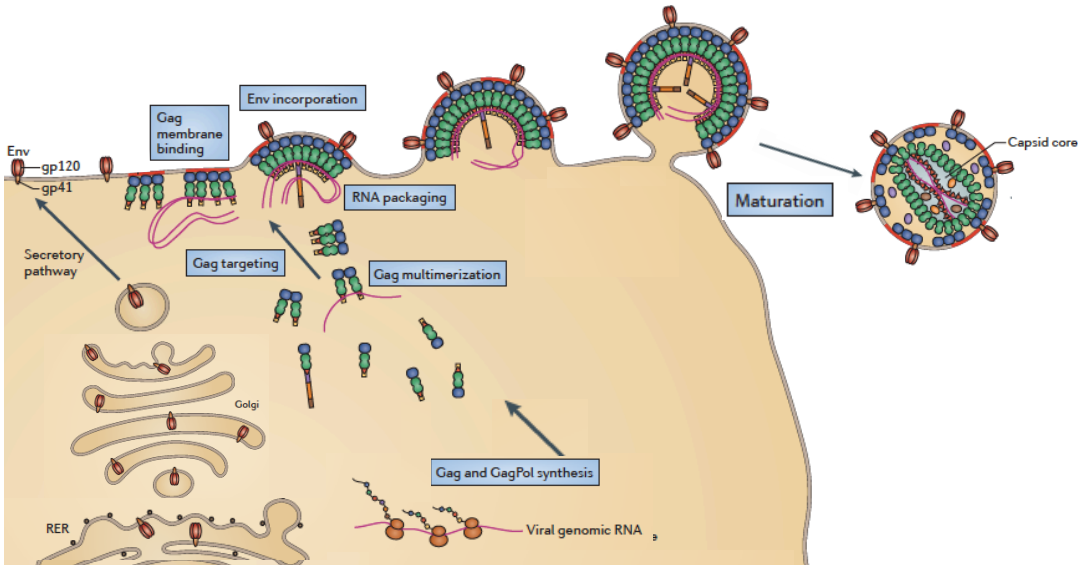

FIG 2. HIV replicative cycle. HIV assembly, release and maduration steps are shown. The Env glycoprotein is synthesized and posttranslationally modified in the endoplasmic reticulum (ER) and the Golgi and transported via the secretory pathway to the plasma membrane. Oligomers of Gag bound to viral RNA are anchored to the plasma membrane through interaction of its amino-terminal myristate with phosphatidylinositol-(4,5)-bisphosphate (PI(4,5)P2). The resulting complex constitutes the immature virion that buds from the plasma membrane. Subsequent cleavage of Gag gives rise to mature virions with conical capside cores. Adapted from (Freed, 2015).

The Env glycoprotein complex gp120/gp41 also promotes fusion of viral and host cell membranes, a process required for gaining access to the cytoplasm of host cells and initiating the infectious replicative cycle. The soluble subdomain gp120 is responsible for recognition of the CD4 receptor (Klatzmann

et al., 1984) and CXCR4/CCR5 coreceptors (Deng et al., 1996; Feng et al., 1996) in host cells. Typically receptor/coreceptor engagement triggers subsequent conformational changes that remodel Env trimers from a close to an open state competent in fusion (FIG 3).

The N- and C- termini of gp120 are positioned close to each other and encircled by four helices of gp41, composing a structural motif that stabilizes the heterodimer configuration (Pancera et al., 2014) (FIG 3ii). Moreover, insertion of a methionine residue into a tryptophan clasp fastens the native metastable conformation of gp41 (Pancera et al., 2014) (FIG 3i). Gp41 contains two distinct types of structural elements that take part in the subsequent steps of the fusion process. The first type is constituted by the membrane-transferring fusion peptide (FP) and the membrane-residing regions membrane-proximal external region (MPER) and transmembrane domain (TMD). The open conformation of Env triggered by receptor/coreceptor binding causes contact loss between gp120 and gp41 and opening of the tryptophan clasp that holds gp41. Consequently, FP is released from its native state conformation and poised for insertion into the target cell membrane. The second type of elements comprise the heptad repeat helical domains (NHR and CHR) that upon gp120-receptor binding, assemble into an energetically stable 6-helix bundle (6-HB) (Melikyan, 2008) (FIG 3iii). Consequently, FP (inserted in the membrane host) and MPER/TMD (anchored to the viral membrane through the TMD) are placed into spatial proximity enabling membrane merge (Blumenthal et al., 2012; Melikyan, 2011).

However, close approximation of membranes pulled together by a growing 6-HB is hampered by the strong, repulsive hydration and electrostatic forces operating at their surfaces, which consequently prevent the initial mixing of their lipid constituents (Chernomordik and Kozlov, 2003; Kozlov et al., 2010). Thus, it has been argued that, beyond the anchoring effect, the N-terminal FP inserted into the target membrane could generate focal points of dehydration and hydrophobic destabilization required for fusion (Apellaniz et al., 2014a).

Complementarily, it has been suggested that MPER/TMD domain might prime the opposing viral membrane for fusion (Apellaniz et al., 2014b; Suarez et al., 2000; Vishwanathan and Hunter, 2008).

The extended gp41 structure that presumably precedes 6-HB formation is denoted as the pre-hairpin intermediate. The mature form of gp160 represents the only viral target for bNAbs. Due to the high dynamism of Env during fusion, conformational information of each of the intermediate states constitutes a powerful tool for the rational design of effective immunogens.

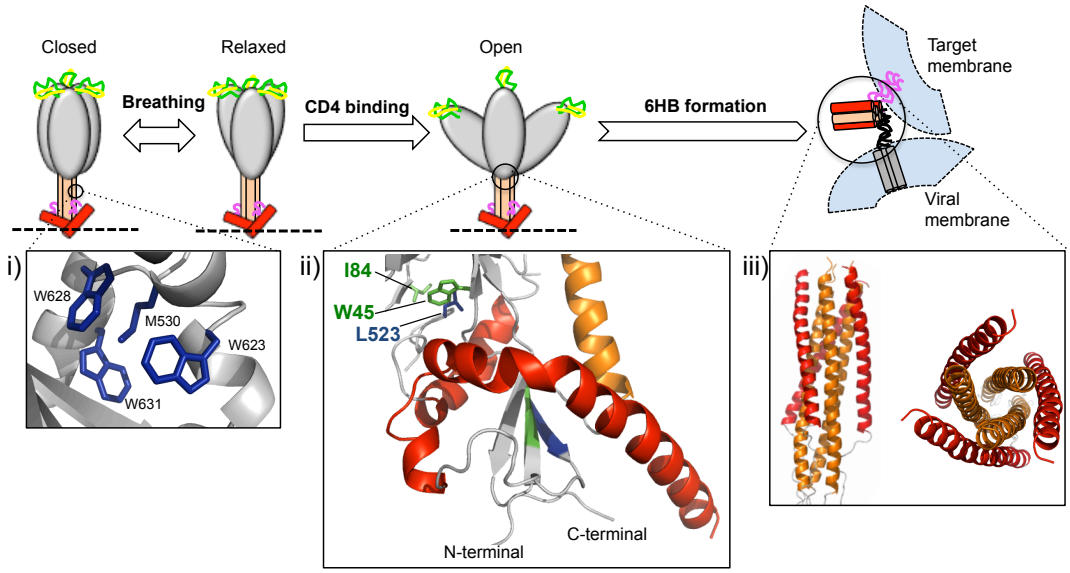

FIG 3. Conformational rearrangement of HIV-1 Env glycoprotein upon fusion activation. Before receptor/coreceptor binding Env trimer alternates between a closed and a slightly more open conformation referred to as relaxed conformation. The equilibrium between both Env states is known as Env breathing. Upon CD4 binding, the clasp formed between gp41 M530 and the surrounding W residues (i) is broken leading to the disassembly of the collar helix (red) that wraps the N- and C- terminus of gp120 (ii). Consequently, the non-covalent interactions displayed in (ii), that kept gp120 and gp41 together, are lost (residues in green and blue belong to gp120 and gp41, respectively). Gp120 release leads to the exposure of the gp41 fusion peptide (FP) that was protected within the subdomains interface. The FP (pink) anchors the plasma membrane of the target cell and the formation of the stable coiled-coil (6-HB) (iii) brings both membranes in close proximity. Finally, the plasma and viral membrane destabilization induced by the FP and MPER, respectively, culminate the fusion process. PDB entries: 4TVP (SOSIP) and 2EZO (6-HB).

1.2.1. Three-dimensional structure of the HIV Env glycoprotein.

Over the last 15 years, extensive effort has been focalized on the production of a high-quality recombinant protein suitable for solving with high-resolution the trimeric structure of the HIV Env. The poor stability of the gp120/gp41complex hampered initial attempts in the field. Several strategies such as the removal of the furin-cleavage site or the addition of heterologous trimerization motifs were followed (Pancera et al., 2005; Yang et al., 2002). However, the resulting trimers failed to adopt a native-like fold (Ringe et al., 2013). A stable trimeric architecture of the complex was finally achieved after incorporation of two modifications in the gp120/gp41 sequence: i) a disulfide bond (SOS) between residues 501 of gp120 and 605 of gp41 (Binley et al., 2000) and ii) an isoleucine-to-proline substitution at position 559 in HR1 of gp41 (IP) (Sanders et al., 2002). The resulting Env trimer based on a clade A BG505 background and truncated at residue 664 provided a high-resolution view of the trimeric structure of Env at 4.7 and 5.8 Å using X-ray crystallography (Julien et al., 2013) and cryo-EM (Lyumkis et al., 2013), respectively. Both initial structures were solved in complex with anti-gp120 bNAbs. However, the antibodies did not alter the native conformation of the protein, as confirmed by the high structural similarity between these initial structures and a recent ligand-free trimer stabilized by an additional disulfide bond within gp120 (Kwon et al., 2015).

The high-resolution structures of the BG505-SOSIP trimer exhibit the antigenic surface of the HIV-envelope glycoprotein in the prefusion state (FIG 4). Gp120 subunit is organized into two parallel major domains (inner and outer domain) linked by a bridging sheet built by four antiparallel strands. This subunit contains different variable loops located at the outside of the structure. Loops V1 and V2 adopt a 4- stranded greek-key β-sheet motif at the top of the trimer forming the trimer apex and maintaining the integrity of the protomer (Julien et al., 2013; Lyumkis et al., 2013). Underneath these loops sit the two anti-parallel β-strands that form the β-hairpin structure of V3, responsible for coreceptor

(CCR5/CXCR4) engagement. On the contrary, V4 and V5 project outward from the surface of gp120 without making contacts with other variable loops. In addition, the surface of gp120 is coated mainly with the high-mannose glycan (Bonomelli et al., 2011; Doores et al., 2010). As compared to the more complex glycans present in monomeric gp120 or gp140 recombinant proteins (Pritchard et al., 2015), the presence of this type of glycan in large proportions (46 % to 98 % of the total glycans) is consistent with the tight assembly of the gp160 trimer that prevents glycan maturation in the Golgi during its biogenesis.

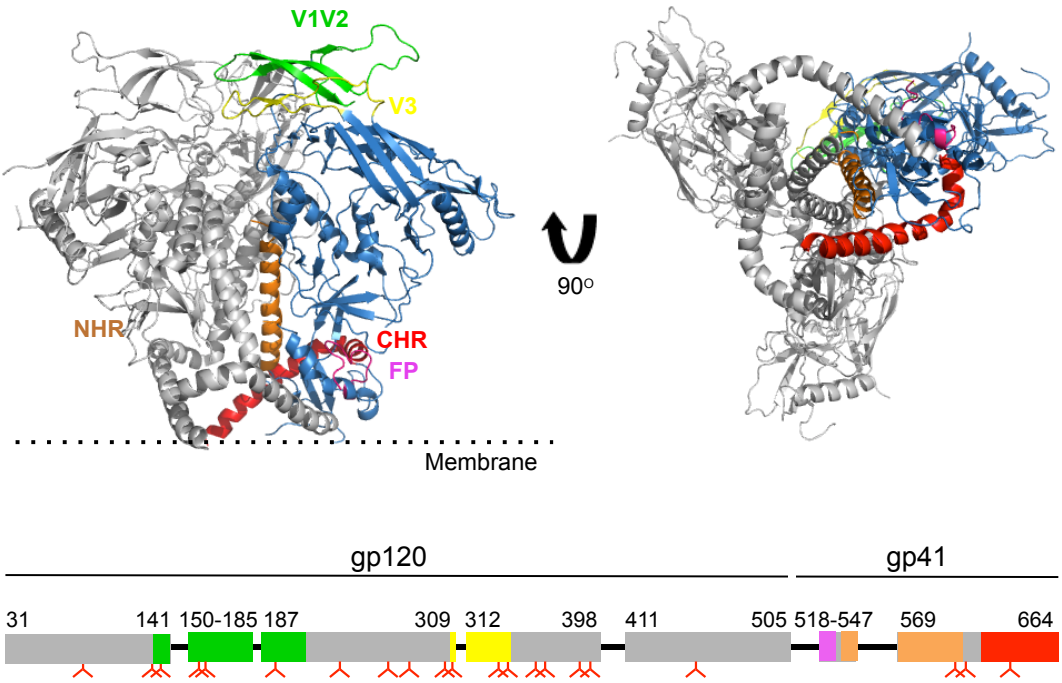

FIG 4. Three-dimensional structure of the prefusion HIV envelope spike. The gp41 subunit constitutes a central stalk of the trimer with the heptad repeat helical domains, NHR (orange) and CHR (red), oriented perpendicular and diagonal to the membrane, respectively. The fusion peptide (pink) is partially solved and adopts an extended conformation. The structure and location of the functional domains within one protomer of gp120 are also highlighted. The hypervariable V1/V2 loops (green) occupy the apex of the trimer, partialy masking V3 loop (yellow) located underneath. The bottom diagram represents the solved residues within gp120 and gp41 and the position of the glycans within each subunit. The structure was rendered by overlapping Env trimer structures with PDB codes 4RCO and 4TPV.

A more complete picture of the structural organization of gp41 could be obtained from the crystal structure of the SOSIP trimer solved at a higher resolution (3.5 Å) (Pancera et al., 2014). As mentioned before, this new

ectodomain structure revealed gp120 N- and C- terminal strands anchored into a hydrophobic pocket formed by a gp41 helix collar at the base of the structure (FIG 3ii). Furthermore, resolution of the protomer structure highlights the complete set of non-covalent interactions between both subunits: i) Leu 523 within a non-structured segment of the N terminus of gp41 interacts hydrophobically with residues Trp 45 and Ile 84 from gp120; ii) the gp41 cysteine loop (Cys 598–Cys 604 disulfide) establishes hydrogen bonds with the N terminus of gp120 and iii) the gp41–gp120 interface builds a hydrophobic pocket where part of the FP is shielded from the solvent until activation of the fusion cascade.

In addition, this structural arrangement provides the grounds to understand fusion activation at the molecular level. In the prefusion conformation state a shorter helix (572–595) of HR1 forms a parallel coiled-coil at the center of the trimer in a position perpendicular to the membrane. On the contrary, a helix (628-664) encompassing most of HR2 forms a long curved helix at the periphery of the protein adopting a diagonal orientation to the membrane (FIG 4). Upon fusion activation, helix (572–595) is extended and arranged with the helices from the neighboring protomers in a coiled-coil conformation. This arrangement leaves hydrophobic grooves on the outer surface of the coiled-coil where HR2 helixes from each protomer of the trimer will bind in an antiparallel fashion (FIG 3iii). The resulting stable core formed by a bundle of 6 helixes represents the post fusion state of gp41.

The 6-HB structure encompassing HR1 and HR2, extended towards the FP (531-581) and MPER (628-681), respectively, has been solved by X-ray crystallography (Buzon et al., 2010). Unfortunately, structural atomic information of residues located beyond Asp664 in the context of the native state of the trimer is missing despite the availability of the CryoEM structure at 8.8 Å of a SOSIP trimer harbouring the MPER and TM domains (Lee et al., 2016). However, the NMR structure of overlapping peptides in membrane mimetics suggests that the MPER/TMD region is organized as a continuous helical

structure with a flexible element at position 690 (Apellaniz et al., 2015). Hence, in a prefusion state, the MPER-TMD region is proposed to insert into the membrane with a tilted orientation and twist at the residue Gly690 to follow a direction parallel to the bilayer normal (FIG 5). This conformation would satisfy most of the aromatic interactions with the membrane interface at its N-terminus and adjust the length of the TMD anchor to the membrane thickness. This structural arrangement is in good agreement with the recent NMR structure of the trimeric TMD solved in a bicelle membrane model (Dev et al., 2016). Similarly, this structure exhibits a kink within a continuous helical TMD monomer dividing the TMD segment into two halves stabilized by different modes of assembly. The N- terminal part is stabilized by a coiled-coil motif (686-696) while the C-terminal part is held together by polar contacts within the hydrophilic core (704-712) (FIG 5).

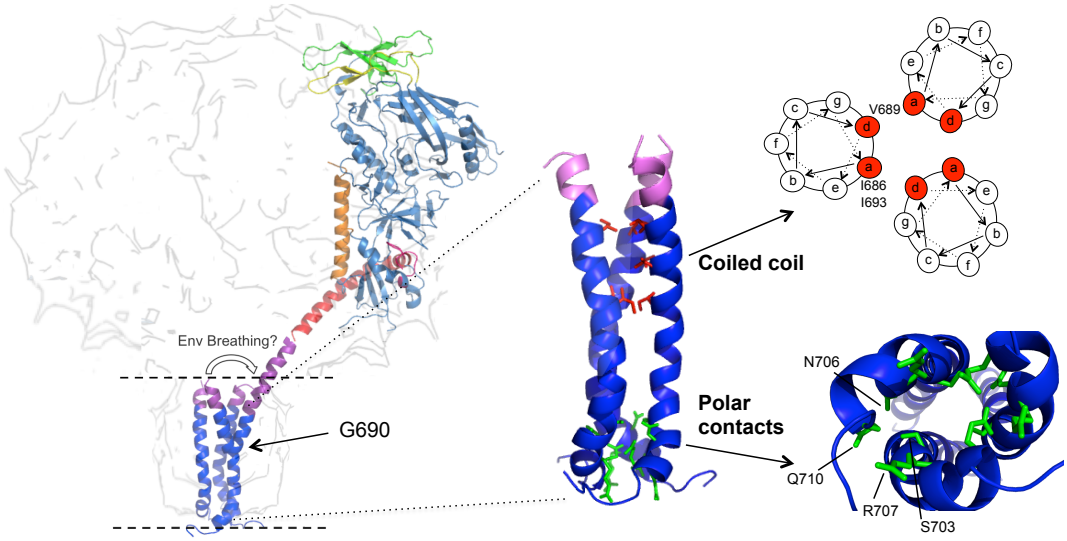

FIG 5. Modelling of the prefusion conformation of the full HIV Env glycoprotein. The overall structure was obtained by overlapping of structures with PDB entries 4TVP (SOSIP), 2MG1, 2MG2 and 2M8M (TMD and MPER) and 5JYN (TMD trimer). The MPER domain is extended towards the TMD as an uninterrupted helix with a flexible kink at position 690 (Apellaniz et al., 2015). This kink bends the TMD helix possibly providing flexibility to the whole trimer to breath between a closed and a relaxed conformation. Close up view of the TMD trimeric domain to highlight the two main interactions responsible for its trimerization. Hydrophobic residues (displayed in red) within the N-terminal half of the structure form a well-defined coiled-coil motif while the C terminal hydrophilic core of the trimer (green) is stabilized by polar contacts.

1.2.2. Anti-HIV broadly neutralizing antibodies

In spite of the accessible location of HIV-1 Env on the virus surface, elicitation of a protective response occurs only in 10-25 % of HIV-infected individuals (Doria-Rose et al., 2009; Stamatatos et al., 2009) of which only 1 % (elite neutralizers) exhibits high neutralization breadth and potency (Simek et al., 2009). The reason for the low frequency of patients capable of developing bNAbs resides on several mechanisms evolved by the virus to escape immune surveillance (Johnson and Desrosiers, 2002). One escape mechanism is based on the poor stability of the gp41/gp120 complex that often causes gp120 dissociation leaving non-functional gp41 stumps on the surface of the virus. These complexes are highly immunogenic and deviate the humoral response to other areas, precluding the development of antibodies that recognize and block functionally relevant, native Env structures (Moore et al., 2006). Moreover, the high mutational rate that arises from the HIV error-prone reverse transcriptase (Parvin et al., 1986), leads to an estimated 35 % sequence variation between virus subtypes known as clades (Gaschen et al., 2002). Another important feature of the virus that contributes to its escape from host immune responses relies on the extensive glycosylation of HIV Env that counts with an average of 24 potential N-glycosylation sites (PNGS) on gp120 and 4 on gp41. The high dense shield of glycans results in functional and conserved epitope masking. In addition, the viral membrane also plays a role in masking the conserved MPER segment possibly by interfering with the generation of an immune response against this region.

1.2.2.1. Epitopes targeted by HIV bNAbs: Sites of vulnerability

The evolutionary pressure imposed by antibody recognition has shaped the properties of the HIV Env glycoprotein. However, sequence and structural conservation of certain regions are required for viral function. Antibody targeting to those key sites known as “sites of vulnerability”, results in viral inhibition (FIG 6A). Production of stable native-like trimmers, accessibility to large cohorts of

infected individuals and development of multiple approaches for antibody isolation has led to identification of multiple, unprecedented bNAbs (Table 1 and FIG 6B). As a result, four main conserved sites susceptible to antibody neutralization were initially delineated within the HIV-Env spike: CD4-binding site on gp120 (CD4bs), V1/V2 site on gp120, glycan-V3 site on gp120 and MPER on gp41. More recently, new sites targeted by bNAbs have been identified on the gp120-gp41 interface (Sattentau, 2014) and within the FP of gp41 (Kong et al., 2016) targeted by bNAbs have been identified.

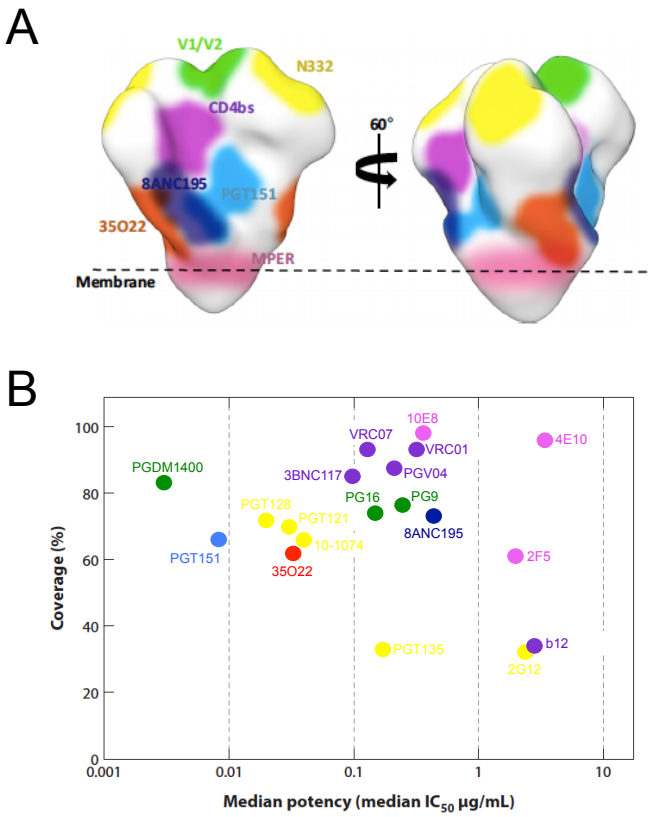

FIG 6. Sites of vulnerability recognized by bNAbs. A) Top and side views of regions on the surface of the HIV-1 Env trimer targeted by bNAbs. Reprinted from (Ward and Wilson, 2015). B) Breadth (percentage of viral clades neutralized with an IC_{50}< 50µg/mL) plotted against their potency of neutralization (median inhibitory concentration for all neutralization-sensible viruses). The bNAbs are colored according to the region targeted in A. Adapted from (Burton and Hangartner, 2016).

Table 1. List of bNAbs against HIV. Binding site specificity, total number of somatic hypermutations (SHM) in the light and heavy chains, length of the CDR-H3 and the tendency to be poly-/autoreactive are listed. Adapted from (Burton and Hangartner, 2016).

Env binding site	bNAb ID	CDR-H3 length	SHM (%) nt		Auto/Poly reactivity	Ref
			Heavy	Light		
CD4bs on gp120	b12	9	13.8	13.4	No	(Barbas et al., 1992; Burton et al., 1994)
	VRC01	14	29.7	16.6	No	(Wu et al., 2010)
	3BNC117	12	23.5	16.6	Yes	(Klein et al., 2012a)
	CH103	15	18.0	10.7	Yes	(Liao et al., 2013)
V1/V2 site on gp120	PG9	30	12.0	9.2	No	(Walker et al., 2009)
	PG16	30	13.1	12.2	No	(Walker et al., 2009)
	PGT145	33	16.2	15.5	n.d.	(Walker et al., 2011)
	CAP256-VRC26.09	39	12.8	9.7	n.d.	(Doria-Rose et al., 2014)
	PGDM1400	34	24.3	11.3	No	(Sok et al., 2014)
Glycan-v3 site on gp120	2G12	16	20.3	12.2	Yes	(Buchacher et al., 1994; Trkola et al., 1996)
	PGT121	26	17.8	15.5	n.d.	(Walker et al., 2011)
	PGT124	26	15.0	16.6	n.d.	(Walker et al., 2011)
	PGT128	21	19.0	8.7	n.d.	(Walker et al., 2011)
	PGT135	20	17.1	15.9	n.d.	(Walker et al., 2011)
	10-1074	26	26.7	30.1	n.d.	(Mouquet et al., 2012)
gp120-gp41 interface	PGT151	28	18.5	12.6	No	(Blattner et al., 2014; Falkowska et al., 2014)
	35O22	16	21.9	22.4	No	(Huang et al., 2014)
	8ANC195	22	27.2	14.9	Yes	(Scharf et al., 2014)
MPER on gp41	2F5	24	12.1	11.8	Yes	(Buchacher et al., 1994; Conley et al., 1994; Muster et al., 1993)
	4E10	20	6.8	4.7	Yes	(Buchacher et al., 1994; Zwick et al., 2001)
	10E8	22	19.4	14.2	No	(Huang et al., 2012)

Glycans were originally considered to decrease HIV immunogenicity since they are derived from the host ER and Golgi pathways during HIV replication. However, due to the immature nature of the glycans and its high dense clustering (not present in host glycoproteins), they constitute key motifs present in many of the binding sites of bNAbs. Specifically, the CD4bs and V1/V2 sites include the N-linked glycan at residue N160 on gp120, whereas the V3 site includes the N-linked glycan at residue N332 on gp120.

The CD4bs is built by the combination of regions from gp120 inner and outer domain together with the bridging sheet (Julien et al., 2013; Lyumkis et al., 2013). This functional site is located between gp120 subunits and therefore shielded by glycans from its own and other adjacent gp120 protomers. This location imposes significant steric constraints for antibody engagement and CD4bs has to be targeted with a specific angle of approach (Ryu and Hendrickson, 2012). Consequently, antibody evolution has evolved towards including gp120 loops D (276–283) and V5 (455-462) and glycan at residue N276 from neighboring gp120 as part of their epitopes (Diskin et al., 2011). V1/V2 site represents a glycopeptide epitope for bNAbs. The peripheral location pointing away from the core of the trimer allows sequence, length and glycosylation pattern diversity of this region without compromising gp120 structure. Hence, bNAbs targeting the V1/V2 loops have evolved to recognize a quaternary-structure involving both glycan contacts and to establish electrostatic sequence-independent interactions between a cationic protein surface in Env and the protruding tyrosine-sulfated anionic CDR-H3 (Gorman et al., 2016; McLellan et al., 2011). Similarly to V1/V2, the glycan-V3 site constitutes a carbohydrate-dependent epitope associated with a protein epitope (Kong et al., 2013; Mouquet et al., 2012; Walker et al., 2011). However, binding to pure high-mannose sugar clusters (Calarese et al., 2003) has been also reported. Consistent with the idea that glycan patches represent immunogenic regions, gp41-gp120 interface includes a glycan patch that extends from gp120 into gp41 (Huang et al., 2014; Scharf et al., 2014).

1.2.2.2. Antibody development during natural infection: unique features of anti HIV-1 bNAbs

Production of bNAbs capable of providing a protective response requires affinity maturation of the surface immunoglobulin (Ig) B-cell receptor (BCR) through somatic hypermutation and isotype-switching (FIG 7). This process is initiated with antigen recognition by the BCR of naïve B-cells that drives crosslinking of antigen receptor causing B-cell activation (Batista and Harwood, 2009). The antigen is internalized, processed and presented in the context of the class II mayor histocompatibility complex (MHC-II). The complex composed of the peptide and the MHC-II is recognized by specific helper T cells that trigger the signaling pathways required for B-cell proliferation. These events occur in the germinal centers of secondary lymphoid organs (Parker, 1993). Normally, helper T cells need to be activated by the same antigen to ensure self-tolerance. However, for virus particles, this linked recognition is less restrictive and do not necessarily require activation of B and T cells through exactly the same protein from the virus.

During B-cell proliferation, each cell division is accompanied by somatic mutations in the V-gene of the Ig, at a rate of 1 per 103 bases, 10^5-10^6 fold greater than the normal rate of mutation across the genome. This event, known as somatic hypermutation (SHM), has the potential to generate create B-cells with modified affinity for a certain antigen (Xu et al., 2007). B-cells with mutations that increase binding affinity for the antigen are selected and continuously subjected to rounds of division and mutation (FIG 7). Upon affinity maturation, selected B-cells can differentiate into plasma cells secreting high-affinity antibodies. Secretion requires isotype switching, a process that involves rearrangement of the C-gene. Alternatively, mature B-cells can differentiate into memory B-cells that confer long-lasting protection against subsequent encounters with the antigen (MacLennan, 1994; Rajewsky, 1996).

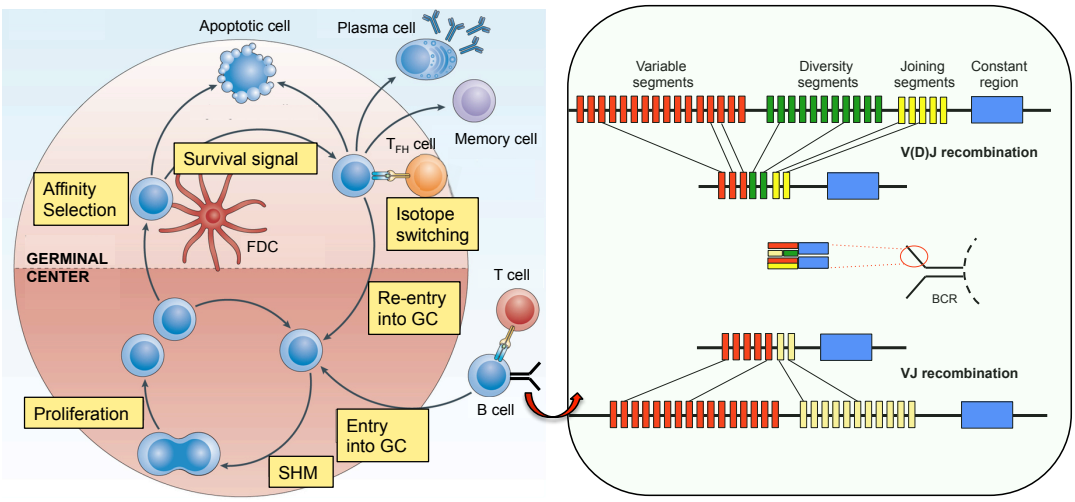

FIG 7. B-cell affinity maturation in the germinal centre (GC). Sequential recombination of the heavy (VDJ) and light (VJ) chain genes gives rise to antigen specific B-cell receptors (BCR) for antigen recognition. The BCR-antigen complex is presented to T cells for its activation and entry to the GC where B-cells undergo affinity maturation through somatic hypermutation (SHM). The resulting BCRs with a slightly different affinity for the antigen are selected by follicular dentritic cells (FDC) to die through apoptosis (mutations that decrease affinity) or to survive (mutations that increase affinity). Surviving B-cells can either undergo the same affinity maturation process to further increase their affinity and specificity for the antigen, or exit the GC as plasma cells or memory B-cells. Plasma cells undergo isotype-switching resulting in the secretion of high-affinity soluble antibody molecules. Adapted from (Heesters et al., 2014).

Chronic HIV infection, caused by an evolving virus, leads to the continuous exposure of variable antigens to B-cells. Hence B-cells have to undergo extensive cycles of affinity maturation in order to yield a high-affinity BCRs (Breden et al., 2011). Consequently, bNAbs isolated from HIV-1 infected individuals are generated 3-4 years after infection (Gray et al., 2011) and contain an unusually high level of SHM (Haynes et al., 2012b) (Table 1). As note before, extensive SHM usually occurs in the CDRs of the Ig gene. However, in the case of HIV bNAbs, the structural framework regions (FWR) also undergo substantial SHM, which is critical for broad neutralization (Klein et al., 2013a). Another remarkable feature of HIV-1 bNAbs is their long heavy chain CDR-H3 sequences (Table 1). Antibodies targeting the V1/V2 or V3 loops and the MPER sequence use long CDR-H3s to penetrate the glycan shield or the viral membrane, respectively. CDR-H3 loops of some bNAb can reach up to 34 residues in length (Table 1) compared to the average of 16 residues for other human Ig CDR-H3s (Tiller et al., 2007). A recent deep-sequencing study

identified up to 3.5 % of human mature naïve B-cells bearing CDR-H3s of a length ≥ 24 amino acids and an even smaller population of 0.43 % with CDR-H3s spanning 28 residues or more (Briney et al., 2012). This low occurrence is due to the auto-reactivity induced by long CDR-H3s that provokes the negative selection of those clones during B-cell development (Wardemann et al., 2003). Nevertheless, pre-existence of mature naïve B-cells with long CDR-H3s might be a prerequisite for generating some of the HIV-bNAbs that reach epitopes deeply located within the Env spike.

Most HIV-1 bNAbs, likely due to the extensive SHM, show very low or no detectable binding to Env when reverted to its non-mutated germline precursor (Kwon et al., 2016a; Ota et al., 2012; Xiao et al., 2009). Consequently, an increasing number of studies focus on B-cell ontogeny of each bNAb in order to identify Env immunogens responsible for their elicitation at different stages of development (Bonsignori et al., 2016; Doria-Rose et al., 2014; Liao et al., 2013). Furthermore, many of the HIV-1 bNAbs are poly-/autoreactive (Haynes et al., 2005; Verkoczy and Diaz, 2014; Wu et al., 2010; Wu et al., 2011) (Table 1). This property is not necessarily linked to the presence of long CDR-H3s, but it may be acquired during B-cell development due to the bypass of tolerance checkpoints (Mouquet and Nussenzweig, 2012; Wardemann et al., 2003). Correlation between polyreactivity and neutralization (Liu et al., 2015) has led to categorize polyreactivity as a mechanism to increased binding affinity by heteroligation (Mouquet et al., 2010) (Klein et al., 2013b).

1.3. BROADLY NEUTRALIZING ANTI-MPER ANTIBODIES: THE AIM OF THIS STUDY

MPER constitutes a conserved tryptophan-rich domain on the Env glycoprotein (FIG 8A) that represents a site of vulnerability targeted by neutralizing antibodies with remarkably high (4E10 and 10E8) (Huang et al., 2012; Muster et al., 1993; Stiegler et al., 2001) and moderate (2F5, Z13e1 and m66.6) (Nelson et al., 2007; Zhu et al., 2011) breadth. The crystal structures of

4E10 and 10E8 antibodies in complex with peptides harboring their epitopes reveal a highly unusual helical conformation of the peptides (Cardoso et al., 2007; Huang et al., 2012) in contrast to the more common extended conformations observed in other antibodies including 2F5 bNAb (Julien et al., 2008; Ofek et al., 2004) (FIG 8A).

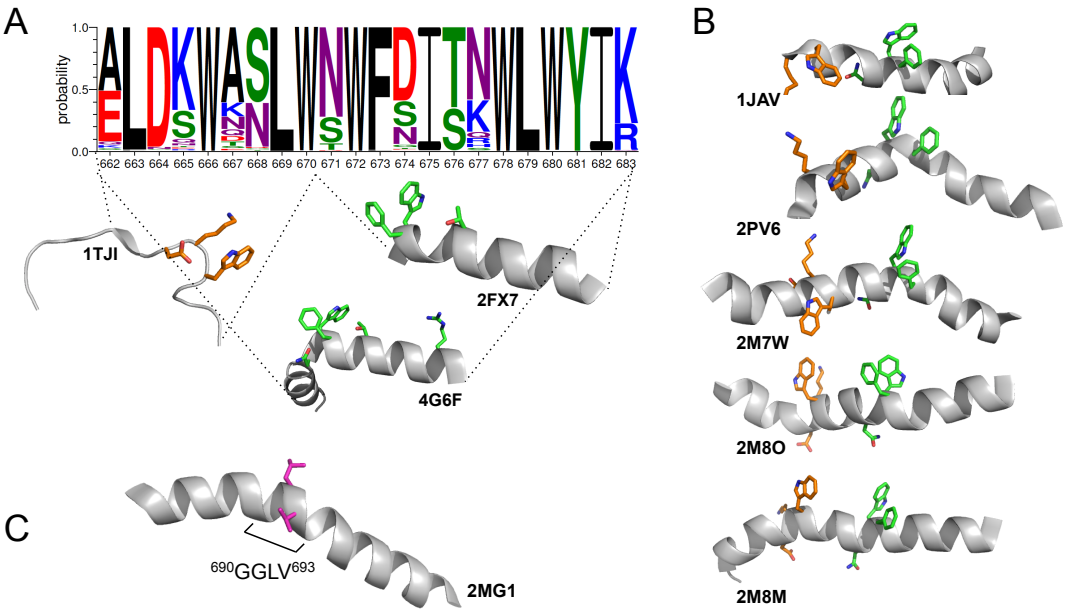

FIG 8. Sequence and three-dimensional structure of MPER. A) WebLogo representation of MPER sequence conservation of all HIV/SIVcpz subtype genomes (filtered web, 5132 sequences) available at the LANL HIV Sequence Database (http://www.hiv.lanl.gov/content/sequence/NEWALIGN/align.html). Cartoon representation of the structures adopted by shorter versions of MPER in complex with the bNAbs 2F5 (PDB code 1TJI), 10E8 (4G6F) and 4E10 (2FX7) are shown. The critical residues for antibody binding are displayed as sticks. B) Helical structures adopted by MPER ligand free peptides. Two flexible segments at the regions targeted by the anti-MPER bNAbs can be distinguished within the overall helical conformation of the peptide. C) Structure of the HIV-1 TMD displaying a hinge at position G690.

NMR structures of several peptides embodying (i) the 2F5 epitope, (ii) the 4E10/10E8 epitope or (iii) peptides combining both epitopes reveal the overall helical conformation of MPER (Apellaniz et al., 2015; Mirassou et al., 2009; Reardon et al., 2014; Schibli et al., 2001; Serrano et al., 2014; Sun et al., 2008). However, segments ^{664}DKW^{666} and ^{671}NWFD^{674} harboring critical residues targeted by 2F5 and 4E10/10E8 antibodies, respectively, show a high

degree of conformational variability among the different structures (FIG 8B). This conformational flexibility is likely related to the critical role of gp41 in mediating viral entry by triggering membrane fusion. These two elements, together with the recently described flexible element ^{690}GGLV^{693} within the TMD (Apellaniz et al., 2015), might function as articulated joints that enable the formation of structural intermediates emerging along the fusion pathway (FIG 8C). Interestingly, the helical segment formed between ^{671}NWFD^{674} and ^{690}GGLV^{693} joints (MPER$_{671\text{-}693}$) has been reported to act as an active domain in membrane fusion by inducing viral envelope phospholipid acyl chain splay (Apellaniz et al., 2014b) (FIG 9).

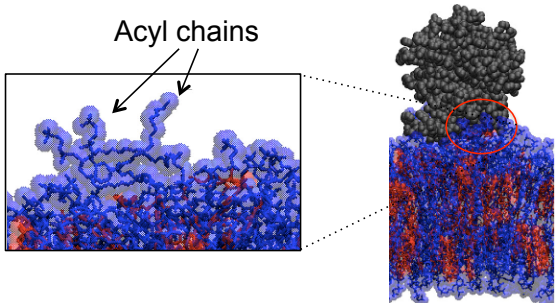

FIG 9. Fusogenicity of MPER$_{671\text{-}693}$. MPER$_{671\text{-}693}$ (black) fusion activity in lipid membranes of POPC (blue) and Chol (red) relies on phospholipid extraction as shown by molecular dynamic simulations (MDS). Taken from (Apellaniz et al., 2014b).

MPER is embedded into the membrane interface hindering recognition and, thus, engagement by antibodies (Nieva et al., 2011). However, bNAbs targeting this conserved region have evolved to incorporate structural elements to both recognize and engage the epitope in a membrane environment. The hydrophobic residues at the apex of the CDR-H3 of anti-MPER antibodies (FIG 10) are involved in mediating epitope recognition in biological membranes and, therefore, they are required for viral blocking (Alam et al., 2007; Cardoso et al., 2005; Huang et al., 2012; Sanchez-Martinez et al., 2006a; Scherer et al., 2010). In addition, several studies have shown the capacity of 2F5 and 4E10 antibodies to directly bind lipids (Alam et al., 2009; Julien et al., 2010; Maeso et al., 2011; Ofek et al., 2004). However, despite multiple similarities encountered

between 4E10 and 10E8 antibodies such as binding overlapping epitopes within MPER, 10E8 lacks the overall membrane binding tendency of 4E10 (Huang et al., 2012; Kwon et al., 2016a), although some authors have reported 10E8-lipid interactions in the context of cholesterol-containing vesicles (Chen et al., 2014).

Lipid interaction has been proposed as a strategy employed by anti-MPER antibodies to increase their neutralization potency either by acquisition of a second binding site and thus, increasing antibody avidity (heteroligation) (Klein et al., 2013b) and/or by providing an opportunity window to capture gp41 fusion intermediates from a membrane pre-concentrated state (Alam et al., 2009). Heteroligation (i.e., to combine strong binding to gp41 and weak binding to viral membrane) might be of special importance for HIV blocking due to its low spike density (Zanetti et al., 2006). Interestingly, although 10E8 antibody does not display strong interactions with membranes, it exhibits higher potency than any anti-MPER reported to date with an IC_{50} mean value of 0.35 µg/mL (Huang et al., 2012) (FIG 6B).

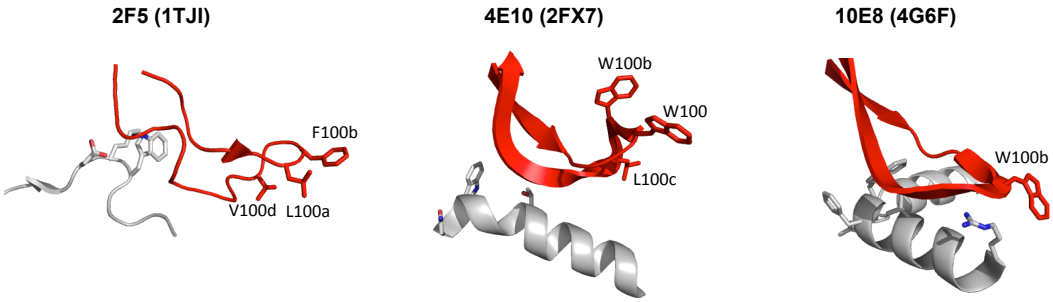

FIG 10. Structure of the CDR-H3 of anti-MPER bNAbs. Depiction of the contacts between CDR-H3 (red) of anti-MPER bNAbs and epitope peptides (gray). Residues critical for neutralization are shown in stick representation.

Due to the critical role in HIV infection exerted by the region targeted by the 4E10 and 10E8 antibodies, a phenomenon at the origin of their exceptional neutralization breadth, these antibodies serve as models of broad protection against HIV infection, particularly for the purpose of vaccine design. This warrants an extensive structural and functional characterization, which is the main objective of this thesis work.

Main goals

1- To generate a platform for the fast and massive production of recombinant anti-MPER antibodies 4E10 and 10E8 in bacteria, and to validate them structurally and functionally.

2- To use the above mentioned expression platform for the production of the following genetically modified recombinant antibodies:
- CDR(H) mutants.
- Cys mutants for labeling with fluorescent probes, and
- *p*BPA mutants for photo-cross-linking assays.

3- To use the above specimens to define the requirements for engaging MPER helix at the membrane interface with the aim of:
- designing effective anti-MPER vaccines.
- optimizing the functional performance of anti-MPER antibodies.

Chapter 2

EXPERIMENTAL TECHNIQUES

This chapter gathers a theoretical overview of the main techniques used during the thesis. A more detailed description of these and additional experimental approaches can be found in the Materials and Methods sections of the following Chapters 3-7.

2.1. RECOMBINANT PROTEIN EXPRESSION

To study the function and/or structure of a protein, recombinant overexpression is generally required due to the low levels present in natural sources. Nowadays, overexpression of many proteins remains a big challenge and therefore, a lot of effort is made to overcome this problem (Makrides, 1996) (Sorensen and Mortensen, 2005). The bacterium *E. coli* is the host of choice in many instances for this purpose due to its low cost, high production yields, easy transformation and the ability to grow to high culture density in fermenters. However, the use of *E. coli* for protein overexpression has certain limitations, including the formation of disulfide bonds.

The cytoplasm of *E. coli* is a reducing environment and therefore proteins with disulfide bonds will generally not fold properly when overexpressed in this compartment. The cytosolic proteins thioredoxins (TrxA, TrxC) and glutaredoxins (GrxA, GrxB, GrxC) catalyze the reduction of proteins by cysteine thiol-disulfide exchange (Aslund and Beckwith, 1999). Consequently, the formation of stable disulfide bonds in the cytoplasm is strongly disfavored. The reductive state of both thioredoxins and glutaredoxins is maintained by the action of thioredoxin (*trxB* gene product) and glutathione reductase (*gor* gene product), respectively (FIG 11).

In the periplasm of *E. coli*, disulfide bond formation can occur and it is actively catalyzed by the Dsb-system in a two-step process (Nakamoto and Bardwell, 2004) (FIG 11). The Dsb-system consists of a set of thiol disulfide oxidoreductases that share the sequence motif Cys-X-X-Cys. It consists of the components DsbA, DsbB, DsbC and DsbD. These proteins not only are able to

catalyze disulfide bond formation, but also to rearrange those that are not present in the native three-dimensional structure of the protein.

Specifically, catalysis of disulfide bond formation is accomplished by the periplasmic protein DsbA (Inaba et al., 2006). This process occurs between consecutive cysteines while the primary structure of the protein emerges into the periplasm. Hence, a proofreading mechanism (Ito, 2010) is required for proteins that have more than two cysteines with nonlinear connectivity in their native conformation. The inner membrane protein DsbC is responsible for the sensing and subsequent isomerization of non-physiological disulfide bonds (McCarthy et al., 2000). The inner membrane proteins DsbB and DsbD catalyze the re-oxidation of DsbA and DsbC, respectively, in order to keep them in their active state (Kimball et al., 2003).

Owing to the crucial role of disulfide bonds in physiological folding and function of various proteins, *E. coli* strains such as Origami or T7 Shuffle (Lobstein et al., 2012) have been engineered. The cytoplasm of these strains is turned into a more oxidizing environment by constructing *trxB* and *gor* null mutants. However, double mutants missing parts of both systems show an impaired growth. This growth defect can be alleviated by the presence of an extragenic suppressor mutation in the *ahpC* gene (Bessette et al., 1999). Suppression of thioredoxin and glutathione reductase reverses the normal role of thioredoxins and glutaredoxins, respectively. Thus, they act as catalysts for the formation of disulfide bonds in the cytoplasm, i.e, they act as oxidases. The *E. coli* T7 Shuffle strain has been further engineered to incorporate the gene of the DsbC isomerase into the genome of the bacteria, which results in its constitutive expression. The activity of this disulfide bond isomerase shuffles incorrect disulfide bonds into their native correct pairing and, therefore, sustains higher yields of the overexpressed recombinant protein.

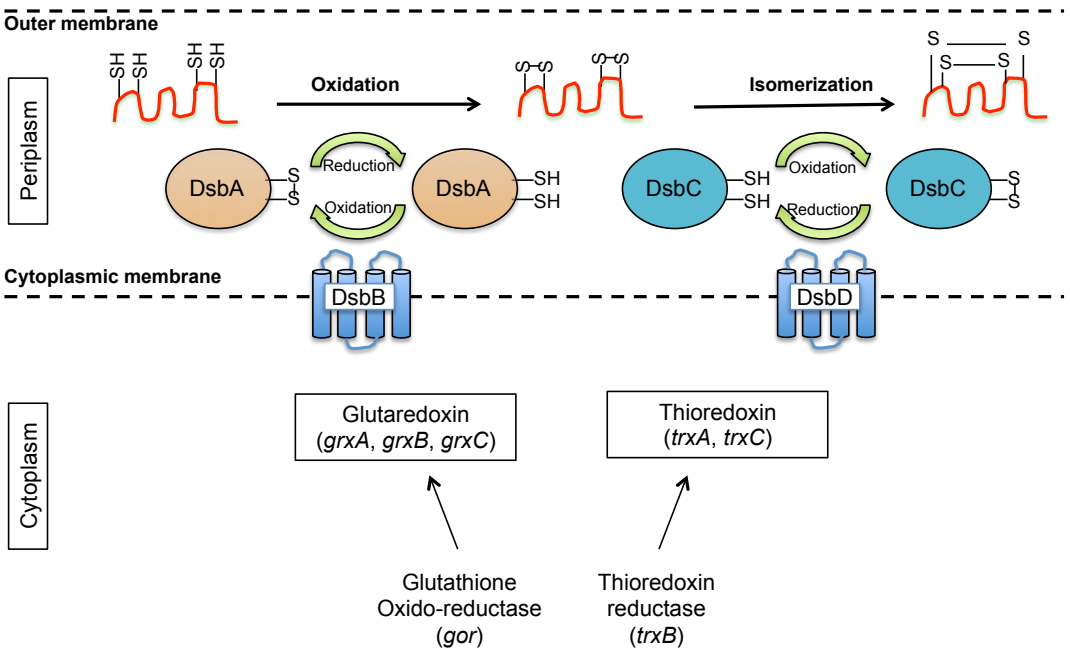

FIG 11. Oxidative protein folding in *E. coli*. The reducing environment derived from the activity of *E. coli* cytoplasmic glutaredoxins and thioredoxins impairs the covalent bond formation of two thiol groups. Hence, proteins containing structural disulfide bonds have to be translocated to the periplasm of *E. coli* where the Dsb-system catalyzes the formation (DsbA) and isomerization (DsbC) of disulfide bridges. Reactivation of DsbA and DsbC is performed by DsbB and DsbD, respectively.

The *E.coli* T7 Shuffle strain has been used in the present doctoral thesis for the overexpression of different neutralizing and non-neutralizing versions of two anti-MPER antigen-binding fragments (Fab), the anti-HIV 4E10 and 10E8 Fab-s.

Fab fragments consist of the region of an antibody that binds the antigen. This region is formed by the entire light chain (LC) of the antibody (V_L and C_L domains) paired with the amino-terminal half of the heavy chain (HC; V_H and C_{H1} domains) (FIG 12A). Folding of the variable domains (V_L and V_H) leads to paratope formation that is comprised of a set of complementarity determining regions (CDR) responsible for the specificity of the Fab.

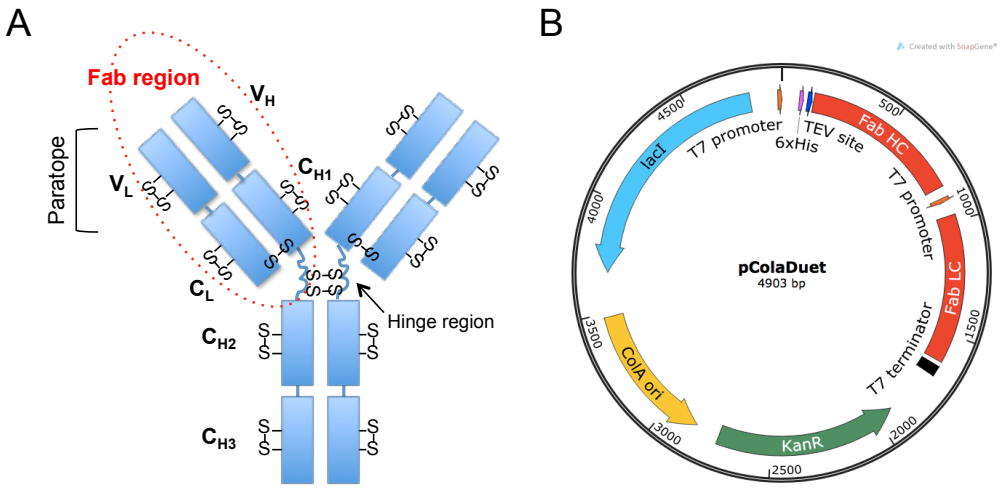

FIG 12. Fab (Fragment, antigen binding) expression system. A) Schematic representation of the HC and LC that constitute the Fab region of an IgG. Each chain consists of different subdomains: V_H (variable heavy domain), C_H (constant heavy domain), V_L (variable light domain) and C_L (constant light domain). Intermolecular and intramolecular disulfide bonds are shown. Pairing of the V_H and V_L give rise to the paratope of the antibody. B) Map representation of the pColaDuet vector employed for the simultaneous expression of two genes from a single plasmid. This vector encodes two separate multiple cloning sites (MCS), each preceded by its own T7 promoter, lac operator, and ribosome binding site (rbs). Besides, the vector contains the low copy ColA replicon and the kanamycin (Kn) resistance gene.

The HC of the Fab was N-terminally fused to a hexahistidine tag followed by a Tobacco Etch Virus (TEV) cleavage site to remove the tag during protein purification. Both chains were cloned into the low copy number plasmid termed pColaDuet (20-40 copies) (FIG 12B). The presence of two multiple cloning sites (MCS) in the plasmid each preceded by the same promoter (T7 promoter) enables coexpression of both chains at the same rate. This strategy favors the correct folding of the Fab leading to the formation of a fully active soluble protein.

2.2. X-RAY CRYSTALOGRAPHY

X-ray crystallography is the premier technique to determine the three-dimensional structure of proteins. This method provides detailed information on

the spatial position of atoms within a protein, which is crucial for determining protein functionality.

2.2.1. Protein crystallization principle

Protein crystallization constitutes the first and generally the limiting step in the process of determining protein structure. Crystallization occurs when the concentration of the protein in a solution is greater than its limit of solubility and therefore, the protein starts to precipitate. In order to obtain high-quality diffraction data, protein precipitation has to evolve in a controlled manner that leads to the formation of ordered crystals with a well-defined internal order (Rupp, 2009).

The common strategy to induce protein crystallization is based on the addition of the so-called “precipitation agents” such as salts that increase the ionic strength of the solution, organic solvents that decrease solvent polarity or organic polymers that promote the exclude-volume effect. Moreover, physical and chemical properties of the system such as temperature or pH can be altered to optimize crystal growth.

The thermodynamic principle that operates in protein crystallization is the minimization of the free energy of the system. In a clear solution, the protein molecules are fully solvated by the water and therefore, thermodynamically stable. However, when the system is brought into a state of limited solubility by the addition of different precipitants, these molecules become no longer solvated. Consequently, the system becomes thermodynamically unstable and undergoes internal changes that lead to the formation of new non-covalent bonds between the molecules that ultimately result in the formation of a solid phase (supersaturation state). A phase diagram represents the physicochemical state of a protein as a function of protein and precipitant concentrations. The solubility curve in a phase diagram represents such equilibrium between solution and solid states (FIG 13A). The supersaturated state can be divided into three separate stages, as schematically illustrated in

the phase diagram (FIG 13A). These zones are governed by a kinetic phenomenon responsible for the spontaneous formation of small microscopic clusters of proteins (nuclei) from which crystals will further grow. Such process requires a large supersaturation in order to overcome the activation energy barrier. This nucleation range takes place in the “labile zone”. Once the solution reaches this zone and the first nuclei are formed, it must enter the “metastable zone”. In this zone, the supersaturation level is not high enough to overcome the energy barrier required for nucleation. However, it allows nuclei growth so that they can evolve towards an ordered solid material. If supersaturation occurs too fast, the solution enters the “precipitation zone” where the protein aggregates in the form of amorphous precipitates.

Vapor diffusion constitutes the most common method used in protein crystallization. This technique is based on water vaporization from a protein droplet to a reservoir solution. Generally, a concentrated solution of a highly purified protein is mixed with an equal amount of precipitant and placed in a tightly closed well that contains a reservoir solution consisting of the precipitating agent(s). The concentration of the precipitants in the reservoir is higher than in the protein droplet, and consequently, the system will tend to reach equilibrium between both solutions. At the beginning, the system is undersaturated, but during equilibration, water molecules will be transferred from the protein droplet to the reservoir. As a consequence, the concentration of the protein and precipitant in the droplet will steadily increase during the equilibration, reaching the supersaturated zone spontaneously. There are two variants of the vapor diffusion technique that essentially differ in the experimental set-up and geometry of the protein droplet relative to the reservoir. In the sitting drop method, the protein is placed horizontally to the reservoir, whereas in the hanging drop method the protein is located above the reservoir in a vertical position (FIG 13B).

Unfortunately, conditions that promote protein crystallization are not predictable and therefore, the process to obtain a new crystal always requires the screening of numerous crystallization solutions.

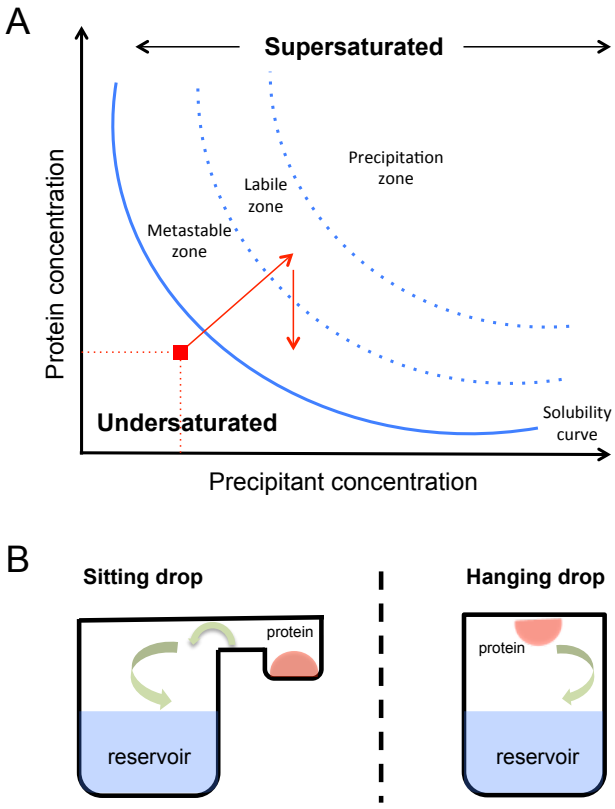

FIG 13 Protein crystallization. A) Phase diagram illustrating the solubility of a protein as a function of the concentration of protein and precipitant. The red dot represents the initial state of a mixture of protein and precipitant. As a result of the diffusion of water molecules from the less concentrated solution (protein droplet) to the more concentrated solution (reservoir), the concentration in the protein drop increases and the solution enters the labile zone where nuclei are formed. Nucleation reduces the amount of protein remaining in the solution and consequently the solution enters the metastable zone were the formed nuclei steadily start to grow resulting in ordered crystals. B) Schematic representation of the two most popular vapor diffusion techniques. The arrows indicate the movement of water molecules in the vapor phase.

2.2.2. Crystal diffraction

X-rays are electromagnetic waves that have a wavelength in the order of the size of an atom (≈1 Å) suitable to obtain structural information at the atomic

level. When a beam of X-rays hits an atom, it sets the electrons into oscillation generating new waves of the same energy as the incident one (Thomson scattering) (FIG 14B). The three dimensional organization of proteins within a crystal can be described by the crystal lattice (FIG 14A). This arrangement places the molecules in atomic planes that enable the interaction of scattered waves when a beam of X-rays hits these ordered structures. The physical phenomenon of positive interaction between waves is called constructive interference. Consequently, the resulting wave presents a greater magnitude and due to this amplification, its intensity can be recorded in a detector device (FIG 14B). In order to record information of all the existing atomic planes, the crystal is repeatedly rotated and exposed to the X-rays beam.

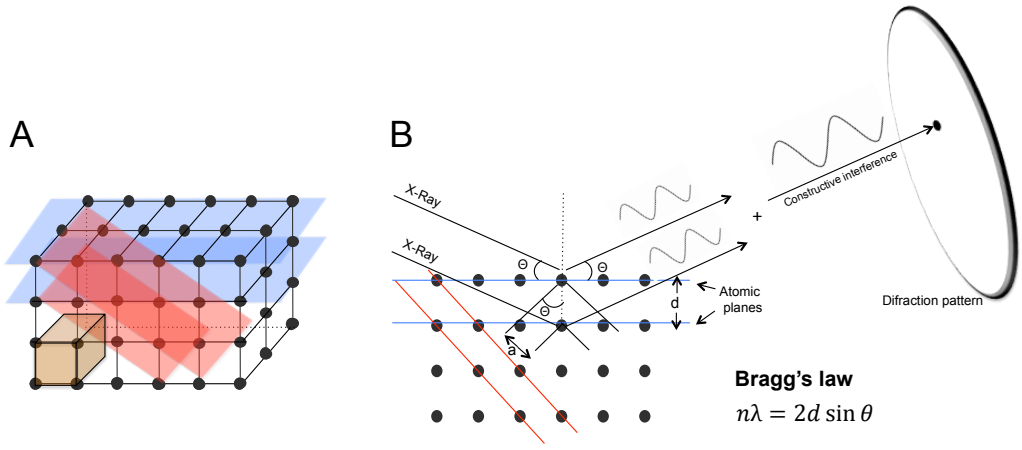

FIG 14 Crystal diffraction. A) Schematic representation of the molecular arrangement inside a crystal (crystal lattice). The planes depicted in red and blue represent two of the multiple atomic planes that coexist inside a crystal. The orange box illustrates a cell unit that constitutes a repeating element that by simple translation can generate the entire crystal. B) X-ray diffraction. The internal organization of the crystal scatters the X-rays in a way that the waves that meet Bragg's law interact with each other (constructive interference). This effect occurs when the difference in the distance travelled between two waves (2a) equals the distance between two atomic planes (d). This effect is translated into a diffraction spot on the detector. The sum of the diffraction spots of numerous planes constitutes the diffraction pattern. The symbol λ corresponds to the wavelength of the incident X-rays, n to an integral number, and Θ to the angle of incidence of the X-rays beam.

The entire set of scattered waves that reach the detector defines the diffraction pattern of a protein crystal. The diffraction pattern is formed by discrete spots, since diffraction will only occur if the waves are in phase when

they emerge from the crystal. This event only occurs when i) the distance between the atomic planes (d-spacing) and ii) the angle of the incident ray meet Bragg's law (FIG 14B). Hence, the diffraction pattern depends on the geometry of the crystal lattice and therefore represents the protein's fingerprint. The mathematical method used to derive a protein structure from the diffraction pattern is called Fourier transform. This function uses the phase, position and intensity of each spot from the diffraction pattern to calculate a electron density map of a cell unit (repeating unit that by simple translation, can generate the entire crystal) to further determine the three dimensional arrangement of the atoms in a protein.

In the present work protein crystallography has been used to determine the atomic structure of different neutralizing and non-neutralizing versions of two anti MPER Fab-s termed 4E10 and 10E8.

2.3. CALORIMETRIC TECHNIQUES

Structural studies constitute a key tool for the elucidation of the functional groups on interacting molecules. Hence, this technique has extended our knowledge of the interacting surfaces between proteins. However, in order to fully understand the energetic forces that drive complex formation, this structural information should be combined with the thermodynamic and kinetic information of the underlying processes. Differential Scanning Calorimetry (DSC) (Doyle, 2004) and Isothermal Titration Calorimetry (ITC) (Damian, 2013; Doyle, 2004) are among the most frequently employed techniques to elucidate thermodynamic information of biological systems. DSC is used for determining the order-disorder transitions (protein folding/unfolding) of proteins, whereas ITC is employed for the characterization of protein-protein interactions.

2.3.1. Principles of Isothermal Titration Calorimetry

ITC is a biophysical technique employed to measure the thermal energy (enthalpy) associated with bimolecular complex formation. The stepwise addition of one of the reactants in a solution containing the other reactant, results in a titration curve from which the binding affinity (K_a), stoichiometry (n), and enthalpy change (ΔH) can be simultaneously determined from a single experiment. Consequently, the free energy change (ΔG) and the entropy change (ΔS) associated with the reaction can be calculated.

Interaction of a protein with its ligand involves disruption and formation of non-covalent bonds. This process is associated with an overall heat change termed enthalpy. Generally, protein-protein interactions are enthalpy driven and therefore they generate exothermic reactions ($\Delta H < 0$). ITC uses the power compensation method for the detection of the enthalpy change upon ligand binding. The calorimeter assembly consists of a reference cell filled with buffer, a sample cell where the protein is placed and a syringe device that holds the ligand (FIG 15A). Both compartments (reference cell and sample cell) are continuously and slowly heated by injecting a small and known amount of energy, necessary to keep both cells at a constant temperature. Injection of the ligand to the sample cell will shift the temperature of that chamber. In the case of a positive increment of temperature, the reaction is termed exothermic. In exothermic reactions, a greater amount of power has to be supplied by the instrument to the reference cell in order to bring the calorimeter back to its steady state. It can be demonstrated that, the applied power administered by the instrument to equalize the temperature between both compartments is directly proportional to the enthalpy of the binding reaction (ΔH).

Elucidation of the binding affinity (K_a) requires the stepwise injection of the ligand in order to generate a titration curve. In the first injection, most, if not all, the ligand will react with the protein in the cell generating a peak of maximum magnitude. As the course of the experiment progresses, the amount

of unbound (free) protein will progressively decrease and consequently, the fraction of ligand injected in the cell that reacts with the protein will also decrease except when very high-affinity complexes are formed. Therefore, the magnitude of the peaks will become smaller until the cell is mostly devoid of free protein (FIG 15B). At this point, saturation is achieved and the small peaks recorded correspond to dilution heat from the injection of the ligand into the sample cell. The heat released/absorbed in each ligand injection is proportional to the area under each peak. Experimental heat can be normalized per mol of injectant and plotted vs the molar ratio [L] / [P] generating a curve called binding isotherm (FIG 15C). A fitting procedure is then employed to determine several thermodynamic parameters of the reaction:

- **Stoichiometry (n)**; determines the number of binding sites of the titrated protein.

- **Binding constant (K_a)**; the slope of the straight portion of the sigmoidal function that defines the isotherm corresponds to the affinity constant of the binding reaction.

- **Enthalphy change (ΔH)**; this parameter can be determined by subtraction of the heat generated by ligand dilution and buffer mismatch (upper plateau) to the maximum amplitude of the sigmoid (lower plateau).

Besides, based on the experimentally determined K_a, the Gibb's free energy change (ΔG) can be calculated from Eq (1) and the entropy change of the system (ΔS) from Eq (2).

$$\Delta G^0 = -RT\ln k_a \quad (1)$$

$$\Delta G^0 = \Delta H^0 - T\Delta S^0 \quad (2)$$

where R corresponds to the gas constant and T to the temperature in Kelvin.

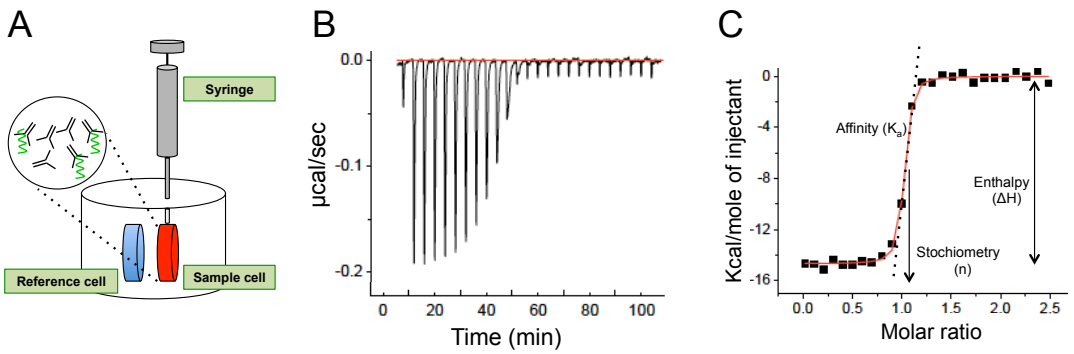

FIG 15 Schematic overview of an ITC experiment. (A) Configuration of an ITC reactor where the reference cell, the sample cell and the syringe are shown (B) Raw ITC data showing a series of consecutive exothermic peaks. After each injection, the total heat released due to protein-ligand interaction is recorded. Excess amount of protein in the cell (in the first half of the experiment) gives rise to peaks with the greatest magnitude. In an average experiment, the successive addition of ligand causes protein saturation and, consequently, a reduction of the size of the peak until only the heat corresponding to dilution is detected. C) The integration of the exothermic peaks give rise to a classical sigmoidal binding isotherm. The solid line corresponds to the fitting of a one-site-model to the experimental data yielding three key thermodynamic parameters; binding constant (Ka), stoichiometry (n) and enthalpy change (ΔH).

Contribution of the enthalpic and entropic components to the overall affinity of a reaction (binding signature) can provide insight into the interaction mechanism. A favorable binding enthalpy ($\Delta H < 0$) is often associated with formation of hydrogen bonds and van der Waals interactions whereas reactions driven by a favorable entropy change ($\Delta S > 0$) indicate conformational changes that involve the release of water molecules from a binding interface (hydrophobic effect) (Holdgate and Ward, 2005).

2.3.2. Principles of Differential Scanning Calorimetry

In differential scanning calorimetry (DSC) the heat induced during the phase transition of a sample is continuously monitored as a function of the temperature. Similarly to ITC, the DSC instrument is equipped with a reference and a sample cell but unlike in ITC, the temperature of both compartments is increased vigorously at a constant rate. In general, high temperature induces a conformational change in the protein that ultimately causes its denaturalization

in the sample cell. This thermal transition consumes additional energy from the electrical supply that is continuously feeding the chamber. Compensation of such temperature drop is recorded, normalized and plotted against the temperature. Integration of the experimental heat curve yields the calorimetric transition enthalpy (ΔH) of the system (FIG 16B).

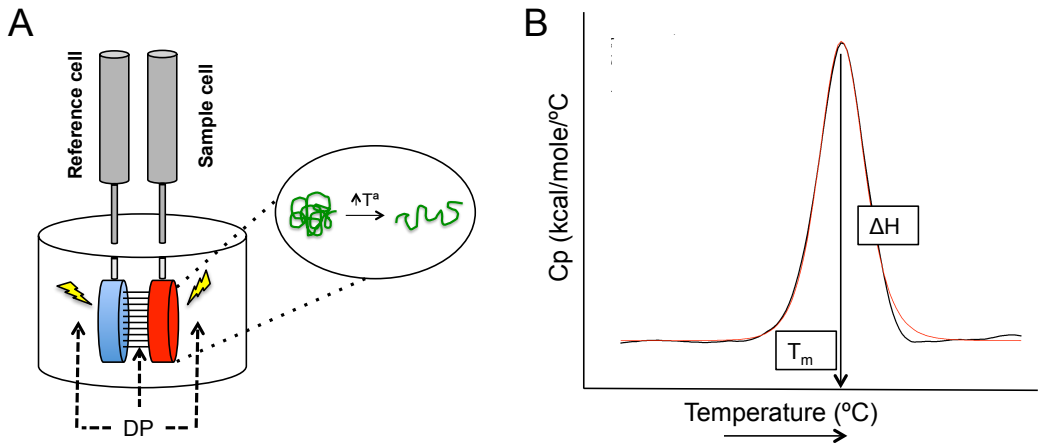

FIG 16 Schematic overview of a DSC experiment. A) Configuration of a DSC reactor where the reference cell and the sample cell are shown (B) Heat flux curve as a function of temperature (black) and fitting of the experimental data to a two-state thermal transition model (red). The thermodynamic parameters T_m (melting temperature) and ΔH (transition enthalpy) can be determined from the temperature at which the maximum heat is recorded and from the integration of the area under the peak, respectively.

In the present work ITC and DSC have been employed to determine the binding thermodynamics and thermal stability, respectively, of different neutralizing and non-neutralizing versions of 4E10 and 10E8 Fab-s to MPER peptides with different lengths.

2.4. SURFACE PLASMON RESONANCE

Optical methods based on the Surface plasmon resonance (SPR) technology (Homola, 2003) are increasingly employed to characterize the binding kinetics of ligands to macromolecules in real time.

Plasmons consist of waves produced by the resonance of free electron clouds on a conductor surface (FIG 17A) (Daghestani and Day, 2010). When a light beam hits the surface of a metallic element, part of that light is used to induce the electron resonance effect, causing a reduction in the intensity of the reflected light. Gold constitutes the preferred metal to induce the formation of surface plasma waves due to its high chemical stability and mass extinction coefficient (σ_{ext}) resulting from its large atomic number. The latest determines the amount of light absorbed and scattered by the metal particle. Hence, metals with large values of σ_{ext} such as gold generate higher contrasts in the signal detected (greater changes between the intensity of the incident and the detected light). The maximum fall of intensity is recorded at a specific combination of the incident light angle θ (known as the resonance angle) and wavelength λ (FIG 17A). The electron resonance is very sensitive to the surrounding environment and therefore, small changes on the surface affecting its physical properties will result in a change in the angle at which the minimum intensity is recorded.

In a SPR experiment a sensor chip made of a thin film of gold supported on a glass surface is employed. The chip is then prepared by immobilization of one of the molecules involved in the interaction. As noted above, when light hits the functionalized gold film, surface plasmons will be generated at critical angles (FIG 17B). In order to monitor the interaction with the immobilized molecule, the analyte is continuously flowed in an aqueous solution through the chip surface (Besenicar et al., 2006; Patching, 2014; Salamon et al., 1997). As the binding event takes place, molecule absorption changes the environment of the chip surface and consequently, the angle, at which the minimum of the intensity of the emerged light its recorded, changes (FIG 17B). The shift of the resonance angle is proportional to the mass of the material bound. Hence, binding will be recorded as response units (RU). Because the amount of free binding sites available at the beginning is very high, a large biomass of molecules will bind to the chip. This event will be registered as a rapid increase of the RUs. The ligand is continuously delivered until the binding equilibrium is

reached and a maximum RU value is obtained. When the solution that passes through the chip is devoid of the analyte, the bound molecules start to dissociate and consequently, a decrease of the RUs is recorded. The curve resulting from plotting RU values against time is called a sensogram and can be used to extract key kinetic and thermodynamic parameters of the binding reaction.

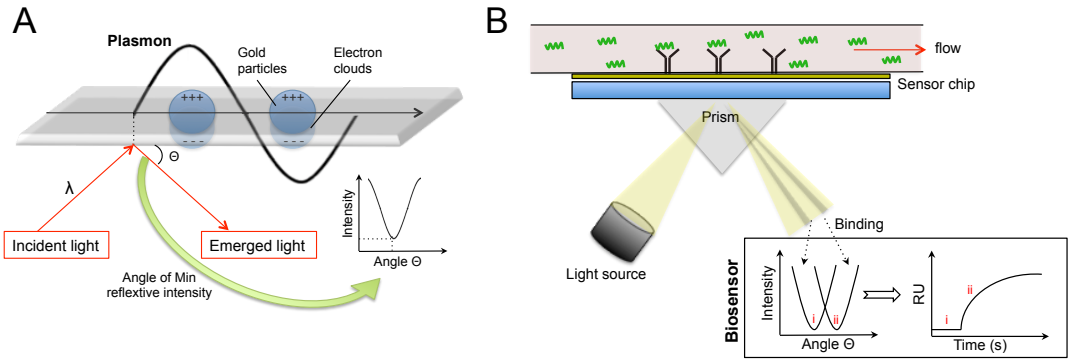

FIG 17. The principle behind SPR and its use in detecting biochemical interactions is illustrated. A) At a certain incident angle, known as the resonance angle, the light hits the electron cloud of a thin film of gold causing the plasmon resonance effect. The resulting wave is called plasmon and its generation constitutes the key principle of the SPR technology. B) SPR detection scheme. The analyte solution is flowed through a sensor chip previously coated with the biomolecule of interest. The binding of analyte molecules to the immobilized molecule changes the angle at which the reflexive intensity is at its minimum [(i) → (ii)]. The change of angle can be monitored as response units (RU), which is proportional to the amount of mass absorbed in the sensor chip. The resulting curve is called sensorgram and the repeated addition of analytes at different concentrations and at different temperatures renders key kinetic and thermodynamic parameters of the reaction.

2.4.1. Calculation of the kinetic and thermodynamic parameters

A SPR sensorgram gives essential information about the kinetics of the interaction. The two key kinetic parameters association rate constant (k_{on}) and dissociation rate constant (k_{off}), are extracted from the behaviour of the binding and unbinding process, respectively. The rate between both constants yields the binding affinity of the system (K_D) Eq (3).

$$K_D = {k_{off}}/{k_{on}} \quad (3)$$

Determination of these parameters gives information of the system in the equilibrium (the state of minimum energy or ground state). In order to gain insight into the molecular mechanism that drives the interaction process, thermodynamic information of the ground and transition states is also required.

The transition state is considered a high energy state formed in the reaction pathway from reactants to products that, when overcome, equilibrium can be subsequently reached. This structure contains partial bonds and therefore it is characterized by a very short lifetime. The thermodynamic signature of the transition and ground states can be obtained from linear fits of experimental binding (K_D) and rate (k_{on} or k_{off}) constants measured at several temperatures employing the van't Hoff and Eyring plots, respectively.

The thermodynamic information relating to the ground state can be extracted from the fitting to the logarithm of K_D values vs the inverse of the temperature at which such constants have been measured. This straight line is defined by van't Hoff's equation (4) and the slope and the intercept on the Y-axis determine ΔH^0 and ΔS^0, respectively (FIG 18). Similarly, representation of the logarithm of either k_{on} or k_{off} divided by the temperature at which each measurement has been performed against the inverse of temperature, results in a plot that can be fitted to the Eyring's equation (5). The slope and Y-axis intercept of the resulting straight line corresponds to the transition state`s parameters; $\Delta H^{0\mp}$ and $\Delta S^{0\mp}$, respectively (FIG 18).

$$lnK_D = (\Delta H^0/RT) - (\Delta S^0/R) \quad (4)$$

$$k = \left({K_B T}/{\hbar}\right) exp({-\Delta G^{0\mp}}/{RT}) \quad (5)$$

where R corresponds to the gas constant, T to the temperature in Kelvin, K_B to Boltzmann constant and $\hbar$ to Planck's constant.

Following Eq (2), the Gibb's free energy value associated with each state can be determined. $\Delta G^{0\mp}$ corresponds to the energy barrier known as the activation free energy and consists of the minimum energy needed by the reaction to reach equilibrium.

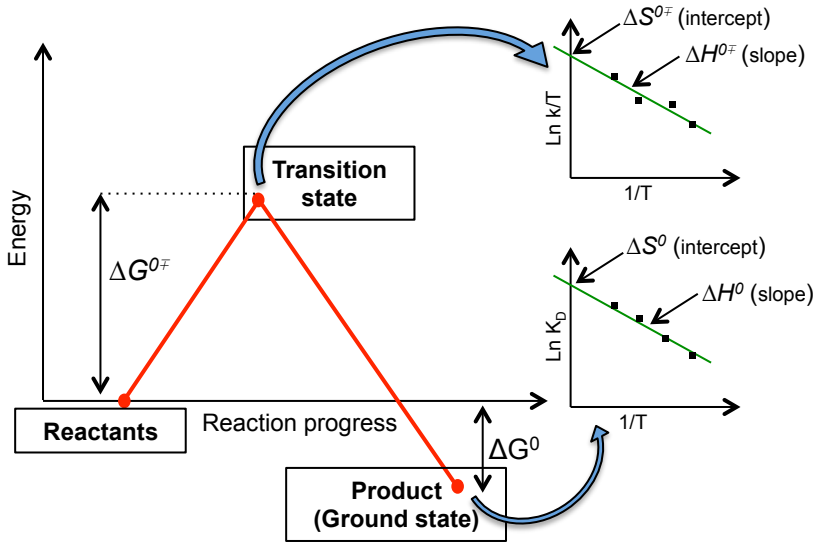

FIG 18. Free energy profile of a reaction. The energy barrier is depicted as $\Delta \boldsymbol{G^{0\mp}}$. Thermodynamic signature of the ground and transition state can be extracted from the Van't Hoff and Eyring equations, respectively (see text above).

In the present work SPR was employed to shed light on the binding mechanism of the 4E10 Fab to a MPER peptide. For that, a comparative study of i) the binding kinetics and ii) the thermodynamic binding parameters of MPER binding at the transition state by a neutralizing and by two non-neutralizing versions of the antibody was performed.

2.5. FLUORESCENCE SPECTROSCOPY

2.5.1. Basis of fluorescence spectroscopy

The electrons within an atom are localized in orbitals that describe the region of probability where they can be found. Formation of covalent bonds

within a molecule implies overlapping of such atomic orbitals leading to the formation of molecular orbitals that predict the location of the electrons shared by the atoms. The number of orbitals must be conserved and therefore when two atomic orbitals are combined, two molecular orbitals with different energy will be formed (FIG 19A). The different energy levels of these molecular orbitals define the electronic transitions allowed in a molecule. The electrons in a covalent bond will occupy the lower energy level called ground state (S_0) leaving the remaining high energy level called exited state (S_1) empty for further occupation if the molecule is exited by an external light source. Hence, if the molecule is exposed to light with an energy that matches the energy difference between two transition states, the energy will be absorbed and the electron from the highest occupied molecular orbital (HOMO) will jump to the lowest unoccupied molecular orbital (LUMO).

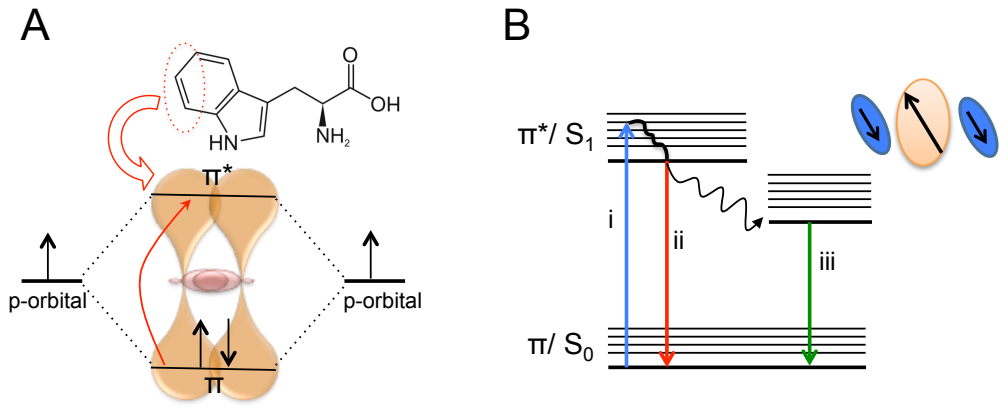

FIG 19. Schematic representation of an electronic transition resulting in fluorescence emission. A) π-bond representation due to overlapping of two p-molecular orbitals. The electrons occupy the orbital of lower energy (bonding orbital) leaving the molecule with higher energy (anti-bonding orbital) empty for further occupation upon molecule excitation B) Energy diagram showing the events that take place when the frequency of the photon that hits a molecule matches the energy difference between two electronic states. (i) The photon is absorbed (blue arrow) and the molecule is excited (its electrons will jump to a higher energy level). Then, (ii) it losses part of the energy by thermal relaxation (curved black line) and the remaining energy is emitted (red arrow) when the molecule goes back to the ground state. In a polar environment, the dipole moment of the fluorophore rearranges the orientation of the solvent molecules resulting in the stabilization of the exited state. Consequently, the photon emitted contains lower energy (iii) and therefore, longer wavelength (green arrow), than the incident photon.

Once the absorption takes place, the exited electron will tend to return to the ground state releasing energy. If the energy is lost in a radiative form (photon emission), the fluorescence phenomenon occurs. The space in between each electronic transition is filled with discrete (quantized) energy levels corresponding to the vibrational motion of the molecule. When energy is applied to the system, the electron can be excited from any of the vibrational levels of S_0 to any of the vibrational energy levels of S_1. The energy difference between those levels is very small leading to a rapid thermal relaxation (10^{-13} sec) of the molecule due to collisions with the solvent. As a consequence, the electron reaches the lowest vibrational level of S1 from where photon emission will occur (fluorescence emission) (FIG 19B). The loss of vibrational energy in the form of heat will result in the emission of a photon with longer wavelength than the photon absorbed. This shift towards longer wavelengths is called Stokes shift (Lakowicz, 2006).

2.5.2. Fluorophores and its use in tracking protein-lipid interactions

In order to use fluorescence spectroscopy for biological applications, non-destructive wavelengths (preferably within the visible region of the electromagnetic spectrum) that induce electron transitions are required. σ-bonds constitute strong bonds due to the high overlap of the atomic orbitals that result from the covalent bond formation between two s-type orbitals. Consequently, the negatively charged electron density is placed in close proximity to the positively charged nucleus implying that the excitation of an electron within that bond will require photons of high energy. On the contrary, the electron density in a p-type orbital is farther away from the nucleus due to its parallel orientation (FIG 19A). Hence, orbital overlapping occurs at a lower extent and the resulting π-bond is weaker. Electrons within π-bonds are therefore delocalized and its excitation can be accomplished with photons of lower energy. Further electron delocalization can be obtained by double bond conjugation that consists on double bonds (formed by the combination of π and σ–bonds) separated by a single bond. The energy of the $\pi \rightarrow \pi^*$ transition

decreases as the number of conjugated double bond increases and, therefore, fluorophores with high absorption in the visible part of the spectrum generally present several conjugated double bonds.

Proteins contain aromatic residues with conjugated double bonds responsible for the intrinsic fluorescence of the protein. Tryptophan (Trp) is the strongest contributor since it has the highest quantum yield (ratio between photons emitted and photons absorbed). Trp fluorescence is sensitive to the local environment due to interactions with the surrounding media during the excited state lifetime. In a polar environment, excitation of π-electrons to a higher energy level produces a magnification of the dipole moment of the Trp compared to that in the ground state. As a consequence, polar solvent molecules interact more tightly with the Trp, lowering the energy of the excited state. This stabilization results in a lower separation between the ground and excited states, which in turns results in a red shift (towards longer wavelengths) of the fluorescence emission (FIG 19B). Hence, Trp can be used as a probe to monitor the change between a hydrophilic and a hydrophobic environment. It constitutes a powerful tool for examining the interactions of proteins with lipids (Ladokhin et al., 2000) based on the intensity change and the displacement of the emission spectra of Trp.

This phenomenon is also found in fluorophores and therefore, other molecules can be used with the same purpose. The natural abundance of this aromatic residue in a protein (generally two or more Trp residues per protein) limits its practical use since interpretation of the overall fluoresce change becomes challenging. Hence, a molecule of 7-nitro-1,2,3-benzoxadiazole (NBD) can be introduced in a protein by site-directed mutagenesis and chemical modification and used as a reporter of the environment surrounding a selected region of the protein under study. In this work, the fluorescence of NBD has been employed to monitor the polar environment of the CDR-H3 of the antibodies 4E10 and 10E8, in particular during their interaction with lipids.

To shed light on the interactions between lipids and proteins a lipid membrane model called liposomes is normally used. A liposome consists of a lipid structure in a bilayer configuration enclosing an aqueous solution. Liposomes of several bilayers (Multilamellar Vesicles, MLV) are spontaneously generated when diluting cylindrical-shaped amphipathic lipid molecules in aqueous solutions. After cycles of i) freezing and thawing and ii) extrusion through membranes with fixed-size nanopores, MLV become vesicles of a certain size that ranges from 100 to 500 nm and with only one bilayer (Large unilamellar vesicles, LUV). Due to this diameter, the local curvature on the bilayer is almost zero, with 49 % of the lipids localized in the inner monolayer and 51 % in the outer monolayer (Mayer et al., 1986) almost resembling the non-existent curvature of the plasma membrane.

2.6. CELL INFECTIVITY AND VIRAL NEUTRALIZATION

The HIV-1 envelope protein induces in some instances an antibody response able to inhibit virus infection. In the present work, the molecular mechanism underlying the activity of two of these HIV-1 neutralizing antibodies has been studied. Aiming to identify the elements of the antibody involved in virus neutralization, different antibody mutants have been generated. The ability to block virus infectivity of these antibody variants was tested in standard neutralization assays reviewed in (Montefiori, 2009) or in our in-house cell entry inhibition assays (FIG 20, see below). In both experiments, the degree of infection was monitored after incubation of pseudovirus with antibodies.

Production of molecularly cloned Env-pseudotyped viruses was carried out in 293T cells. 293T cells are derived from human embryonic kidney 293 cells that express the SV40 Large T-antigen, which allows episomal replication of transfected plasmids containing the SV40 origin of replication. To produce pseudovirus, these cells are co-transfected with an Env-expressing plasmid (pIII-Env or JRCSF) plus an env-deficient HIV-1 genome backbone plasmid (pCMV8.91) and a plasmid encoding the reporter green fluorescent protein

(GFP) (pWPXL-GFP). LTR and Ψ sequences are only present in this latter plasmid. Consequently, generated pseudovirus particles packing the GFP-encoding gene are able to infect cells but unable to produce infectious progeny virions. Upon infection, GFP expression allows detection of a single round of viral infection. As a host cells line TZM-bl cells are employed which are based on a HeLa cell line derived from the cell line JC.53. TZM-bls cells have been genetically modified for the stable expression of the viral receptor/coreceptor (CD4/CCR5). Infectivity of the pseudotyped viruses and therefore, neutralization efficiency of the antibodies, was determined from the reduction in the number of GFP-positive cells (infected cells) in samples incubated with increasing amounts of antibody as compared to a control sample without antibody. The quantitative measurement of GFP-expressing cells was accomplished by using flow cytometry. The IC_{50} value, at which 50 % inhibition is obtained, was used to compare antibody potency. This value was derived from plots of inhibitor concentration versus percentage inhibition.

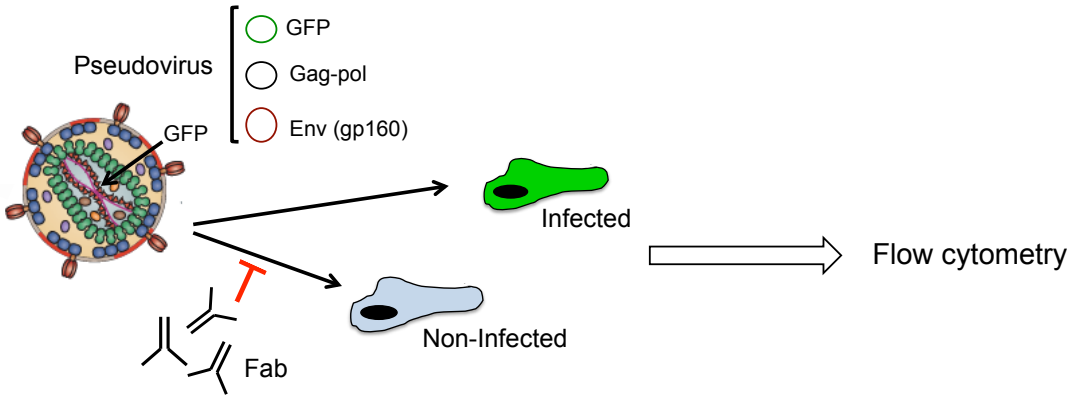

FIG 20. GFP fluorescence-based cell entry inhibition assay. Env-pseudotyped viruses were produced by co-transfection with an Env-deficient HIV-1 genome plasmid, an Env-expressing plasmid and a plasmid encoding the reporter fluorescence protein GFP. Pseudovirus infection was monitored by the amount of GFP expressing TZM cells (cells in green). Antibody-pseudovirus binding hampers cell infection. The rate between infected (green) and non-infected cells in the presence of a Fab variant was measured by flow cytometry and determines the neutralization activity of the antibody. The virus particle was taken from (Freed, 2015).

Chapter 3

FUNCTIONAL BINDING OF THE RECOMBINANT 4E10 FAB TO EPITOPE PEPTIDES

3.1. INTRODUCTION

The aromatic-rich MPER peptide connects the ectodomain of the HIV-1 gp41 with the TMD anchor (FIG 21A). The remarkable high hydrophobicity-at-interface of MPER predicts its stable association with the external leaflet of the viral membrane (Huarte et al., 2008; Saez-Cirion et al., 2003; Suarez et al., 2000). This implies that orientation and accessibility of this vulnerable Env site may mainly depend on interactions of MPER residues with the membrane interface, in addition to motional restrictions imposed by the TMD anchor (Montero et al., 2012). In the current model, the MPER helix is predicted to associate with the membrane interface with its axis approximately parallel to the plane of the membrane up to residue Lys683, where the peptide would bend by 90º to allow insertion of the TMD in a perpendicular orientation. However, experimental data supporting a kink at the MPER-TMD connection have not been reported (FIG 21B).

Recent NMR characterization of the gp41 MPER-TMD region by using three overlapping synthetic peptides (Apellaniz et al., 2015), confirmed the adoption of main α-helical conformations by MPER and TMD in a membrane environment, but ruled out the existence of the kink at position Lys-683 predicted to mark the initiation of the TMD (FIG 21B). The data also revealed that the MPER-TMD connection, spanning residues ^{671}NWFDITNWLWYIK^{683}-^{684}LFIMIVGGLV^{693}, embodies a continuous helix (MPER-N-TMD helix) delimited by two hinge segments (underlined) (FIG 21B). To evaluate the contribution of the MPER-N-TMD helix (ITNWLWYIK) to binding energy, we have produced 4E10 Fab in bacteria (Fab4E10r), and then performed binding experiments by ITC in which we compared the $MPER_{(671-693)}$ peptide with the canonical MPER-representing $MPER_{(656-683)}$ peptide. The data indicated higher affinity of the $MPER_{(671-693)}$ peptide for Fab410r, which also comprised a neutralization-relevant ligand when incorporated into liposome-based vaccines. Together,

these results suggest that preserving an intact MPER-N-TMD helix is required for a vaccine to effectively elicit anti-MPER antibodies.

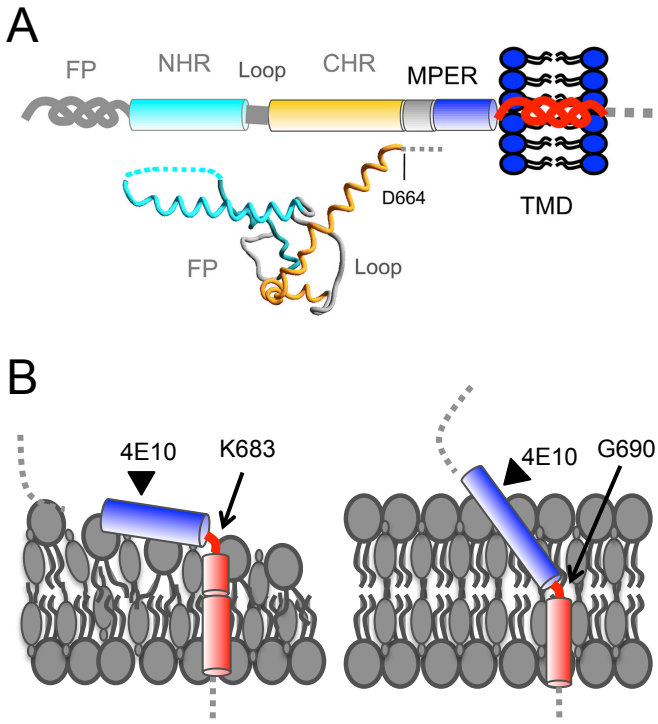

FIG 21. Organization of the HIV-1 gp41 MPER-TMD region. A) Diagram underlining the most important structural constituents of the membrane-anchored gp41 ectodomain. The same color code has been used to depict the gp41 ectodomain pre-fusion structure below (PDB code 4TVP). B) Membrane topology predicted for the MPER-TMD region attending to its hydrophobicity distribution (left) and to the recent NMR characterization of the MPER-TMD region (Apellaniz et al., 2015) (right).

3.2. MATERIALS AND METHODS

3.2.1. Materials

The peptides used in the structural and affinity studies were synthesized in C-terminal carboxamide form by solid-phase methods using Fmoc chemistry, purified by reverse phase high pressure liquid chromatography (HPLC), and characterized by matrix-assisted time-of-flight (MALDI-TOF) mass spectrometry

(purity > 95 %). Peptides were routinely dissolved in dimethylsulfoxide (DMSO, spectroscopy grade) and their concentration determined by the bicinchoninic acid microassay (BCA) (Pierce, Rockford, IL, USA) or using absorbance at 280nm. Goat anti-human IgG-Fab antibody was purchased from Sigma (St. Louis, MO). Secondary antibodies conjugated to horseradish peroxidase (HRP), goat (anti-human kappa light-chain)-HRP, goat (anti-human IgG)-HRP, and goat (anti-murine IgG)-HRP, were purchased from Life Technologies (Carlsbad, CA).

3.2.2. Expression and purification of 4E10 Fab.

4E10 Fab-s were cloned in pColaDuet and produced in *E. coli* T7-shuffle strain (see section 2.1). Protein expression was induced with 0.4 mM isopropyl-D-thiogalactopyranoside (IPTG) when the culture reached an optical density (OD) of 0.8. Cells were harvested at 8,000 $\times$ *g* after over-night (o/n) expression at 18 ºC. Cells were resuspended in a buffer containing 50 mM HEPES pH 7.5, 500 mM NaCl, 35 mM imidazole, DNase (Sigma-Aldrich) and an EDTA-free protease inhibitor mixture (Roche, Madrid Spain). Cell lysis was performed using an Avestin Emulsiflex C5 homogenizer. Cell debris were removed by centrifugation, and the supernatant from each culture was purified following various chromatography principles. First, Fab-s were purified using a nickel-nitrilotriacetic acid (Ni-NTA) resin (GE Healthcare). Elution was performed with 500 mM imidazole, and the fractions containing the his-tagged proteins were pooled, concentrated and dialyzed against 50mM sodium phosphate pH 8.0, 300mM NaCl, 1mM DTT, 0.3mM EDTA in the presence of the protease TEV. His tag-free Fab-s were then further purified thought an additional Ni-NTA column step. The flow through was dialyzed o/n at 4 ºC against sodium acetate pH 5.6 10 % glycerol and loaded into a MonoS ion exchange chromatography (IEC) column (GE Healthcare). Elution was carried out with a potassium chloride gradient and the fractions containing the purified Fab concentrated and dialyzed against a buffer containing 10 mM sodium phosphate, pH 7.5 120 mM NaCl and 10 % glycerol.

3.2.3. Isothermal titration calorimetry

Calorimetric titration experiments were performed with a VP-ITC microcalorimeter instrument (MicroCal, Northampton, MA) at 25 ^{o}C. Prior to the experiment, proteins were dialyzed o/n at 4 ºC against 10 mM sodium phosphate, 150 mM NaCl and 10 % glycerol at pH 7.5, and degassed just before the measurement. The buffer was supplemented with 5 mM dodecyl-phosphocholine (DPC). Fab4E10r (3 µM) was titrated with 40 µM of peptide (dissolved in dialysis buffer supplemented with 5mM DPC). The volume of each injection was 10 µL. Peptide dilution heat was subtracted from the experimental and final data. The binding isotherms were fitted to a one-site binding model using the program ORIGIN 7.0. The fitting yields the stoichiometry (n), the binding constant (K_D) and the enthalpy ($\Delta H°$) of the binding reaction.

3.2.4. Membrane binding assays

Vesicle flotation experiments in sucrose gradients were performed following a method described earlier (Yethon et al., 2003). In brief, 100 µl of a sample containing rhodamine (Rho)-labeled liposomes (1.5 mM lipid concentration) was adjusted to a sucrose concentration of 1.4 M in a final volume of 300 µl, and subsequently overlaid with 400 and 300 µl-layers of 0.8 and 0.5 M sucrose, respectively. The gradient was centrifuged at 436,000 $\times$ g for 3 h in a TLA 120.2 rotor (Beckman Coulter, Brea CA, USA). After centrifugation, four 250 µl-fractions were collected. Material adhered to tubes was collected into a 5th fraction by washing the tubes with 250 µl of hot (100º C) 1 % (w/v) Sodium dodecyl sulfate (SDS) after the other fractions had been taken from the tube.

3.2.5. Crystallization of 4E10 Fab-peptide complex

Co-crystals of Fab 4E10 in complex with the peptide $MPER_{(671-683)}$ were prepared by the hanging drop method. The Fab-peptide complex in the presence of detergent dihexanoyl-phosphocholine (DHPC) at 3 mM was concentrated to 2.5 mg/ml and mixed with a reservoir solution composed of 200 mM sodium acetate, 30 % PEG 8,000, and 100 mM sodium cacodylate (pH 6.5). Suitable crystals grew to full size within a few days at 20 °C, after which they were transferred to mother liquor supplemented with 20 % glycerol, and subsequently frozen and stored in a vessel containing liquid N2 .

3.2.6. Data collection and structure refinement

Diffraction data from a single crystal was collected on beamline BL5A of the Photon Factory (Tsukuba, Japan) under cryogenic conditions (100 K). Diffraction images were processed with the program MOSFLM and merged and scaled with the program SCALA of the CCP4 suite (Evans, 2006). The three-dimensional structure was determined by molecular replacement using the coordinates of 4E10 (PDB entry 2FX7) with the program PHASER (McCoy et al., 2007). The initial model was further refined with the programs REFMAC5 (Murshudov et al., 1997) and COOT (Emsley et al., 2010). Validation was carried out with PROCHECK (Laskowski et al., 1993). Data collection and refinement statistics are given in Table 2.

3.3. RESULTS

3.3.1. Energetics of 4E10 binding to $MPER_{(656-683)}$ and $MPER_{(671-693)}$ and structural model

Conservation of a continuous helical connection between MPER and TMD is likely to affect antibody binding to this region. Supporting this idea, it

has been demonstrated that the gp41 TMD plays a pivotal role in orienting the epitope recognized by the 4E10 antibody (Montero et al., 2012). Therefore, we selected the 4E10 antibody and the peptides $MPER_{(656-683)}$ (truncated at Lys-683) and $MPER_{(671-693)}$ (containing the full MPER-N-TMD helix) to determine the importance of this element on the energetics of antibody binding.

ITC experiments were carried out using the 4E10 Fab expressed in bacteria. To validate this recombinant Fab4E10r, it was crystallized in complex with the peptide NWFDITNWLWYIK-*KKK* ($MPER_{(671-683)}$) (FIG 22 and Table 2). The crystal structure of the recombinant 4E10 Fab-peptide complex solved at 2.10 Å was essentially indistinguishable from that of the Fab obtained by papain digestion of the recombinant IgG (rmsd = 0.20 Å) (Cardoso et al., 2007). The ITC experiments were conducted in the presence of the detergent DPC to mimic the composition of the buffer employed in the NMR experiments. The fitting of the binding isotherm to a one-site binding model yielded three key thermodynamic parameters in a single experiment (binding constant, K_D, change of enthalpy, $\Delta H°$, and stoichiometry of the reaction, n) (FIG 23A).

The titration experiments demonstrated that both peptides engage with the Fab with high affinity (nM range) driven by favorable non-covalent interactions ($\Delta H° < 0$). Notably, the Fab4E10r exhibited 6-fold higher affinity for $MPER_{(671-693)}$ than for $MPER_{(656-683)}$. Comparison of the thermodynamic parameters for the binding equilibria revealed significant differences in the relative contribution of the entropy ($-T\Delta S°$) and enthalpy ($\Delta H°$) terms for the binding of each peptide to the Fab. Specifically, the entropy loss of the peptide $MPER_{(671-693)}$ upon binding to the antibody ($-T\Delta S° = 1.8$ kcal mol^{-1}) is greatly reduced in comparison with that of the short version $MPER_{(656-683)}$ ($-T\Delta S° = 9.8$ kcal mol^{-1}). Thus, these observations suggest that $MPER_{(671-693)}$ is a better ligand than $MPER_{(656-683)}$ due to an optimization of the hydrophobic surfaces in contact with Fab, and/or to lower levels of conformational and roto-translational restrictions upon binding. The thermodynamic signature of $MPER_{(671-693)}$ (high affinity and pre-organization in a membrane-mimetic environment) could be a

desirable property for the design of better vaccines, as previously discussed for the case of epitope-scaffolds (Correia et al., 2010).

Table 2. X-ray data collection and refinement statistics[a]

	4E10 + peptide
Data collection	
Space group	C2
Cell dimensions	
a, *b*, *c* (Å)	157.3, 44.6, 85.4
α, β, γ (°)	90.0, 113.8, 90.0
Resolution (Å)	44.7–2.1 (2.21–2.10)
No. reflections (total)	166,559 (18,803)
No. reflections (unique)	30,114 (3,540)
R_{merge} (%)[b]	10.3 (37.1)
$I / \sigma I$	14.0 (4.3)
Completeness (%)	94.2 (76.6)
Redundancy	5.5 (5.3)
Refinement	
Resolution (Å)	44.7–2.10
R_{work} / R_{free} (%)[c]	16.2 / 20.6
No. atoms	
Protein	1,641
Peptide	159
Other (not solvent)[d]	12
Solvent	309
B-factors	
Protein	30.9
Peptide	41.8
Other (not solvent)[d]	34.6
Solvent	33.4
Ramachandran plot	
No. Preferred regions, %	344, 91.2%
No. Allowed regions, %	32, 8.5%
No. Outliers, %	1, 0.3 %
R.M.S. deviations	
Bond lengths (Å)	0.013
Bond angles (°)	1.52

[a] Values in parentheses are for highest-resolution shell.

[b] $R_{merge} = \Sigma_{hkl}\Sigma_i|I(hkl)_i - [I(hkl)]| / \Sigma_{hkl}\Sigma_i I(hkl)$.

[c] $R_{work} = \Sigma_{hkl} |F(hkl)_o - [F(hkl)_c]| / \Sigma_{hkl} F(hkl)_o$; R_{free} was calculated exactly as R_{work}, where $F(hkl)_o$ values were taken from 4 % of data not included in the refinement.

[d] Data corresponds to two glycerol molecules.

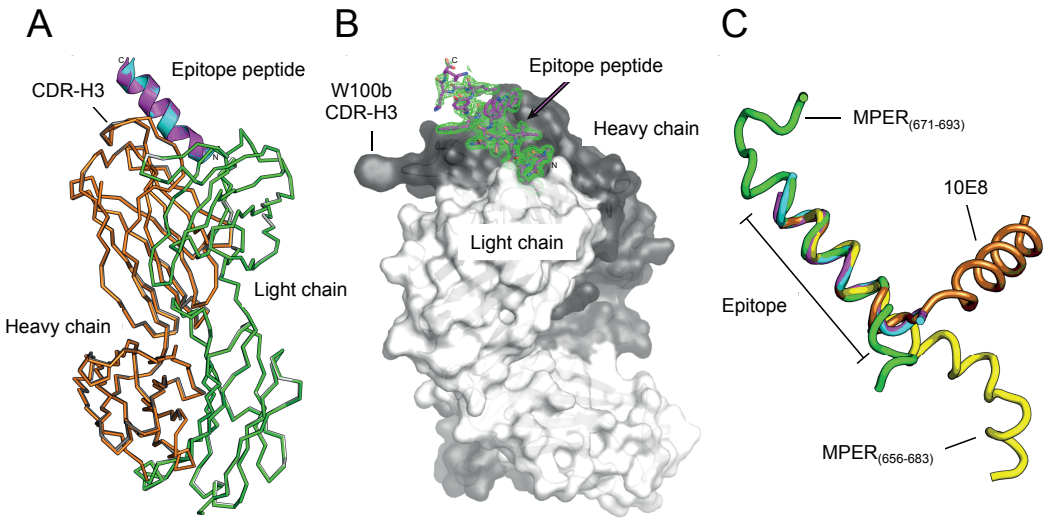

FIG 22. X-ray diffraction of recombinant Fab 4E10. A) Comparison of the crystal structures of recombinant Fab (this work, 2.10 Å) and Fab obtained upon cleavage of IgG (PDB entry 2FX7). The overall rmds of the main chain atoms between the two structures is 0.20 Å. The orange and light green ribbons depict the heavy and light chain of the recombinant Fab, whereas the gray ribbons correspond to the 2FX7 structure (barely discernible due to superposition of the ribbons of the recombinant Fab). The peptide bound to the Fab is shown in the cartoon representation, where magenta and cyan correspond to recombinant and IgG-derived Fab-s, respectively. B) Sigma-A weighted electron density of the peptide bound to recombinant Fab contoured at 1.0 σ. The location of the residue $Trp100_{HC}$ at the tip of the CDR-H3 of the Fab is indicated. C) Comparison of coordinates of five different peptides superposed between residues 674 and 683. The peptides correspond to recombinant Fab (magenta), 2FX7 structure (cyan, rmsd = 0.26 Å), $MPER_{(656-683)}$ (yellow, rmsd = 0.56 Å), $MPER_{(671-693)}$ (green rmsd = 0.82), and that of peptide bound to Fab 10E8 (orange, PDB entry 4G6F, rmsd = 0.32 Å).

To obtain molecular models of the peptides bound to the Fab, the constant helical region (residues 674-683) was employed to superpose the NMR coordinates of the peptides in DPC with those of the peptide-epitope obtained in the crystal structure with Fab (FIG 23B). The structure of $MPER_{(656-683)}$ in DPC superimposes well with the short peptide epitope in the crystal structure, including the orientation of the side chains of the residues buried in the paratope (^{671}NWF--T--LW^{680}) (FIG 23B, left). In contrast, the coordinates of the $MPER_{(671-693)}$ in DPC show a disorganized hinge segment at its N-terminal region (FIG 23B, right). Hence, this superposition suggests that the segment ^{671}NWF^{673} must reorient for binding adequately to the antibody. Conversely, the other residues (674-683) superpose with those of the Fab-bound peptide with remarkable exactitude.

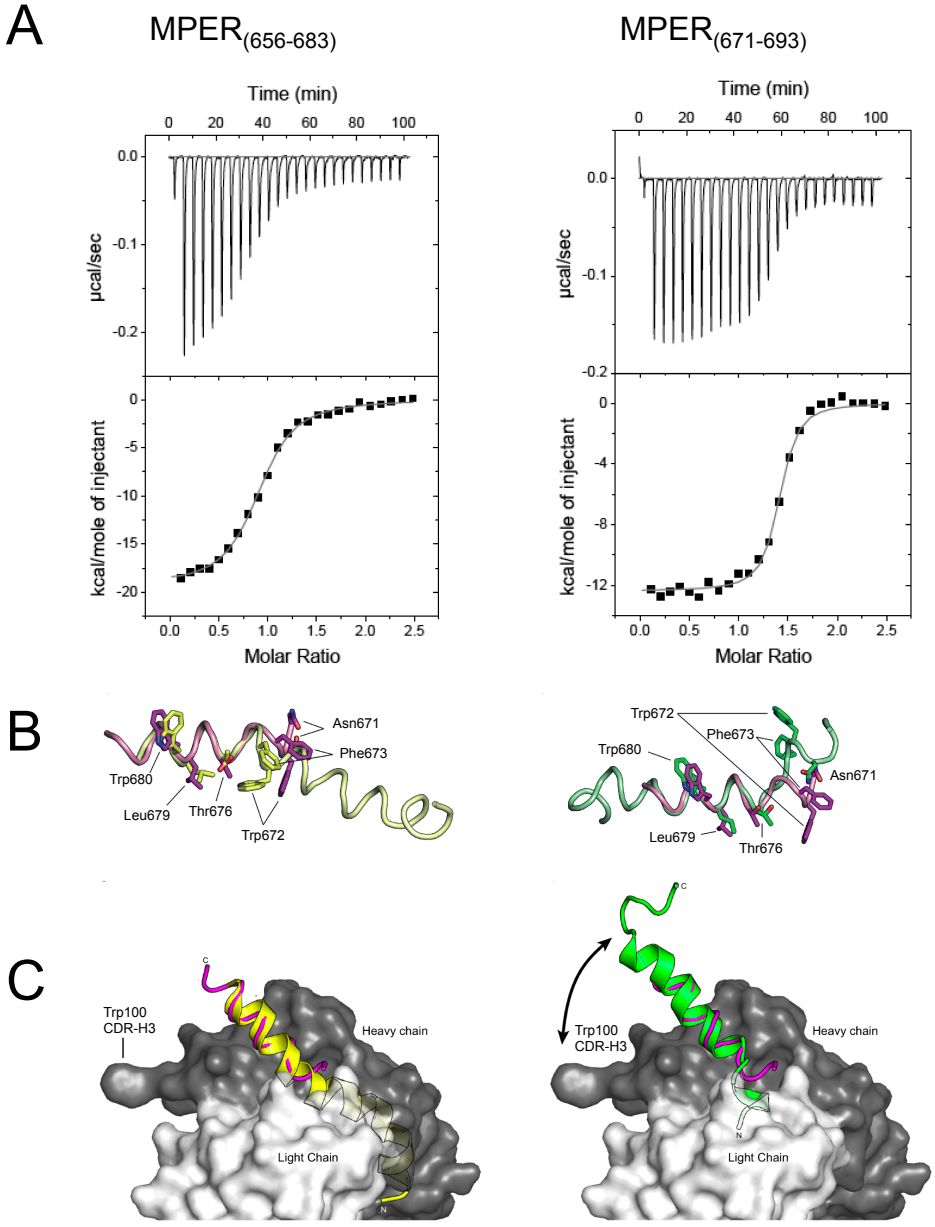

FIG 23. Binding to Fab4E10r by ITC and structural comparison. A) Binding isotherms of $MPER_{(656-683)}$ and $MPER_{(671-693)}$ to Fab4E10r. The upper panels indicate the heat released upon consecutive injections of peptide into Fab4E10r in the calorimeter cell. Lower panels: integrated heats (symbols) and non-linear least-squares fit (line) of the data to a one site binding model. The thermodynamic parameters of binding for $MPER_{(656-683)}$ were K_D = 119 ± 10 nM, $\Delta H°$ = −19.2 kcal mol^{-1}, $-T\Delta S°$ = 9.8 kcal mol^{-1} and stoichiometry n = 0.90. The thermodynamic parameters for $MPER_{(671-693)}$ were K_D = 18 ± 2 nM, $\Delta H°$ = −12.4 kcal mol^{-1}, $-T\Delta S°$ = 1.8 kcal mol^{-1} and stoichiometry n = 1.4. B) Fitting of $MPER_{(656-683)}$ and $MPER_{(671-693)}$ DPC structures into the Fab-bound peptide. Indicated side chains correspond to residues with highest buried surface area upon interaction. C) Modeled orientation of $MPER_{(656-683)}$ and $MPER_{(671-693)}$ in the recombinant Fab. Fab-bound peptide is depicted as a magenta ribbon. The modeled peptides $MPER_{(656-683)}$ and $MPER_{(671-693)}$ are depicted in yellow and green, respectively. The light and dark surface corresponds to the HC and LC chains, respectively.

The superposition of these two peptides on the Fab (FIG 23C) suggests the molecular basis of the higher affinity of a peptide extended at the C-terminal but not at the N-terminal end. Elongation of the peptide at the N-terminus ($MPER_{(656-683)}$) must force the peptide to adopt a conformation different from that observed in solution to avoid steric clashes with the Fab (FIG 23C, left). On the contrary, the additional residues at the C-terminus of $MPER_{(671-693)}$ do not clash with the antibody, reducing the conformation penalty upon binding compared with $MPER_{(656-683)}$. Moreover, the orientation of the C-terminal residues of $MPER_{(671-693)}$ with respect to the long CDR-H3 loop of the antibody habilitates the peptide to engage in additional non-covalent interactions with the antibody (FIG 23C, right).

3.3.2. Binding to peptide-liposome vaccines

As put forward by the previous antigenicity results, peptide structuring in a membrane environment may influence 4E10 antibody binding, and hence, modulate interactions with cognate B-cell receptors. It has been argued that interactions with the membrane surface may be key for the selection of MPER conformations that induce specific antibodies (Alving et al., 2012; Montero et al., 2012), while lipid binding by anti-MPER antibodies has been hypothesized to increase avidity (Klein et al., 2013b; West et al., 2014). Thus, we formulated the $MPER_{(656-683)}$ and $MPER_{(671-693)}$ peptides with truncated or conserved MPER-N-TMD helix, respectively, as potential liposomal vaccines. Vaccine antigenicity was assessed using a strategy similar to that described in a preceding study (Serrano et al., 2014). Those experiments based on Fab flotation experiments (FIG 24A) included a Fab mutant with the CDR-H3 loop tip ablated as a negative control. The Fab4E10r-Δloop mutant binds peptide epitopes in solution with comparable affinity but it is not neutralizing (Apellaniz et al., 2014b), which allows discriminating functional vs. non-functional binding.

Both, Fab4E10r-WT and Fab4E10r-ΔLoop co-floated with the liposomes that contained $MPER_{(656-683)}$ peptide (FIG 24B). Fab4E10r-WT was also

recovered from floating fractions that contained liposomes decorated with the $MPER_{(671-693)}$ peptide. In contrast, practically all Fab4E10r-Δloop was recovered from pellets under these conditions (FIG 24B). Finally, none of the Fab-s co-floated appreciably with control liposomes devoid of peptide under otherwise similar experimental conditions. In conclusion, the neutralizing function and the binding to $MPER_{(671-693)}$ inserted into liposomes were both dependent on the 4E10 CDR-H3 loop, a correlation not observed for the $MPER_{(656-683)}$ peptide. The existence of a binding-function correlation in the case of the liposome-$MPER_{(671-693)}$ vaccine suggests that this formulation could be relevant to target 4E10-like B-cell receptors.

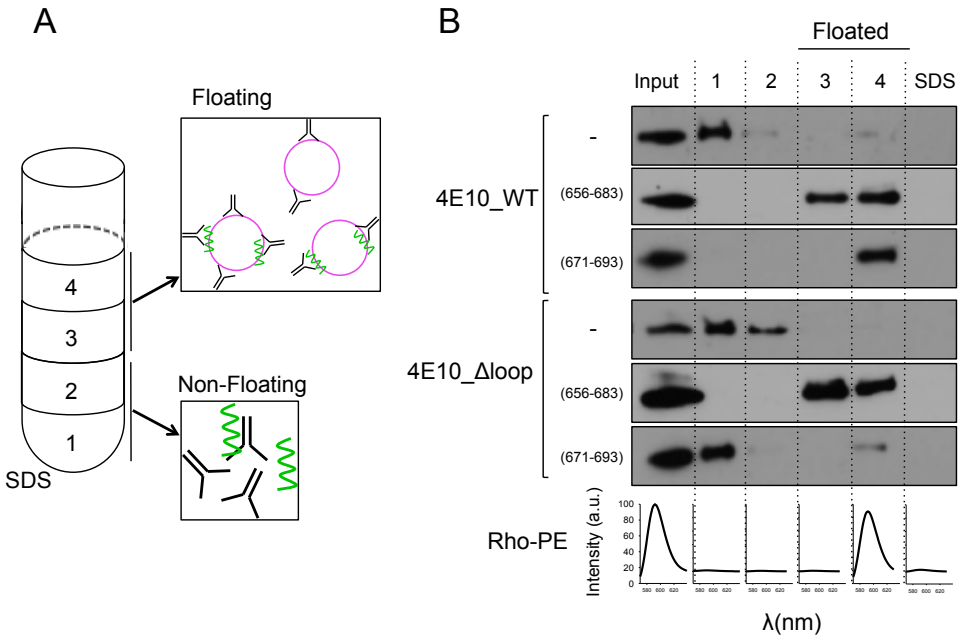

FIG 24. Correlation between 4E10 antibody function and binding to liposomal vaccines. A) Schematic representation of a flotation experiment to assess antibody binding to liposomes and liposomes-peptide complexes. Lipid vesicles in the absence or presence of peptide were pre-incubated with the antibody fragments and subjected to a sucrose gradient. Upon separation of the species based on their different densities, the sample is divided into 4 different fractions. An additional sample was obtained from the material attached to the surface of the tube upon addition of SDS for its removal. The liposomes are located in the upper floated (light) fractions 3 and 4 and detected from the fluorescence emission of the fluorescently labeled lipid Rho-PE. Fractions 1, 2 and SDS contained the non-floated (dense) material. Location of the antibody was detected by western blot (WB). B) Membrane partitioning of Fab4E10r-WT or Fab4E10r-ΔLoop to liposomes devoid of peptide and $MPER_{(656-683)}$ or $MPER_{(671-693)}$-containing liposomes.

3.4. DISCUSSION

The existence of a continuous MPER-N-TMD helix motif may have implications for the definition of the neutralization-competent MPER structure (Montero et al., 2012) and, consequently, for the design of surrogates with the capacity to generate humoral responses against the MPER C-terminal region (Burton et al., 2012). Recreating this structure has been the aim of many studies employing representative MPER peptides truncated at position Lys-683 and liposomes. As previously shown by us and other groups (Alving et al., 2012; Dennison et al., 2011; Kim et al., 2013; Maeso et al., 2011; Serrano et al., 2014; Venditto et al., 2013), formulations of this kind are usually poorly immunogenic and raise cross-reactive antibodies targeting the MPER N-terminal region, i.e., directed to sites overlapping 2F5/M66.6 epitope residues. However, they seemingly fail to direct responses to the C-terminal epitopes recognized by 4E10 and 10E8 antibodies.

Structural data and MDS of $MPER_{(656-683)}$ (Serrano et al., 2014) suggest two different causes for this phenomenon. On the one hand, modeling of the $MPER_{(656-683)}$ DPC structure into the 4E10 paratope reveals that the N-terminal side must reorient to avoid steric clashes. Thus, the presence of a well-defined helix preceding the ^{671}NWFD^{674} segment reduces 4E10 affinity for $MPER_{(656-683)}$. On the other hand, MDS studies put forward that the C-terminal 4E10/10E8 key epitope residues can orient towards the lipid bilayer hydrocarbon core (Serrano et al., 2014). In combination, these two effects would hamper interaction of the membrane-inserted $MPER_{(656-683)}$ with B-cell receptors. ITC results indicate that peptide binding is limited by the entropic cost. Therefore, pre-formation of the MPER-N-TMD helix in a membrane mimetic medium appeared to elicit tighter binding to the 4E10 antibody. In addition, membrane-inserted $MPER_{(671-693)}$ peptide, which mostly exhibited insertion orthogonal to the lipid bilayer plane in previous MDS studies (Apellaniz et al., 2014b), efficiently bound to functional 4E10, while binding to the neutralization-deficient mutant was severely affected. Thus, preservation of the MPER-N-TMD helix

motif might be important for functional antibody and B-cell receptor binding. Consistently, MPER-N-TMD-specific IgG was recovered from rabbit sera upon immunization with CpreTM but not from rabbits immunized with the NpreTM peptide-based formulations (Apellaniz et al., 2015).

Chapter 4

STRUCTURAL AND THERMODYNAMIC BASIS OF EPITOPE BINDING BY NEUTRALIZING AND NON-NEUTRALIZING FORMS OF 4E10

4.1. INTRODUCTION

The conserved MPER domain has been proposed to function in gp41-mediated HIV-1 membrane fusion by perturbing the lipid packing of the viral envelope (Apellaniz et al., 2011; Apellaniz et al., 2014b; Salzwedel et al., 1999). This region is critical for viral entry and is highly conserved, as evidenced by the MAb 4E10, which binds to the MPER C-terminal helix and neutralizes up to 98 % of global HIV-1 strains (Binley et al., 2004; Huang et al., 2012; Kwong and Mascola, 2012). Due to its exceptional neutralization breath, 4E10 has served as a model of broad protection against HIV infection, and consequently has been the subject of extensive structural and functional characterization, particularly for the purpose of vaccine design (Burton et al., 2004; Kwong and Mascola, 2012; Montero et al., 2008; Zwick, 2005).

The first crystal structure of the 4E10 Fab in complex with a 13-residue-long peptide containing the gp41 core epitope ^{671}NWFDIT^{676} revealed the critical binding interactions (Cardoso et al., 2005). The residues of this peptide in contact with the Fab (Trp672, Phe673, Ile675, and Thr676) all gathered at one face of the helix. A second crystal structure of Fab 4E10 bound to an extended peptide epitope ^{671}NWFDITNWLWYIK^{683}-*KKK* was subsequently reported (Cardoso et al., 2007). This peptide (MPER$_{671\text{-}683}$) displays an affinity three orders of magnitude higher than that of the shorter version (Brunel et al., 2006). The enhanced affinity of the longer peptide is due to additional interactions between the extra helical turn of MPER$_{671\text{-}683}$ (Leu679 and Trp680) and the antibody. Based on the structural data available, the 4E10 epitope was lengthened to comprise the motif ^{672}WFX(I/L)(T/S)XX(L/I)W^{680} with residues at Env positions 672, 673, 675, 676, 679 and 680, located on the hydrophobic face of the amphipathic helix comprising the “neutralizing face” of the epitope. These conclusions were reinforced when stabilization of the helical structure at the non-binding face by covalently “stapling” residues 678 and 681, was shown to further enhance peptide affinity (Bird et al., 2014).

It has been proposed that the hydrophobic CDR-H3 loop of 4E10 interacts with lipids of the viral envelope (Cardoso et al., 2005). This hypothesis was further elaborated after observing that binding of Fab and single-chain variable fragment (scFv) of 4E10 to liposomes composed of viral lipids is governed by the hydrophobicity of its unusually long and highly flexible CDR-H3 loop (Alam et al., 2009; Apellaniz et al., 2014b; Scherer et al., 2010). In particular, Scherer *et al.* (Scherer et al., 2010) found a direct correlation between lipid binding and neutralizing activity for 4E10 IgGs bearing substituted Trp residues at the apex of the CDR-H3. For example, the double mutation $W_{H100}D/W_{H100B}D$ (termed WDWD) exhibits poor affinity for lipids and undetectable activity in standardized viral neutralization assays. These authors concluded that hydrophobic residues of the apex region of CDR-H3 are required for MPER recognition through favorable lipid interactions in the context of the viral envelope.

In crystal structures of 4E10 Fab-peptide complexes, the long CDR-H3 loop required for neutralization extends beyond the bound helical peptide in an orientation that suggests its apex could contact the viral membrane and contribute to neutralization (Cardoso et al., 2007; Cardoso et al., 2005). Using a recombinant variable fragment (Fv) fragment (composed of V_H + V_L) it was shown that mutating a Trp residue of the apex does not change the binding mode of a scaffold-protein containing the sequence of the core epitope peptide (Xu et al., 2010). Later, studies employing the same Fv fragment suggested that the 4E10 paratope is flexible and undergoes a large restructuring process upon binding to peptide (Finton et al., 2014; Finton et al., 2013). Specifically, this conformational change would involve a shift of *ca.* 12 Å of the CDR-H3 loop, and especially of the apex segment (Finton et al., 2013). The possibility that the loop undergoes significant restructuring during peptide binding implies that mutations that abolish neutralization may alter the CDR-H3 conformational equilibrium, and through this mechanism, hamper peptide recognition. Opposing this data, co-crystals obtained in the presence of phosphatidic acid, phosphatidylglycerol, and glycerol phosphate reveal two binding sites involving

the CDR-H1 loop on the surface of 4E10 paratope facing the membrane (Bird et al., 2014; Irimia et al., 2016). This crystallographic analysis revealed the presence of these pockets in the unbound and complex-bound conformation of the 4E10 antibody consistent with the simultaneous accommodation of the phospholipid head-group moieties and peptide epitope within 4E10 paratope. Besides, the crystal structures reveal a 9 Å movement of the CHR-H3 inferring possible hydrophobic interactions between the residues of the loop and the lipid tails. Although this mode of interaction could account for the higher binding affinity of the antibody to its epitope in the context of lipid membranes, mutagenesis studies will be necessary to evaluate the functional role of these subsites during viral neutralization by 4E10.

To determine the differences between neutralizing and non-neutralizing 4E10 Fab-s at the molecular level, we have determined high-resolution crystal structures of two non-neutralizing Fab-s bearing mutations in the CDR-H3 loops. The overall structure of the non-neutralizing antibodies and those of the WT Fab-peptide complexes previously reported (Apellaniz et al., 2015; Cardoso et al., 2007; Cardoso et al., 2005) are nearly indistinguishable, except for some differences in the conformation of the CDR-H3 apex. Following strategies delineated in our previous studies, the structural data were complemented with a detailed kinetic and thermodynamic analysis of the ($MPER_{671-683}$) peptide binding mechanism, not only at equilibrium, but also at the transition state (Kiyoshi et al., 2014; Kiyoshi et al., 2015). We show that neutralizing and non-neutralizing Fab-s recognize the helical ($MPER_{671-683}$) peptide by means of nearly identical mechanisms at both the energetic and atomic levels. In particular, the novel crystal structure of the ligand-free Fab indicates that the CDR-H3 loop does not undergo significant conformational changes during recognition of the epitope. Comparison of the structures of Fab in the bound and free states revealed loss of flexibility in the CDR loops during peptide engagement, except for the apex region of the CDR-H3, which remained relatively flexible. In contrast to the common structural and energetic mechanism describing the binding of neutralizing and non-neutralizing Fab to

$MPER_{(671-683)}$ in solution, the non-neutralizing forms of 4E10 Fab were defective in binding to an MPER that was anchored to the plasma membrane *via* the gp41 TMD (Montero et al., 2012), which was otherwise efficiently recognized by the neutralizing WT Fab. Collectively, our data support the notion that the hydrophobic CDR-H3 apex governs recognition of the MPER epitope, constrained in a membrane context, a process required for efficient neutralization of the virus.

4.2. MATERIALS AND METHODS

4.2.1. Materials

The peptides used in the structural and affinity studies were synthesized as described in 3.2.1. The following reagents were obtained through the NIH AIDS Reagent Program, Division of AIDS, DAIDS, NIAID, NIH: The IgG1 MAb, 4E10, from H. Katinger (Polymun Scientific GmbH, Vienna, Austria), pNL4-3.Luc.R-.E- from N. Landau (Aaron Diamond AIDS Research Center, The Rockefeller University), TZM-bl cells from J. C. Kappes, X. Wu and Tranzyme Inc., and plasmids encoding Env from the HIV-1 isolates: SS1196.1 clone 1 (SVPB9) from D. Montefiori and F. Gao (Duke University Medical Center), Bal.26 from J. Mascola (Vaccine Research Center, NIH), and JR-CSF from I. Chen (David Geffen School of Medicine, University of California Los Angeles) and Y. Koyanagi (Institute for Virus Research, Kyoto University). A plasmid encoding the engineered HIV-1 Env, SF162.LS, was kindly provided by N. Haigwood (Oregon National Primate Center, Beaverton, OR), and a plasmid encoding the VSV-G Env was provided by Patricia Villace (CSIC, Madrid). A hybridoma cell line producing the murine MAb 17/9, which recognizes the HA-tag sequence, DVPDYA, was kindly provided by R. Stanfield and I. A. Wilson (The Scripps Research Institute, La Jolla, CA); this IgG1 MAb was produced and purified from ascites fluid by Maine Biotechnology Services Inc. (Portland, ME). Recombinant gp41 (r-gp41; HIV-1MN isolate) was purchased from

ImmunoDiagnostics (Woburn, MA). A peptide bearing the MPER sequences residues 667-683 (MPER667-683; HXB2 numbering) from HIV strain JR-CSF gp41 (NH^{3+}-ASLWNFDITKWLWYIK-SGK-(biotin)-$CONH_2$) was purchased from United Biosystems (Herndon, VA) at > 95 % purity.

4.2.2. Mutagenesis and production of 4E10 Fab-s.

For the generation of the Fab 4E10-ΔLoop mutant, the hydrophobic CDR-H3 loop apex (residues $Trp100_{HC}$-$Gly100a_{HC}$-$Trp100b_{HC}$-$Leu100c_{HC}$) was deleted through site-directed mutagenesis. The resulting gap between residues $Gly99_{HC}$ and $Gly100d_{HC}$ was filled with a SG linker. In the case of the Fab WDWD, residues $Trp100_{HC}$ and $Trp100b_{HC}$ were substituted with Asp. Genetic modifications of the constructs were carried out with the KOD-Plus mutagenesis kit (Toyobo, Osaka, Japan) following the manufacturer's instructions. Experimental procedures described in 3.2.2 were followed for the production and purification of Fab-s.

4.2.3. Crystallization of ligand-free Fab and Fab-peptide complexes.

Crystals of unbound WT 4E10 Fab, as well as crystals of WDWD or ΔLoop in complex with $MPER_{(671-683)}$, were prepared by the hanging drop method. The crystals of unbound WT Fab were obtained by mixing 0.5 µl of protein at 3 mg/ml with 0.5 µl of a solution containing 15 % (w/v) PEG 20,000 and 100 mM MES (pH 6.5). To obtain crystals of non-neutralizing Fab-s in complex with peptide, first antibody and epitope were mixed at an approximate molar ratio of 1:1.3 (protein:peptide) and subsequently concentrated to 3 mg/ml. Suitable crystals of WDWD-$MPER_{(671-683)}$ were obtained by mixing 2 µl of the solution containing protein and peptide with 2 µl of a solution composed of 200 mM ammonium acetate, 34 % PEG 8,000, and 100 mM Tris-HCl (pH 8.4). Similarly, co-crystals of ΔLoop Fab with epitope bound were obtained by mixing the complex with a solution composed of 200 mM ammonium acetate, 30 %

PEG 8,000, and 100 mM Tris-HCl (pH 8.5). In both cases crystals grew to full size within a few days at 20 °C. Suitable crystals were identified, harvested and briefly transferred to mother liquor supplemented with 25 % (v/v) ethyleneglycol (unbound Fab) or 15 % (v/v) glycerol (WDWD and ΔLoop Fab-s in complex with $MPER_{(671-683)}$), and frozen and stored in a vessel containing liquid N_2.

4.2.4. Data collection and structure refinement

Diffraction data from a single crystal of the unbound Fab were collected at beamline I02 of the Diamond Light Source (Oxfordshire, UK) under cryogenic conditions (100 K). Diffraction data of the WDWD and ΔLoop Fab-s in complex with $MPER_{(671-683)}$ were collected in beamline BL5A of the Photon Factory (Tsukuba, Japan) also under cryogenic conditions (100 K). Diffraction images were further processed as described in 3.2.6 using the coordinates of recombinant WT Fab described in chapter 3. The crystal of unbound WT Fab was partially twinned (ratio 70/30) as determined with the program REFMAC5 during the refinement stage. Data collection and structure refinement statistics are given in Table 4.

4.2.5. Differential scanning calorimetry (DSC)

The heat capacity of individual Fab-s was measured using a VP-DSC system (MicroCal, Northampton, MA). All calorimetric scans were performed in a buffer composed of 10 mM NaH_2PO_4 (pH 7.5), 150 mM NaCl, and 10 % glycerol. Protein samples at 10 μM were heated from 30 to 90 ºC at a scanning rate of 1 ºC min^{-1}. The ORIGIN software package (MicroCal) was used for data collection and analysis. The buffer baseline was subtracted from the raw data, which were normalized by protein concentration to obtain thermodynamic parameters and then fitted to a to a non-two-state model.

4.2.6. Surface Plasmon Resonance (SPR)

Temperature-dependence SPR experiments were performed on a Biacore T200 instrument (GE Healthcare). 4E10 Fab-s, WT, WDWD and ΔLoop, were dialysed against running buffer (10 mM HEPES-NaOH, pH 7.5, 150 mM NaCl, 3 mM EDTA, and 0.1 % (v/v) Tween-20). An antibody-capture method was used to obtain the binding response of the $MPER_{(671-683)}$-Fab interaction. An anti-human IgG-Fab secondary antibody was immobilized on a Biacore CM5 chip (GE Healthcare) to surface densities of ~15,000 response units (RU). For that purpose, the chip was first activated with N-hydroxysuccinimide and N-ethyl-N'-(3-dimethylaminopropyl) carbodiimide hydrochloride as previously described (Kiyoshi et al., 2014; Kiyoshi et al., 2015; Sakamoto et al., 2009). After immobilizing the anti-human Fab antibody, the remaining active groups on the surface of the chip were blocked by flowing 100 ml of 1 M ethanolamine. The Fab variants were subsequently captured to surface densities of ~1400 RU. For these experiments, the lysine residues of the standard $MPER_{(671-683)}$ were substituted for Arg as previously described ($MPER_{(671-683)}R$) (Huang et al., 2012). This peptide was flowed over the immobilized Fab-s at 30 µl/min in increasing concentrations from 7.8 to 500 nM. The association and dissociation phases were 120 and 200 s, respectively. Regeneration was achieved after completion of each sensorgram by injecting a solution of 10 mM glycine-HCl, pH 1.5, for 30 s at a flow rate of 30 µl/min. Association (k_{on}) and dissociation (k_{off}) rate constants were determined with the Biacore T200 evaluation software (GE Healthcare). The dissociation constant (K_D) was calculated from the ratio of the rate constants ($K_D = k_{off} / k_{on}$). Changes in enthalpy (ΔH_{vH}) and entropy (ΔS_{vH}) were calculated from the slope and intercept, respectively, of the temperature dependence of the dissociation constant using the van't Hoff approximation (Sakamoto et al., 2009) (see section 2.4.1). The activation energy parameters were obtained from the temperature dependence of each kinetic rate constant according to the Eyring equation (Cleland and Northrop, 1999) (see section 2.4.1).

4.2.7. Dot-blot PsV binding assay

Decreasing amounts of the HIV-1 isolate JR-CSF PsV were spotted (1 µL) onto Hybond C nitrocellulose (GE Healthcare). The membrane was then blocked with 5 % fat-free milk in PBS (Blocking Buffer) o/n, and incubated for 1 hour with Fab antibodies (0.2 µg/ml) in Blocking Buffer at RT. The membranes were washed 3 times, 10 min each with PBS, and soaked with primary antibody (goat anti- Human Fab specific (Santa Cruz) at a 1:2,000 dilution. The membranes were washed again, and then incubated 1h with HRP-conjugated secondary antibodies (GE Healthcare) at a 1:2,000 dilution. After washing with PBS, binding was detected using SuperSignal West Pico Chemiluminescent Substrate (Thermo Scientific).

4.2.8. Cell lysate production

Cell lysate production was carried out as previously described (Montero et al., 2012). 293T cells were transiently transfected with 1 µg plasmid DNA encoding recombinant MPER proteins, MPER-TM1 and MPER-PGDFR, using the XtremeGENE 9 transfection reagent (Roche, Basel, Switzerland), according to the manufacturer's instructions, at a ratio of 1:6 (i.e., µg DNA to µL transfection reagent). Cells were cultured in 6-well plates (Sarstedt, Numbrecht, Germany) in Dulbecco's modified Eagle's medium (DMEM; Life Technologies, location) supplemented with 10 % (v/v) fetal calf serum (FCS; Life Technologies) and 1 mM L-glutamine (Life Technologies) at 37 °C and 5 % CO_2. After 48 hours, the cells were washed four times in phosphate-buffered saline (Life Technologies), and recovered from the plate with 1 mM Na_2EDTA-NaOH, pH 8.0 (Bioshop, Burlington, Canada). Cells were pelleted by centrifugation for 5 min at 350 $\times$ *g*, resuspended in 200 µL lysis buffer comprising a protease-inhibitor cocktail (complete ULTRA Tablets, mini, EDTA-Free; Roche) diluted 1:12 in (250 mM sucrose and 0.5 mM Na_2EDTA-NaOH, pH 8.0). Cell lysates were produced by 30 passages through a 22-gauge needle followed by two 15-s pulses with a Virsonic sonicator (VirTis, Gardiner,

NY). Total protein content was quantified using the Bradford reagent (Bio-Rad Protein Assay, BioRad, Mississauga, Canada) following the manufacturer's instructions; lysates were stored at -80 °C.

4.2.9. Enzyme-linked immunosorbent assays (ELISAs)

Wells of high-binding microtiter plates (Corning Inc., Corning, NY) were coated o/n at 4 °C with 35 µL/well of one of the following diluted in Tris-buffered saline (TBS; 50 mM Tris-HCl, pH 7.5, 150 mM NaCl): (i) cell lysate (the equivalent of 10 µg protein), (ii) r-gp41 (50 ng), (iii) biotinylated $MPER_{667-683}$ peptide (400 ng), or (iv) TBS containing 2 % (w/v) bovine serum albumin (TBS-BSA; Sigma-Aldrich). Wells were blocked for 1 h at room temperature (RT) with TBS-BSA, then washed twice with TBS containing 0.1 % (v/v) Tween-20 (TBS-T), once with TBS, then incubated for 2 h at RT with the indicated dilutions of 4E10 IgG1, 17/9 IgG1 or one of the 4E10 Fab-s (WT, WDWD, ∆Loop) diluted in TBS-T containing 5 % (w/v) non-fat dried milk (5 % NFDM; Bio-Rad). After five washes with TBS-T followed by one with TBS, bound 4E10 IgG or 4E10 Fab-s were detected with goat (anti-human kappa light chain IgG)-HRP, and bound 17/9 IgG1 with goat (anti-murine IgG)-HRP, diluted 1:500 and 1:1,000, respectively, in 5 % NFDM. After 1 h incubation at RT, plates were washed five times in TBS-T and once in TBS. Bound HRP was detected using 400 ng/ml 2'2'-azino-bis-3-ethylbenzthiazoline-6-sulfonic acid (ABTS; Sigma-Aldrich, St. Louis, MO) in developer solution comprising a 1:1.5 ratio of citrate (0.1 M, pH 2.4) and phosphate (0.2 M, pH 9.2) buffers, along with 0.03 % (v/v) H_2O_2. Absorbance was measured at 405 – 490 nm, using a Tecan Infinite M200 Pro microplate reader (Tecan, Mannedorf, Switzerland).

4.2.10. HIV-1 envelope neutralization assays

Neutralization assays were performed using a single-round infection assay with envelope (Env)-pseudotyped virus (PsV) as described previously

(Seaman et al., 2010). Briefly, PsVs were produced by co-transfection of 293T cells with (i) an Env-negative HIV genomic vector that carries a firefly luciferase reporter gene (pNL4.3.Luc.R.E-), and (ii) a plasmid carrying an HIV envelope gene expression cassette. 293T cells (2 x 106 cells) were co-transfected with plasmid DNA at ratios of 1:3 to 1:20 µg pNL4.3.Luc.R.E- plasmid DNA to µg HIV Env+ plasmid DNA and 54 µg polyethylenimine (PEI; Polysciences, Warrington, PA). Plasmids encoding Env from HIV-1 isolates and controls include: SF162.LS, SS1196.1 clone 1 (SVPB9), or JR-CSF, or with a plasmid expressing the Env from vesicular stomatitis virus (VSV-G) (to produce a negative-control PsV). PsVs were harvested from cell-free supernatants 72 h post-transfection, passed through a 0.45 µm-filter, diluted 1:10 in 10X phosphate-buffered saline (Life Technologies), aliquoted, and stored at -80 °C.

PsV infection is measured using a luciferase-based assay in TZM-bl cells, with neutralization being measured as a reduction in luciferase activity following single-round infection. TZM-bl cells were seeded o/n (10,000/well) in flat-bottom 96-well plates (Corning) in a total volume of 200 µL DMEM supplemented with 10 % heat-inactivated FCS and 1 mM L-glutamine (DMEM-ΔFCS). Three-fold serial dilutions of the appropriate MAb or Fab concentration were prepared in DMEM-ΔFCS in a total volume of 150 µL, and added in triplicate to the wells of a separate round-bottom 96-well plate (Corning). PsVs were added at 200 TCID50/well in a total volume of 50 µL DMEM-ΔFCS supplemented with 25 µg/mL diethylaminoethyl-dextran hydrochloride (DEAE-Dextran; Sigma-Aldrich), and plates were incubated for 1 h at 37 °C and 5 % CO2. Following incubation, media was removed from wells of the TZM-bl-seeded 96-well plates, and PsV-MAb/Fab samples were transferred to the plates. Control wells comprising TZM-bl cells only (cell control), and virus only (virus control) were also included. After a 72-h incubation, media was removed from wells, 50 µL Glo lysis buffer (Promega, Madison, WI) was added to each well, and lysis was allowed to proceed at RT with gentle rocking for 5 min. One-Glo luciferase substrate (Promega) (50 µL/well) was added and incubated for five min at RT. Samples were transferred (50 µL/sample) to 96-well, white solid

plates (Thermo Fisher Scientific, Waltham, MA) and luciferase activity was measured using a Tecan Infinite M200 Pro multi-mode plate reader (Tecan). All values are reported as relative luminescence units (RLU), and neutralization was calculated with respect to cell- and virus-control wells using the following formula: 1 - [(RLUsample wells – RLUcells-only wells) / (RLUvirus-only wells – RLUcells-only wells)] x 100. The 50 % inhibitory concentration (IC_{50}) concentration is calculated as the antibody/Fab concentration producing a 50 % reduction in RLU compared to the level in the virus-control wells after subtraction of cell-control RLU.

4.3. RESULTS

4.3.1. Crystal structures of non-neutralizing 4E10 Fab-s

Modification of the flexible, hydrophobic CDR-H3 loop may result in impaired neutralizing 4E10 activity (Alam et al., 2009; Apellaniz et al., 2014b; Scherer et al., 2010; Xu et al., 2010). To investigate this phenomenon at the molecular level, we determined the crystal structure of two different non-neutralizing 4E10 Fab-s mutated at the CDR-H3 loop, which were generated as follows: (i) truncating the hydrophobic apex by replacing the $Trp100_{HC}$-$Gly100a_{HC}$-$Trp100b_{HC}$-$Leu100c_{HC}$ sequence with a Ser-Gly dipeptide (termed ΔLoop); and (ii) substituting the aromatic $Trp100_{HC}$ and $Trp100b_{HC}$ residues for polar-charged Asp residues, hence reducing the hydrophobicity while preserving the length of the loop (termed WDWD and previously described by Scherer *et al*. (Scherer et al., 2010)). Recombinant Fab-s were expressed in *E. coli* without loss of performance or change of structure with respect to the Fab obtained by papain cleavage of IgG (Apellaniz et al., 2015). Compared with WT antibodies (IgG and its Fab fragment) the ΔLoop and WDWD Fab-s did not exhibited neutralizing activity in a standard assay (Table 3). The 4E10 IgG exhibits higher neutralization potency than that of the Fab fragment, (6.5-fold) in good agreement with observations reported in a previous study (4.4-fold) (Klein

et al., 2009). The molecular basis of this gap in neutralization potency is still unclear, although it might reflect the effect of avidity at the two available 4E10 sites in the Env trimer (Leaman et al., 2015).

Table 3. Neutralization of primary isolate viruses by 4E10 IgG, WT, and mutant Fab-s.[a]

	Tier 1A	Tier 1B	Tier 2	Control
Antibody	**SF162.LS**	**SS1196.1**	**JRCSF**	**VSV-G**
4E10 IgG	21[b]	21	20	> 200
4E10 WT Fab	146	155	106	> 200
4E10 WDWD Fab	> 600	> 600	> 600	> 200
4E10 ΔLoop Fab	> 600	> 600	> 600	> 200

[a] The data shown are from one of two experiments, both of which gave similar results.

[b] IC50 values, nM.

High-resolution crystal structures of WDWD or ΔLoop in complex with $MPER_{(671-683)}$ were determined at 1.81 and 1.70 Å, respectively (Table 4). The two complexes crystallized in the same space group as that reported for the WT Fab obtained either from papain-treated IgG or by heterologous expression in *E. coli (Apellaniz et al., 2015; Cardoso et al., 2007)*. The superposition of the three crystal structures showed that they are nearly indistinguishable from each other (FIG 25). The root-mean square deviation (rmsd) values between the coordinates of WT and WDWD, and between WT and ΔLoop were 0.20 and 0.29 Å, respectively. A significant difference was found in the conformation of the CDR-H3 apex of WT compared with that of ΔLoop because the latter construct is two residues shorter in this region. This conformational change brings the apex of the CDR-H3 of ΔLoop Fab closer to the peptide, generating an H-bond between residue Trp680 of the peptide and the backbone oxygen of the residue Gly_{H100A} of ΔLoop (distance = 2.7 Å) (FIG 26 and Table S1). A similar H-bond was observed in one copy of the crystal structure of WT Fab in complex with a peptide containing α-aminoisobutyric acid at position Trp678 (Cardoso et al., 2007).

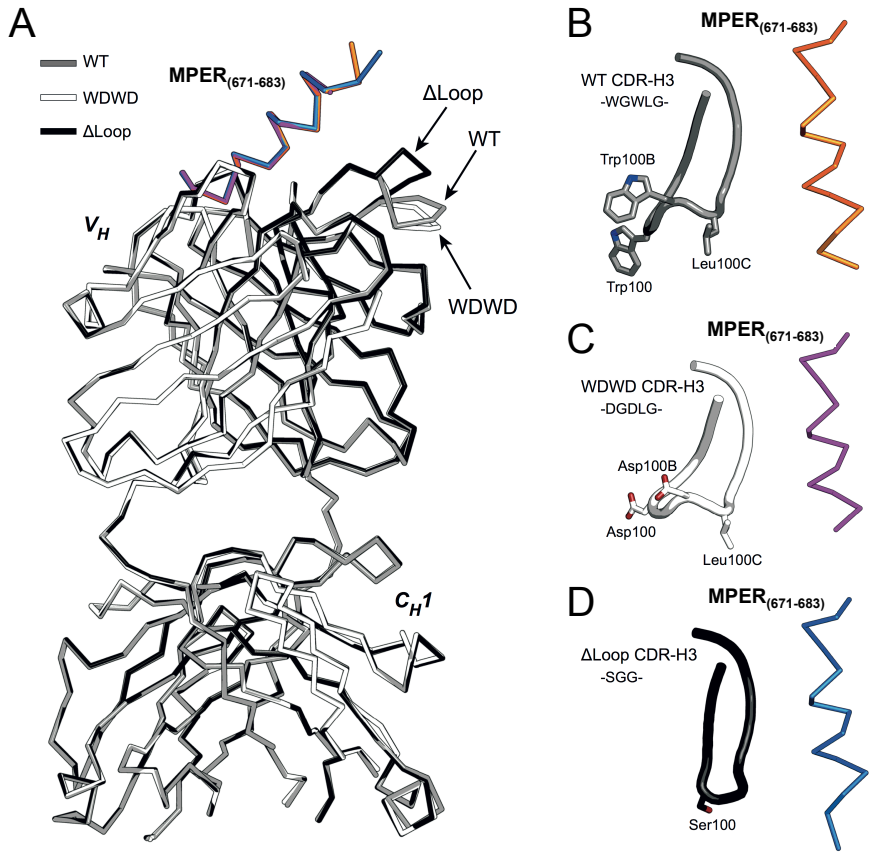

FIG 25. Crystal structures of neutralizing and non-neutralizing 4E10 Fab-s. (A) Superposition of the backbone atoms of WT (gray), WDWD (white), and ΔLoop (black). The rmsd of the backbone coordinates of the HC of WT with those of WDWD was 0.20 Å, and with those of ΔLoop 0.29 Å. The arrows point at differences in the conformation of the apex region of the CDR-H3 loop. The $MPER_{(671-683)}$ peptide bound to WT, WDWD, and ΔLoop Fab is shown in orange, magenta, and blue, respectively. (B-D) Close-up view of the conformation of the CDR-H3 loop (residues 95-100J) of (B) WT, (C) WDWD, and (D) ΔLoop with respect to the peptide. Residues with side chains within the region 100-100D are depicted.

Other polar and nonpolar interactions between the peptide and WT Fab were very well conserved in the WDWD and ΔLoop Fab-s (FIG 26). Key H-bonds between peptide residues Asn671, Trp672, Asp674 and Thr676 and the Fab-s (Table S1), as well as the non-polar interaction surface involving the residues Asn671, Trp672, Phe673, Ile675, Thr676, Leu679 and Trp680 of the peptide, are well preserved in the three crystal structures (Table S2 and S3). Moreover, the values of buried surface area (BSA) calculated with PISA (Krissinel and Henrick, 2007) corresponding to the interaction surface between the peptide and the heavy or the light chain of the Fab remain essentially

unchanged in the three crystal structures (Table S2 and S3). The total BSA for WT, WDWD, and ΔLoop were within 2 % of each other; 1,487; 1,482; and 1,511 Å^2, respectively.

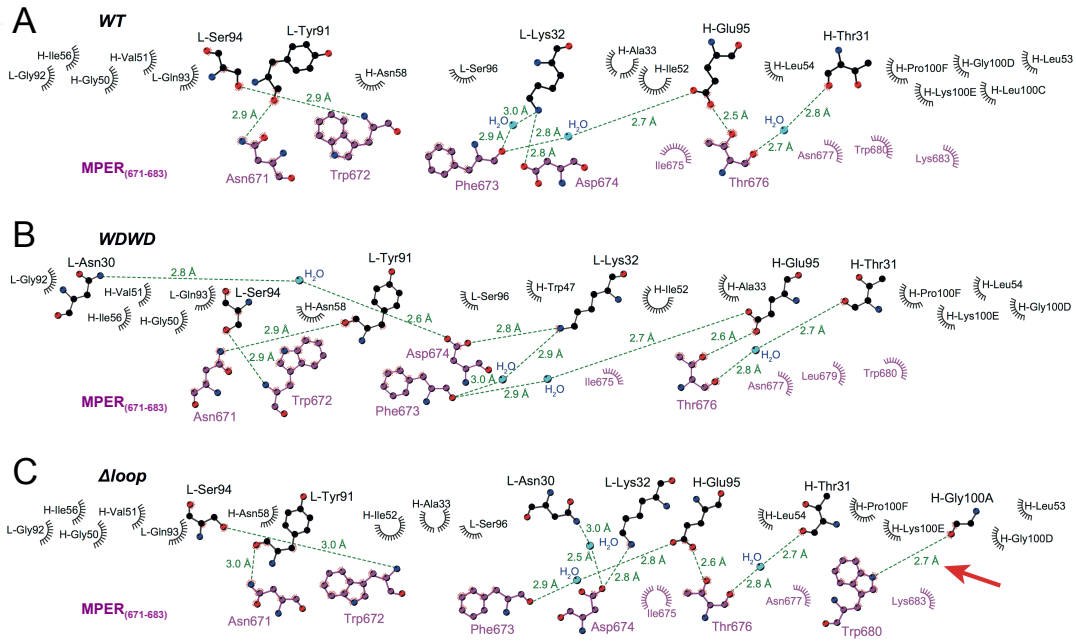

FIG 26. Interaction network of MPER$_{(671-683)}$ peptide with neutralizing and non-neutralizing 4E10 Fab-s. Diagram for WT (A), WDWD (B), and ΔLoop (C). Residues corresponding to the Fab (upper half) and the peptide (bottom half) are labeled in black and magenta, respectively. Water molecules are labeled in cyan. H-bonds and their distances are depicted with green lines. Residues engaging in direct or water-mediated H-bonds are shown in ball and stick representation. Residues displaying non-polar and van der Waals interactions are represented by spiked semi-circles. The red arrow in panel (C) points at the unique Fab-protein interaction observed in the complex with ΔLoop. The figure was generated with LIGPLOT+ (Wallace et al., 1995).

The shape complementarity coefficient (Sc), a parameter that quantifies the complementarity between protein/protein interfaces (Lawrence and Colman, 1993) was also very similar among the three Fab-s. The Sc values calculated for the interface formed between the HC and MPER$_{(671-683)}$ in the three crystal structures were in the narrow range of 0.77-0.78, whereas those between the LC and the peptide were in the range 0.80-0.82. The potential lipid-binding site located in the CDR-H1 loop also remained unchanged in the three crystal structures. We note that a water molecule takes the position occupied by the

phosphate ion reported in the PDB structure with entry code 4NHC and (Bird et al., 2014) (data not shown).

Table 4. Data collection and refinement statistics. Statistical values given in parenthesis refer to the highest resolution bin.

Data Collection	**ΔLoop + MPER$_{(671-683)}$**	**WDWD + MPER$_{(671-683)}$**	**WT unbound**
Space Group	C 2	C 2	P 2_1
Unit cell			
a, b, c (Å)	157.5, 44.7, 85.3	157.3, 44.9, 86.2	44.7, 134.2, 81.9
α, β, γ (°)	90.0, 113.6, 90.0	90.0, 114.6, 90.0	90.0, 90.0, 90.0
Resolution (Å)	36.1 – 1.70	44.5 – 1.81	44.7 – 2.48
Wavelength	1.000	1.000	1.000
Observations	313,934 (31,932)	265,738 (37,906)	79,271 (11,742)
Unique reflections	59,239 (7,703)	50,189 (7,203)	32,268 (4,692)
$R_{merge.}$ (%)[a]	8.8 (39.1)	9.9 (66.7)	7.2 (21.5)
$R_{p.i.m.}$ (%)	4.2 (21.0)	4.6 (31.1)	5.6 (16.4)
$CC_{1/2}$	1.00 (0.87)	1.00 (0.78)	0.99 (0.93)
$I / \sigma (I)$	12.5 (3.3)	11.9 (2.8)	9.7 (4.2)
Multiplicity	5.3 (4.1)	5.3 (5.3)	2.5 (2.5)
Completeness (%)	98.3 (88.5)	99.7 (99.1)	98.4 (98.7)
B-factor (Wilson Plot) (Å^2)	11.8	16.4	17.1
Refinement Statistics			
Resolution (Å)	36.1 – 1.70	44.5 – 1.81	44.7 – 2.48
Reflections R_{work}/R_{free}	56,860 / 2,379	48,180 / 2,007	30,609 / 1,632
R_{work} / R_{free} (%)[b]	14.7 / 17.8	16.3 / 18.8	18.3 / 23.1
No. atoms (protein)	3,336	3,346	6,541
No. atoms (peptide)	159	129	-
No. atoms (solvent)	590	412	135
No. atoms (other)	25	18	-
B-factor (protein) (Å^2)	24.7	27.7	25.1
B-factor (peptide) (Å^2)	31.9	44.8	-
B-factor (solvent) (Å^2)	35.4	33.0	20.8
B-factor (other) (Å^2)	34.9	36.7	-
Ramachandran Plot			
Preferred (%)	89.9	91.2	88.7
Allowed (%)	9.8	8.5	11.0
Outliers (%)	0.3	0.3	0.3
RMSD Bond (Å)	0.013	0.015	0.008
RMSD Angle (°)	1.53	1.63	1.27
Coordinate error (Å)	0.08	0.10	0.13
PDB entry code	5CIN	5CIL	5CIP

[a] $R_{merge} = \Sigma_{hkl} \Sigma_i |(I(hkl)_i - [I(hkl)]| / \Sigma_{hkl} \Sigma_i I(hkl)$.

[b] $R_{work} = \Sigma_{hkl} |F(hkl)_o - [F(hkl)_c]| / \Sigma_{hkl} F(hkl)_o$; R_{free} was calculated as R_{work}, where $F(hkl)_o$ values were taken from ~4-5 % of data not included in the refinement.

4.3.2. Mechanism of binding and stability of neutralizing and non-neutralizing 4E10 Fab-s

The structural data gathered so far has not satisfactorily explained the poor neutralization performance of the two CDR-H3 mutants, given the minimal structural differences among the Fab-s. To further characterize the molecular basis for these large differences in neutralization potency, we performed a comparative functional and thermodynamic analysis employing WT, ΔLoop and WDWD Fab-s.

DSC measurements demonstrated that the CDR-H3 mutations did not affect the stability of the ligand-free forms of the Fab-s (FIG 27). The melting temperatures (T_M) determined from the mid-point unfolding transition of WT Fab, WDWD, and ΔLoop were 70, 72, and 72 ºC, respectively. Therefore, decreasing the hydrophobicity of CDR-H3 at the apex translates into a modest increase in the thermostability of the Fab-s (ΔT_M = 2 °C).

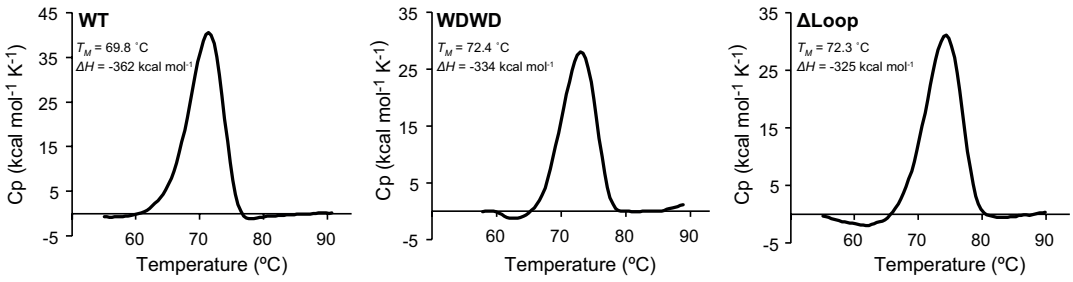

FIG 27. Thermal stability by DSC. DSC thermograms for WT, WDWD and ΔLoop are shown as indicated in the panels. Unfolding of the three Fab-s shows a single thermal transition between 30 and 90 °C. The midpoint of the thermal unfolding (T_M) and the associated enthalpy (ΔH) are also given.

Kinetic and thermodynamic parameters governing $MPER_{(671-683)}$ peptide binding were next examined by SPR as previously described (Kiyoshi et al., 2014; Kiyoshi et al., 2015). FIG 28 shows the sensorgrams corresponding to the binding of the $MPER_{(671-683)}$ peptide to immobilized WT, WDWD and ΔLoop Fab-s, illustrating the effect of mutations in the apex of the CDR-H3 loop on the

association (k_{on}) and dissociation (k_{off}) rate constants. The values of k_{on} and k_{off} for WT Fab at room temperature were 5.2×10^4 M^{-1} s^{-1} and 1.1×10^{-3} s^{-1}, respectively, corresponding to a dissociation constant (K_D) of 21 nM (FIG 28A and Table 5). The small values of k_{off} indicate slow dissociation of the peptide from the Fab, consistent with tight binding of the epitope-peptide to the antibody under these experimental conditions. The values of k_{on}, k_{off}, and K_D were also determined for the WDWD and ΔLoop Fab-s (FIG 28A and Table 5). Ablation of the hydrophobic CDR-H3 tip did not appreciably affect peptide affinity (K_D = 18 nM). However, compared with the WT Fab, the slower k_{on} in ΔLoop was compensated by a slower k_{off}, suggesting that the intact loop establishes faster interactions with the peptide, but at the same time its release from the paratope is also accelerated. The slower dissociation rate observed for the ΔLoop Fab could be explained by the stronger H-bond between the Gly_{H100A}(O) of the Fab and Trp680(Nξ) of the peptide (FIG 26 and Table S1). The double mutation introduced in WDWD Fab decreased the affinity slightly (K_D = 41 nM) because of a faster k_{off} with respect to the WT Fab, which was not compensated with a faster k_{on} (Table 5). Although these differences are arguably small, the data suggest that the more hydrophobic loop of WT Fab facilitated binding of $MPER_{(656-683)}$ more effectively than the polar WDWD.

The van't Hoff thermodynamic parameters for the WT Fab and the mutated CDR-H3 Fab-s were obtained from the temperature dependence of K_D (FIG 28B and Table 5). The change of enthalpy associated with the binding of WT Fab was negative ($\Delta H° < 0$, exothermic reaction), whereas the contribution from the entropy energetic term ($-T\Delta S°$, calculated at 25 ºC) was small and positive. These values suggested that binding was essentially driven by favorable non-covalent interactions between Fab and peptide. The thermodynamic parameters obtained at equilibrium for the non-neutralizing WDWD and ΔLoop Fab-s exhibited the same thermodynamic signature (Table 6), although the entropic cost in the case of the WDWD mutant was slightly higher ($-T\Delta\Delta S°$ = 1.5 kcal mol^{-1}), which could account for the decrease in affinity observed for this Fab.

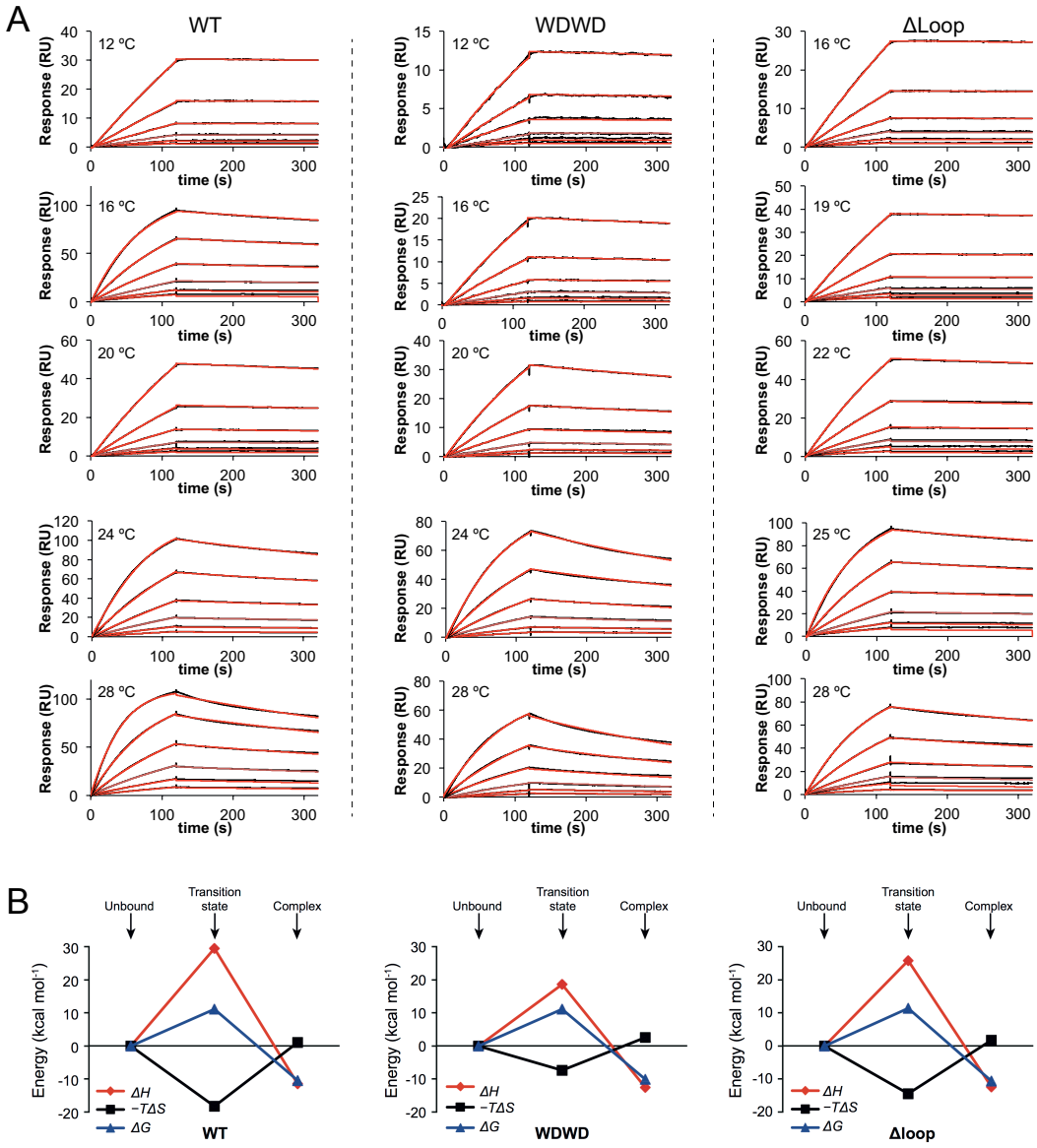

FIG 28. Kinetic and thermodynamic characterization of Fab-peptide binding by SPR. (A) Sensorgrams corresponding to the binding of $MPER_{(671-683)}$ to a surface decorated with WT (left), WDWD (center), or ΔLoop (right) Fab-s (immobilization levels were ~1400 RU) at the temperatures indicated in each panel. The concentration of peptide injected in each run is indicated. Black and red curves correspond to the experimental data and best fit (using the Biacore T200 evaluation software), respectively. (B) Evolution of the thermodynamic parameters along the reaction coordinate. Thermodynamic parameters corresponding to the transition state and at equilibrium were obtained from the temperature dependence of k_{on} and K_D using the Eyring and van't Hoff equations, respectively. The change of Gibbs energy (ΔG), change of enthalpy (ΔH), and change of entropy ($-T\Delta S$) are shown in blue, red and black, respectively. Values are given in **Table 5**. The double dagger symbol (‡) indicates the transition state.

Table 5. Kinetic parameters of binding of Fab 4E10 to MPER$_{(671-683)}$R

Fab	k_{on} ($M^{-1}s^{-1}$)	k_{off} (s^{-1})	K_D (nM)
WT	5.2×10^4	1.1×10^{-3}	21
ΔLoop	2.9×10^4	5.3×10^{-4}	18
WDWD	4.7×10^4	1.9×10^{-3}	41

Differences in the binding mechanism arising from fluctuating loop conformations could be more evident at the transition state, *i.e.* before reaching the final conformation of the complex. Hence, the activation free energy ($\Delta G^{\ddagger}$, the double dagger symbol refers to the transition state) of each Fab-peptide complex was determined from the temperature dependence of k_{on} (FIG 28B and Table 5). The transition state in the three Fab-s was governed by the unfavorable enthalpy term ($\Delta H^{\ddagger} > 0$), reflecting the destruction of non-covalent interactions during the rate-determining step. The unfavorable enthalpy term was partially counterbalanced by favorable entropic contributions ($-T\Delta S^{\ddagger} < 0$). Due to the differences in mass and charge in the CDR-H3 loop of the mutated Fab-s with respect to WT, we expected to see dissimilar activation barriers for binding reactions requiring conformational changes of the loop. However, the resulting $\Delta G^{\ddagger}$ values were strikingly similar for the three Fab-s (Table 5). Therefore, the shared thermodynamic signature at the transition state in the three constructs examined suggests that rearrangement of water molecules at the contact interface, rather than major alterations of CDR-H3 loop conformation, plays a key role on the activation of the binding process.

Table 6. Thermodynamic parameters of binding of Fab 4E10 to MPER$_{(671-683)}$R

Fab	ΔG (kcal mol^{-1})	ΔH (kcal mol^{-1})	$-T\Delta S$ (kcal mol^{-1})	$\Delta G^{\ddagger}$ (kcal mol^{-1})	$\Delta H^{\ddagger}$ (kcal mol^{-1})	$-T\Delta S^{\ddagger}$ (kcal mol^{-1})
WT	-10.5	-11.5	1.0	11.1	29.4	-18.3
ΔLoop	-10.6	-12.4	1.7	11.4	25.8	-14.5
WDWD	-10.1	-12.6	2.5	11.2	18.6	-7.4

4.3.3. Crystal structure of 4E10 Fab in the unbound state

The thermodynamic data described above argue against major conformational changes occurring in the 4E10 paratope during $MPER_{(671-683)}$ peptide binding. This conclusion differs from that reported with the ligand-free Fv fragment (Finton et al., 2013). In that study it was shown that a large segment of the CDR-H3 loop (including the apex region) adopts a significantly different conformation in the unbound state, resulting in occlusion of the paratope. To solve this paradox, and to allow direct structural comparison between the Fab-peptide complex, and those previously reported in the literature (Bird et al., 2014; Cardoso et al., 2007; Cardoso et al., 2005), we determined the crystal structure of unbound 4E10 Fab (FIG 29).

Single crystals of unbound WT 4E10 Fab were obtained in a solution containing 15 % PEG 20,000 and 100 mM MES at pH 6.5. The best diffracting crystal achieved a resolution of 2.48 Å in spacegroup $P2_1$, which was different from the spacegroup (C2) where the crystal of the Fab in complex with peptide was obtained (Table 4). Consequently, the packing forces experienced by protein chains of the unbound and the bound Fab-s were different. Despite this difference, the structures of unbound and bound Fab were essentially identical (rmsd = 0.32 Å) (FIG 29).

The electron density corresponding to residues of the apex of CDR-H3 (W_{H100}–G_{H100D}) was weak, indicative of dynamic disorder (FIG 29 and 30A). Importantly, the conformation of the CDR-H3 loop, in its entire length, is nearly identical to that of the bound form of WT but clearly different to that of the unbound form of the F_V fragment (FIG 30B). We also note that the putative lipid-binding site located in CDR-H1 also remains virtually unchanged with respect to the Fab with peptide bound (data not shown).

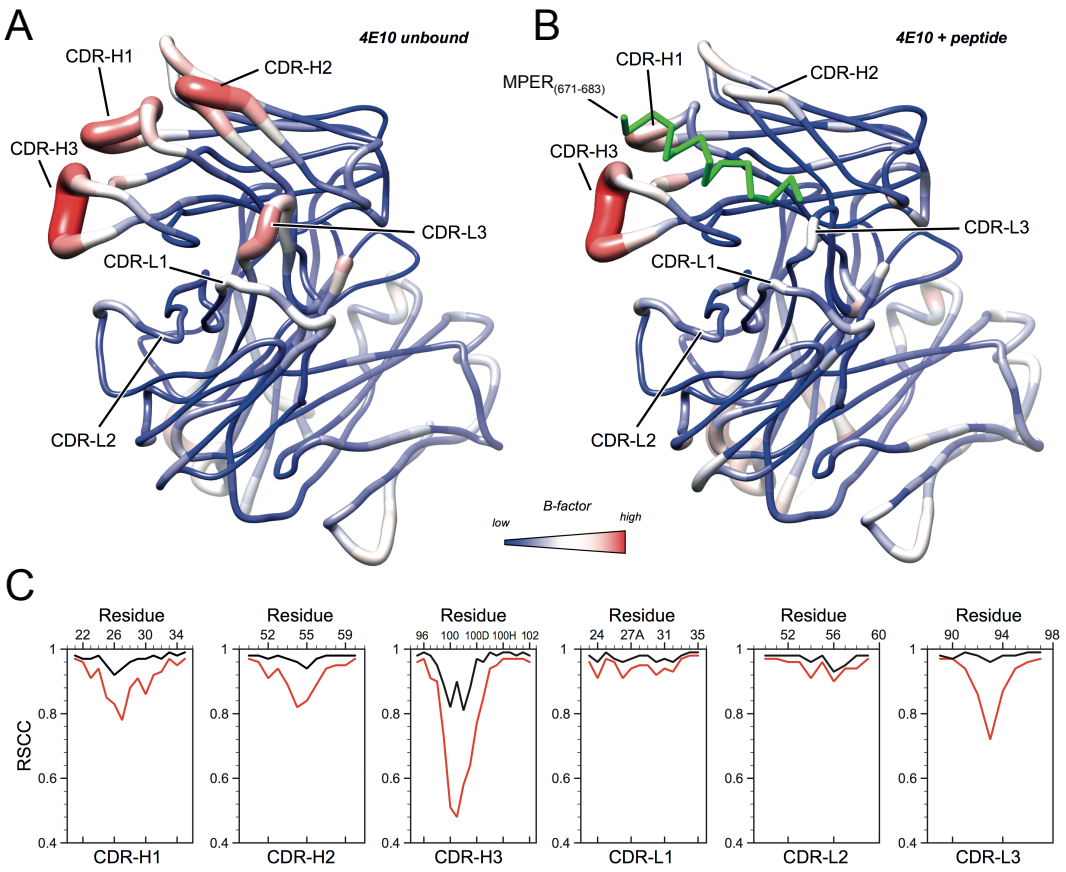

FIG 29. Comparison of the ligand-bound and ligand-free forms of 4E10 Fab. Sausage (tubular) representation of B-factors of ligand-free (A) and ligand-bound (B) 4E10 Fab. Higher B-factors are depicted by red and thick tubes. For the unbound form of 4E10, the blue-white-red gradient corresponds to B-factor values of 12.6, 36.6 and 100.9 Å^2, respectively. For the peptide-bound form, the blue-white-red gradient corresponds to B-factor values of 21.8, 40.0 and 90.2 Å^2, respectively. These values correspond to the minimum, a midpoint, and the maximum B-factor values of each crystal structure. Both molecules are oriented to display the paratope CDR loops at the front plane. In panel (B) the bound peptide is represented with a green ribbon. (C) Per-residue real-space correlation coefficient (RSCC, a measure of the fit between the model and the experimental electron density) of the six hypervariable loops of 4E10 Fab in the unbound (red) and bound (black) state. Lower correlation values indicate less agreement between the model and the experimental electron density, suggesting the regions with lower RSCC are more dynamically disordered. The RSCC values were calculated using PHENIX (Adams et al., 2010).

Crystallographic models contain dynamic information in the form of B-factors and dynamic contact networks (van den Bedem et al., 2013), and thus the comparison of models of the same protein in the bound and unbound state may reveal regions of altered dynamics. The antibody employs the CDRs H1 (^{25}SGGSFSTYAL^{34}), H2 (^{50}GVIPLLTITNYA^{60}), H3

(^{95}EGTTGWGWLGKPIGAFAH^{102}), and L3 (^{89}QQYGQSLST^{97}) to engage MPER$_{(671-683)}$ (Cardoso et al., 2007). The CDR-L2 (^{50}GASSRPS^{56}) does not engage with the peptide, whereas CDR-L1 (^{24}RASQSVGNNKLAW^{35}) only makes minor contacts (Cardoso et al., 2007). Comparison of bound and unbound 4E10 Fab models revealed a reduction in the backbone dynamics (B-factors) of several CDR loops in the bound state according to their involvement in peptide binding (FIG 29A,B and 31).

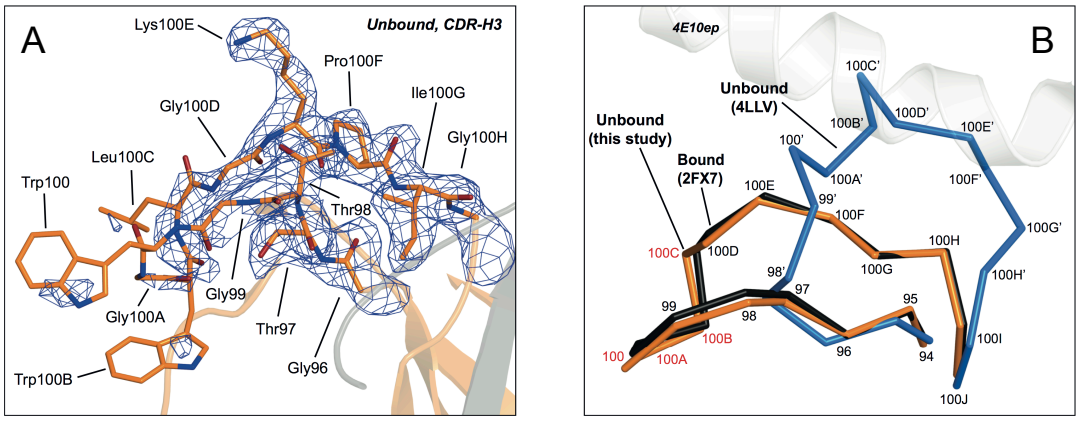

FIG 30. Conformation of CDR-H3 in the unbound form. (A) Sigma-A weighted electron density map of the CDR-H3 of unbound WT Fab (σ = 1.0). Electron density for the residues of the apex (^{100}WGWLG^{100D}) is only visible at low contouring levels (σ ~ 0.5, not shown) but sufficient to allow modeling of the residues. (B) Comparison of conformations of the CDR-H3 in the unbound form of Fab (orange), in the reported Fab-peptide complex (PDB entry code 2FX7, black), and in the reported structure of the unliganded Fv fragment (PDB entry code 4LLV, blue). Sequence numbers are given.

To strengthen the conclusions about the dynamic behavior of the CDR loops of Fab upon binding, we calculated the real-space correlation coefficient (RSCC, (Jones et al., 1991)) with PHENIX (Adams et al., 2010) (FIG 29C). The RSCC values for residues of the CDRs H1, H2, H3 and L3 are greater in the bound form than in the unbound form. This observation is explained by a better fitting of the electron density to the model, which can be qualitatively interpreted as a reduction in dynamic disorder. These differences cannot be attributed to the resolution of the crystal structures, since the average value of RSCC for the entire structure of bound (RSCC = 0.97) and unbound Fab (RSCC = 0.95) was comparable to each other. Although RSCC values for all residues of the CDR-

H3 increased upon binding of the peptide, it is also certain that residues of the apex (^{99}GWGWL^{100C}) displayed a noticeable residual disorder as judged from the values of RSCC (< 0.90). In contrast to the CDR loops described above, CDRs L1 and L2 exhibited very little reduction of mobility, consistent with their minor role in binding. Similar results are observed in the average plots of six other crystal structures of 4E10 with various peptides bound (FIG 32).

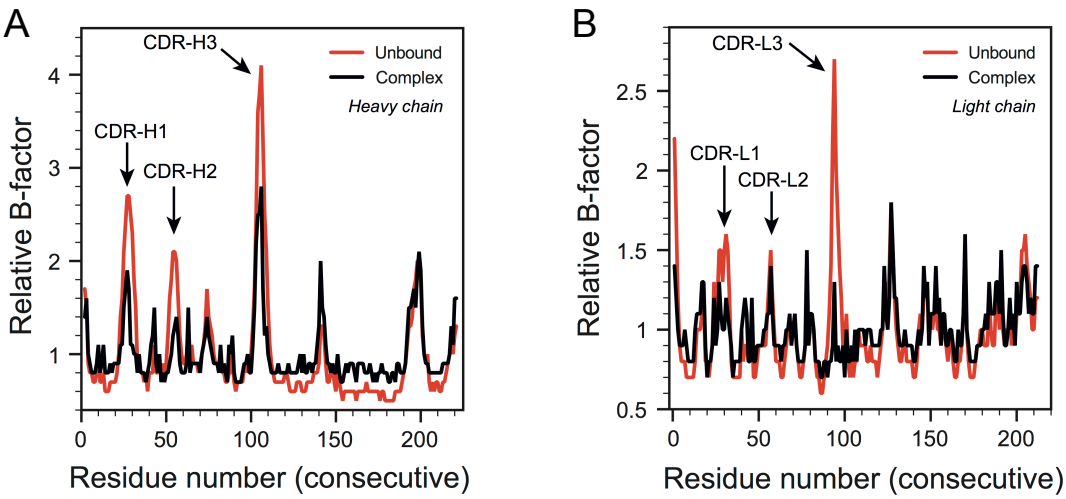

FIG 31. Crystallographic B-factors of Fab in the bound and unbound state. (A) HC. (B) LC. Relative B-factors are plotted to facilitate the comparison between crystal structures at different resolutions and quality. The relative B-factors were obtained by normalization with respect to the average B-factor of each structure.

These results have proved that the binding process resulted in minor conformational adjustments mostly involving a change of mobility of the CDR loops after the antibody comes into contact with the epitope. Importantly, our results indicate that the hydrophobic cavity accommodating the peptide remains intact even in the absence of peptide.

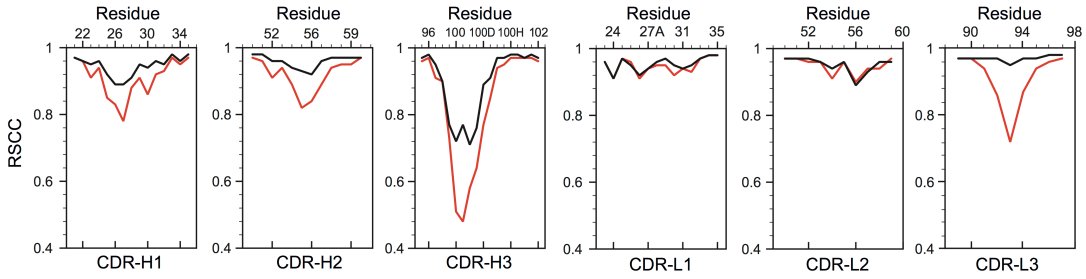

FIG 32. Analysis of residues of the apex region of CDR-H3. Comparison of RSCC between unbound Fab (red lines, also shown in FIG 29C) and the arithmetic average RSCC of six crystal structures of 4E10 Fab with various types of peptide bound (black lines). The PDB entry codes of the crystal structures employed to prepare these plots were 1TZG (short peptide epitope), 2FX7 ($MPER_{(671-683)}$), 2FX8 (peptide constrained with a α-amino isobutyric acid), 2FX9 (peptide with a thioether intramolecular bond), 4NHC (stapled peptide), and 4NGH (stapled peptide with a phosphate tether).

4.3.4. PsV neutralization and binding to the MPER in the context of the plasma membrane

The above results describing the structure and energetics of peptide binding to the 4E10 Fab-s indicated that mutation of the CDR-H3 apex do not alter the ability of the antibody to interact with the peptide. Yet, a PsV-based neutralization assay (Table 3) showed that the Fab mutants had lost all neutralization activity compared to that of WT IgG and WT Fab. The results displayed on FIG 33 confirmed the inability of the non-neutralizing Fab to bind to PsV particles under the experimental conditions that otherwise sustain dose-dependent binding of the WT-4E10 Fab and the anti-gp120 PG9 antibody, the latter being employed as a positive control of Env expression. Thus the dramatic differences in biological activity were mirrored by differences in binding of the Fab-s to the immobilized PdVs, further supporting that preservation of a solvent-exposed, flexible and hydrophobic CDR-H3 loop apex is required for binding and neutralization in the biological context.

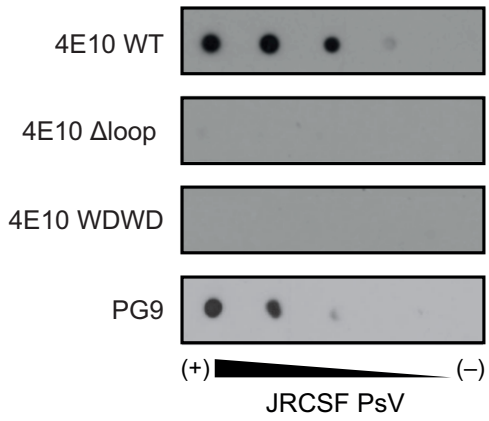

FIG 33. JRCSF PsV recognition by dot-blot. Decreasing amounts of PsVs (from left to right) were spotted onto Hybond C nitrocellulose.

The results in FIG 34 strengthen the conclusion that availability of the WT CDR-H3 apex contributes to additional interactions with membrane components as previously suggested (Cardoso et al., 2005; Huarte et al., 2008; Lorizate et al., 2006; Montero et al., 2012; Sanchez-Martinez et al., 2006b; Scherer et al., 2010; Sun et al., 2008). The DNA vaccine candidates, MPER-TM1 and MPER-PDGFR (Montero et al., 2012), express fusion proteins comprising: (i) an N-terminal HA tag, (ii) the MPER, (iii) either the TMD of gp41 followed by 27-AA of the cytoplasmic domain (TM1), or that of the platelet-derived growth-factor receptor (PDGFR). These fusions are expressed in the context of the plasma membrane, however the PDGFR TMD has been shown to reduce exposure of the 4E10 epitope (Montero et al., 2012), and to a lesser extent, the 10E8 epitope (unpublished data, N.G.). The titrations shown in FIG 34A indicate that IgG and Fab WT engaged effectively with the 4E10 epitope presented in the context of the plasma membrane (EC50 of ca. 0.1 and 1 nM, respectively). By comparison, in the range of measured concentrations, binding to MPER-TM1 was negligible for the WDWD and ΔLoop mutants (FIG 34A, bottom panels). None of the antibodies bound directly to the plasma membrane of cells devoid of an MPER construct (squares and dotted lines), demonstrating that the binding scored for the WT IgG and Fab under our experimental conditions was strictly dependent on the presence of the MPER epitope.

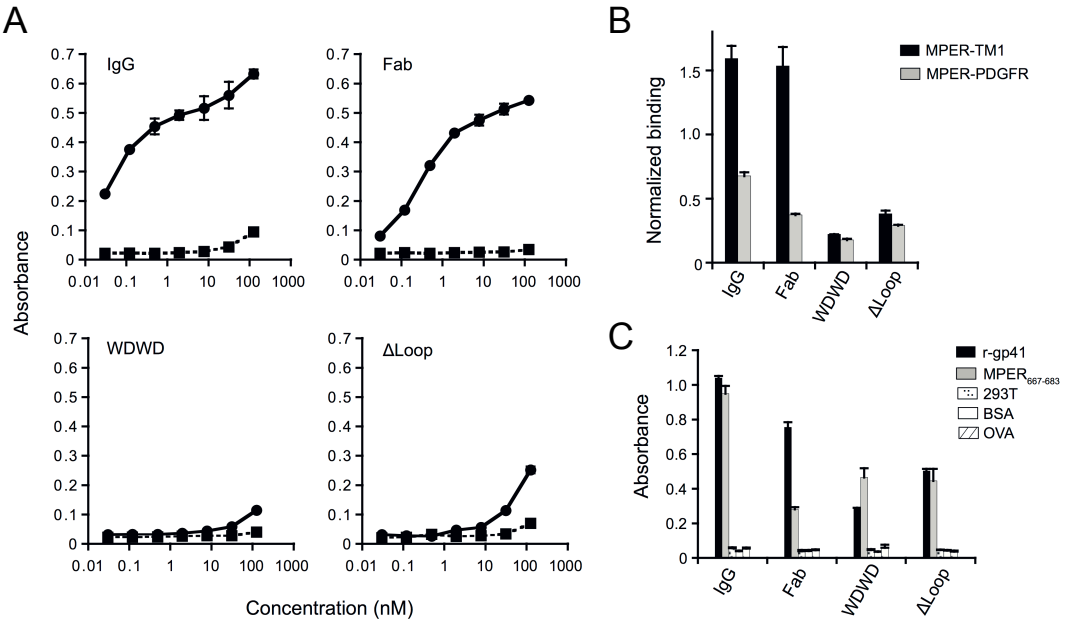

FIG 34. Alterations in the CDR-H3 of 4E10 Fab impacts the binding of Fab-s to its cognate epitope in the context of the plasma membrane. (A) Cell vesicles displaying the MPER-TM1 protein product (solid line), and 'empty' control vesicles (dashed lines) were probed with 4E10 IgG and Fab-s (WT, WDWD, ΔLoop) at the indicated concentrations. (B) Cell vesicles bearing recombinant MPER proteins (MPER-TM1: black bars; MPER-PDGFR: grey bars) were probed with 20 nM 4E10 IgG and Fab-s, and 20 nM 17/9 IgG (binds to an HA tag located at N-terminus of the MPER constructs and is used to assess cell-surface expression). Absorbance values were normalized to the cell-surface expression of the constructs (*i.e.*, Absorbance $4E10_{IgG\ or\ Fab\text{-}s}$/Absorbance $17/9_{IgG}$). (C) Binding of 20 nM 4E10 IgG and Fab-s to recombinant gp41, the $MPER_{667\text{-}683}$-peptide, and assay controls ('empty' 293T cell lysates, BSA and ovalbumin). For all experiments, absorbance at 405 - 490 nm was recorded. Error bars represent standard error of the mean. The data shown are from one of two (FIG34C and D) or three (FIG34A) experiments, all of which gave similar results.

A previous work (Montero et al., 2012) showed that, in comparison to the MPER-TM1 construct, binding of 4E10 IgG to the MPER-PDGFR construct was significantly reduced; this was also observed to a lesser extent for the bNAb, 10E8, whose epitope overlaps with that of 4E10 (unpublished data; N.G. & J.K.S.), but not for bNAb 2F5 (Ofek et al., 2010), whose epitope is on the N-terminal helix of the MPER (Montero et al., 2012) These results reflect the ability of the TMD to affect the positioning of bN epitopes in the C-terminal helix of the MPER, but not in its N-terminal helix. The binding of the WT and mutant Fab-s, particularly the ΔLoop Fab, to the MPER-TM1 and MPER-PDGFR constructs was assessed in relation to 4E10 IgG. FIG 34B shows that, as

expected, binding to the MPER-PDGFR construct by the 4E10 IgG and WT Fab was significantly reduced, whereas the mutant WDWD and ΔLoop Fab-s bound negligibly to both constructs. The influence of membrane was finally inferred from control ELISAs performed using recombinant gp41 ectodomain or $MPER_{667-683}$ peptide adsorbed to plates (FIG 34C). Experiments in the absence of membranes showed for the three Fab-s comparable levels of binding to these antigens, which do not correlate with their neutralizing capacities (Table 3).

4.4. DISCUSSION

The HIV-1 bNAbs isolated to date provide templates for rational vaccine design, facilitate the understanding of immune pathways and molecular processes that confer broad protection, and constitute the basis for immunotherapies with the potential to effectively prevent and treat HIV-1 infection (Burton and Mascola, 2015; Klein et al., 2013b; Kwong and Mascola, 2012). The 4E10 bNAb targets the conserved MPER C-terminal helix and displays near pan-neutralizing activity in standard panels of HIV strains and isolates (Binley et al., 2004; Huang et al., 2012; Kunert et al., 1998; Muster et al., 1994; Muster et al., 1993; Purtscher et al., 1994; Stiegler et al., 2001). Thus, 4E10 constitutes a bNAb model particularly useful to study the molecular basis underlying HIV neutralization breath mediated through MPER recognition.

The neutralizing activity of 4E10 is strictly dependent on aromatic residues of the CDR-H3 loop (Alam et al., 2009; Scherer et al., 2010). Here, we have studied the mechanistic basis of this requirement by characterizing structurally and functionally WDWD and ΔLoop, two Fab variants mutated at the critical apex region of the CDR-H3 loop. Thus, we have performed crystallographic, kinetic and thermodynamic studies on neutralization-active and neutralization-inactive Fab-s, and compared their 4E10-epitope binding mechanisms at the molecular level. The recombinant Fab-s were obtained by

heterologous expression in the cytoplasm of *E. coli*, avoiding aberrant forms that may occur upon refolding of inclusion bodies.

The crystal structures of 4E10 Fab WT, WDWD and ΔLoop determined in complex with the epitope-peptide revealed combining sites and bound helical peptides essentially indistinguishable from each other (FIG 25). From these results, we have concluded that mutations in the CDR-H3 apex abolishing neutralization neither affect the collective set of interactions between Fab and the peptide (FIG 26 and Table S1-S3), nor change the configuration of the proposed lipid-binding subsite in significant ways (not shown). The only visible differences were restricted to the CDR-H3 loop apex, which remains exposed to solvent, *i.e.*, does not contact the bound peptide (FIG 25). The mutated loop region in WDWD displays essentially the same conformation as that in WT Fab and very similar interactions (BSA and H-bond pattern) despite the large differences in the loop hydrophobicity (FIG 26 and Table S1-S3). In contrast, the backbone of the shorter loop of ΔLoop approaches the helical peptide as a result of the deletion of two residues of the CDR-H3 apex (FIG 25), thereby strengthening an H-bond between the Fab and Trp680 of the peptide (FIG 26 and Table S1). Thus, the structural data demonstrate that an antibody bearing a short and non-hydrophobic CDR-H3 loop is capable of engaging with the helical MPER epitope as much or even more effectively than the WT Fab. These observations may have important implications for the design of anti-MPER vaccines.

It has been proposed that the long CDR-H3 loop enhances paratope flexibility to effectively capture the membrane-inserted MPER (Montero et al., 2012) by means of an induced-fit mechanism. Consistent with this idea, crystallographic studies on the unliganded 4E10 variable domain Fv revealed large conformational changes of CDR-H1 and, more prominently, of CDR-H3 (FIG 30B). The position of CDR-H3 in the unliganted Fv shields the epitope-binding pocket, creating an electropositive and unspecific lipid-binding subsite (Finton et al., 2014; Finton et al., 2013; Xu et al., 2010), but different from that

later proposed by Bird *et al.* (Bird et al., 2014; Irimia et al., 2016). Based on the structural data obtained with the Fv fragment, it was proposed that a large portion of the CDR-H3 undergoes a large conformational change from the unbound to the bound state. If this was the case, mutations blocking the neutralizing activity could also impact the conformational equilibrium of the CDR-H3 in the unbound form, and thus alter the overall epitope-binding function of the paratope.

In contrast to that prediction, the binding affinities of $MPER_{(671-683)}$ peptide at equilibrium for the three Fab-s were strikingly similar (FIG 28A and Table 5). Similarly, the free energy changes at the rate-determining step (transition state) of the three versions of the Fab were nearly identical to each other (FIG 28B and Table 5). Given the differences in size and polarity of CDR-H3 in WT and mutated Fab-s, this result does not support a major restructuring of the loop during the activation stage of peptide binding.

To tackle the disagreement between the reported unliganded structure of the Fv fragment (Finton et al., 2013), and our thermodynamic data obtained with a Fab construct, we determined the crystal structure of WT Fab in the absence of peptide. Consistent with the thermodynamic analysis, the crystal structure of the ligand-free 4E10 Fab displayed a paratope structurally similar to that found in the solved Fab-peptide complexes (FIG 29 and 30). Notwithstanding the overall similarity, higher degree of dynamic disorder was detected at the CDR loops implicated in peptide binding in the ligand-free Fab (FIG 29 and 31). Specifically, peptide engagement reduced the mobility of CDRs H1, H2, H3, and L3 to a noticeable extent. The flexibility of the CDR-H3 loop, critical for neutralization, decreased markedly although we note that significant residual disorder remained in its apex region even in the presence of bound peptide. In contrast, the flexibility of CDRs L1 and L2 did not change significantly between bound and unbound forms of the Fab. These findings support the crystal structure of the peptide-free Fab described in our work and

observed by Wilson *et al* (Irimia et al., 2016) as a relevant reference to describe the conformation of 4E10 Fab in the unliganded state.

Thus, the kinetic, thermodynamic and structural data gathered herein indicated limited conformational changes of the Fab upon epitope binding (essentially the immobilization of certain CDR loops), suggesting a flexible lock-and-key binding mechanism. The underlying reason explaining the conformational differences between the CDR-H3 (and CDR-H1) in the unbound forms of the short Fv and the longer Fab constructs (movement of backbone atoms of up to 14 Å in W_{H100} ((Finton et al., 2014; Finton et al., 2013), FIG 30B) was not clarified at this time. We suggest that the difference could be explained by the low pH required to crystallize the Fv construct (pH 4.6) and/or to different structural stabilities of these two specimens. In the unbound structure of Fv, the residues of the CDR-H3 move towards the empty pocket of the peptide-binding site, establishing numerous hydrophobic contacts with other CDR-H3 loops of other molecules of the asymmetric unit, and thus achieving maximum stability and minimizing their exposure to the low pH environment of the aqueous solution (Finton et al., 2013). In contrast, although the crystal structures of unbound and bound forms of Fab were obtained each in a different space group (thus experiencing different structural constraints and packing forces), the CDR-H3 loop remains in a similar conformation. In addition, the thermal stability (as judged from the T_M values) for the smaller 4E10 Fv fragments (T_M = 52 ºC, (Finton et al., 2014)) is significantly lower than those of the Fab fragments (T_M = ~70 ºC, FIG 27). Therefore the combination of lower stability, extreme crystallization conditions, and crystal packing forces may all have induced a non-native conformation of the CDR-H3 loop in the crystal structure of the Fv fragment.

It has been speculated that length, hydrophobicity and conformational flexibility of the 4E10 CDR-H3 loop apex may govern the interactions with the viral membrane (Cardoso et al., 2007; Cardoso et al., 2005). The structural and thermodynamic results obtained with WDWD formally demonstrate that length

and flexibility are not sufficient to elicit viral neutralization. Thus, maintaining an accessible hydrophobic patch at the apex of the flexible CDR-H3 emerges as a stringent requirement for the neutralizing activity of 4E10. Assuming that a common mechanism (*i.e.* conformational stabilization) applies to all CDR loops involved in binding, the high mobility of CDR-H3 indicates the existence of yet additional interactions with antigen that are not satisfied by contacts with $MPER_{(671-683)}$ peptide in solution.

The Fab binding activity in dot-blot and cell-lysate ELISA supports the idea that additional CDR-H3 interactions can be fulfilled in the context of the membrane (FIG 33 and 34). In the cell lysate ELISA, the MPER-TM1 construct was employed to constrain the MPER and position it on the membrane surface. In contrast to what was observed for $MPER_{(671-683)}$ binding in solution, the capacity of the Fab-s to bind MPER-TM1 was correlated with their neutralization activity. Because the range of concentrations allowing for effective Fab-MPER-TM1 binding was sufficiently low, direct association with membranes was negligible, as reflected by the lack of binding to “empty” cell lysates (FIG 34). Importantly, binding by WT 4E10 IgG and Fab to the MPER-PDGFR construct was weak relative to MPER-TM1 (FIG 34). As the PDGFR TM region has been shown to improperly constrain the MPER (Montero et al., 2012), this result supports the necessity of proper tethering by the TMD to optimally expose the MPER in the context of the plasma (or viral) membrane. Thus, overall, results from this and previous cell-lysate ELISAs (Montero et al., 2012) strongly suggest that the hydrophobic CDR-H3 loop enables direct binding to an MPER epitope that achieves its neutralization-competent antigenic structure through membrane insertion and tethering via an appropriate TMD (Huarte et al., 2008; Lorizate et al., 2006; Montero et al., 2012; Montero et al., 2008; Sun et al., 2008).

Together with the realization that antibodies bearing shorter and less hydrophobic CDR-H3 loops may display equal or even higher affinity towards peptides like $MPER_{(671-683)}$, these findings should have important implications

for anti-MPER vaccine development. Moreover, our results also suggest that a vaccine devoid of lipid might elicit high-affinity antibodies against the MPER C-terminal helix. However, since antibodies with short-polar CDR-H3 loops are arguably easier to produce, the generated responses are likely to comprise non-neutralizing antibodies for the most part. On the other hand, accessibility to the MPER epitope inserted in membranes appears to correlate with the neutralization competence for 4E10-related antibodies. Taken together, the data presented here further support the vaccine-design strategy of replicating the neutralization-competent structure of the MPER on the viral membrane surface to elicit HIV-1 neutralizing antibodies.

4.5. SUPPLEMENTARY DATA

Table S1. Hydrogen bonds between 4E10 and MPER$_{(671-683)}$.

		WT	ΔLoop	WDWD
Residue1	**Residue 2**	**Distance (Å)**		
H-Ile56	Pep-Trp672	3.21	3.32	3.23
H-Glu95	Pep-Thr676	2.50	2.61	2.64
H-Leu100C[a]	Pep-Trp680	3.30	2.73	3.31
L-Tyr91	Pep-Asn671	2.93	2.97	2.93
L-Ser94	Pep-Trp672	2.91	2.96	2.91
L-Ser94	Pep-Asn671	3.30	3.39	3.33
L-Lys32	Pep-Asp674	2.80	2.77	2.81

[a]In ΔLoop this residue corresponds to Gly100A.

Table S2. Interaction surface between the LC of 4E10 Fab-s and MPER$_{(671-683)}$.

	WT	WDWD	ΔLoop
Residue	**BSA (Å^2)**		
L-Asn30	9.2	11.9	11.4
L-Lys32	28.6	29.8	27.7
L-Gln89	3.8	3.7	4.0
L-Tyr91	38.2	38.6	38.9
L-Gly92	13.5	13.2	14.1
L-Gln93	12.5	14.8	14.7
L-Ser94	58.5	57.4	56.7
L-Ser96	12.5	12.4	12.8
Subtotal	177	182	180
Pep-Asn671	62.9	64.4	60.9
Pep-Trp672	22.3	22.3	23.4
Pep-Phe673	80.1	79.5	79.5
Pep-Asp674	32.9	34.1	34.1
Subtotal	198	200	201
TOTAL	375	382	381

Table S3. Interaction surface between the HC of 4E10 Fab-s and MPER$_{(671-683)}$.

	WT	WDWD	ΔLoop
Residue		**BSA (Å^2)**	
H-Ser28	0	8.0	0
H-Thr31	46.9	51.3	44.6
H-Tyr32	6.2	7.1	2.9
H-Ala33	25.5	24.2	25.7
H-Leu34	0	0.2	0.2
H-Ser35	7.5	7.8	7.6
H-Trp47	17.9	18.6	17.3
H-Gly50	6.7	7.2	7.3
H-Val51	1.8	2.2	2.0
H-Ile52	56.9	59.1	56.9
H-Leu53	35.4	9.0	34.9
H-Leu54	30.0	34.5	32.2
H-Ile56	26.4	27.9	27.2
H-Thr57	0.4	0.7	0.5
H-Asn58	53.7	53.7	52.7
H-Glu95	13.6	13.2	13.1
H-Leu100C[a]	12.5	12.2	23.6
H-Gly100D	7.4	7.4	6.7
H-Lys100E	59.4	61.0	56.9
H-Pro100F	55.4	55.8	57.8
H-Gly100H	27.7	27.8	28.0
H-Phe100J	13.1	12.8	13.7
Subtotal	504	501	512
Pep-Trp672	160.1	160.9	161.1
Pep-Phe673	78.3	79.9	79.3
Pep-Ile675	38.7	35.5	41.8
Pep-Thr676	97.5	94.7	94.9
Pep-Asn677	44.8	48.9	45.3
Pep-Trp678	9.4	0	11.9
Pep-Leu679	54.7	66.3	56.7
Pep-Trp680	89.0	85.8	95.9
Pep-Lys683	35.8	31.0	31.5
Subtotal	608	603	618
Total	1,113	1,104	1,130

[a]In ΔLoop this residue corresponds to Gly100A.

Chapter 5

STRUCTURAL BASIS FOR HIV-1 NEUTRALIZATION THROUGH THE MOLECULAR RECOGNITION OF 10E8 HELICAL EPITOPE AT THE MEMBRANE INTERFACE

5.1. INTRODUCTION

The 10E8 antibody achieves potent and broad HIV-1 neutralization by targeting MPER within gp41 (Huang et al., 2012; Kim et al., 2014). It appears that this potency is developed after extensive somatic hypermutation of the heavy-chain complementarity determining regions 2 and 3 (CDR-H2 and CDR-H3, respectively) (Soto et al., 2016). The exceptionally high degree of conservation of the MPER sequence (Montero et al., 2008; Zwick, 2005) justifies immunotherapeutic approaches based on the 10E8 antibody (Asokan et al., 2015; Barbian et al., 2015; Kwon et al., 2016a; Pegu et al., 2014; van Gils and Sanders, 2014). Supporting its functional activity in vivo, 10E8 confers complete protection to rhesus macaques against infection by a simian immunodeficiency virus–HIV chimera (Pegu et al., 2014). Remarkably, the 10E8 antibody is less effective than many anti-gp120 antibodies in neutralization assays, but provides the strongest protection in vivo (van Gils and Sanders, 2014). Also, consistent with a higher degree of cross-reactivity, 10E8 neutralizes SIVs that infect chimpanzees and gorillas with nanomolar potency (Barbian et al., 2015), surpassing the efficacy of other bNAbs directed against different vulnerability regions on Env. Engineered versions of the 10E8 with improved solubility have been recently reported (Kwon et al., 2016a), a finding that broadens the therapeutic potential of this bNAb (Asokan et al., 2015; Pegu et al., 2014).

In addition, the advantageous properties of 10E8 could be employed for the development of anti-HIV-1 vaccines (Burton and Mascola, 2015; Kwong and Mascola, 2012; Montero et al., 2008; Zwick, 2005). However, an important hurdle in this research effort is the observation that the functional properties of 10E8 are not adequately explained by its binding properties to MPER epitope peptides (Huang et al., 2012; Kim et al., 2014). In comparison to other MPER-specific neutralizing antibodies, 10E8 exhibits greater potency (mean IC_{50} value below 1 µg/mL) and lacks the lipid binding and auto-reactivity properties previously thought to limit the usefulness of MPER in the conception of an

effective HIV-1 vaccine (Huang et al., 2012). However, 10E8 binding affinities have been reported to be lower than those of the less-potent neutralizing antibodies, 2F5 and 4E10 (Huang et al., 2012). Thus, the comparatively poor performance of 10E8 remains at odds with the expectation that tight binding between antibody and epitope underpins the potent biological activity of this antibody, either by stabilizing the MPER domain in a conformation that is incompatible with membrane fusion, or by ensuring the full occupancy required to completely inactivate Env trimers (Kim et al., 2014).

Moreover, some mutations in 10E8's CDR-H3 affect viral neutralization more strongly than binding to MPER (*e.g.* W100b$_{HC}$A), whereas other mutations reduce binding significantly without markedly affecting the neutralizing activity of the antibody (*e.g.* Pro100f$_{HC}$Ala) (Huang et al., 2012). Inspection of the crystal structure of the 10E8 Fab in complex with MPER$_{(656-683)}$ peptide further reveals this incongruity (Huang et al., 2012). The quantification of the interaction surface at the apex of the CDR-H3 loop (Trp100b$_{HC}$) performed with PISA indicated that only a small fraction of the surface of this residue (<15 %) directly contacts the peptide, whereas the majority of it remains exposed to the solvent. This observation could explain why substitutions of this residue do not abrogate engagement to MPER peptide; however they do not explain its critical role in neutralization. These puzzling observations have obscured the underlying 10E8 mechanism of action, and have thwarted a faithful definition of the antigen structure mediating the biological activity of this important antibody.

In this study, we have elucidated the structure of the 10E8 Fab in complex with a peptide antigen whose affinity has been optimized by the addition of native residues belonging to the gp41 TMD (MPER$_{(664-690)}$) (Apellaniz et al., 2015). The dissection of the structural and energetic factors governing the recognition of the epitope in membrane environments explains the potent neutralization capabilities of the antibody. The full-length Env trimer in complex with 10E8 has been recently solved by cryo-EM (Lee et al., 2016). However, the limited resolution (8.8 Å) limited the atomistic understanding of the interactions

happening between antigen and antibody. Our structural, energetic and functional data clarifies critical aspects of the mechanism of recognition of the epitope of 10E8 in membranes in light of the cryo-EM structure reported (Lee et al., 2016), and also previous studies (Bird et al., 2014; Huang et al., 2012; Irimia et al., 2016; Kwon et al., 2016a). We propose that the helical scaffold of the MPER/TMD region of gp41, strengthened by nonpolar interactions with membrane lipids, is of biological relevance for the generation of potent anti-MPER bNAbs.

5.2. MATERIALS AND METHODS

5.2.1. Materials

The peptides used in the structural and affinity studies were synthesized as described in 3.2.1. Vector pEVOL, encoding a tRNA synthetase suitable for the incorporation of the photoreactive amino-acid, p-benzoylphenylalanine (*p*BPA), was a gift from Prof. P. G. Schultz (The Scripps Research Institute), and, *p*BPA was purchased from Bachem. 4-Chloro-7-Nitrobenz-2-Oxa-1,3-Diazole (NBD) was from Molecular Probes. The rest of the plasmids and antibodies were obtained as indicated in 4.2.1.

5.2.2. Fab-s production and characterization.

Experimental procedures described in 3.2.2 and 4.2.2 were followed for the mutation, expression and purification of Fab-s. ITC and DSC measurements were carried out as described in 3.2.3 and 4.2.5, respectively. For thermal stability determination in the presence of the ligand, the complex was formed by the addition of the peptide at a molar ratio of ~1:1.5 (Fab:peptide). Antibody binding to PsVs and 293-T lysate cells expressing DNA constructs encoding the MPER-TM1 or the MPER-PDGFR (see section 4.2.8 for sample production)

was assessed as previously described in 4.2.7 and 4.2.9, respectively. PsV neutralization was performed as described in section 4.2.10.

5.2.3. Crystallization of 10E8 Fab-peptide complex

Crystals of the complex between 10E8 Fab (3 mg L^{-1}) and the peptide $MPER_{(664-690)}$ added at a molar ratio of ~1:1.5 (Fab:peptide) in the presence of 2.5 mM DPC were grown in a solution of 50 % (v/v) 2-methyl-2,4-pentanediol, 200 mM phosphate, and 100 mM TRIS (pH 8.5) at 20 °C. A single protein crystal was harvested and stored in liquid nitrogen until data collection at the synchrotron. Data collection, processing and structure calculations are described in 3.2.5. The previous crystal structure of 10E8 (PDB entry code 4G6F) was used as a model to determine the structure by the method of molecular replacement. The relative angle between 4E10 (PDB entry 4XBG) and 10E8, as well as other calculations were carried out with CHIMERA (Pettersen et al., 2004). Data collection and refinement statistics are summarized in Table S4. The phosphate groups were modeled based on five conditions: (i) The difference electron density fo-fc and 2fo-fc maps showed strong electron density features before the phosphate moiety was modeled. Typical σ values for the fo-fc map were 4.7-8.2. Typical σ values for the 2fo-fc map were 2.0-3.3. (ii) When modeled, the phosphate ions engaged in non-covalent interactions with the neighboring residues. (iii) A water molecule could not properly account for the electron density (see below). (iv) A water molecule modeled at the position of the phosphorous atom could not engage in H-bonds with neighboring residues. (v) Other molecules present in the solution like TRIS, 2-methyl-2,4-pentanediol, DPC, or glycerol did not seem to fit the electron density.

5.2.4. *p*BPA photo cross-linking assays

For the photo cross-linking experiments, an amber codon specific for an engineered tRNA that translates the unnatural amino acid, p-benzoylphenylalanine (*pBPA*), was genetically encoded in the DNA sequence of the 10E8 Fab. Procedures to express a 10E8 Fab mutein bearing *p*BPA instead of Trp at position $100b_{HC}$ were adapted from previous reports (Abe et al., 2012; Young et al., 2010). Synthesis of Fab and the engineered tRNA was induced with 0.4 mM IPTG and 4 % (w/v) arabinose, respectively, in LB medium supplemented with 0.2 mg/L *p*BPA. For the photo-cross-linking experiment, samples containing Fab bearing the $W100b_{HC}$*p*BPA substitution at 1.5 µM and peptides at 10 µM were irradiated with UV light at 365 nm for 20 min at 4 °C using a UVP B-100AP lamp. Peptide binding in solution and in lipid membranes was accomplished in the presence of 5 mM of DPC or 1.5 mM of large unilamelar vesicles (LUVs), respectively. The LUVs were composed of 1,2-dioleoyl-*sn*-glycero-3-phosphatidylcholine (DOPC), 1,2-dioleoyl-*sn*-glycero-3 phosphatidylethanolamine (DOPE), 1,2-dioleoyl-*sn*-glycero-3-phosphatidylserine (DOPS), and egg sphingomyelin (SM) (27:29:14:30, mole ratio), and were produced by extrusion through two stacked polycarbonate membranes with a nominal pore size of 0.1 µm (Nuclepore Inc.). Fab heavy-chain-peptide adducts were separated by SDS-PAGE and stained with Coomassie blue. Alternatively, they were identified by WB using a sandwich comprising a goat (anti-human Fab) antibody (Sigma) and a mouse (anti-goat) antibody-HRP conjugate (Santa Cruz). Photo-cross-linked products were monitored using an LAS-4000 image analyzer (GE Healthcare).

5.2.5. NBD-Fab fluorescence measurements

Labeling the Fab with the polarity-sensitive NBD probe was performed as described previously (Heuck et al., 2000; Shepard et al., 1998). In brief, a cysteine-substituted Fab mutant ($W100b_{HC}C$) was first generated by site-directed mutagenesis as described in 4.2.2, then the mutated Fab was

produced and modified with a sulfhydryl-specific iodoacetamide derivative of NBD. Fluorescence-emission spectra were recorded with the excitation wavelength fixed at 470 nm. An emission spectrum of a sample lacking the fluorophore was subtracted from the spectrum of the equivalent sample containing the fluorophore. Fluorescence spectra of NBD were obtained upon incubation of NBD-labeled Fab (0.5 μM) with liposomes composed of DOPC:DOPE:DOPS:SM (27:29:14:30 mole ratio, total lipid concentration 250 μM) containing increasing amounts of peptide $MPER_{(671-686)}$ (1.7 and 6.8 μM) or $MPER_{(671-693)}$ (0.2, 0.65, 1.7, 3.4, and 6.8 μM) termed H(686) and H(693), respectively.

5.3. RESULTS

5.3.1. Design and characterization of an optimized peptide epitope for 10E8.

The existence of the continuous H2 α-helix at the MPER/TMD junction (FIG 35A) (Apellaniz et al., 2015), forced to revise models which had assumed that the interfacial MPER helix bends at position Lys683 to promote the insertion of the TMD perpendicular to the plane of the membrane (Dennison et al., 2009; Huarte et al., 2008; Kim et al., 2013; Lorizate et al., 2006; Schibli et al., 2001; Sun et al., 2008). We hypothesize that peptides that conserve the continuous helical MPER/TMD domain might function as a helical scaffold to increase the affinity of antibodies targeting the C-terminal subregion of the MPER as shown in chapter 3. We therefore designed the $MPER_{(664-690)}$ peptide, *KKKK*-^{664}D**K**WA**S**LW-**NW-F**DI**T**NW**LW**YI**K**LFIMIVG^{690}-*KKKKK*, to cover the entire length of the H1-H2 helices (FIG 35B), and to include all the residues reported to establish contacts with the antibody (in bold, (Huang et al., 2012)). We postulated that, in the context of a membrane environment, this elongated peptide constitutes the *bona fide* antigenic structure recognized by the antibody at membrane interfaces.

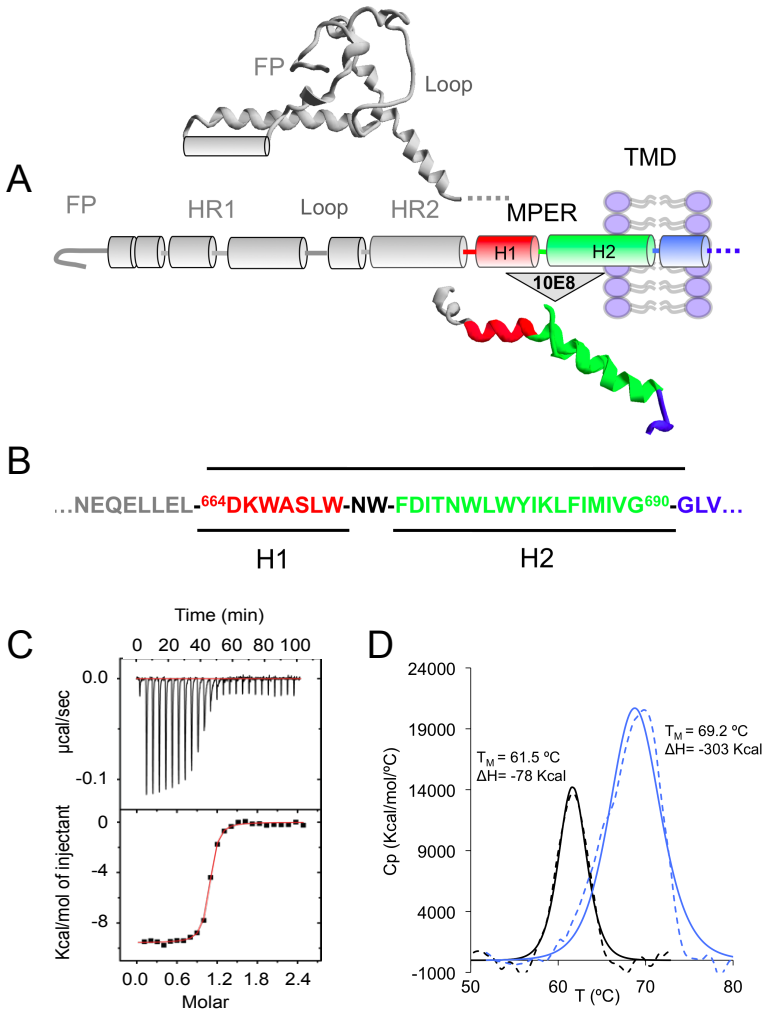

FIG 35. MPER$_{(664-690)}$ peptide design and binding energetics to Fab 10E8 in membrane mimicking environments. A) Structural elements of gp41. The ectodomain pre-fusion structure of gp41 (PDB entry 4TVP) is depicted in a ribbon and tube representation above the diagram illustrating the relative positions of the most important constituents in the sequence. The ribbon structure below the diagram was modeled by superposing the NMR structures of MPER$_{(656-683)}$ and MPER$_{(671-690)}$ peptides solved in DPC micelles (PDB entries 2M8O and 2MG3, respectively), and supports the existence of two distinct helical segments: H1 and H2. B) Env sequence covered by the MPER$_{(664-690)}$ peptide. C) Binding isotherm of the MPER$_{(664-690)}$ peptide to Fab 10E8 as measured by ITC. The thermodynamic parameters of binding are listed in Table 7. D) Thermal stability of the Fab-peptide complex by DSC. DSC thermograms (dotted lines) and curve fitting (solid lines) for 10E8 Fab before (black) and after titration with peptide (blue) are shown. Unfolding of the Fab shows a single thermal transition in both cases. The midpoints of the thermal unfolding (T_M) and the associated enthalpies (ΔH) are given.

To determine the binding signature and the stability of complexes between Fab and the MPER$_{(664-690)}$ peptide in a membrane-mimetic

environment, high-resolution thermodynamic techniques in the presence of DPC micelles were employed (FIG 35C and D). Titration of 10E8 Fab with $MPER_{(664-690)}$ produced a high-affinity value of 9.6 ± 1.0 nM (FIG 35C and Table 7). The binding free energy ($\Delta G° = -10.9 \pm 0.1$ kcal mol^{-1}) resulted from favorable non-covalent interactions between peptide and antibody ($\Delta H° = -9.6 \pm 0.1$ kcal mol^{-1}), and also from the entropic component, which contributed little but favorably to the affinity ($-T\Delta S° = -1.3 \pm 0.2$ kcal mol^{-1}).

Table 7. Thermodynamic parameters of binding of Fab 10E8 to the peptide $MPER_{(664-690)}$ and peptides based on Helix 2. Peptides H2(683), H2(686), H2(690) and H2(693) corresponds to $MPER_{(671-683)}$, $MPER_{(671-686)}$, $MPER_{(671-690)}$, and $MPER_{(671-693)}$, respectively.

Peptide	K_D *(nM)*	*ΔG° (kcal mol^{-1})*	*ΔH° (kcal mol^{-1})*	*-TΔS° (kcal mol^{-1})*[a]	*n*[b]
$MPER_{(664-690)}$	9.6 ± 1.0	−10.9 ± 0.1	−9.6 ± 0.1	−1.3 ± 0.2	1.0 ± 0.1
H2 (683)	746 ± 307	−8.3 ± 0.3	−3.3 ± 0.3	−5.0 ± 0.6	0.9 ± 0.1
H2 (686)	369 ± 84	−8.7 ± 0.1	−9.6 ± 0.5	0.9 ± 0.6	0.9 ± 0.1
H2 (690)	10 ± 1.6	−10.9 ± 0.1	−8.4 ± 0.1	−2.5 ± 0.2	0.8 ± 0.1
H2 (693)	9.4 ± 2.0	−10.9 ± 0.1	−9.0 ± 0.1	−1.9 ± 0.2	1.3 ± 0.1

[a] Temperature was 298 K.
[b] *n* refers to the molar ratio peptide/protein.

The thermal stability of the Fab in the presence and absence of $MPER_{(664-690)}$ was examined by differential scanning calorimetry (DSC) (FIG 35D). The data clearly demonstrated that the antibody is greatly stabilized in the complex with peptide with respect to the unbound form. The melting temperature (T_M, representing the unfolding mid-point) for the complex increases remarkably with respect to that for the unbound form of the Fab ($\Delta T_M = 7.7 \pm 1.0$ ºC). In addition, the unfolding enthalpy ($\Delta H°_{DSC}$) of the Fab was significantly increased upon formation of the complex with the peptide ($\Delta\Delta H° = 225$ kcal mol^{-1}). Thus, the thermodynamic analysis indicates that the $MPER_{(664-690)}$ peptide binds with high-affinity and specificity to the Fab in the presence of DPC micelles.

5.3.2. Crystal structure of $MPER_{(664-690)}$ peptide-10E8 Fab complex

The X-ray crystal structure of the complex between peptide and Fab in the presence of DPC micelles was determined at 2.4 Å resolution (FIG 36A and Table S4). The model comprised residues 1-215 (HC) and 2-210 (LC) of the Fab, and residues 669-689 of $MPER_{(664-690)}$ peptide. Residues 664-668 of the peptide were not observed in the electron density because of dynamic disorder, consistent with the idea that the H1 helix is not essential for the recognition of Env by this antibody (FIG 36B-E and 37A) (Huang et al., 2012; Kwon et al., 2016a; Lee et al., 2016). The region H2 adopted a helical conformation, which is very well conserved among all the structures available for 10E8 (Huang et al., 2012; Kwon et al., 2016a) (FIG 37A). The last residue of the H2 region of $MPER_{(664-690)}$, Gly690, and the additional Lys residues flanking the sequence of the peptide were not observed in the electron density, reflecting dynamic disorder. Interestingly, with respect to the previous structure with $MPER_{(656-663)}$ epitope bound (Huang et al., 2012), the antibody exhibited an unusually large degree of flexibility at the elbow region between the variable and constant regions (FIG 37B) (Stanfield et al., 2006). The flexibility of the elbow region could facilitate the accessibility of the native gp41 epitope, being partially restricted by the gp120 component of Env and by the viral membrane (Huang et al., 2012; Lee et al., 2016).

The bound peptide adopts a canonical α-helix throughout the sequence, except for residues at the N-terminal region 669LWN671 (FIG 36C and D). No evidence of a kink at position Lys683 was found, in agreement with previous NMR results (Apellaniz et al., 2015). The 10E8 Fab is perfectly adapted to recognize the α-helical structure of the peptide as evidenced by the high value of the shape-complementarity parameter (Sc = 0.79) (Lawrence and Colman, 1993). The epitope is held tightly to the antibody by numerous contacts between a large patch of non-polar residues at both the CDR-H3 of the Fab and the peptide, and by H-bonds between main-chain atoms of the antibody and critical residues Trp672 and Lys683 of the peptide (Table S5 and S7).

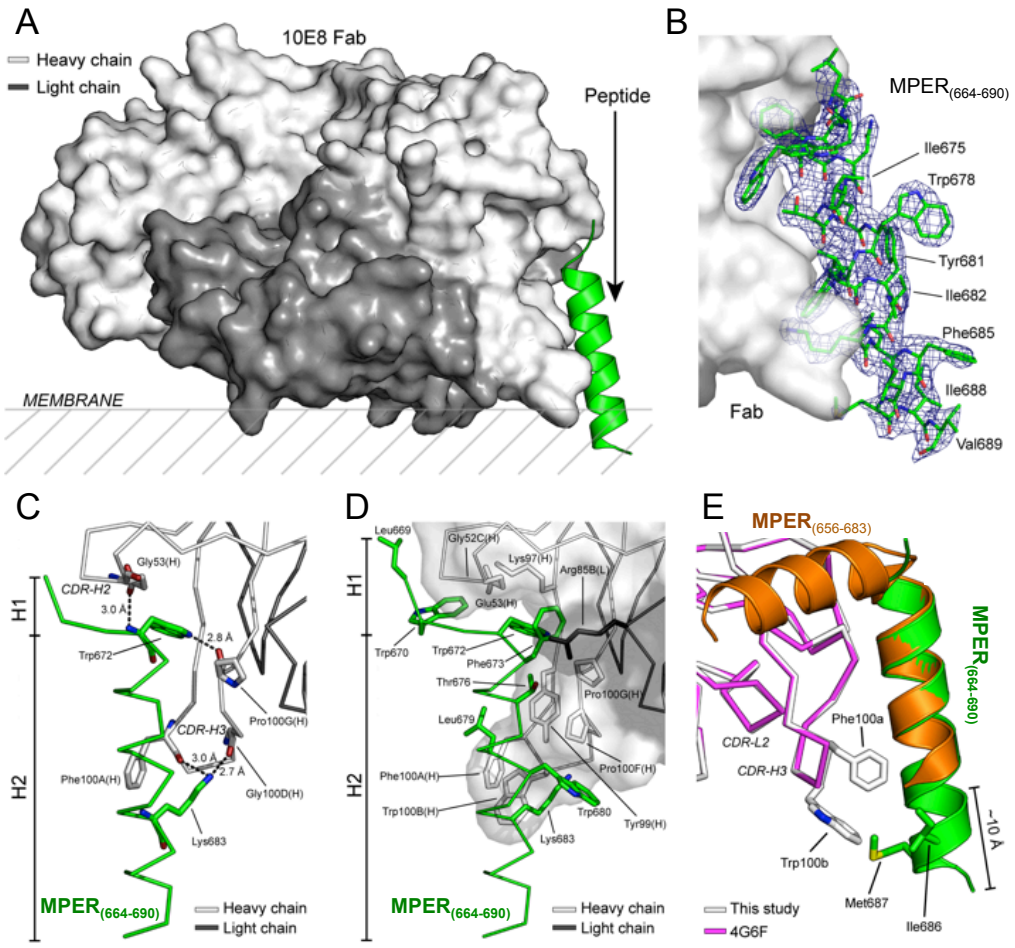

FIG 36. Crystal structure of the complex between Fab 10E8 and MPER$_{(664-690)}$ peptide determined at 2.4 Å resolution in the presence of DPC. A) Overall structure of the complex. The surface of the heavy and light chains of the Fab are shown in light and dark gray, respectively. The MPER$_{(664-690)}$ peptide is depicted as a green helix. The hypothetical location of the viral membrane is shown (see **FIG 40** for more details). B) Sigma-A weighted electron density map (blue mesh) of MPER$_{(664-690)}$ peptide bound to the Fab at a contouring level of σ = 1.0. The peptide is depicted as green sticks. Numerous peptide hydrophobic residues (labeled) remain exposed even after engagement with the Fab. C) H-bond network between peptide and Fab. Bond distances are shown. The peptide and Fab are depicted in green and gray sticks, respectively. D) Interaction surface between peptide and Fab. The majority of interacting residues are non-polar. E) Comparison of the conformation of MPER$_{(656-683)}$ peptide (PDB entry 4G6F) and the optimized peptide (this study) bound to 10E8. The Fab and peptide from the previously published structure are depicted in magenta and orange, respectively. The Fab and peptide from this study are shown in light gray and green, respectively. Side-chains of residues Phe100a$_{HC}$ and Trp100b$_{HC}$ of the Fab, and Ile686 and Met687 of the peptide are depicted to illustrate additional interactions.

The interaction area between Fab and MPER$_{(664-690)}$ peptide covers only 31 % of the surface of the peptide as calculated with the PISA server, leaving numerous aromatic and hydrophobic residues prone to interact with other

peptide moieties in the crystal. The assembly of peptides at crystal-contact regions minimizes the degree of exposure of these hydrophobic residues, resembling the organization of a bilayer (FIG 38A). In particular, the two juxtaposing MPER-N-TMD helices share an overall organization similar to that observed in the recent 3-D reconstruction of Env-10E8 complex at 8.8 Å resolution (Lee et al., 2016) (FIG 38B). Consequently, an approximate orientation of the Fab-peptide complex with respect to the plane of the membrane in the crystal structure can be extrapolated (see also below).

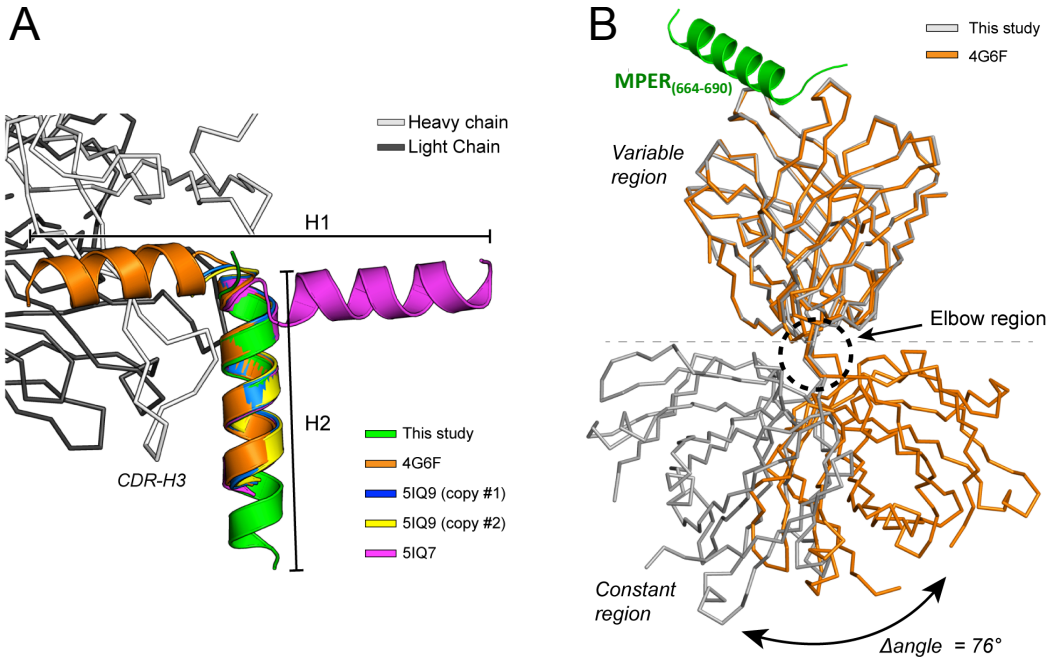

FIG 37. Binding properties of 10E8. A) Comparison of the conformation of the peptide bound to 10E8 Fab in multiple crystal structures. The peptide bound to the Fab in this study and in PDB entries 4G6F, 5IQ9 (two copies) and 5IQ7 are shown in green, orange, blue, yellow and magenta, respectively. Residues of the variable region (10-90) of the LC were employed for superposition of the structures, achieving RMSD values in the range of 0.19-0.34 Å. The region H1 appears in multiple conformations or it is not observed, whereas H2 remains essentially unchanged. The crystal structure of the Fab determined in this study is depicted with light (HC) and gray (LC) ribbons. B) Domain rotation (elbow angle). Comparison of two structures of 10E8 Fab with peptide bound. Gray and magenta ribbons correspond to the structure determined in this study and with PDB entry 4G6F, respectively. The angle of the constant region with respect to the variable region shifts by 34° between the two structures, producing a conformational change (swinging-like movement) that is clearly visible in the figure. The elbow angles were calculated with the program RBOW.

The unprecedented detail of the structure of the extended region of $MPER_{(664-690)}$ peptide (TMD residues ^{684}LFIMIVG^{690}) visualized for the first time in the complex with 10E8 reveals that residues Ile686 and Met687 are located in the proximity of the crucial residues $Phe100a_{HC}$ and $Trp100b_{HC}$ of the Fab (FIG 36E). The combined buried surface area (BSA) of these four residues increased by 99 Å with respect to the complex between 10E8 and a peptide with a shortened C-terminal region (Table S7). The enlarged interaction surface in the complex with the longer peptide is expected to favorably contribute to the high-affinity between antibody and antigen.

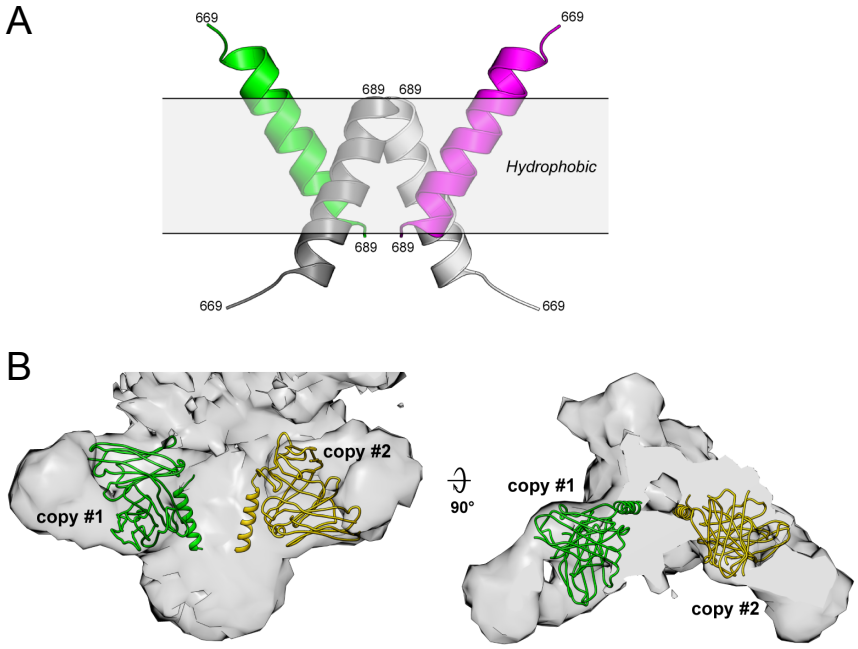

FIG 38. Intermolecular peptide-peptide interactions in the crystal. A) Close-up view of several peptides arranged in a micelle-like aggregate in the crystal structure of $MPER_{(664-690)}$ bound to Fab. The micelle-like aggregate is made of two pseudo-dimers, and stabilized by numerous hydrophobic residues of the peptide not interacting with the Fab. The micelle-like aggregate mimics the environment of a biological membrane, and is presumably surrounded by detergent molecules (DPC) from the crystallization buffer, although we note that no molecules of detergent were observed in the electron density. The approximate region occupied by the non-polar residues is indicated by the gray box. B) The X-ray structure of the variable region of 10E8 in complex with the $MPER_{(664-690)}$ peptide was fitted into the electron density map of EnvΔCT-PGT151-10E8 (Entry code EMD-3312).

5.3.3. Relevance of the extended region of MPER$_{(664-690)}$ peptide for binding

To establish the functional relevance of the interactions between 10E8 and the helical epitope extending beyond residue Lys683, the peptide epitopes H2(683), H2(686), H2(690) and H2(693) lacking the H1 region of MPER were generated by progressively adding helical turns to their C-terminus (FIG 39A). Titration experiments with these peptides revealed different binding patterns depending on the extent of the elongation (FIG 39B and Table 7). The affinity of the peptides increased in the order H2(683) < H2(686) ≪ H2(690) ≈ H2(693). Importantly, the dissociation constant of the two longest H2 peptides H2(690) and H2(693) (10 ± 1.6 and 9.4 ± 2.0 nM, respectively) is comparable within error to that of the MPER$_{(664-690)}$ peptide (9.6 ± 1.0 nM), demonstrating that the H1 region of MPER does not contribute to high-affinity binding by this antibody. The thermodynamic signature is dominated by the large and favorable contribution of the enthalpy term, except for the shorter H2(683) peptide in which both entropy and enthalpy terms contribute similarly to binding.

To obtain direct evidence about the non-polar contacts between the tip of the CDR-H3 and residues downstream position Lys683 of the peptide, we carried out photo-cross-linking experiments. The 10E8 Fab was modified with the UV-sensitive unnatural amino acid p-benzoylphenylalanine (*p*BPA) (Abe et al., 2012; Young et al., 2010), which was genetically encoded at position Trp100b$_{HC}$ of the antibody (FIG 39C). The Fab-peptide complexes were subjected to UV light and the formation of adducts analyzed by SDS-PAGE. An additional band corresponding to cross-linked peptide and Fab HC was observed in samples containing Fab and H2(690) or H2(693), but not with H2(683) or H2(686) (FIG 39C). The new band was absent in the Fab:peptide samples before irradiation (CTL lane) demonstrating it is specifically generated by UV-mediated cross-linking. Thus, inclusion of the full MPER-N-TMD helix (H2) sequence enabled additional interactions with the tip of the 10E8 CDR-H3, increasing significantly the affinity for the antibody.

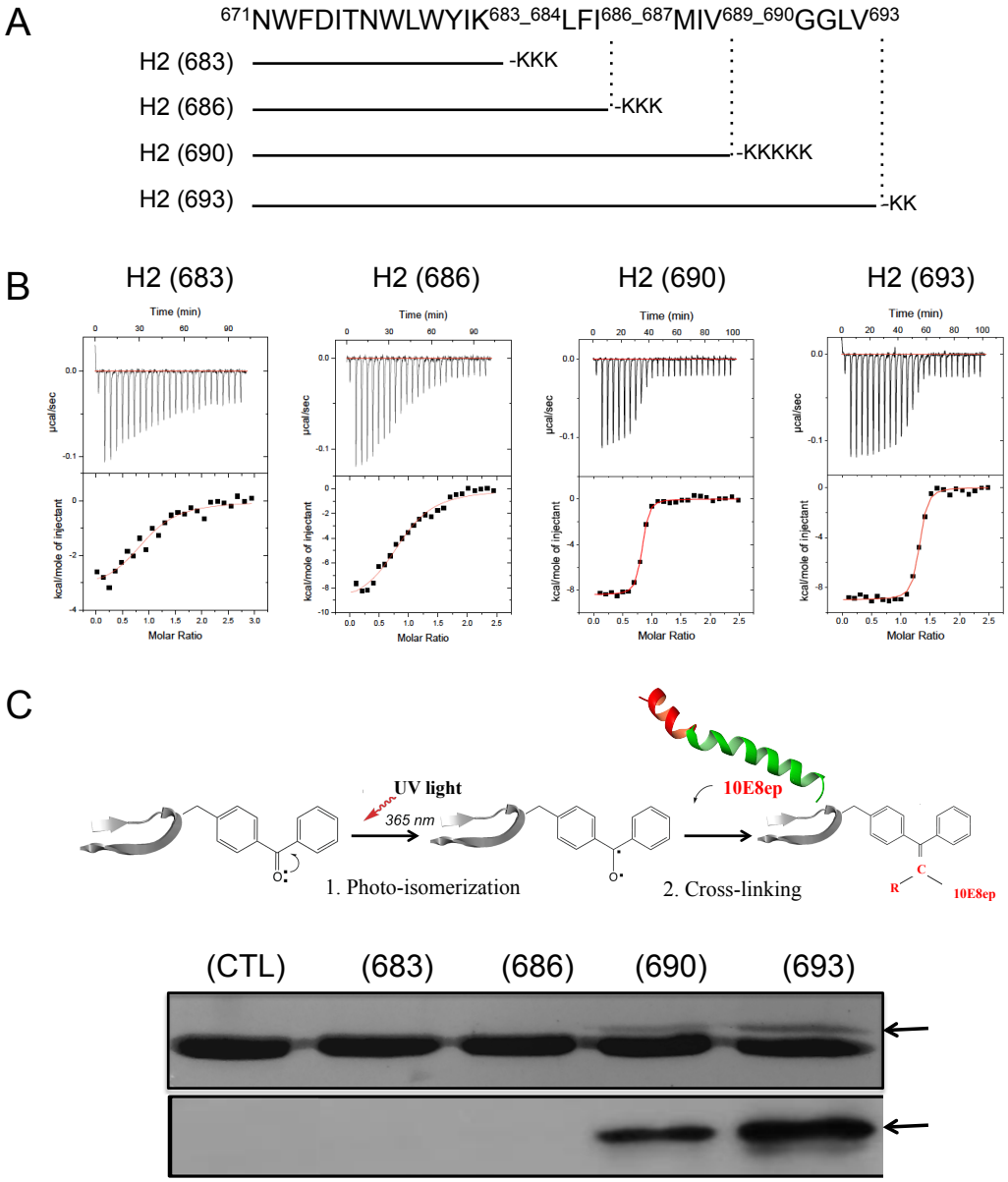

FIG 39. Binding of peptides spanning Helix-2 to Fab 10E8 in the presence of DPC. A) Overview of the sequences of the H2 peptides displaying increasingly elongated C-termini. The four peptides differed in the number of consecutive helical turns following position 683. B) Binding isotherms of the H2 peptide epitopes to Fab 10E8 examined by ITC. The thermodynamic parameters of binding are displayed in Table 7. C) Photo cross-linking between Fab 10E8 and the peptides. Chemical structure and schematic mechanism for the formation of a covalent bond between Fab-*p*BPA and peptide upon irradiation with u.v. light (top panel). Protein bands were detected by Coomassie-blue staining or by WB using 4E10 antibody (center and bottom panels, respectively). The arrows point to the position of the photo-cross-linked product. (CTL, control 10E8 Fab without peptide). Peptides H2(683), H2(686), H2(690) and H2(693) corresponds to $MPER_{(671-683)}$, $MPER_{(671-686)}$, $MPER_{(671-690)}$, and $MPER_{(671-693)}$, respectively.

5.3.4. Recognition of the MPER-N-TMD helix at the membrane interface

A previous report employing short lipids revealed the orientation of 4E10 Fab with respect to the plane of the membrane (Irimia et al., 2016). Because the bNAbs, 10E8 and 4E10, recognize approximately the same segment of MPER, we inferred the relative orientation between antibodies by simply superimposing the coordinates of the peptide in the crystal structures (RMSD = 0.25 Å) (FIG 40A, left). The comparison revealed that the arrangement of 10E8 Fab is different from that of the 4E10 Fab, with each antibody binding a somewhat different face of the peptide; consequently, they approach the helix from different orientations with an estimated difference of 30°. According to this simple model, 10E8 would approach the epitope from a direction parallel to the plane of the membrane.

This model predicts that the variable and constant regions of the 10E8 LC interact, at least weakly, with the surface of the viral membrane. This hypothesis was reinforced by two separate observations from the crystal structure (FIG 40A). First, a phosphate ion bound to the CDR-L2 of 10E8 occupies a similar position to that of a lipid bound to 4E10 (PDB entry 4XBG). And second, three phosphate ions, scattered across the constant region of the LC, occupy positions consistent with the location of the headgroups of lipid molecules. This region of the antibody is expected to sit on the viral membrane when bound to Env (Lee et al., 2016). Collectively, the model in FIG 40A suggests that the Fab region of the 10E8 antibody approaches laterally to the MPER helix, the peptide being inserted obliquely into the lipid bilayer.

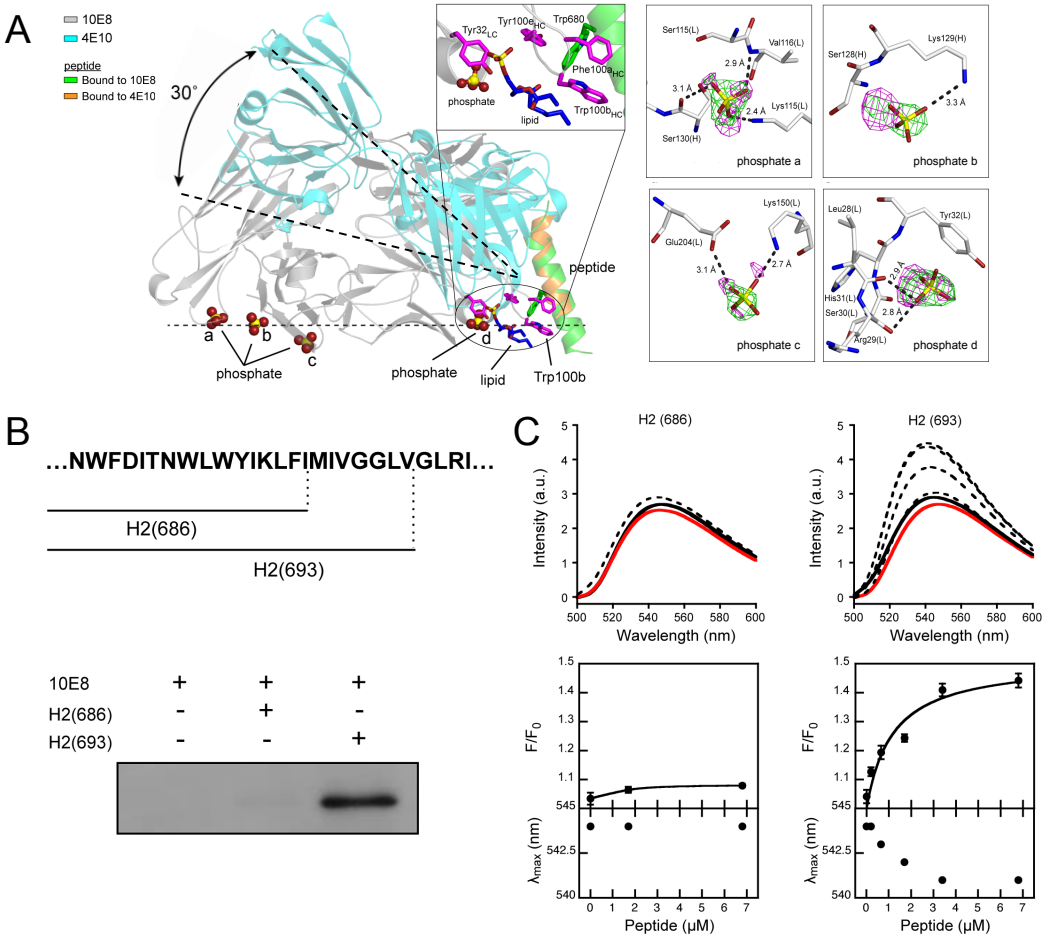

FIG 40. Binding to the membrane-inserted epitope. A) Model of the recognition of the epitope by 10E8 and 4E10 Fab in membranes. Left: Relative orientation of 10E8 (gray) with respect to 4E10 (PDB entry 2FX7, cyan) after superimposing residues 673-678 of the peptide bound in both structures (RMSD = 0.25 Å). The lipid molecule bound to 4E10 was obtained from the PDB entry 4XCN. Carbon, oxygen and phosphate atoms of the lipid are depicted in blue, red and yellow, respectively. Several phosphate ions (red and yellow) bound to 10E8, suggesting a putative orientation of the antibody with respect to the surface of the viral membrane (dotted line). Inset: Close-up view of the residue Trp100b$_{HC}$ (magenta) of 10E8 (gray) and the lipid molecule (blue) bound to 4E10 (cyan). Right: Difference electron density map at the location of each phosphate (a-d) shown as a green mesh. Difference fo-fc electron density map (magenta mesh) was obtained by placing a water molecule at the position of the phosphate ion and subsequently refined with REFMAC5. Maps are shown at a contouring level of σ = 3. C (see materials and methods). B) Photo-cross-linking of Fab 10E8 with peptides H(686) and H(693) inserted in membranes detected by WB. C) Membrane insertion of the 10E8 CDR-H3 apex. Top panels: Spectra of NBD emission upon incubation of NBD-Fab in solution (red traces), with liposomes devoid of peptide (black solid traces) or with LUV-peptide complexes with increasing amounts of H2(686) or H2(693) (black dotted traces in left and right panels, respectively). Bottom panels: Fractional changes (top) and maximum shifts (bottom) of NBD emission deduced from the spectra. The initial fluorescence (F_0) was determined from NBD-Fab in buffer samples (red traces). Final fluorescence values (F) were measured after the addition of LUV-peptide complexes (black traces). Lipid concentration was fixed at 250 μM. Means ± S.D. of three independent experiments are represented. The lines correspond to the best fit of the experimental values to a hyperbolic function. Peptides H2(686) and H2(693) correspond to MPER$_{(671-686)}$, and MPER$_{(671-693)}$, respectively.

The orientation of 10E8 Fab with respect to the membrane places the CDR-H3 tip immersed into the lipid bilayer. Hence, if the hydrophobic interactions with the C terminus of the peptide described above were relevant for the activity of the antibody they must occur inside the membrane (FIG 40). To test this prediction, we used Fab-s incorporating *p*BPA, or Fab-s labeled with the polarity-sensitive fluorescent probe NBD, and compared their interactions with the short H2(686) and long H2(693) peptides inserted in membranes (FIG 40B and C). In this experiment, we first established conditions for the quantitative partitioning of the peptides into large unilamellar vesicles (LUVs) (FIG 41). Incubation of the LUV-peptide complexes with 10E8 W100b$_{HC}$*p*BPA Fab, followed by irradiation with UV-light, generated Fab-peptide adducts in the presence of the long peptide H2(693) peptide, but not in the presence of the shorter H2(686) (FIG 40B). This experiment corroborated that the interactions observed in presence of DPC micelles (FIG 39C) are also reproduced in the environment of biological membranes.

To determine the degree of penetration of the CDR-H3 apex of Fab 10E8 into lipid membranes, Trp100b$_{HC}$ was replaced by Cys, and modified chemically by attaching an NBD dye to its sulfhydryl group (Heuck et al., 2000; Shepard et al., 1998). The fluorescence intensity of NBD increases and shifts to shorter wavelengths upon transferring from an aqueous solvent into the less polar environment of the bilayer (FIG S1). Thus, the extent of the interaction between the labeled NBD-Fab and the membrane was evaluated by comparing the emission of fluorescence of NBD before and after incubation with LUV-peptide complexes (FIG 40C). The fluorescence spectrum of NBD did not change appreciably upon incubation of the labeled Fab with bare vesicles, or with vesicles containing the short H2(686) peptide (FIG 40C). In contrast, incubation of Fab with vesicles containing the longer peptide H2(693) enhanced fluorescence emission, accompanied by a shift of the maximum towards lower wavelengths. Importantly, the changes described correlated with the density of H2(693) in the membrane (FIG 40C), and were not observed with vesicles decorated with a the H2(693) peptide bearing a double-Ala substitution for

residues Trp672 and Phe673 (FIG S1B); this result strengthens the conclusion that a change in polarity sensed by the Fab-probe is the consequence of specific binding to the H2(693) peptide. Collectively, the results in FIG 40 suggest that recognition of the epitope in a membrane setting requires the interaction with the tip of the 10E8 CDR-H3, an idea that is further reinforced by the data from the crystal complex (FIG 36).

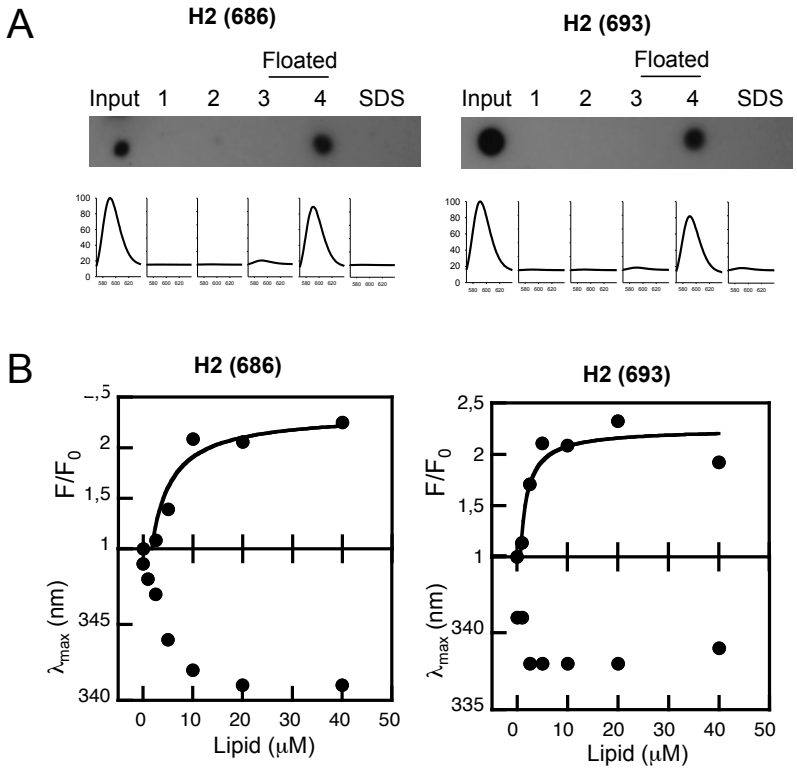

FIG 41. Peptide-liposome complex formation. A) Incorporation of H2(686) or H2(693) into liposomes was determined after flotation of the complexes in a sucrose gradient. Rh-PE-labeled liposomes and peptides were incubated at the same concentrations as in photo-cross-linking assays (1.5 mM and 10 μM, respectively) (see section 3.2.4 for more details). B) Titration experiments following the changes in peptide Trp fluorescence intensity that occur upon membrane insertion. Changes in fractional intensity (top) and maximum emission wavelength (bottom) were measured upon incubation with increasing concentrations of lipid vesicles. Peptide concentration was 0.5 μM. The lines correspond to the best fit of the experimental values to a hyperbolic function. Saturation values indicate that quantitative incorporation of peptide can be attained with lipid concentrations higher than 50 μM. Peptides H2(686) and H2(693) correspond to $MPER_{(671-686)}$ and $MPER_{(671-693)}$, respectively.

5.3.5. Biological activity

We next evaluated binding for 10E8 in membrane-like environments in relation to its biological activity by producing 10E8 Fab-s bearing substitutions in the critical CDR-H3 loop (Table 8, FIG 42 and 43). Two separated Ala substitutions, namely P100f$_{HC}$A, and W100b$_{HC}$A, were selected based on previous work indicating a lack of correlation between affinity for the peptide and neutralization potency (Huang et al., 2012). In addition, Fab 10E8 muteins bearing conservative W100b$_{HC}$Y and non-conservative W100b$_{HC}$D substitutions were prepared to determine the role of the aromatic residue, Trp100b$_{HC}$, in optimizing the Fab-antigen hydrophobic contact surface (Table S7).

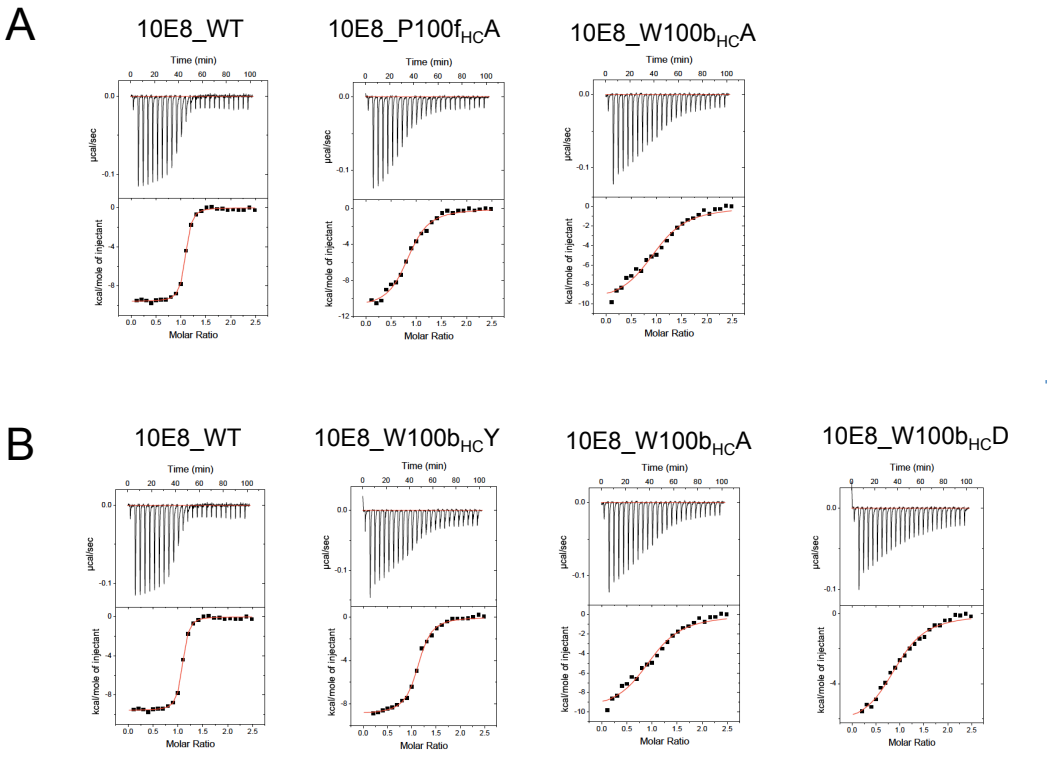

FIG 42. MPER$_{(664-690)}$ peptide binding to CDR-H3 10E8 Fab mutants by ITC. A) Binding of Fab mutants with Ala substitutions P100f$_{HC}$A and W100b$_{HC}$A, reflecting higher affinity of the former (Table 8), and correlating with its higher neutralization potency (**FIG 43**C). B) Effect of substitutions at position 100b$_{HC}$ critical for neutralization. The Fab containing the conservative W100b$_{HC}$Y substitution displayed the highest affinity (Table 8), which also correlated with its comparatively higher neutralizing activity (FIG 43C).

Titration of the muteins with peptide in solution (FIG 42 and Table 8) revealed diminished affinity for the MPER($_{664-690}$) peptide between 5- and 39-fold. The experimental order of affinities was WT > W100b$_{HC}$Y > P100f$_{HC}$A > W100b$_{HC}$A ≈ W100b$_{HC}$D. Examination of the thermodynamic parameters did not clarify the energetic mechanism behind the loss of affinity, although we note that in all cases the weaker binding was still governed by a favorable change of enthalpy ($\Delta H < 0$ kcal mol^{-1}).

The ranking of affinities changed when the sequence encompasing MPER($_{664-690}$) was presented in the context of immobilized pseudovirus (PsV) particles (FIG 43A). The dose-dependent binding of the Fab-s to immobilized PsV particles diminished gradually for P100f$_{HC}$A and W100b$_{HC}$Y variants, and was undetectable for W100b$_{HC}$A or W100b$_{HC}$D variants. Thus, in the context of the viral surface the P100f$_{HC}$A variant bound more efficiently to the 10E8 epitope than the conservative W100b$_{HC}$Y one.

Table 8. Thermodynamic parameters of binding of Fab 10E8 CDR-H3 muteins to the peptide MPER$_{(664-690)}$.

Antibody	K_D (nM)	$\Delta G°$ (kcal mol^{-1})	$\Delta H°$ (kcal mol^{-1})	$-T\Delta S°$ (kcal mol^{-1})[a]	n[b]
WT	9.6 ± 1.0	−10.9 ± 0.1	−9.6 ± 0.1	−1.3 ± 0.2	1.0 ± 0.1
P100f$_{HC}$A	161 ± 22	−9.2 ± 0.1	−11.1 ± 0.2	1.9 ± 0.3	0.8 ± 0.1
W100b$_{HC}$Y	52 ± 12	−9.9 ± 0.1	−8.9 ± 0.1	−1.0 ± 0.2	1.1 ± 0.1
W100b$_{HC}$A	361 ± 82	−8.8 ± 0.1	−10.0 ± 0.5	1.2 ± 0.6	1.0 ± 0.1
W100b$_{HC}$D	375 ± 66	−8.7 ± 0.1	−6.5 ± 0.3	−2.2 ± 0.4	1.0 ± 0.1

[a] Temperature was 298 K.
[b] n refers to the molar ratio peptide/protein.

To determine if this effect was induced by membrane anchoring, the MPER($_{664-690}$) peptide was next presented in the plasma membranes of cells expressing the fusion polypeptide, MPER-TM1, which comprises (i) an N-terminal HA tag, (ii) the MPER residues, and (iii) the TMD residues of gp41 followed by 27-AA of the gp41 cytoplasmic domain (MPER-TM1; FIG 43B, left) (Montero et al., 2012). Previous studies of MPER-TM1 revealed that the 4E10 epitope is well exposed for antibody binding when constrained by the gp41 TMD; in contrast, 4E10 binds weakly to a construct in which the gp41 MPER-

TMD junction is disrupted by fusion to another receptor's 20-AA membrane-proximal external region and TMD (MPER-PDGFR) (see also chapter 4). In this previous work, the C-terminal helix of the MPER was envisioned as being continuous with the gp41 TMD helix; this arrangement was thought to fully expose the MPER for 4E10 docking (Montero et al., 2012).

FIG 43B shows that both 4E10 and 10E8 IgGs bind tightly to the MPER-TM1 in the context of the plasma membrane. These antibodies engaged with the MPER-TM1 construct as effectively as the 17/9 IgG, which binds to the solvent-exposed HA epitope and served to normalize expression levels (Montero et al., 2012). A comparable degree of binding was observed for the WT 10E8 Fab, thereby sustaining side-by-side comparative assessment of its CDR-H3 muteins. The binding pattern of substituted Fab-s to MPER-TM1 coincided with that previously observed in PsVs. In contrast, the MPER-PDGFR construct was a poor ligand for both the 4E10 and 10E8 IgGs, and for the 10E8 Fab and its muteins, whereas, 2F5, whose epitope is on the N-terminal sub-region of the MPER, was marginally affected (FIG 43B, right). None of the mutant Fab-s bound to the MPER-PDGFR in the membrane context. These results reflect the ability of the gp41 TMD residues to affect the positioning of 10E8 epitope at the membrane interface, and demonstrate the requirement of the hydrophobic CDR-H3 tip for the occurrence of the recognition process.

The differences observed in binding of the 10E8 Fab and its muteins to PsVs or MPER-TM1 were mirrored by differences in their neutralization potencies (FIG 43C). The neutralization assays confirmed the previously reported detrimental effects induced by the $P100f_{HC}A$ and $W100b_{HC}A$ substitutions (Huang et al., 2012), which rendered a less potent, but still functional Fab, and an almost non-neutralizing variant, respectively. Moreover, in comparison to the $W100b_{HC}A$ mutein, the Fab bearing the conservative $W100b_{HC}Y$ substitution gained neutralization potency. However, the activity of the $W100b_{HC}Y$ variant was lower than that of the $P100f_{HC}A$ variant. Finally, the non-conservative $W100b_{HC}D$ substitution rendered a Fab devoid of all activity.

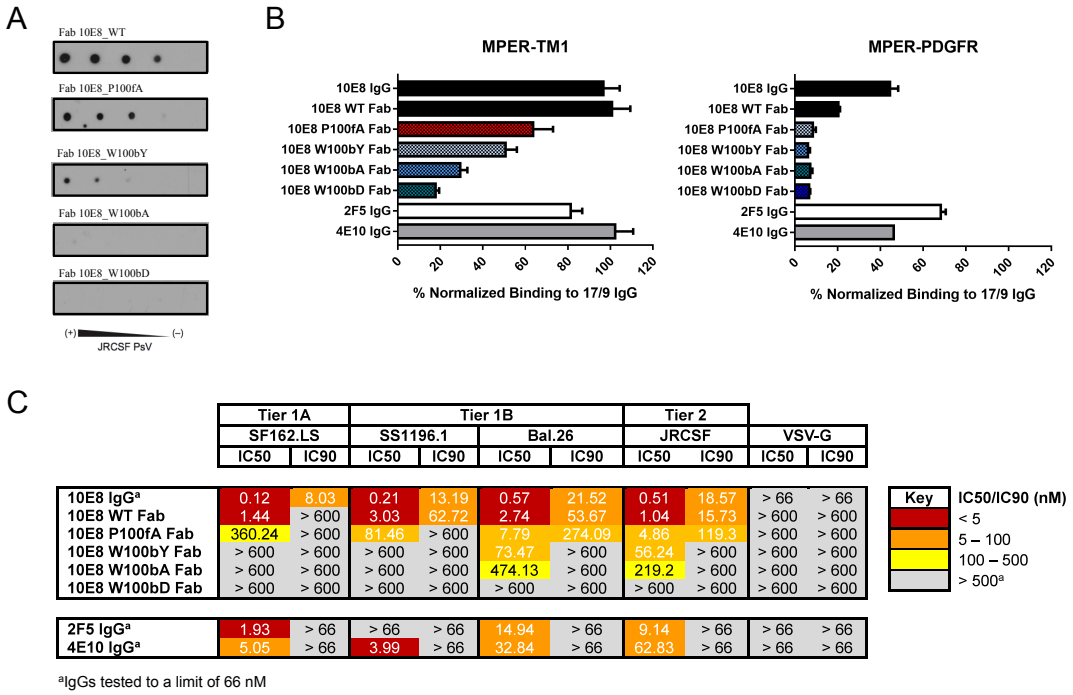

C

	Tier 1A		Tier 1B				Tier 2			
	SF162.LS		SS1196.1		Bal.26		JRCSF		VSV-G	
	IC50	IC90	IC50	IC90	IC50	IC90	IC50	IC90	IC50	IC90
10E8 IgG[a]	0.12	8.03	0.21	13.19	0.57	21.52	0.51	18.57	> 66	> 66
10E8 WT Fab	1.44	> 600	3.03	62.72	2.74	53.67	1.04	15.73	> 600	> 600
10E8 P100fA Fab	360.24	> 600	81.46	> 600	7.79	274.09	4.86	119.3	> 600	> 600
10E8 W100bY Fab	> 600	> 600	> 600	> 600	73.47	> 600	56.24	> 600	> 600	> 600
10E8 W100bA Fab	> 600	> 600	> 600	> 600	474.13	> 600	219.2	> 600	> 600	> 600
10E8 W100bD Fab	> 600	> 600	> 600	> 600	> 600	> 600	> 600	> 600	> 600	> 600
2F5 IgG[a]	1.93	> 66	> 66	> 66	14.94	> 66	9.14	> 66	> 66	> 66
4E10 IgG[a]	5.05	> 66	3.99	> 66	32.84	> 66	62.83	> 66	> 66	> 66

Key	IC50/IC90 (nM)
	< 5
	5 – 100
	100 – 500
	> 500[a]

[a]IgGs tested to a limit of 66 nM

FIG 43. Effect of substitutions in CDR-H3 on Fab binding to MPER in the context of the plasma membrane and correlation with neutralizing activity. A) JRCSF PsV recognition by 10E8 Fab and mutein Fab-s in a dot-blot assay. Decreasing amounts of PsV (from left to right) were spotted onto nitrocellulose membranes and probed with 10E8 Fab and its muteins. B) Cell lysates bearing recombinant MPER proteins (MPER-TM1: left; MPER-PDGFR: right) were probed with 20 nM IgG or Fab, as indicated, and binding signals were normalized to that of 20 nM 17/9 IgG, which binds to N-terminal HA tags on both constructs. C) Neutralization profile of a panel of PsVs bearing HIV Env or that of vesicular stomatitis virus (negative control). IC_{50} and IC_{90} values for 2F5, 4E10 and 10E8 IgGs, 10E8 Fab and its muteins are shown.

5.4. DISCUSSION

In this work, we have provided new insights into the molecular mechanism linking the binding of the helical epitope at the membrane interface with the biological function of 10E8. The chemically heterogeneous membrane interface region allows multiple types of non-covalent lipid-peptide interactions (White et al., 2001; White and Wimley, 1999). Importantly, aromatic residues, and particularly Trp, have a tendency to preferentially locate within this region (McDonald and Fleming, 2016; Wimley and White, 1996). Thus, interactions with lipids and the spatial arrangement of favorably inserted aromatic residues

may influence the orientation of MPER epitopes at the membrane surface, the mechanism of antibody docking, or both. Our previous data (chapter 3) suggested that preservation of the continuous MPER-N-TMD helix observed by NMR studies (Apellaniz et al., 2015) could be critical for high affinity binding to epitopes of the C-terminal MPER sub-region when inserted into the membrane (FIG 35A). The peptide $MPER_{(664-690)}$ was designed to preserve this element while including all residues that were in contact with the 10E8 antibody in the first reported structure of the Fab-peptide complex (FIG 35B). This optimized peptide was bound with high affinity by the 10E8 Fab forming a stable complex in the presence of DPC micelles (FIG 35C and D).

Recent crystallographic studies (Kwon et al., 2016a) and cryo-EM reconstructions (Lee et al., 2016) together with previous data regarding the binding of 10E8 to peptides systematically substituted with Ala (Huang et al., 2012), indicated that 10E8 binding affinity is primarily mediated by its mode of recognition of the shorter ^{671}NWFDITNWLWYIK^{683} sequence. However, structure resolution of the complete helix ^{671}NWFDITNWLWYIKLFIMIVG^{690} in complex with Fab adds three important factors to our understanding of the 10E8 epitope.

First, we propose the absence of a kink interrupting the MPER helix at position Lys683 and the oblique insertion of the whole structural element into the membrane. A widely assumed model suggests that the MPER helix inserts in parallel to the membrane interface and kinks at position Lys683 to allow the perpendicular insertion of the TMD helix starting at position Leu684 (Huarte et al., 2008; Kim et al., 2013; Ofek et al., 2004; Schibli et al., 2001; Sun et al., 2008). Accordingly, it has been proposed that anti-MPER antibodies approach from above the membrane-inserted MPER epitopes (Cardoso et al., 2005; Lorizate et al., 2006; Ofek et al., 2004; Song et al., 2009; Sun et al., 2008). In contrast, our crystallographic data (FIG 36, 38 and 40) support more recent models suggesting that the main axis of the uninterrupted helix of the epitope forms an oblique angle with respect to the membrane plane (Apellaniz et al.,

2015; Irimia et al., 2016), with some intermolecular contacts made by the anti-MPER Fab-s occurring at the vertex, after engaging with the helix surface facing the membrane (Irimia et al., 2016; Lee et al., 2016). The absence of a kink at position Lys683 is also supported by the recent structural resolution of a trimeric TMD sequence embedded in lipid bicelles (Dev et al., 2016).

Second, our data clearly suggest the active participation of residues beyond Lys683 in the interaction with Fab in the membrane environment. Titration, photo-cross-linking data, and structural analysis revealed the involvement of residues Ile686 and Met687 in establishing non-polar contacts with the CDR-H3 apex residue, Trp100b$_{HC}$; the interaction surface of this residue is doubled in the presence of the long peptide (FIG 36E, 39 and Table S7). Collectively, the identification of several phosphate groups on the surface of the antibody in the crystal structure (FIG 40A), and the capacity of the Fab to recognize the membrane-anchored peptide (FIG 43B and C) suggest that key Fab-peptide interactions required for the effective neutralization occur within the membrane interface. It appears that the maximum binding potential of 10E8 emerges from the simultaneous interactions of Trp100b$_{HC}$ with TMD residues Ile686 and Met687 and phospholipids (FIG 36E and 40A).

And third, the mutational analysis of the 10E8 CDR-H3 region indicates that preservation of such interactions directly correlates with the neutralizing activity of the antibody (Table 8 and FIG 43). Thus, the binding of the 10E8 Fab and its muteins to Env-bearing PsVs or to the MPER-TM1 polypeptide in the context of the plasma membrane reflected with remarkable accuracy their neutralizing activity (FIG 43). The model displayed in FIG 44, which combines the high-resolution structural information described in this work, with that derived from cryo-EM reconstructions (Lee et al., 2016), provides a putative mechanism to explain that correlation.

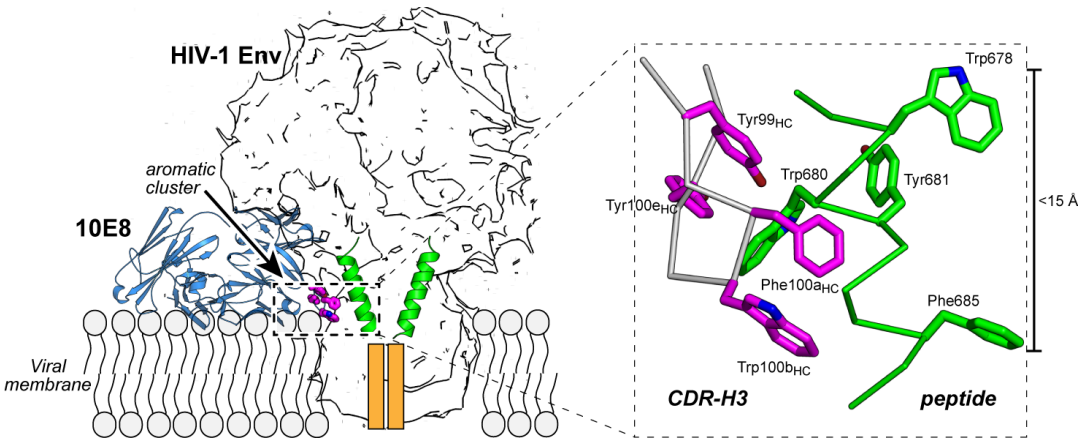

FIG 44. Model for 10E8 epitope binding at the viral membrane interface. A silhouette model of the trimer of Env from Lee *et al.* (Lee et al., 2016) was employed to illustrate the figure. To facilitate the understanding of the model, only two MPER epitopes (green helices) are shown. The antibody is shown in blue, and the critical aromatic cluster depicted as magenta sticks. Orange boxes represent deeper segments of the TMD. Inset: close-up view of the aromatic residue cluster stabilizing the MPER-N-TMD helix at the membrane interface. Residues contributed by Fab and gp41 are depicted in magenta and green, respectively.

We conclude that high-affinity binding to the 10E8 epitope at the membrane interface requires engagement with the N-terminal core-epitope residues, and establishment of a firm grip along the full MPER-N-TMD helix, including the interaction between Trp100b$_{HC}$ and TMD residues, Ile686 and Met687. Assuming that a recently reported trimeric structure might represent the organization of the TMD in the native Env (Dev et al., 2016), full achievement of that interaction implies that the 10E8 antibody engages the epitope after rotation and uplifting of the TMD helix. Thus, the stringent dependence on the aromatic nature of the Trp100b$_{HC}$ residue for biological activity might be due to the fact that, to establish an effective grip, the CDR-H3 apex must submerge in the membrane interface (McDonald and Fleming, 2016), and establish at the deepest level tight contacts with the C terminus of the MPER-N-TMD helix surrounded by membrane phospholipids. Holding the helices in the uplifted position observed in the 10E8-bound form of the Env trimer (Lee et al., 2016) would be energetically favored by the network of interfacial aromatic residues that are contributed upon binding by both the Fab and the MPER-N-TMD helix (FIG 44, inset). We speculate that the stabilization of monomeric helices in this state might be incompatible with the progression of

Env-mediated fusion explaining, at least in part, the mechanism by which 10E8 blocks viral fusion.

In summary, the model proposes that, for effective neutralization, the antibody must combine the specific binding to MPER residues transiently exposed to solvent at the membrane surface, with establishment of downstream interactions with the TMD at the deepest levels of the membrane interface. We propose that vaccines incorporating membrane-stabilized, MPER-N-TMD helix structures, bearing the range of (i) orientations, (ii) depths of penetration and (iii) angles suggested by the model, will more effectively elicit 10E8-like antibodies.

5.5. SUPLEMENTARY DATA

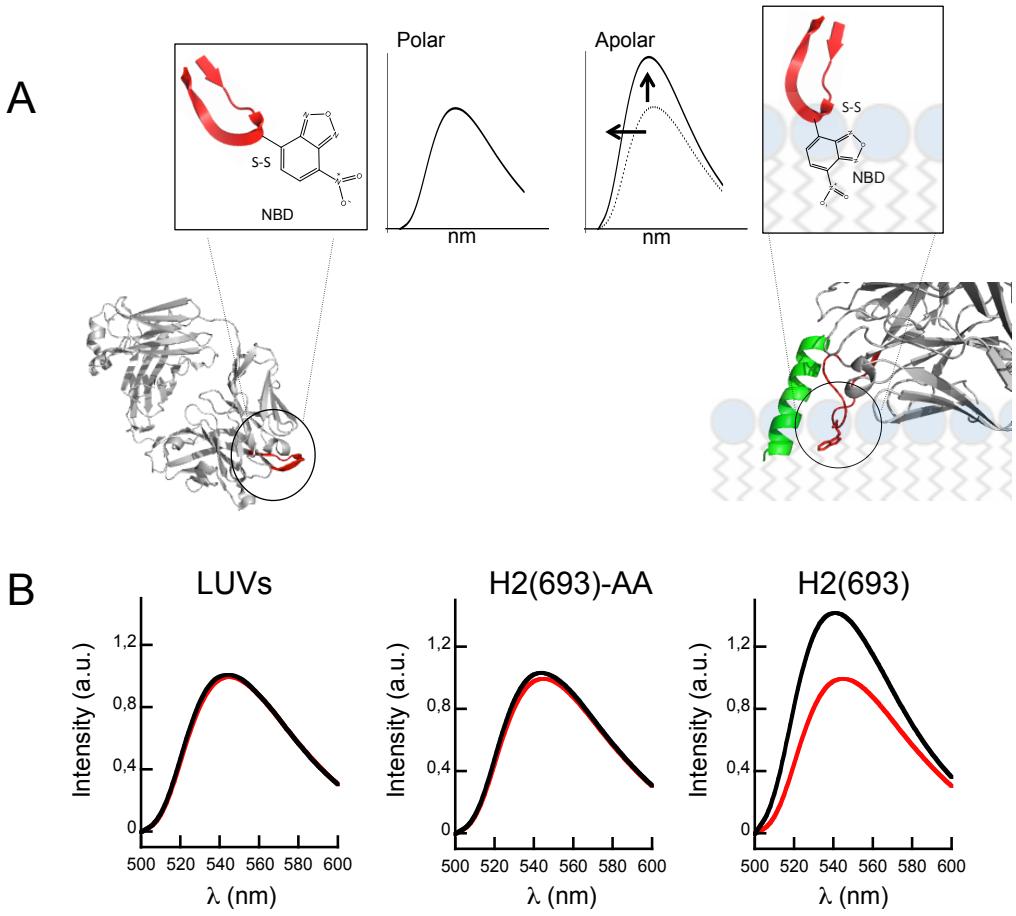

FIG S1. Membrane penetration of NBD covalently attached to 10E8 Fab. A) Strategy of labeling and spectroscopic properties of the NBD-Fab in solution or upon membrane insertion. B) Emission spectra of the labeled 10E8 NBD-Fab (0.5 μM) obtained in presence of bare liposomes (left), liposomes containing H(693)-AA (center) or liposomes containing H(693) (right). Lipid and peptide concentrations were 250 and 6,8 μM respectively. In H(693)-AA sequence key epitope residues Trp672/Phe673 were substituted by Ala. Red traces correspond to spectra obtained in solution with maximum emission normalized to 1. Peptides H2(686) and H2(693) correspond to $MPER_{(671-686)}$ and $MPER_{(671-693)}$, respectively.

Table S4. Data collection and refinement statistics (molecular replacement)[a,b]

	10E8 + $MPER_{(664-690)}$
Data collection	
Space group	I 2 2 2
Cell dimensions	
a, *b*, *c* (Å)	66.6, 81.2, 254.2
a, b, g (°)	90.0, 90.0, 90.0
Resolution (Å)	52.4 - 2.40 (2.49 - 2.40)
R_{merge}	4.6 (20.2)
I / s*I*	34.0 (8.0)
Completeness (%)	90.0 (56.2)
Redundancy	9.7 (7.0)
Refinement	
Resolution (Å)	52.4 – 2.40
No. reflections	24,462
R_{work} / R_{free}	19.2 / 23.4
No. atoms	
Protein	3,360
Peptide	201
Ligand/ion	35
Water	132
B-factors	
Protein	40.0
Peptide	59.5
Ligand/ion	30.0
Water	48.2
R.m.s. deviations	
Bond lengths (Å)	0.011
Bond angles (°)	1.3

[a]Data obtained from a single crystal.
[b]Values in parentheses are for highest-resolution shell.

Table S5. Hydrogen-bond connectivity between 10E8 and two distinct peptides.

		$MPER_{(664-690)}$	**$MPER_{(656-683)}$**
Peptide	**10E8**	**Distance (Å)**	
Trp670	H-Glu53	-	2.8
Trp672	H-Glu53	3.0	3.1[a]
Trp672	H-Pro100G	2.8	2.9
Lys683[b]	H-Phe100A	3.0	3.0
Lys683[b]	H-Gly100D	2.7	2.9

Table S6. Interaction surface of the LC of 10E8 Fab with two distinct peptides.

	$MPER_{(664-690)}$	**$MPER_{(656-683)}$**
Residue	**BSA (Å^2)**	
L-Arg91	15.7	16.3
L-Arg95B	69.3	49.9
Subtotal	*85.0*	*66.3*
Pep-Asn671	1.5	-
Pep-Trp672	10.4	10.9
Pep-Phe673	63.7	54.6
Pep-677	1.0	-
Subtotal	*76.6*	*65.4*
Total	**161.6**	**131.7**

Table S7. Interaction surface of the HC of 10E8 Fab with two distinct peptides.

	$MPER_{(664-690)}$	$MPER_{(656-683)}$
Residue	**BSA (Å^2)**	
H-Asp28	-	14.4
H-Asn31	16.6	33.2
H-Trp33	27.3	29.2
H-Arg50	7.9	5.9
H-Thr52	4.9	4.6
H-Pro52B	29.9	23.8
H-Gly52C	52.8	58.5
H-Glu53	59.0	59.7
H-Ser56	9.5	7.1
H-Asp58	3.6	6.9
H-Lys97	53.2	46.1
H-Tyr98	3.1	4.1
H-Tyr99	80.1	81.4
H-Phe100A	98.4	80.1
H-Trp100B	63.2	32.2
H-Ser100C	1.4	5.1
H-Gly100D	16.7	16.2
H-Tyr100E	32.0	25.3
H-Pro100F	67.7	65.5
H-Pro100G	63.6	62.1
H-Gly100H	-	0.1
H-Glu100I	0.6	1.4
H-Glu100J	4.5	5.3
Subtotal	*695.8*	*668.3*
Pep-Leu-661	-	1.8
Pep-Asp664	-	0.2
Pep-Lys665	-	22.0
Pep-Ser668	-	53.9
Pep-Leu669	67.4	28.2
Pep-Trp670	41.4	11.7
Pep-Asn671	27.8	34.3
Pep-Trp672	129.3	134.2
Pep-Phe673	84.4	94.1
Pep-Thr676	49.2	48.4
Pep-Asn677	17.0	19.6
Pep-Leu679	51.0	46.2
Pep-Trp680	66.1	64.3
Pep-Ile682	6.0	15.0
Pep-Lys683[a]	84.0	106.8
Pep-Ile686	29.8	-
Pep-Met687	19.6	-
Subtotal	*672.9*	*680.5*
Total	**1368.7**	**1348.8**

[a]This residue is a Arg in the structure of 10E8 with $MPER_{(664-690)}$.

Chapter 6

DUAL ROLE OF THE APEX OF THE CDR-H3 OF 4E10 FAB IN BINDING TO MPER AT THE MEMBRANE INTERFACE

6.1. INTRODUCTION

The bNAb 4E10 antibody targets the highly conserved vulnerability MPER site on gp41 and it is classified among the HIV antibodies with the highest neutralization breadth described so far (Binley et al., 2004; Kwong and Mascola, 2012). Previous research has shown that hydrophobic and aromatic residues belonging to the apex of the CDR-H3 of 4E10 are essential for viral neutralization (Alam et al., 2009; Apellaniz et al., 2014b; Scherer et al., 2010). Despite the direct implication of the CDR-H3 apex in the neutralization potency exerted by the 4E10 antibody, the crystal structures of the peptide-Fab complexes revealed that the CDR-H3 apex remains solvent-exposed and oriented in a direction opposite to the location of the bound peptide (Bird et al., 2014; Cardoso et al., 2007; Cardoso et al., 2005; Irimia et al., 2016). In contrast, the crystal structure of the functionally similar antibody 10E8 revealed that the apex of the CDR-H3 sits along the helical peptide placing the $Trp100b_{HC}$ at the apex, into close contact with the TMD (Huang et al., 2012). This conformation allows the establishment of the non-covalent interactions between the $Trp100b_{HC}$ at the apex of the CDR-H3 and the gp41 TMD N-terminus described in the previous chapter. Interestingly, those interactions can explain the correlation that is observed between the binding strength of 10E8 to the epitope and the intensity of the neutralization response by the antibody.

The unusual length and hydrophobicity of the CDR-H3s shared by both antibodies suggest however that a mechanism similar to the one described for 10E8 could operate for 4E10. In the latter case, membrane insertion and subsequent interaction with gp41 TMD would imply the reorientation of the CDR-H3 apex with respect to the position observed in crystals of Fab-peptide complexes. Supporting this possibility a recent crystallographic study by the group of Wilson (Irimia et al., 2016) indicates that the presence of lipids might trigger a conformational change of the CDR-H3 of 4E10. Hence, the 4E10 CDR-H3 could undergo a conformational change to insert into the viral membrane,

placing the apex in the vicinity of the gp41 TMD, and enabling the full engagement of the MPER/TMD epitope by the antibody.

Herein we sought to (i) test the hypothesis that the CDR-H3 of 4E10 reorients upon interaction with membranes, and (ii) to establish the importance of this conformation for the neutralization potency of the antibody. With that aim in mind, we monitored the position of the two Trp residues, at positions 100_{HC} and $100b_{HC}$, upon membrane binding by replacing each of them with the polarity reporter probe NBD. In addition, proximity of each Trp to the TMD of gp41 was assessed using the photo-active amino acid *p*BPA. From these experiments, we inferred the relative position of the Trp residues at the apex of the CDR-H3 with respect to the MPER/TMD region when inserted into the membrane.

Our results demonstrate that both Trp residues immerse in the membrane when the Fab partitions into vesicles. Moreover, it is revealed that the CDR-H3 deploys $Trp100b_{HC,}$ but not $Trp100_{HC,}$ in the immediate vicinity of the TM region of gp41 suggesting that only one strand of the loop sits on the MPER/TMD helix. The specific roles of these hydrophobic residues were further supported by the absence of correlation between membrane binding and neutralization observed for a set of mutants that were designed to modify the hydrophobicity, the length, and the order of the residues of the apex of the CDR-H3.

Collectively, the data suggest that the apex of the CDR-H3 loop plays a dual role during viral neutralization by (i) promoting association to the membrane and (ii) stabilizing the antibody-epitope complex in a membrane environment. The efficient antibody neutralization is dependent on both Trp residues. A stable 4E10-MPER/TMD interaction, occurring through one single strand of the CDR-H3 loop, requires simultaneous interactions with membrane lipids. This is in contrast to the 10E8 antibody whose CDR-H3 loop embraces the MPER/TMD helix using both strands of the CDR-H3 (see chapter 5). These findings suggest specificities for the mechanism of viral neutralization by 4E10,

inspiring the design of novel vaccines capable of inducing antibodies with a 4E10-like neutralization breadth.

6.2. MATERIALS AND METHODS

6.2.1. Materials

The peptides used in the structural and biophysical studies were synthesized as described in 3.2.1. Vector and antibodies were obtained as indicated in 5.2.1.

6.2.2. Production and characterization of Fab-s.

Experimental procedures described in 3.2.2 and 4.2.2 were followed for the mutation, expression and purification of Fab-s. ITC and DSC measurements were carried out as described in 3.2.3 and 4.2.5, respectively. Antibody binding to empty VL (DOPC:DOPE:DOPS:SM:Chol) (14:16:7:16:47 mole ratio) LUVs and to POPC: Chol (1:1) membrane embedded-$MPER_{(671-693)}$ was carried out as described in 3.2.4. Photo cross-linking and NBD fluorescence assays were performed as described in 5.2.4 and 5.2.5, respectively. LUVs used for fluorescence measurements in the presence of $MPER_{(671-693)}$ was carried out in the absence of Chol rendering to the following LUV composition; DOPC:DOPE:DOPS:SM (27:29:14:30 mole ratio) due to the fusogenic activity of the peptide in liposomes enriched in cholesterol (Apellaniz et al., 2014b).

6.2.3. Crystallization and data collection of 4E10 Fab mutant Npro in complex with $MPER_{(671-683)}$ peptide.

Crystals of the complex between Npro Fab (3 mg L^{-1}) and the peptide $MPER_{(671-683)}$ added at a molar ratio of ~1:1.3 (Fab:peptide) were grown in a

solution of 100 mM NaAc pH 5, 34 % PEG 4000, 225 mM NH_4Ac at 18 °C. A single protein crystal cryoprotected with 10 % glycerol was harvested and stored in liquid nitrogen until data collection at the synchrotron. Diffraction data from a single crystal was collected on beamline BL13-XALOC of the ALBA Cell Synchrotron (Barcelona, Spain) under cryogenic conditions (100 K). Diffraction images were further processed as described in 3.2.6 using the coordinates of recombinant WT Fab described in chapter 3. Data collection and refinement statistics are summarized in Table 10.

6.2.4. Cell entry inhibition

For the cell infection inhibition assays (Julien et al., 2010; Serrano et al., 2014), HIV-1 pseudoviruses were produced by transfection of human kidney HEK293T cells with the full-length env clone JR-CSF (kindly provided by Jamie K. Scott and Naveed Gulzar, Simon Fraser University, BC, Canada) using calcium phosphate. Cells were co-transfected with vectors pWXLP-GFP and pCMV8.91, encoding a GFP and an env-deficient HIV-1 genome, respectively (provided by Patricia Villace, CSIC, Madrid). After 24 h, the medium was replaced with Optimem-Glutamax II (Invitrogen Ltd, Paisley, UK) without serum. Three days after transfection, the PsV particles were harvested, passed through 0.45 µm pore sterile filters (Millex® HV, Millipore NV, Brussels, Belgium) and finally concentrated by ultracentrifugation in a sucrose gradient. Neutralization was determined using TZM-bl target cells (AIDS Research and Reference Reagent Program, Division of AIDS, NIAID, NIH, contributed by J. Kappes). Samples were set up in duplicate in 96-well plates, and incubated for 1.5 h at 37 °C with a 10-15 % tissue culture infectious dose of PsV. After antibody-Psv co-incubation, 11,000 target cells were added in the presence of 30 µg/mL DEAE-dextran (Sigma-Aldrich, St-Louis, MO). Neutralization levels after 72 hours were inferred from the reduction in the number of GFP-positive cells as determined by flow cytometry using a BD FACSCalibur Flow Cytometer (Becton Dickinson Immunocytometry Systems, Mountain View, CA).

6.3. RESULTS

6.3.1. The two Trp residues of the apex of the CDR-H3 loop insert into membranes.

Previous mutational studies have demonstrated the critical importance of the two Trp residues at the apex of the CDR-H3 of 4E10 for the neutralization of the virus (Alam et al., 2009; Scherer et al., 2010). It has been suggested, but not rigorously demonstrated, that these residues insert into membranes. Liposome flotation assays displayed in FIG 45A illustrate conditions for the membrane interaction of the 4E10 Fab with membranes. In those assays, liposome-Fab complexes formed both in the absence (top) and in the presence (bottom) of epitope peptide.

A previous study had suggested that the apex undergoes a conformational change in the presence of lipids (FIG 45B), but it was unclear whether the apex would insert deeply into the membrane or not. We further employed a molecular sensor introduced at the position of each Trp (100_{HC} and $100b_{HC}$) to monitor the insertion of each residue into the membrane. Each Trp was mutated to a Cys residue and covalently linked to a NBD molecule by a disulfide bond. The resulting NBD-labeled Fab-s were used to determine their interaction with the membrane by monitoring changes in the fluorescence of the NBD moiety. In particular, a shift of the maximum of emission to a shorter wavelength is suggestive of transfer of the NBD moiety from a high to a low polarity environment such as that of the hydrophobic environment of the membrane. This change is generally accompanied by an increase of the intensity of fluorescence. Incubation of each of the NBD-Fab-s just described above with increasing concentrations of virus-like (VL) LUVs resulted in an increment of the NBD-fluorescence intensity and a displacement of the maximum of emission from 543 nm to 539 nm consistent with immersion of the NBD moiety of each construct in the bilayer (FIG 45C).

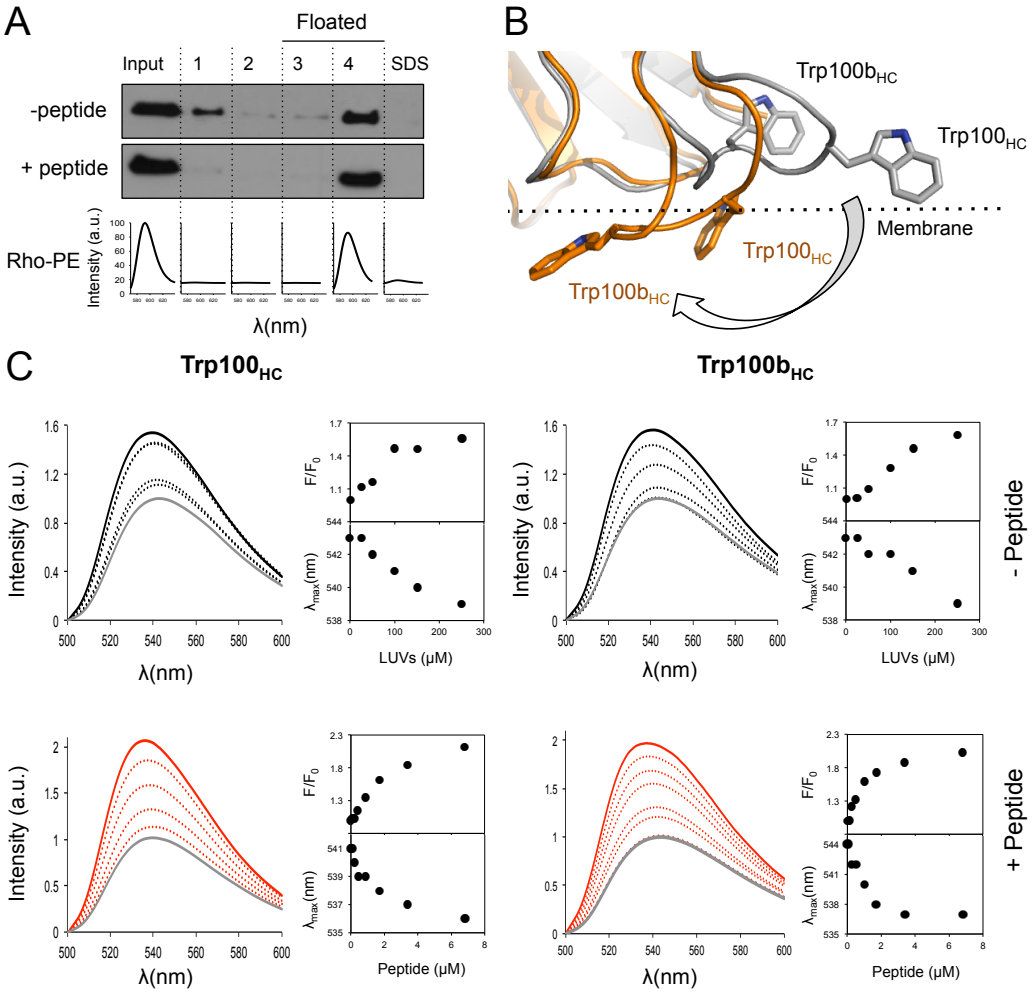

FIG 45. Membrane insertion of positions 100$_{HC}$ and 100b$_{HC}$ of the CDR-H3 of 4E10. A) Membrane partitioning of 4E10 Fab into LUVs in the absence (top) and presence (bottom) of MPER$_{(671-693)}$ in a sucrose gradient. Location of the LUVs in the third and fourth fractions (i.e., floated fractions) was detected from the Rho-PE emission (bottom panel) and the presence of Fab-s in the different fractions probed in WB. B) Cartoon representation of the putative CDR-H3 movement resulting from the Fab interaction with membrane. Superimposed structures of the 4E10 Fab in complex with MPER$_{(671-683)}$ (PDB entry 2FX7) and in complex with the lipid PA (6:0) (PDB entry 4XBG) are depicted in gray and orange, respectively. Residues Trp100$_{HC}$ and Trp100b$_{HC}$ are shown in stick representation and the approximate position of the surface of the membrane indicated by the dotted line (inferred from the position of bound lipids, not shown). C) Fluorescence emission spectra of Fab-s labeled at positions 100$_{HC}$ or 100b$_{HC}$ with NBD. Top panels: Emission spectra of NBD were measured after incubation of NBD-Fab in solution (gray traces) or in the presence of increasing concentrations of VL vesicles (black traces). Bottom panels: Emission spectra of NBD-Fab labeled after incubation with liposomes devoid of peptide (gray traces) or containing increasing amounts of peptide MPER$_{(671-693)}$ (red traces). For each set of spectra the right-side plots display the relative changes of fluorescence (top) and the position of the wavelength at the maximum intensity (bottom). The initial fluorescence (F_0) was determined from the maximum intensity of the spectrum of NBD-Fab in buffer (top panels, gray traces) or that of NBD-Fab in the presence of bare liposomes (lower panels, gray traces). The values of fluorescence (F) were obtained after the addition of LUV (top panels, black traces), or of LUV-peptide complexes (bottom panels, red traces), respectively.

The emission of fluorescence of the NBD moiety also increased upon incubation of the NBD-labeled Fab-s with liposomes containing increasing concentrations of the $MPER_{(671-690)}$ peptide. This is a clear evidence that the antibody is recognizing the liposome-embedded epitope at membrane interfaces (FIG 45C). Interestingly, the changes of fluorescence (wavelength and intensity) of the NBD moiety upon interaction with bare vesicles or with peptide-liposome complexes were remarkably similar in the two positions examined. This observation suggested that the two Trp residues occupying these positions in the WT antibody would insert in the membrane to a similar extent (FIG 45C).

6.3.2. Estimation of the proximity of each Trp residue of the apex to MPER under different environments.

In chapter 5 we have identified, for the first time, non-covalent interactions between the CDR-H3 tip of a broad neutralizing antibody and residues of gp41 fully embedded in the membrane (downstream of Lys683) resulting in the strengthening of the binding affinity for the peptide and increasing its neutralization potency. Taking into account that the Trp residues at the apex of the CDR-H3 of 4E10 penetrate into the lipid membrane, we hypothesized that the tip of the CDR-H3 may also interact with residues of MPER-TMD after the conformational change proposed in FIG 45B, optimizing the antibody interaction with the epitope in a membrane environment (FIG 46A).

In order to verify this hypothesis, photo cross-linking experiments with a genetically encoded photoreactive non-natural amino acid were conducted (FIG 46). Positions 100_{HC} and $100b_{HC}$ of the CDR-H3 were substituted with the photoreactive amino acid p-benzoylphenylalanine (*p*BPA). The resulting Fab mutants were irradiated with UV-light in the presence of peptides of various lengths including peptides that encompassed the MPER/TMD sequence. When the photoreactive amino acid *p*BPA occupied the position $100b_{HC}$ of the Fab, an SDS-PAGE gel revealed an additional band of higher molecular weight

corresponding to the Fab-peptide adduct. This band resulted from the formation of a covalent bond between the *p*BPA moiety and residues of the peptide but was absent when *p*BPA was introduced in the position of $Trp100_{HC}$ (FIG 46B). Importantly, the same photo-crosslinking pattern (positive crosslinking when *p*BPA was introduced at position $100b_{HC}$, but not at position 100_{HC}) was observed in the presence of lipid membranes (FIG 46B). This latter observation suggests that the $Trp100b_{HC}$ of the WT Fab locates in the immediate vicinity of the gp41 TMD in the viral membrane.

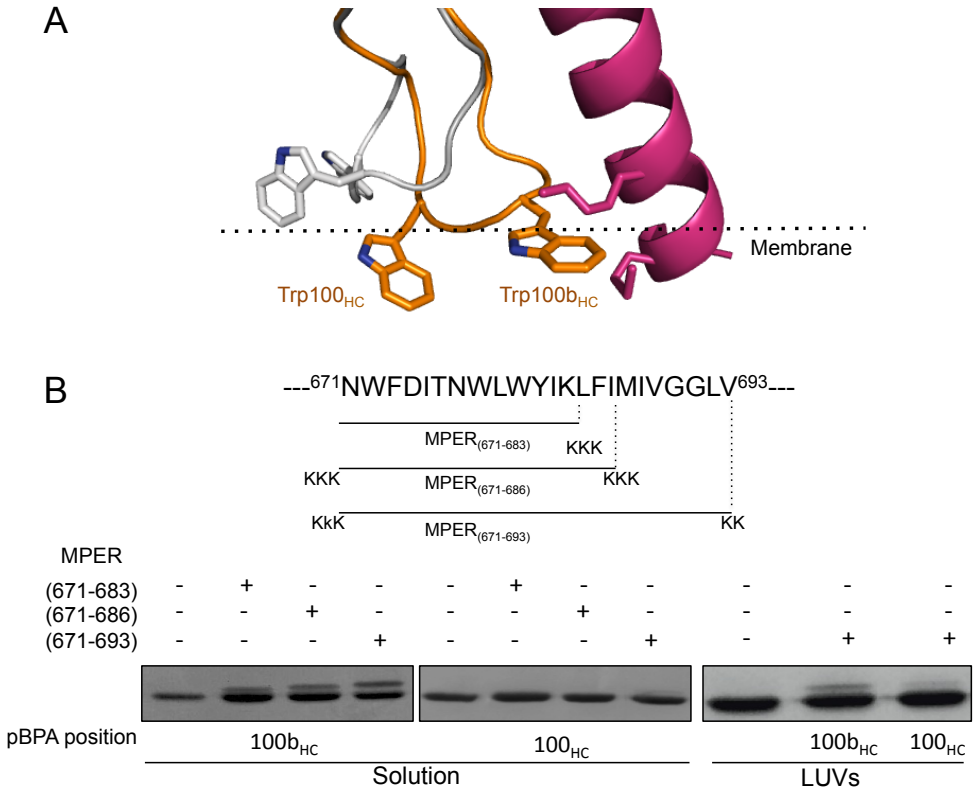

FIG 46. Binding of 4E10 Fab to $MPER_{(671-683)}$ peptide. A) To illustrate the conformational change of the CDR-H3 loop, Fab structures in previous **FIG 45**A have been rotated. In addition the relative position of the bound peptide is shown. The long peptide was modeled by superposing the $MPER_{(671-683)}$ peptide co-crystallized with the 4E10 Fab (PDB entry 2FX7) and the $MPER_{(664-690)}$ peptide bound to 10E8 Fab (Chapter 5). B) Photo cross-linking between 4E10 Fab labeled with *p*BPA at position 100_{HC} or $100b_{HC}$, and MPER peptides spanning part of the TMD. The experiment was carried out in the presence of DPC (solution), or POPC:Chol LUVs.

6.3.3. Design of CDR-H3 apex mutants to evaluate interactions with MPER/TMD.

In order to determine the functional relevance of the two Trp residues of the apex without mutating them, we elongated the CDR-H3 loop. Thus, with the idea of separately repositioning each Trp100b$_{HC}$ and Trp100$_{HC}$, we constructed two different CDR-H3 mutants in which either the N-terminal side or the C-terminal side of the apex was shifted by introducing two Pro residues (FIG 47A). Specifically two proline residues were inserted between Gly100c$_{HC}$ and Lys100d$_{HC}$, or between Thr98$_{HC}$ and Gly99$_{HC}$, to render two mutants termed Cpro or Npro, respectively (FIG 47A). Based on the recent crystal structure of 4E10 in complex with micelles of PA (6:0) (Irimia et al., 2016), the Trp100b$_{HC}$ residue in the mutant Npro would remain in a similar position to that in WT Fab and therefore in close proximity to the peptide. In contrast, in Cpro the residue Trp100b$_{HC}$ is expected to shift its position with respect to the peptide (FIG 47A). In principle, the opposite behavior is expected for Trp100$_{HC}$, i.e., shifted in Npro and unaltered in Cpro.

We first verified that the mutations were not detrimental to the stability of the antibodies (Table 9). Second, we employed X-ray crystallography to determine the position of the CDR-H3 apex. Despite the high-resolution achieved (1.48 Å) the position of the Trp100b$_{HC}$ in Npro could not be confirmed because this region was disordered in the crystal (FIG 47B and Table 10). Except for this region, the structure of the Fab was essentially indistinguishable to that of WT Fab (rmsd = 0.13 Å). No crystal of Cpro was obtained. In principle, Npro and Cpro retained the same CDR-H3 loop hydrophobicity. Accordingly, both mutants interacted to the same extent with lipid vesicles (FIG 47C). In those experiments, the mutant Δloop resulting from the ablation of the CDR-H3 apex (Apellaniz et al., 2014b) was used as negative control of membrane binding (bottom panel). Thus, Npro and Cpro displayed equal capacities for partitioning into membranes, which otherwise were comparable to that of the WT antibody (FIG 45A).

Table 9. Thermal stability, inhibition potency and thermodynamic parameters of binding of peptide $MPER_{664-690}$ to 4E10_WT and mutants in the presence of DPC.

4E10 Antibody	T_M (ºC)	ΔT_M (ºC)	*HXB2* IC_{50}[a]	*JRCSF* IC_{50}[a]	K_D (nM)	$\Delta H°$ (kcal mol^{-1})	$-T\Delta S°$ (kcal mol^{-1})[b]	n[c]
WT	69.8	n.a.	0.21 ± 0.02	1.3±0.1	4.6 ± 1.5	-15.1 ± 0.2	3.7	1.0 ± 0.1
Npro	68.6	1	0.30 ± 0.08	6.5 ± 1.6	6.2 ± 1.3	-12.8 ± 0.1	1.6	1.1 ± 0.1
Cpro	67.5	2.3	6.4 ± 1.4	17 ± 4	6.9 ± 1.5	-15.2 ± 0.2	4.0	1.0 ± 0.1

a *(µg/mL)*
b Temperature was 25 °C.
c n refers to the molar ratio peptide/protein.

Table 10. Data collection and refinement statistics (molecular replacement)[a,b]

	4E10 mutated
Data collection	
Space group	C2
Cell dimensions	
a, *b*, *c* (Å)	157.5, 44.5, 85.1
α, β, γ (°)	90.0, 113.7, 90.0
Resolution (Å)	22.3 – 1.49 (1.57 – 1.49)
R_{merge} (%)	8.1 (20.2)
$I / \sigma I$	11.9 (2.4)
Completeness (%)	99.5 (99.5)
Redundancy	6.0 (5.8)
Refinement	
Resolution (Å)	22.3 – 1.49
No. reflections	88,093
R_{work} / R_{free}	17.6 / 20.3
No. atoms	
Protein	3,328
Peptide	138
Ligand/ion	13
Water	329
B-factors	
Protein	17.4
Peptide	25.2
Ligand/ion	22.5
Water	25.7
R.m.s. deviations	
Bond lengths (Å)	0.013
Bond angles (°)	1.5

[a]Data obtained from a single crystal.
[b]Values in parentheses are for the highest-resolution shell.

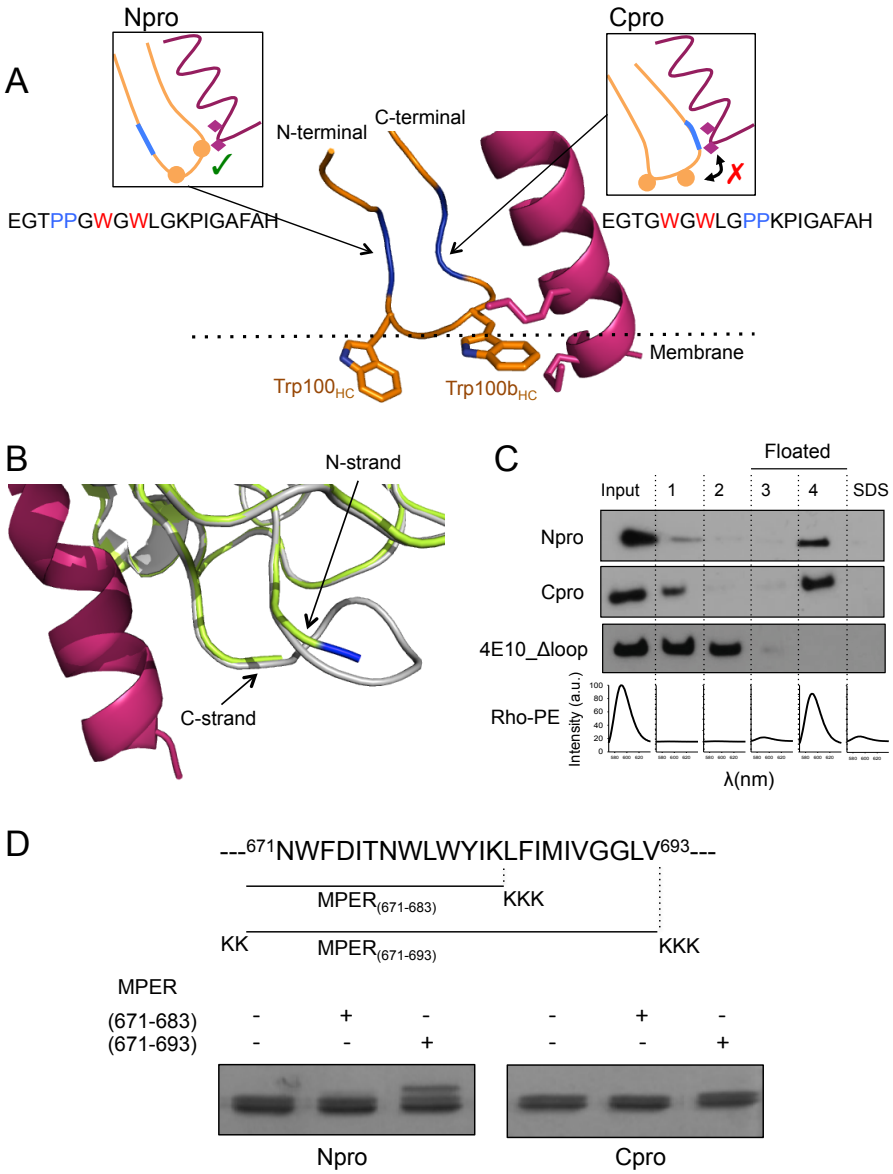

FIG 47. Design and properties of 4E10 Fab-s with extended CDR-H3 loops. A) Schematic representation. Cpro was generated by the introduction of two prolines between Gly100c$_{HC}$ and Lys100d$_{HC}$ (in blue) resulting in the predictable displacement of Trp100b$_{HC}$ away from the peptide in WT Fab. The mutant Npro was prepared by introducing two prolines between residues Thr98$_{HC}$ and Gly99$_{HC}$ (also in blue). B) Superposition of the crystal structure of 4E10_WT (gray) (PDB entry 2FX7) and Npro (green) bound to MPER$_{(671-683)}$ (dark pink). One of the proline residues introduced in the apex was observed in the structure. Other residues of the apex (PGWGWL) were disordered. C) Flotation assay to assess membrane partitioning of Npro and Cpro mutants to VL vesicles. Location of the liposomes and Fab-s was detected from the Rho-PE emission (bottom panels) and by WB analysis, respectively. D) Photo cross-linking experiment of Npro and Cpro mutants, each modified with *p*BPA at position 100b$_{HC}$, with MPER peptides of different lengths in the presence of DPC. Ablation of the CDR-H3 apex yielded a construct that we termed Δloop (Apellaniz et al., 2014b) that was used as a negative control of membrane binding.

Photo cross-linking experiments in which Trp100b$_{HC}$ was replaced by *p*BPA, confirmed the proximity of this position of the apex to MPER in the bound state of Npro, but not in that of Cpro (FIG 47D). The displacement of the photoreactive *p*BPA in the Cpro variant resulted in the inability of the Fab to form a covalent adduct with the peptide, indicating that *p*BPA does no longer remain near the peptide in this mutant (FIG 47D). On the contrary, the mutant Npro displayed the same photo-crosslinking pattern as that of WT Fab (FIG 46B and 47D).

6.3.4. Functional characterization of 4E10 Fab-s with extended CDR-H3 loops.

The previous results are consistent with the design presented in FIG 47A, thereby allowing the specific assessment of the importance of the Trp100b$_{HC}$ TMD interaction for the neutralizing activity of 4E10. Thus, the effects of Npro and Cpro mutations were subsequently tested in cell entry assays (FIG 48 and Table 9). The Npro mutant was almost indistinguishable from the WT in assays based on a sensitive HXB2 strain, while the IC_{50} of the Cpro mutant increased 20 fold. In the more resistant JRCSF strain the differences were not so marked, but Cpro was still deficient in viral inhibition. Thus, despite the similar capacities for interacting with membranes, the Cpro mutant did not interact with TMD through Trp100b$_{HC}$ and displayed weaker biological activity in comparison with Npro.

To determine if weaker binding to epitope was at the origin of this phenomenon we carried out ITC experiments. Titration of WT, Npro and Cpro antibodies with MPER$_{(664-690)}$ in the presence of DPC revealed that the three Fab-s engaged the peptide with nearly identical affinity (K_D values were 4.6, 6,2 and 6.9 nM for WT, Npro and Cpro, respectively) (FIG 49A and Table 9). Moreover, no significant differences in the relative contribution of the enthalpy and entropy to the binding free energy to the peptide were observed (Table 9).

We next investigated the impact of these mutations (Npro and Cpro) in the binding to the epitope presented in an environment that better mimics the viral membrane (FIG 49B). To that purpose, and prior to each assay, the MPER was anchored to liposomes through the N terminus of the TMD. The binding of the Fab to the anchored MPER was estimated from the relative abundance of antibody co-floating with the vesicles (fractions 3 and 4) as detected by western-blot in a flotation assay.

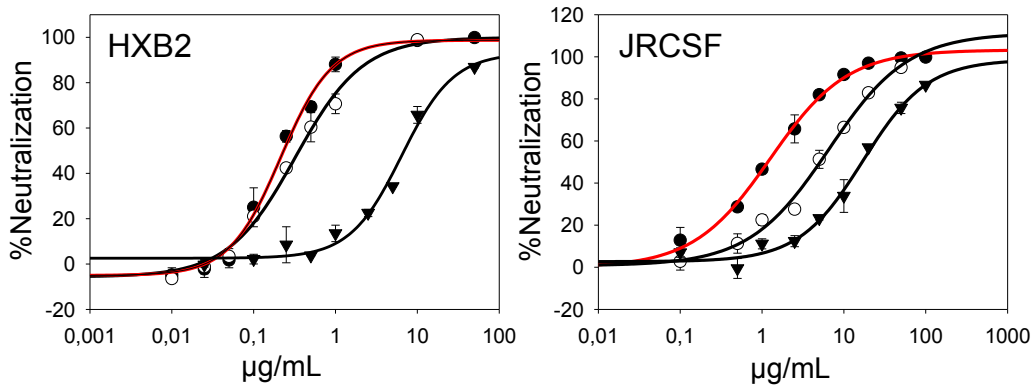

FIG 48. Functional characterization of 4E10 Fab-s with extended CDR-H3 loops. Neutralization potency of 4E10 WT (filled circles, red line) Npro (empty circles) and Cpro (filled triangles) against PsV HXB2 (top panel) and JRCSF (bottom panel).

Efficient binding of the Fab to the peptide inserted into the membrane was achieved with WT 4E10 and with Npro Fab, as demonstrated by the high abundance of these two antibodies in the fractions co-floating with the liposomes. In contrast, a significant fraction of the Cpro mutant was observed in the dense fractions suggesting a defect in binding of this mutant to the membrane-inserted peptide (FIG 49B). Under these experimental conditions the position $100b_{HC}$ of the *p*BPA-Npro mutant remains in close proximity to the peptide in a lipid membrane similarly to the WT 4E10 Fab. This conclusion is deduced from the additional band corresponding to cross-linked adduct in the SDS-PAGE of the sample containing the *p*BPA-Npro mutant pre-incubated with peptide-vesicles complexes (FIG 49C). In combination, these results suggest

that the assay carried out in solution did not capture all the complexity of the binding events that must occur in the environment of the viral membrane.

In conclusion, results displayed in FIG 48 and 49 indicated that preserving the position of Trp100b$_{HC}$ in close proximity to the MPER/TMD region is not only critical for the neutralization potency of the antibody, but also for epitope binding in a membrane context.

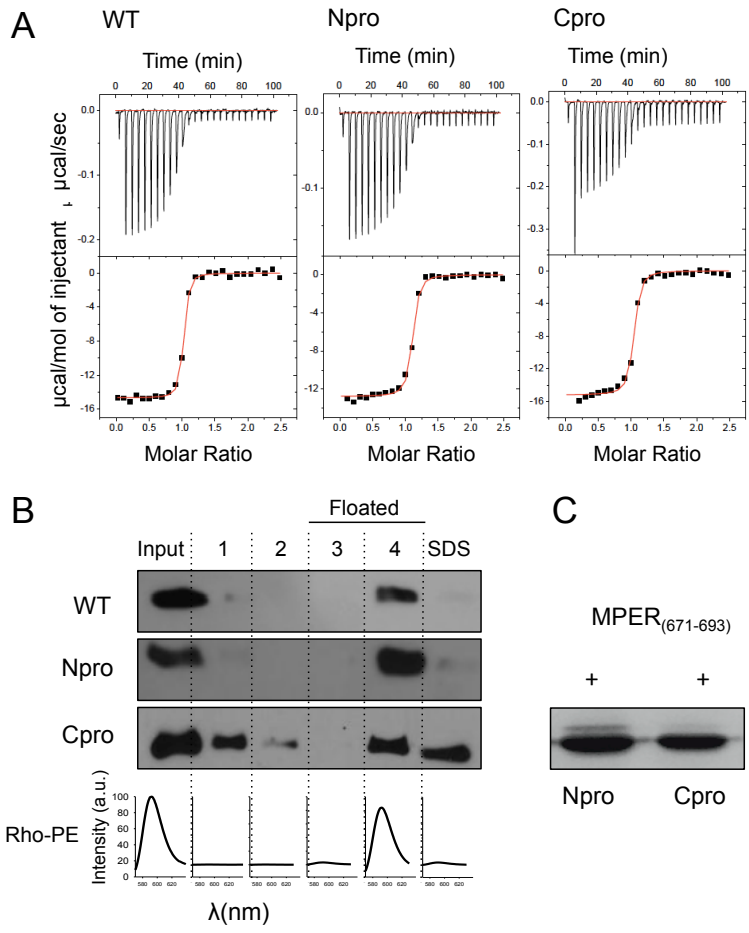

FIG 49. Epitope binding by 4E10 Fab-s with extended CDR-H3 loops. A) Binding isotherm of MPER$_{(664-690)}$ to 4E10 WT, Npro, and Cpro in the presence of DPC. B) Epitope recognition in the presence of lipid membranes. Flotation experiment was carried out to evaluate the binding of 4E10 WT and the CDR-H3 elongated mutants (Npro and Cpro) to VL membranes or to the epitope MPER$_{(671-693)}$ anchored to POPC:Chol LUVs. C) Photo cross-linking of Trp100b$_{HC}$ of Npro and Cpro mutant Fab-s with the MPER$_{(671-693)}$ peptide under the same conditions as the flotation assay in panel B.

6.3.5. Effect of the interfacial hydrophobicity of the CDR-H3 apex on membrane binding and neutralization potency of the 4E10 bNAb.

The interaction of 4E10 with membranes through the CDR-H3 has been proposed as the element governing the neutralization potency of the antibody. However we have identified direct interactions between Trp100b$_{HC}$ and the peptide that strengthen their affinity when the epitope is embedded in the membrane, increasing viral inhibition. Hence, CDR-H3 hydrophobicity appears not to be the only property influencing the neutralization potency of the antibody. Specifically, the CDR-H3 apex hydrophobicity in Npro and Cpro mutants remains unchanged with respect to the WT, enabling them partitioning into membranes to comparable extents (FIG 47C), but only the former displays a comparable neutralizing activity (FIG 48).

To obtain additional insights into the correlation between the hydrophobicity of the CDR-H3 apex, membrane binding and neutralization potency, we generated several versions of 4E10 Fab differing in the composition and sequence order of the residues comprising the apex of the CDR-H3 loop (i.e. WGWL) listed in FIG 50A. Thus, interfacial hydrophobicity of this region was altered by i) mutating one (W100$_{HC}$C, or W100b$_{HC}$C) or both (W100$_{HC}$Y/W100b$_{HC}$Y, or W100$_{HC}$D/W100b$_{HC}$D) Trp residues of the loop with residues of different hydrophobicity; ii) substitution of the residue L100c$_{HC}$ of the CDR-H3 apex with a Trp residue to render the 3W mutant that displays an increased interfacial hydrophobicity, and (iii) swapping the apex with the functional CDR-H3 apex (LFGV) of the anti-MPER antibody 2F5. The “LFGV” region of the antibody 2F5 has an active role in mediating lipid binding and antibody neutralization of 2F5 without binding to MPER (Julien et al., 2010) in a similar manner as that proposed for the 4E10 antibody. In addition, 4E10 Fab mutants that conserved the hydrophobicity but differed in other aspects of the CDR-H3 were also prepared. These included mutants with unchanged amino acid composition but scrambled sequences (Scr-1; Scr-2; Scr-3) and the previously analyzed Npro and Cpro mutants containing longer CDR-H3 loops.

The ability of the mutated Fab-s to bind to the membrane was assessed by vesicle flotation and WB, whereas the hydrophobicity of the resulting sequences were calculated using the Wimley and White (WW) hydrophobicity-at-interface scale (FIG 50B) (Wimley and White, 1996). When the value of the ΔG_{iwu} (free energy of transfer from bilayer interface to water, also termed free energy of partitioning) of the CDR-H3 apex was decreased below the level of the WT antibody (<4.2 kcal/mol), it resulted in a severe defect of membrane binding for most of the mutations evaluated (FIG 50B). Lower values of ΔG_{iwu} also translated into a diminished capacity of the antibody to block the entry of the virus into the cell (FIG 50B and C). Interestingly, although the mutants W100C and W100bC displayed the same hydrophobicity, they displayed a different membrane binding profile. Removal of the interfacial Trp amino acid at position $100b_{HC}$ resulted in the loss of antibody partitioning into lipid membranes revealing that the magnitude of the hydrophobicity of the apex is not the only factor governing the binding of the antibody to the lipid membrane.

As expected, we observed a broad spectrum of neutralization responses among antibodies sharing sequences of constant hydrophobicity (FIG 50B and C). Fab 4E10 WT, Scr-1, Scr-2 and Scr3, sharing exactly the same residue composition but different sequence order at the CDR-H3 apex, displayed different neutralization capacities. This result suggested an important role for each residue of the apex in a sequence-dependent manner, in addition to their contribution to the overall hydrophobicity of the loop. Increasing the number of Trp residues in the apex enhanced the binding to the liposomes, as expected from the greater hydrophobicity, but did not increase the neutralization response (FIG 50B and C). Based on these results, it is suggested that, although not sufficient, a minimum hydrophobicity in the CDR-H3 is required to exert some viral neutralization, since 4E10 Fab mutants with reduced hydrophobicity (ΔG_{iwu} < 1 kcal/mol) are expected to have a very poor neutralization competence (IC_{50} > 100 μg/mL) (extracted from FIG 50C).

A

Fab Name	CDR-H3 sequence
3W	EGTTGWGWWGKPIGAFAH
WT	EGTTGWGWLGKPIGAFAH
Scr-1	EGTTGLGWWGKPIGAFAH
Scr-2	EGTTGGWWLGKPIGAFAH
Scr-3-	EGTTGWWGLGKPIGAFAH
Npro	TTPPGWGWLGKPIGAFAH
Cpro	EGTTGWGWLGPPKPIGAF
W/Y-W/Y	EGTTGYGYLGKPIGAFAH
2F5loop	EGTTGLFGVGKPIGAFAH
W_{100}/C	EGTTGCGWLGKPIGAFAH
W_{100b}/C	EGTTGWGCLGKPIGAFAH
W/D-W/D	EGTTGDGDLGKPIGAFAH

B

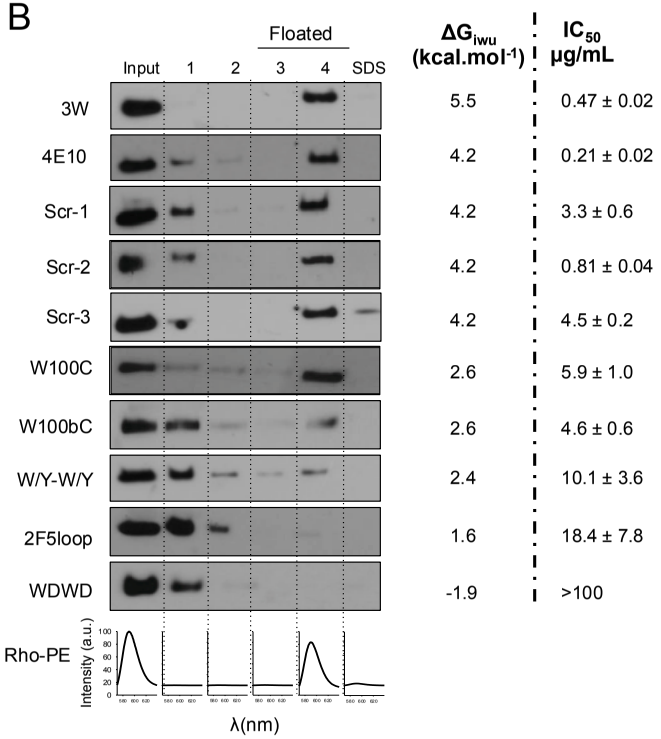

C

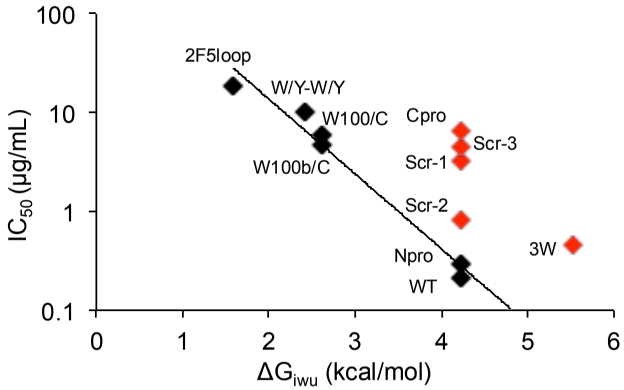

FIG 50. Sequence-dependent properties of 4E10. A) Sequences of the CDR-H3 loops in 4E10 mutants. Residues modified in the apex of the CDR-H3 (apex is defined as residues WGWL) are indicated in red while the amino acids introduced within the CDR-H3 loop are shown in blue. Positions 100 and 100b occupied by Trp residues in the WT antibody are highlighted in bold. B) Binding to VL liposomes, hydrophobicity-at-interface, and neutralization potency against HXB2 PsV, of the Fab variants. C) Hydrophobicity (ΔG_{iwu}, kcal/mol) vs. viral neutralization potency (IC50, µg/mL) is plotted for each mutant Fab. Black symbols were adjusted to a non-linear exponential regression with a R^2 value of 0.9722

6.4. DISCUSSION

Mutational studies demonstrate that the hydrophobic and aromatic residues at the apex of the CDR-H3 of anti-MPER antibodies are essential for viral neutralization (Alam et al., 2009; Apellaniz et al., 2014b; Huang et al., 2012; Julien et al., 2010; Scherer et al., 2010). Concretely, Trp residues at positions 100_{HC} and $100b_{HC}$ are required for the biological activity of the bNAb 4E10. Despite their importance, the location of those residues when the antibody binds MPER in a membrane context is unknown. In this regard, knowledge on the neutralization-competent structure adopted by the CDR-H3 apex could help elucidate the molecular mechanism by which 4E10 blocks the virus.

Comparison of the crystal structures of the 4E10 antibody in the unbound and the bound forms reveals a reduction of the B-factors of the regions encompassing the CDRs H1 (^{25}SGGSFSTYAL^{34}), H2 (^{50}GVIPLLTITNYA^{60}), H3 (^{95}EGTTGWGWLGKPIGAFAH^{102}), and L3 (^{89}QQYGQSLST^{97}) as a consequence of peptide binding (see chapter 4). Even though the residues at the apex Trp100_{HC}−Leu$100c_{HC}$ slightly decrease their b-factors, they remain highly dynamic suggesting their predisposition to establish further interactions, for example, in the context of the viral membrane. However, the CDR-H3 apex projects away from the bound helical peptide and, therefore, establishment of membrane interactions imply the reorientation of that stretch of the loop. In agreement with this idea, we have formally shown that both Trp residues of the CDR-H3 apex interact with the lipid membrane (FIG 45). Hence, we propose that the affinity for the membrane interface of the two Trp residues provides the driving force for the structural reorientation of the CDR-H3 loop towards the lipid, as inferred from the recent crystallographic structure of 4E10 co-crystallized with micelles of the lipid PA (6:0) (Irimia et al., 2016).

We also demonstrate that the Trp residues at the apex of the CDR-H3 play a role beyond promoting lipid membrane interaction. Thus, by incorporating

a genetically encoded photo-activable amino acid, we show that Trp100b$_{HC}$ efficiently engages with MPER/TMD and that such interaction is critical for the neutralization potency of the antibody (FIG 46-48). In contrast, direct interaction between Trp100$_{HC}$ and the peptide was not observed in the photo cross-linking assays. This difference suggests that both Trp residues do not contribute equally to the biological function of the antibody. Hence, Trp100$_{HC}$ must contribute to the overall activity of the antibody by stabilizing the antibody-peptide complex in a more indirect manner.

The biological relevance of the position of the Trp100b$_{HC}$ to mediate additional interactions with the TMD was further emphasized by results obtained using an engineered mutant where the position of Trp100b$_{HC}$ was shifted. The displacement of Trp100b$_{HC}$ had a deleterious effect on the ability of the antibody to interact with the MPER/TMD region, neutralize PsVs, and efficiently engage the epitope when embedded in the membrane. However, the value of the affinity constant (K_D) of 4E10 to MPER peptide solubilized with the detergent DPC was unaltered. These results clearly indicate that binding in solution does not completely capture the complex process of neutralization occurring at the constrained environment of the viral membrane. To mimic that complexity, we employed a more elaborated assay in which the peptide is pre-immobilized in the surface of liposomes. Results of these experiments correlated with the biological activity more accurately.

The discrepancy between the experiments performed in solution and in lipid membranes can be explained as follows. In solution, the highly flexible CDR-H3 undergoes a large oscillation from a closed (PDB entry 2FX7) to an open conformation (PDB entry 4XBG), transiently placing the Trp100b$_{HC}$ of the apex near the peptide. Hence, the otherwise weak Trp100b$_{HC}$-MPER interaction in solution can be captured by the photo cross-linking assay without reflecting a gain of enthalpy and binding affinity. On the contrary, in the presence of the membrane, the hydrophobicity of the two Trp residues would shift this equilibrium towards the closed conformation, where the CDR-H3 is positioned

close to the TMD inside the lipid membrane. Rigidifying the conformation of the CDR-H3 inside the membrane would restrict the mobility of Trp100b$_{HC}$ thus intensifying the interaction with the N-terminus of the TMD. Consequently, specific interactions involving Trp100b$_{HC}$ with this region of gp41 might occur in a manner analogous to that of the 10E8 antibody (see chapter 5).

The data presented herein further suggest that in the presence of a lipid membrane, Trp100b$_{HC}$–MPER/TMD interactions are stabilized by the surrounding lipids, decreasing the dissociation rate constant (k_{off}) of the peptide-lipid-antibody complex. It is likely that full stabilization of such complex would require the presence of Trp100$_{HC}$. Interaction of Trp100$_{HC}$ with surrounding lipids in a way previously suggested by Irimia *et al* (Irimia et al., 2016) with the simultaneous interaction of the Trp100b$_{HC}$ reported here with the TMD (FIG 51) could represent the neutralization competent conformation adopted by the apex of the CDR-H3. We speculate that the resulting gp41-antibody-lipid complex involving both CDR-H3 Trp residues would efficiently zip the contact surface between the antibody and gp41 interrupting MPER conformational changes during the fusion process and, ultimately, preventing viral infection.

Supporting additional, more specific, roles for the CDR-H3 aromatic residues, we also show that, although necessary, hydrophobicity is not sufficient to trigger the neutralization levels of the parental antibody. In particular, shuffling the residues of the apex region of the CDR-H3 of 4E10, while keeping a constant hydrophobicity, (or even increasing the hydrophobicity by the incorporation of an additional Trp residue) resulted in lower neutralization potency. These observations highlight the importance of preserving the specific amino acid sequence of the apex to exert its biological function, a requirement most likely arising from the adoption of a particular neutralization competent conformation.

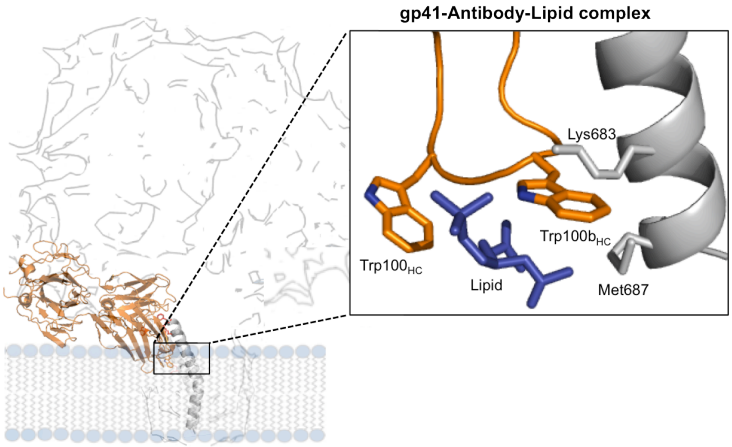

FIG 51. Model of the gp41-4E10 antibody-lipid complex. 4E10 antibody is shown in orange, the MPER/TMD region in gray and the lipid molecule in blue. Inset: close-up view of the gp41-4E10 antibody-lipid complex showing interaction of Trp100b$_{HC}$ with residues M687 and I686 of the TMD. A lipid molecule located in between both Trp residues of the CDR-H3 acts as additional glue for enhancing the stability of the complex. PDB entry 4XBG and the MPER$_{(664-690)}$ peptide bound to Fab 10E8 from chapter 5 was used to build the model.

In summary, we report the dual role of the two Trp residues of the apex of the CDR-H3 of 4E10, and specially that of Trp100b$_{HC}$, for the recognition of gp41 at the membrane interface, and for its neutralization potency. This work contributes to (i) clarify the molecular basis by which the 4E10 antibody exerts effective neutralization, and (ii) to guide future formulations to design and to develop an efficient vaccine against HIV infection based on anti-MPER antibodies.

Chapter 7

CONTRIBUTION OF PERIPHERAL MEMBRANE INTERACTIONS TO MPER HELICAL EPITOPE RECOGNITION AND INFECTION BLOCKING BY 4E10

7.1. INTRODUCTION

The bNAb 4E10 displays an extreme breadth of HIV-1 neutralization (98 % of viruses blocked in standard infectivity tests (Binley et al., 2004; Huang et al., 2012; Zwick et al., 2001)) and thus constitutes a model system for structure-guided vaccine design and immunotherapeutics (Huang et al., 2012; Kim et al., 2014; Klein et al., 2013b; Montero et al., 2008). This bNAb targets an epitope on the gp41 subunit: the section at the base of the MPER helix in contact with the viral membrane interface. Since the viral membrane takes part in the stabilization of the MPER helix, it is amply assumed that antibodies targeting this MPER-membrane site are polyspecific, showing capacity to bind lipid moieties (Chen et al., 2014; Irimia et al., 2016; Matyas et al., 2009; Sanchez-Martinez et al., 2006a). In fact, some researchers consider these antibodies as generally auto-reactive, and postulate that their natural production is limited by B-cell tolerance mechanisms (Doyle-Cooper et al., 2013; Haynes et al., 2005; Verkoczy et al., 2014).

Experimental evidence suggesting that 4E10 binds to phospholipids, particularly anionic species as phosphatidylserine (PS), cardiolipin (CL) or phosphatidylinositol (PI), has been obtained in several laboratories during the last decade (Finton et al., 2013; Haynes et al., 2005; Matyas et al., 2009; Sanchez-Martinez et al., 2006b). A binding pocket was proposed to exist within the 4E10 paratope to accommodate the polar head groups of PS or CL (Finton et al., 2013). According to this proposal, the 4E10 paratope with lipid bound would differ structurally from the paratope with peptide epitope bound. This concept has been challenged by us and by recent reports showing the crystal structures of the unbound Fab forms and Fab-lipid complexes (Bird et al., 2014; Irimia et al., 2016) (see also chapter 4). Co-crystals obtained in the presence of phosphatidic acid (PA), phosphatidylglycerol (PG), and glycerol phosphate reveal two binding sites on the surface of 4E10 paratope that approaches the membrane, which involve residues of the heavy-chain complementarity determining region 1 (CDR-H1) (Irimia et al., 2016). This crystallographic

analysis is also consistent with the simultaneous accommodation of the phospholipid head-group moieties and bound peptide epitope within the 4E10 paratope, and underscores the role of the hydrophobic CDR-H3 in establishing interactions with the lipid tails.

Here, we have attempted to discern the specific roles played by membrane lipids in the 4E10 neutralization mechanism. To that end, we have run liposome-flotation assays (physical separation), which have been subsequently complemented with spectroscopic titration assays using Fab-s labeled with the polarity-sensitive probe NBD. Direct partitioning of the 4E10 antibody from the aqueous phase into membranes was driven by the favorable electrostatic interactions between the membrane and paratope surfaces. In contrast, electrostatic forces were not required to trigger the process of binding to peptide epitope when anchored to the membrane. However, it is worth noting that electrostatic forces, were in general beneficial for binding to the epitope-anchored peptide, and that these favorable interactions correlated with the neutralizing activity of the 4E10 antibody. Collectively, our observations support the view that favorable, albeit unspecific, interactions between 4E10 and lipids play a central role in the neutralization mechanism by 4E10. The implications of these findings for the natural production and biological function of this antibody are discussed.

7.2. MATERIALS AND METHODS

7.2.1. Materials

The peptides used in the structural and biophysical studies were synthesized as described in 3.2.1. Expression vector and antibodies were obtained as indicated in 5.2.1.

7.2.2. Fab-s production and characterization.

Experimental procedures described in 3.2.2 and 4.2.2 were followed for the mutation, expression and purification of Fab-s. ITC, flotation, NBD fluorescence, photo cross-linking and cell entry inhibition measurements were carried out as described in section 3.2.3, 3.2.4, 5.2.5, 5.2.4 and 6.2.4, respectively.

7.3. RESULTS

7.3.1. Partitioning of 4E10 into membranes depends on anionic phospholipids.

We first determined the partitioning of the 4E10 antibody into membranes using a vesicle flotation assay. Initial experiments were aimed at establishing the contribution of each lipid present in the VL mixture, mimicking the viral envelope composition (FIG 52A) (Huarte et al., 2016). A major fraction of the input antibody was recovered from the upper fractions, co-floating with the VL vesicles. Subtraction from the VL mixture of individual zwitterionic phospholipids (sphingomyelin (SM), or phosphatidylethanolamine (PE)), or cholesterol (Chol) did not abolish membrane binding. However, removal of the anionic phosphatidylserine (PS) prevented 4E10 to bind to the liposomes. To determine if binding is specific for PS, or is a more general electrostatic effect, we replaced PS with other anionic phospholipid species (i.e. PG, PI, PA or CL). The result shown in FIG 52B clearly shows that binding of 4E10 to liposomes is restored for all anionic compositions tested.

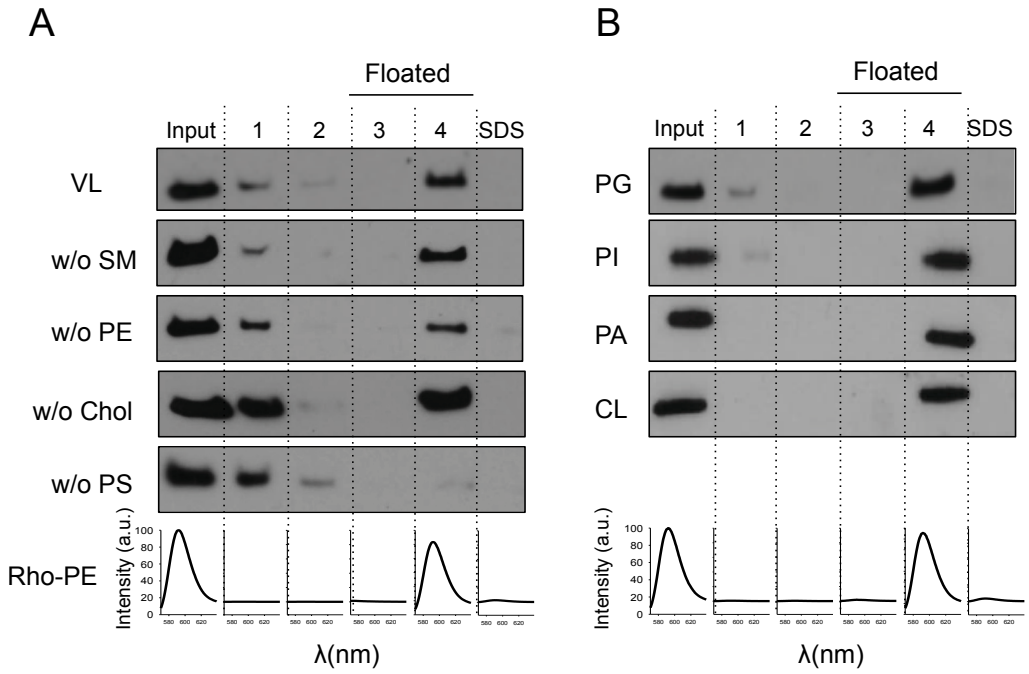

FIG 52. Partitioning of the anti-MPER 4E10 Fab into membranes. A) Effect of the constituent lipids of the VL mixture on 4E10 membrane partitioning in a sucrose gradient. Lipid vesicles pre-incubated with the Fab were subject to centrifugation. Based on their different densities, the sample was divided into four different fractions. An additional fraction employing SDS was collected, representing the material attached to the surface of the tube. Location of the liposomes in the third and fourth fractions (i.e., floating fractions) was detected from the Rho-PE emission (bottom panels). The presence of Fab was probed by WB**.** B) Effect of replacing PS by other anionic phospholipids; PG, PI, PA or CL.

7.3.2. Basic residues of the paratope promote partitioning into the membrane.

The previous flotation experiments suggest that electrostatic interactions with anionic phospholipids promote the partitioning of 4E10 into membranes. Inspection of the surface of the paratope in contact with the membrane interface reveals a positively charged region close to the binding site of the antibody (Irimia et al., 2016) (FIG 53A). Thus, we sought to elucidate the relevance of this region for the electrostatic interaction with the membrane. We designed two Fab mutants substituting separately the basic residues $Arg73_{HC}$ or $Lys100e_{HC}$ by Glu (R73E and K100eE mutants, respectively, FIG 53A). We assumed that such charge-reversing substitutions reduced the overall positive net charge at

the base of the antibody making it less prone to interact electrostatically with negatively charged membranes. In addition, the analysis included a negative control designated as BS, in which Ser-to-Ala mutations at positions 28 and 30 of the CDR-H1 were prepared. These substitutions did not appreciably alter the surface charge of the paratope, even if involving residues located in a recently described lipid-binding site (Irimia et al., 2016).

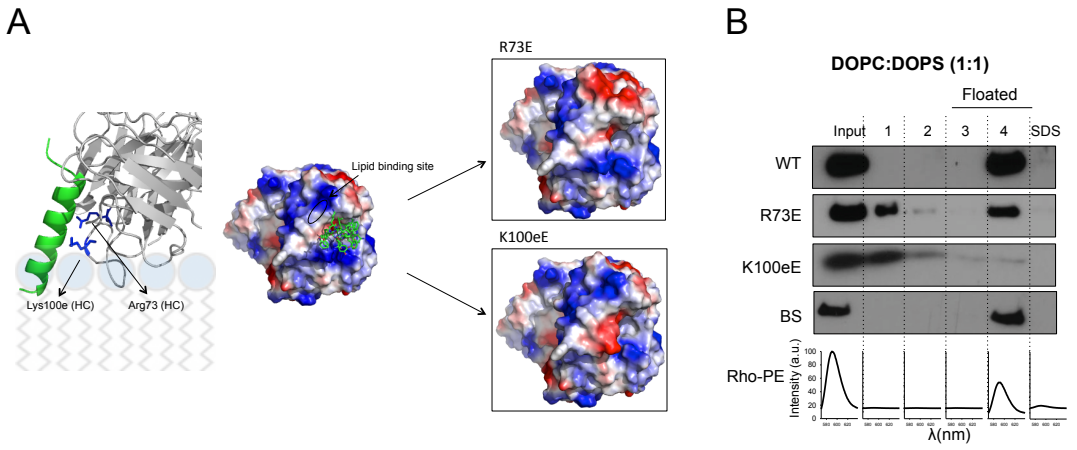

FIG 53. Design of 4E10 variants with exposed basic residues of the paratope mutated. A) Effect of R73E and K100eE substitutions on the surface charge of the paratope. B) Membrane partitioning as measured by flotation assays using vesicles containing 50 mol % of anionic lipid (PS). BS stands for a negative control with a double Ser-to-Ala substitution at positions 28 and 30 of the heavy chain.

FIG 53B illustrates the membrane-binding phenotypic traits resulting from the mutations. To make a more robust comparison, these assays employed membranes containing high levels of PS (PC:PS 1:1, mole ratio). As expected, intensifying the electrostatic interaction promoted association of all input WT antibody with LUVs (see below). In contrast, association of R73E to vesicles was reduced by approximately 50 %. Consistent with an even weaker partitioning in membranes, the K100eE mutant was barely recovered in the floating fractions containing the vesicles. The negative BS control reproduced the behavior of the WT antibody. We arrived at similar conclusions using VL vesicles (see below).

7.3.3. Functional characterization of the charge-reversing mutants.

We next examined the role of electrostatic forces in the biological function of the 4E10 antibody (FIG 54, 55 and Table 11). First, ITC experiments were conducted to assess the effect of the above described mutations on the affinity of 4E10 for the peptide (FIG 54A). The calculated K_D values were all in the nM range (Table 11). A significant reduction of affinity for the epitope peptide (≈20-fold) was only observed in the case of the K100eE mutant.

To examine the effect of the mutations in a membrane context, flotation experiments were next carried out comparing bare VL vesicles with VL vesicles containing the peptide (FIG 54B). In the absence of peptide, the most conspicuous effect was observed for the K100eE mutant, which again did not appreciably associate with membranes in the VL system (left panel). As compared to WT or BS, a lower level of binding to LUVs was also evident for the R73E mutant. Addition of peptide resulted in the complete association of the WT and BS antibodies with VL vesicles (FIG 54B, right panel). By comparison, although a significant increase with respect to the bare vesicles was evident, association of R73E and K100eE variants with vesicles containing peptide was still not complete.

Table 11. Thermodynamic parameters of binding of Fab 4E10 mutants to the MPER peptide and their neutralization potencies.

Antibody (4E10)	*K_D (nM)*	*ΔG° (kcal mol^{-1})*	*ΔH° (kcal mol^{-1})*	*-TΔS° (kcal mol^{-1})[a]*	*n^b*	*HXB2- IC_{50} (μg/mL)*	*JRCSF- IC_{50} (μg/mL)*
4E10_WT	4.6 ± 1.5	-11.4 ± 0.2	-15.1 ± 0.2	3.7	1.0 ± 0.1	0.21 ± 0.02	1.26 ± 0.09
BS	12.2 ± 2.5	-10.8 ± 0.1	-11.7 ± 0.1	0.9	1.3 ± 0.1	0.38 ± 0.03	1.59 ± 0.27
R73E	12.8 ± 3.5	-10.8 ± 0.1	-14.7 ± 0.2	3.9	1.1 ± 0.1	5.3 ± 0.4	13.2 ± 3.5
K100eE	91 ± 14	-9.6 ± 0.2	-10.4 ± 0.2	0.7	1.4 ± 0.1	3.3 ± 0.2	12.7 ± 4.0

[a] Temperature was 298 K.
[b] ***n*** refers to the molar ratio peptide/protein.

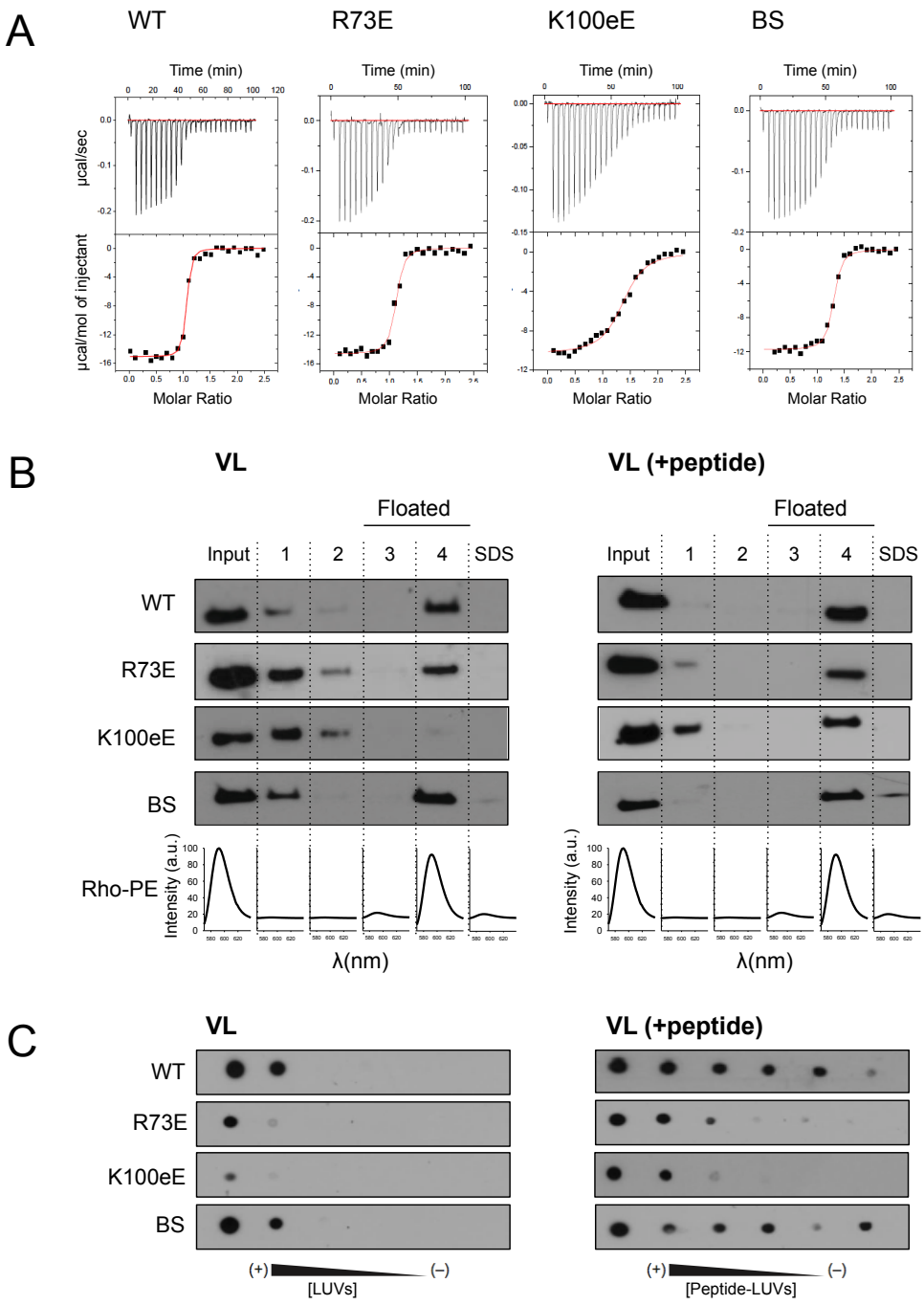

FIG 54. Functional characterization of 4E10 mutants. A) Binding isotherms of the MPER peptide epitope to Fab 4E10 examined by ITC. The upper panel indicates the heat released upon consecutive injections of 10 μL of peptide solution (40 μM) into Fab (3 μM) in the calorimeter cell, and the lower panel the integrated heats (symbols) and non-linear least-squares fit (solid line) to the data using a one site binding model with the program ORIGIN 7.0. The thermodynamic parameters of binding are displayed in Table 11. B) Flotation experiments in the presence of VL LUVs (left) or VL LUVs containing $MPER_{(671-693)}$ peptide (right). C) Recognition of VL LUVs (left) or VL LUVs containing $MPER_{(671-693)}$ peptide (right) as determined by dot blot analysis.

The previous flotation results were obtained under conditions that promote membrane partitioning (i.e., high lipid concentration). In this regard, they allow discerning high-to-moderate from low range of membrane affinities. To establish further differences in affinity, and distinguish between high and moderate affinity conditions, membrane concentration was titrated down in dot-blot assays (FIG 54C). In this approach, physical separation is attained after washing the nitrocellulose membranes, where the liposomes were previously spotted, several times to remove loosely bound Fab. For the matter of comparison, measuring conditions were initially set up to reproduce the relative binding observed in flotation assays (i.e., to match signals of the Fab-s recovered in the floating fractions). These experiments underscored the lower capacity of the charge-reversing R73E and K100eE mutants for partitioning into VL membranes, as well as their lower affinity for VL vesicles containing the epitope peptide.

To establish a correlation between biological function, binding to membrane-embedded epitope and membrane partitioning, the mutants were tested in neutralization assays (FIG 55A). The increment of the IC_{50} values as compared to the WT antibody indicated that the capacity for inhibiting PsV cell entry of both polarity-reversed mutants, R73E and K100eE, was reduced approximately by an order of magnitude (FIG 55A and Table 11). As above, the negative BS control reproduced for the most part the behavior of the WT Fab. Finally, dot-blot assays indicated that the reduced levels of infection-inhibition appeared to correlate well with lower binding of the mutant antibodies to PsV immobilized on a solid substrate (FIG 55B). Overall, these results revealed a correlation between direct binding to immobilized PsVs (FIG 55B) and direct binding to immobilized vesicles containing the epitope peptide (FIG 54C).

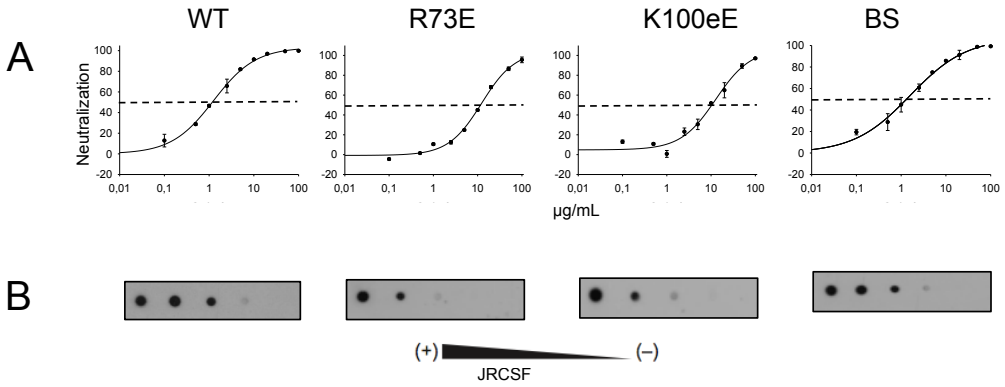

FIG 55. Neutralization profiles of the 4E10 mutants (II). A) JRCSF PsV neutralization capacity of the different mutants. B) JRCSF PsV recognition as determined by dot blot analysis. Decreasing amounts of PsV (from left to right) were spotted onto nitrocellulose membranes and probed with 4E10 Fab and its mutants.

7.3.4. Contribution of the electrostatic interactions to 4E10 partitioning into membranes.

The results displayed in FIG 52-55 and chapter 6 warrant the consideration of 4E10 interaction with membranes as a partitioning process contributed by electrostatic forces and the hydrophobic effect, respectively. Thus, this nonspecific association is more accurately described by a partition coefficient rather a binding constant which assumes the formation of Fab:lipid stoichiometric complexes. To gain insight into the relative contribution of electrostatic interactions we sought to analyze the partitioning process quantitatively by performing spectroscopic titration assays (FIG 56).

In chapters 5 and 6 we have shown that the polarity-sensitive NBD probe replacing for Trp at the position 100b of the CDR-H3 can be used to monitor Fab insertion into the membrane. FIG 56A illustrates the changes in NBD fluorescence that occur upon incubation of the labeled NBD-Fab 4E10 with increasing concentrations of VL or PC:PS lipid vesicles. In the presence of VL vesicles NDB emission shifts toward shorter wavelengths and increases in intensity (FIG 56A, leftmost panel), indicating the movement of the dye (and therefore the apex of the CDR-H3) from its original location surrounded by

solvent molecules, to a more hydrophobic environment. In line with the absence of interactions deduced from the flotation assays (FIG 52B), the fluorescence of the NBD-Fab did not change upon incubation with vesicles devoid of PS (FIG 56A, left-center panel). Changes in NBD emission were more marked when vesicles composed of PC:PS were used as model membranes instead (FIG 56A, right panels), reinforcing the idea that favorable electrostatic interactions promote 4E10 partitioning.

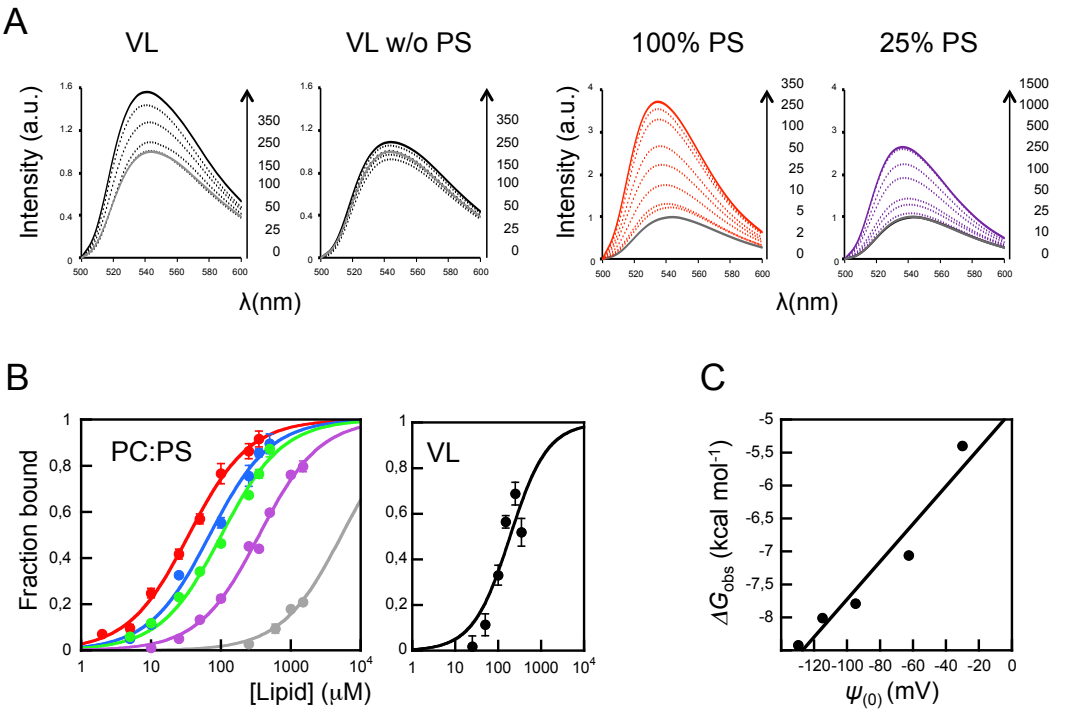

FIG 56. Binding of 4E10 to LUVs monitored by changes in NBD fluorescence. A) Changes of NBD-4E10 fluorescence in the presence of increasing concentrations of liposomal lipid as indicated in the panels. 150 nM of NBD-Fab was used. B) Titration of NBD-labeled Fab with LUVs. The fraction of Fab bound was plotted as a function of the concentration of lipid accessible (half the total lipid concentration) for vesicles containing different mol percentages of PC:PS as follows: 90:10 (gray); 75:25 (magenta); 50:50 (green); 25:75 (blue); 0:100 (red). The molar fraction partition coefficients, K_x, were calculated from the best fit of Equation 1 to the data (curves). Each symbol on the plot represents an average of three independent experiments (±S.D. if larger than symbol). C) Plot of the free energy of partitioning versus the membrane-surface potential in the previous lipid vesicles.

Titration experiments were next conducted to calculate the mole-fraction partition coefficients (K_x) with different mol percentages of monovalent acidic

phospholipid in the membrane (FIG 56B, left panel). Association with vesicles increased with the PS content, following the pattern expected from the contribution of favorable electrostatic interactions (Arbuzova et al., 1997). Plotting the observed partitioning free energy (ΔG_{obs}) versus the surface potential calculated according to standard methodologies (McLaughlin, 1989), yielded a value of ca. -5 kcal mol^{-1} for membranes lacking net charge (FIG 56C). This value indicates that, in the absence of anionic PS, a lipid concentration of *ca.* 15 mM would be required for 50 % of the Fab be bound to membrane. By comparison, the value measured for pure PS vesicle was ΔG_{obs} = - 8.8 kcal mol^{-1}. A simple calculation, reveals that lipid diluted three orders of magnitude (i.e., 17.5 μM) is sufficient to attain a similar extent of Fab binding. Interestingly, a K_x in the order of 0.6×10^6 was measured for the VL mixture (FIG 56B, right panel), which renders a ΔG_{obs} value in the range of those measured in vesicles containing 50-25 mol % of PS (FIG 56C). This suggests that in VL vesicles, besides the electrostatic attraction, additional factors favor water-membrane partitioning of the antibody.

7.3.5. Contribution of the electrostatic interactions with membrane to 4E10 epitope peptide binding

To infer how electrostatically-driven membrane partitioning contributes to epitope recognition, we conducted experiments with PC:PS vesicles-containing the epitope peptide $MPER_{(671-693)}$ (FIG 57). Consistent with previous flotation results (FIG 55), comparison of NBD emission spectra obtained upon incubation with vesicles containing 25 or 50 % of PS reveals the favorable contribution of anionic phospholipids and peptide epitope to Fab partitioning (FIG 57A). Titration curves based on those spectra allowed determination of the actual K_x values (FIG 57B). Overall, the presence of peptide resulted in an increment of the partitioning constant, the effect being more pronounced with the highest proportion of PS.

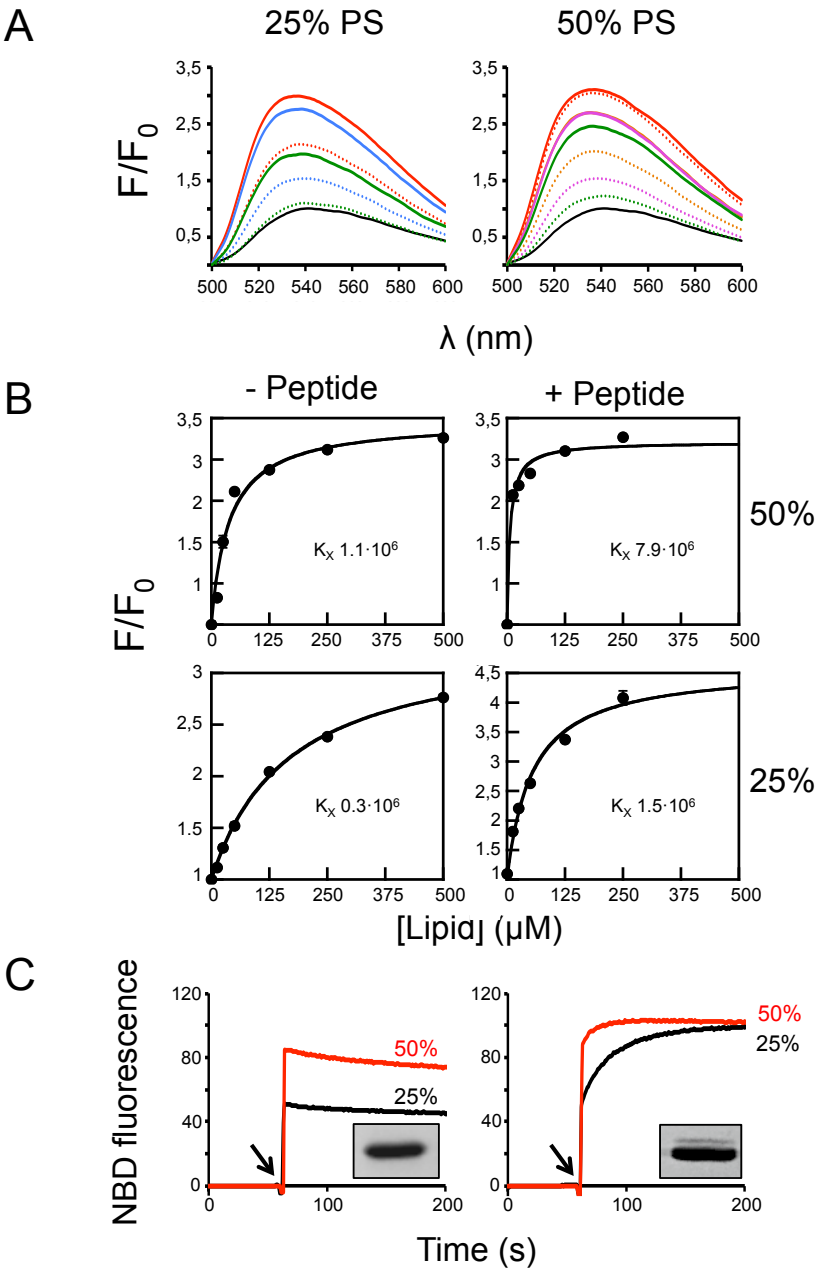

FIG 57. Effect of electrostatic interactions on epitope recognition. A) Changes of NBD-4E10 fluorescence emission spectra in the presence of increasing concentrations of vesicles (500-250-50 μM and 500-100-50-25 μM in the case of LUVs with 25 and 50 % PS, respectively), were measured in the absence (dotted lines) or in the presence of 1.7μM of $MPER_{(671-693)}$ peptide (solid lines). B) Effect of PS on promoting partitioning into vesicles with and without $MPER_{(671-693)}$ peptide. Solutions of NBD-Fab were titrated with PC:PS LUVs as indicated. Each data point is the average of three titrations (± SD) experiments as the one in the previous panel. C) Kinetics of NBD-Fab incorporation into bare vesicles containing 25 or 50 % of PS (left panel) or into the same vesicles loaded with 1.7μM $MPER_{(671-693)}$ peptide (right panel). Peptide interaction with 25 % PS vesicles was confirmed by the presence of an adduct band in a photo cross-linking assay (insets). The arrow indicates NBD-Fab addition. Lipid concentration was 100 μM.

To study in more detail the combined effect of electrostatic interactions with membrane surface and peptide recognition, we next performed a kinetic analysis. FIG 57C displays the kinetic traces of the fluorescence intensity change that occurs upon injection of NBD-Fab (arrow) into buffer containing LUVs (left panel), or buffer containing LUV-peptide complexes (right panel).

Inclusion of 25 or 50 mol % PS LUVs (top panel) resulted in a sudden increase of fluorescence intensity followed by a signal plateau, consistent with the fast process of membrane association (left panel). In contrast, upon addition of the same vesicles containing the peptide, the sudden increase was followed by a second phase, in which the fluorescence signal increased gradually, leveling off at later times (right panel). Thus, whereas the fast phase of the NBD change can be ascribed to spontaneous membrane insertion, the slower incorporation of Fab that remained in solution appears to be driven by specific peptide-recognition. Association of slow binding rates with peptide engagement was actually demonstrated by photo cross-linking experiments. To that end, the 4E10 Fab was modified with the UV-sensitive unnatural amino acid *p*BPA (Abe et al., 2012; Young et al., 2010), which was genetically encoded at position $Trp100b_{HC}$ of the antibody as previously described in chapter 6. Adduct formation was detected by SDS-PAGE only when the lipid vecicles harboring the $MPER_{(671-693)}$ peptide were subjected to UV light (FIG 57C, insets). Interestingly, the peptide-dependent slower phase observed for the 50 % mol PS LUVs (right panel, red line) was faster than that observed with 25 % mol PS. Thus, the PS appeared to have two effects. On the one hand, and as previously described, PS promoted higher levels of spontaneous incorporation. On the other hand, PS promoted faster recognition of the epitope peptide by the fraction of the unbound Fab.

Pre-attachment of 4E10 molecules to the membrane of pre-activated virions has been postulated as a mechanism favoring viral neutralization (Alam et al., 2009; Haynes et al., 2010). This two-step model assumes that the fraction of 4E10 antibody pre-bound to the membrane engages with gp41 upon

fusion activation. FIG 58 illustrates experiments performed to address the capacity of the Fab pre-bound to membrane for encountering and effectively engage the inserted epitope. To ensure that all added Fab actually bound first to membranes, we increased the lipid concentration in the assay, as well as the PS content in the vesicles. As explained in the diagram displayed in FIG 58A, under these conditions the slower process of peptide engagement can be subsequently scored by photo cross-linking assays.

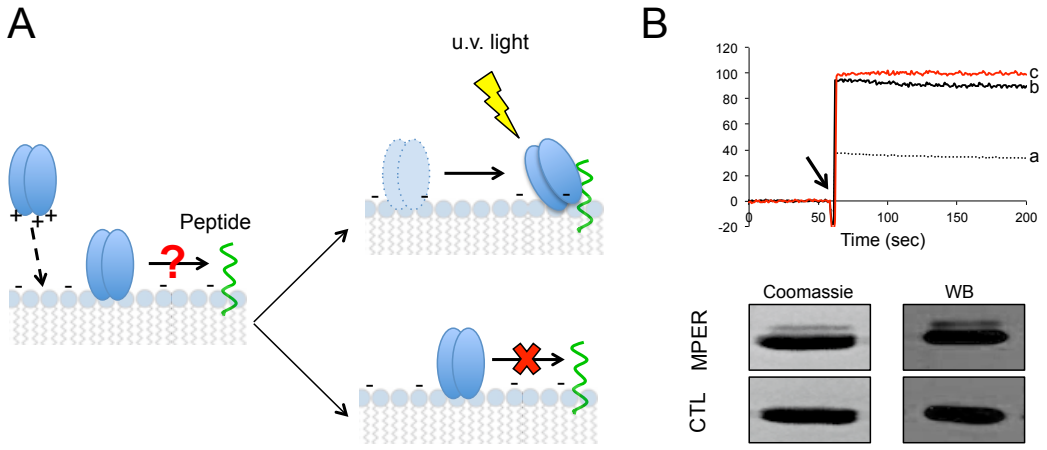

FIG 58. Epitope recognition of 4E10 antibody prebound to membrane A) Schematic representation of the assay showing the two possible events that can take place when negatively charged lipids drive fast and complete partitioning of the 4E10 antibody to the membrane surface of vesicles containing embedded epitope peptides. The upper right panel illustrates the movement of the antibody through the membrane surface until peptide encounter that results in efficient epitope engagement. The opposite situation is displayed in the lower right panel, where the 4E10 antibody remains bound to the membrane in the initial position and therefore far away from the peptide. B) Upper panel: kinetics of NBD-Fab incorporation into pure PS vesicles in the presence (red line) or absence of $MPER_{(671-693)}$ peptide (black solid line). The arrow indicates NBD-Fab addition to a sample of buffer (a), 250 μM LUVs (b) and 250 μM LUVs containing 1.7 μM $MPER_{(671-693)}$ peptide. Lower panels: Photo cross-linking experiment of Fab 4E10-*p*BPA to $MPER_{(671-693)}$ peptide inserted into 250 μM of pure PS LUVs (top). In the bottom panel, the $MPER_{(671-693)}$W672A-F673A (CTL) peptide was used as a control for spontaneous cross-linking due to antibody-peptide proximity within the membrane. Protein bands were detected by Coomassie staining or Western-blot (right and left panels, respectively).

As expected, Fab addition to vesicles composed of 100 % PS resulted in an abrupt increase of fluorescence both in the presence and in the absence of epitope peptides. The Fab-peptide complexes formed under these conditions were subjected to UV light and the formation of adducts analyzed by SDS-

PAGE and WB. An additional band corresponding to cross-linked peptide ($MPER_{(671-693)}$) and Fab HC was observed (FIG 58B, lower panel). The same cross-linking pattern was obtained when the peptide was added to pre-incubated Fab-100 % PS vesicles to assure Fab-membrane pre-binding (data not shown). However in negative control samples that contained a peptide with crucial residues for antibody binding mutated to Ala ($MPER_{(671-693)}$ /W672A-F673A) the additional band resulting from the cross-linking was absent (FIG 58B, lower panel). This control was included to assure that the signal came from specific peptide binding and discard spontaneous cross-linking arising from the high density of Fab-peptide pre-concentrated on the membrane surface.

7.4. DISCUSSION

The Env complex embodies the entry machinery of the HIV-1 and constitutes its main antigen (Karlsson Hedestam et al., 2008; Wyatt and Sodroski, 1998). The gp41 MPER is highly conserved across the different HIV-1 strains and isolates, and is functionally involved in assisting the membrane fusion process that culminates with cell infection (Apellaniz et al., 2014b; Saez-Cirion et al., 2002; Salzwedel et al., 1999). Due to its high degree of sequence conservation and the key role played by this element in the viral cycle, the bNAb 4E10 raised against the MPER exhibits an unusual neutralization breadth (Kwong and Mascola, 2012; Montero et al., 2008; Zwick, 2005). It has been hypothesized that affinity for membranes may sustain the neutralization capacity of the 4E10 antibody (Alam et al., 2009; Cardoso et al., 2005; Chen et al., 2014; Dennison et al., 2009; Finton et al., 2013; Huarte et al., 2008; Irimia et al., 2016; Matyas et al., 2009; Sanchez-Martinez et al., 2006b; Scherer et al., 2010; Sun et al., 2008). However a systematic, quantitative assessment of 4E10 partitioning into membranes, was so far lacking. Thus, a detailed examination of the process was important for two reasons: i) to establish the lipid specificity range, which allows contrasting the assumption that lipid auto-reactivity can prevent the production 4E10-like antibodies through vaccination;

and ii) to establish the contribution of membrane-assisted MPER engagement to the biological function of 4E10.

7.4.1. Functional relevance of spontaneous partitioning

Our data demonstrate that 4E10 partitioning into membranes is due to unspecific binding to negatively charged membrane surfaces promoted by basic residues exposed on the paratope, and not through the specific recognition of a particular phospholipid head-group. In this regard, 4E10 qualifies better as a peripheral membrane protein that uses electrostatic and hydrophobic forces in concert for translocating into membranes (see for reviews: (Gelb et al., 1999; McLaughlin and Aderem, 1995; Mulgrew-Nesbitt et al., 2006)). Through this work the dependence of 4E10 membrane partitioning on the electrostatic interaction has been assessed by employing two complementary approaches: i) altering the surface charge of the Fab paratope via mutagenesis (FIG 53 and 55); and ii) altering the membrane density of monovalent anionic phospholipid (FIG 56).

As expected from the unspecific nature of the interaction, mutation of basic residues to render R73E or K100eE variants hampered direct partitioning. However, albeit less potent, these mutants were still active in neutralization assays, an effect that correlated with lower binding to immobilized PsVs or VL vesicles containing peptide. Thus, although comprising a modulatory factor for the amount of membrane-bound antibody, and hence, potency, partitioning driven by electrostatic interaction was not absolutely required for the neutralizing activity of the antibody.

Results obtained altering the charge surface density of the membrane further demonstrate that the combination of electrostatic and non-polar interactions can quantitatively explain the membrane binding behavior of 4E10 (FIG 56). Contribution of both components to 4E10-membrane partitioning is qualitatively illustrated in FIG 59. To further isolate the electrostatic contribution

of the paratope surface from the contribution of the CDR-H3 hydrophobicity to membrane binding, we added to the comparison Fab-s with the H3 loop apex ablated (ΔLoop variants in FIG 59, right-most panels). The membrane binding of the WT Fab under the conditions of the flotation experiments is summarized in the left panel: predominant recovery of Fab bound to membrane in the absence of peptide (top), and full binding to VL-peptide complexes (bottom). Reducing negative charge at the paratope surface (K100eE mutant, top, center), ablates the spontaneous interaction with VL membranes, and diminishes the Fab fraction bound to VL-peptide complexes. The Fab fraction bound to VL-peptide complexes was even lower upon removal of the CDR-H3 apex (K100eE/ΔLoop mutant, top, left). When the net surface charge of the membrane is set to 0, a similar trend can be observed for the Fab WT, i.e., absence of binding to LUVs devoid of peptide, and reduction of the bound amount in the case of LUV-peptide complexes (VL w/o PS, bottom center and left panels).

All in all, these data support the spontaneous interaction of 4E10 with membranes, i.e., in the absence of peptide ligand anchored to the bilayer, and that such interaction can contribute to the more efficient recognition of the membrane-bound epitope. This is in contrast to the 10E8 interaction with membranes, which is strictly dependent on binding to the membrane-inserted epitope (chapter 5). However, the 10E8 bNAb displays higher potency than the 4E10 antibody (IC_{50} mean values of 1.93 and 0.35 μg/mL for 4E10 and 10E8, respectively) and this phenomenon occurs without exhibiting binding to anionic phospholipid (Huang et al., 2012; Kwon et al., 2016a). This important difference suggests that 4E10 and 10E8 mechanisms for engaging MPER helix at membrane interfaces and exert neutralization are essentially different (see general discussion chapter).

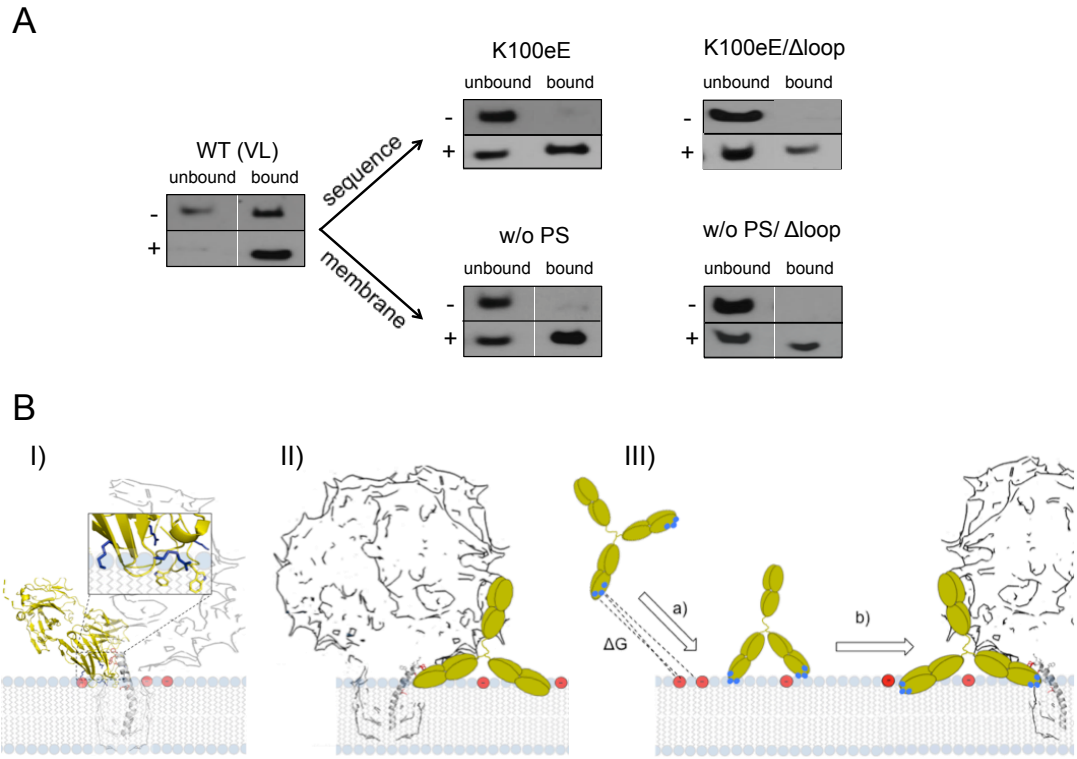

FIG 59. Summary of electrostatic/hydrophobic interactions favoring 4E10 partitioning into membranes (A) and mechanisms to explain their involvement in MPER helix engagement (B). See text for details**.**

7.4.2. Implications for the mechanism of neutralization

The peripheral membrane interaction described in this chapter may condition the mechanism of neutralization. FIG 59B illustrates the three, non-exclusive mechanisms that have been invoked to explain the role of membrane interactions in the process of neutralization by 4E10 antibody, namely:

I) Structural adaptation (FIG 59B, left panel): the insertion of helical MPER epitope onto the membrane interface imposes structural adaptations to the mechanism of recognition within the two-dimensional membrane milieu (Sanchez-Martinez et al., 2006b; Scherer et al., 2010). It has been reported that PS becomes accessible at the external leaflet of membranes in mature virions (see for a discussion on this issue: (Huarte et al., 2016)). Our data suggest that

4E10 takes the advantage of favorable electrostatic interactions with PS to enhance affinity for the membrane-bound epitope ligand (FIG 54 and 57), most likely by providing an optimal orientation of the antibody with respect to the membrane.

II) Avidity increase (FIG 59B, center): In the order of 10 Env complexes incorporate per virion, meaning that the non-immunogenic lipid component of the envelope constitutes the main structural-functional element of the HIV particle accessible from the external milieu (Zhu et al., 2006). The reduced epitope accessibility arising from the low spike density precludes bi-functional binding and has been thus regarded to as an evasion mechanism (Klein et al., 2013b). Lipid polyreactivity could sustain an increase in IgG avidity by endowing 4E10 with the capacity for directly interacting with membranes (Haynes et al., 2010; Klein et al., 2013b). Although our data support this notion, they imply that 4E10 interactions are driven by unspecific electrostatic interactions, which would be particularly intense at the high effective concentration of lipid that an unbound Fab would sense after engagement of the Env epitope by the other IgG Fab.

III) Pre-concentration in the viral membrane (FIG 59B, right): several authors have proposed a two-step mechanism for neutralization according to which 4E10 first attaches to the viral membrane (Alam et al., 2009; Haynes et al., 2010). This reversible step would be required to ensure subsequent binding to target MPER epitope, which is transiently exposed after fusion activation. Pre-attachment implies: a) sufficient free energy for driving spontaneous partitioning; and b) competence of the Fab pre-bound to membranes for subsequent specific binding of epitope ligand. Our data (FIG 56) are consistent with partitioning constants in the range of those measured for peripheral membrane proteins (Mulgrew-Nesbitt et al., 2006). Moreover, by combining fluorescence spectroscopy and photo-cross-linking assays we were able to demonstrate the specific epitope binding competence of pre-bound antibody

(FIG 58B). Thus, in principle our *in vitro* data employing model systems support the feasibility of this mechanism.

Collectively, the data support the idea that direct membrane interaction is of high relevance for the activity of the 4E10 antibody. In addition to the previously proposed mechanisms by which membrane binding contributes to 4E10-induced neutralization, our data suggest that the electrostatic component promoting membrane binding likely maximizes the efficiency of the antibody to target the pre-hairpin intermediate that emerges upon activation of the fusion process.

Chapter 8

GENERAL DISCUSSION

The high degree of conservation of the MPER together with the exceptional breadth of the antibodies that recognize this motif make the HIV-1 MPER epitope an important target for vaccination purposes. However, MPER mimotopes incorporated in different vaccine formulation formats have failed to elicit broadly neutralizing responses. In this context, the identification of the relevant Env-antibody interactions that are crucial for neutralization might provide relevant information for future vaccine design.

8.1. PROPOSED ROLES FOR THE CDR-H3 APEX OF ANTI-MPER ANTIBODIES IN THE VIRAL NEUTRALIZATION MECHANISM.

The hydrophobic and aromatic residues at the apex of the CDR-H3 loop have been proven essential for the biological function of anti-MPER antibodies. Several models have been postulated to explain the role of this element. Some proposals picture the CDR-H3 loop as an element whose only role is to confer the ability to bind membranes and, therefore, increase avidity (Klein et al., 2013b) and/or pre-concentrate the antibody in the viral membrane prior to fusion (two-step model) (Alam et al., 2009). Others suggest a more specific role of the apex of CDR-H3 in mediating viral inhibition. One of the these alternative, non-exclusive, views known as structural fixation has proposed that the residues of the apex of CDR-H3 correctly align the antibody with respect to gp41 and the viral membrane. Hence, the membrane-bound state would represent the optimal conformation for specific recognition of the epitope, with lipid interactions playing stabilizing roles in the process (Sanchez-Martinez et al., 2006a; Scherer et al., 2010).

In addition, an even more active role of the CDR-H3 has been proposed (Sun et al., 2008). According to this model, the initial attachment of the apex to the membrane facilitates the encounter with the epitope by recognition of certain exposed residues. These initial interactions, together with changes in the local environment of the peptide caused by the hydrophobic residues of

CDR-H3 would cause rotation of MPER. Reorientation of the side chains of key residues towards the antibody paratope would culminate with the extraction of the peptide from the membrane for a more complete and tight epitope binding.

To shed light on the mechanism by which 4E10 and 10E8 exert neutralization, in this thesis we sought to determine (i) the implication of the CDR-H3 loop in viral blocking (chapters 3-6) and (ii) the biological function of the membrane-binding phenomenon (chapters 5 and 7).

8.2. THE MEMBRANE TOPOLOGY OF THE MPER/TMD REGION CONDITIONS THE ANGLE OF APPROACH TO THE EPITOPE.

Information about the neutralization competent structure of the region of Env targeted by the 4E10 and 10E8 antibodies is crucial for understanding the neutralization mechanism of these antibodies. The epitopes of these two bNAbs have been initially described to contain MPER residues prior to Lys/Arg683. A model based on hydrophobicity distribution (Dennison et al., 2009; Huarte et al., 2008; Kim et al., 2013; Lorizate et al., 2006; Schibli et al., 2001; Sun et al., 2008) assumed an interfacial MPER helix inserted parallel to the membrane plane, a 90º kink at position Lys683, and the TMD inserting in perpendicular orientation with respect to the membrane plane (FIG 60, left). This model has been recently challenged by an NMR study of overlapping peptides that suggested a continuous helical structure of the MPER/TMD region that inserts into the membrane with a tilted orientation, until residue Gly690, where it twists to follow a direction parallel to the bilayer normal (Apellaniz et al., 2015).

The data presented in chapters 5 and 6 of this thesis work indicate that the epitopes of 4E10/10E8 extend beyond residue Lys/Arg683, encompassing the N-terminus of the TMD. The high-resolution crystal structure of a peptide comprising the MPER/TMD junction in complex with the 10E8 antibody (chapter 5) revealed that this region adopts a continuous α-helix in agreement with the

previously reported NMR data (Apellaniz et al., 2015) (FIG 60). Moreover, photo cross-linking assays described in these chapters, demonstrated the formation of additional interactions between the Trp100b$_{HC}$ of antibodies 4E10 and 10E8 with residues of the TMD in a membrane environment, thereby strengthening the notion that residues within the N terminus of the TMD are part of the 4E10/10E8 epitope. Hence, our results are not consistent with the MPER resting parallel to the membrane plane when targeted by the 4E10 or 10E8 antibodies because that topology would place the Trp100b$_{HC}$ pointing away from the TMD, i.e., precluding the formation of additional interactions between this residue and the TMD.

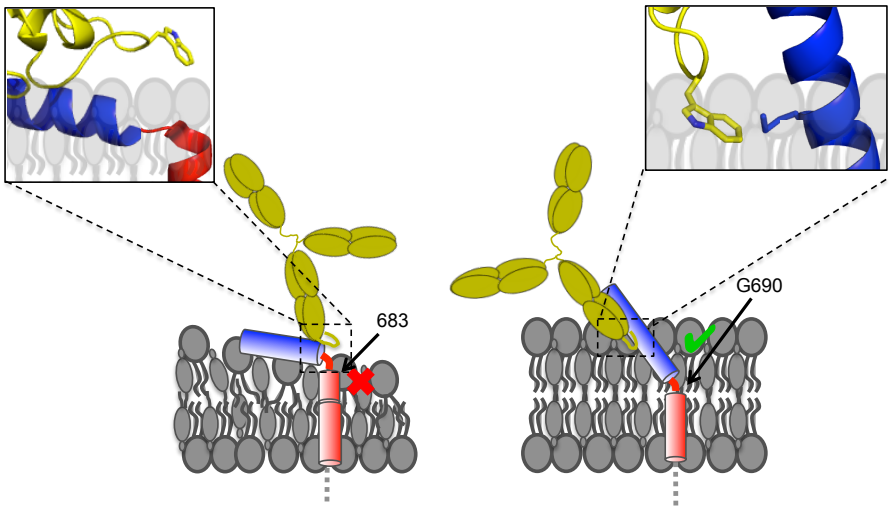

FIG 60. Proposed models for MPER/TMD topology in the lipid bilayer and implications for antibody binding. Left panel: attending to the hydrophobicity distribution of individual helices (which do not consider the possibility of oligomeric states), the MPER helix would sit on the membrane interface with its main axis parallel to the membrane plane. A kink at position Lys683 allows perpendicular insertion of the TMD and places residues from this domain away from the Trp100b$_{HC}$. Hence, this topology would preclude additional interactions between the antibody and the TMD. Right panel: topology based on the recent NMR characterization of this region (Apellaniz et al., 2015). This topology allows the formation of additional interactions between the antibody and the TMD in concordance with the photo cross-linking results described in chapters 5 and 6. The atomic coordinates for the 10E8 structure described in chapter 5 were used to infer the orientation of the antibody CDR-H3 loop in both cases (insets).

Furthermore, the alternative MPER topology supported by our data revises the proposed angle of interaction of the anti-MPER antibodies targeting the MPER/TMD junction (Cardoso et al., 2005; Kwon et al., 2016b; Lorizate et

al., 2006; Ofek et al., 2004; Song et al., 2009; Sun et al., 2008). Hence, the data presented in this thesis disagree with the assumption that the 4E10 and 10E8 antibodies approach their epitope from top, with the longitudinal axis of the Fab adopting an orientation perpendicular to that of the MPER α-helix in the membrane interface (FIG 60, left). Instead, our data rather support an oblique angle of docking, in agreement with the recent Cryo-EM structure of a full gp160 trimer in complex with the 10E8 antibody (Lee et al., 2016) and the structural data of the 4E10 antibody co-crystalized with a PA lipid (Irimia et al., 2016) (FIG 60, right).

8.1. MODEL PROPOSED FOR ANTIBODY 4E10 DOCKING TO THE MPER/TMD HELIX

Binding of the 4E10 antibody to native Env trimers varies between HIV-1 isolates depending on the neutralization-sensitivity. This phenomenon has been explained attending to the different degrees of epitope exposure that arise from Env packing (Chakrabarti et al., 2011). Hence, pre-attachment is limited to sensitive virus isolates (tier 1a/1b), which are characterized by partially open conformations of the Env proteins. However, in spite of the inability of this antibody to bind neutralization-resistant isolates (tier 2 and 3), the 4E10 antibody can neutralize a wide range of these virus variants by targeting the pre-hairpin intermediate that emerges upon activation of the fusion process (Frey et al., 2008; Gustchina et al., 2008). Hence, 4E10 mAb is effective only for a restricted period of time during viral infection (Binley et al., 2003; Dimitrov et al., 2007). Due to the requirement of receptor engagement to gain access to its MPER epitope, it is likely that the 4E10 antibody has evolved to maximize its activity during the short time of the fusion process. Attending to the results presented in chapter 7, we propose that the 4E10 antibody increases its on-rate against receptor-activated gp41 through membrane binding (FIG 61).

4E10-membrane interactions are driven by the combination of hydrophobic (mainly due to the Trp residues at the CDR-H3 apex) and

electrostatic interactions. Defined lipid-binding sites have been proposed either to coexist in the apo and holo forms of 4E10 (Irimia et al., 2016) or to be present only in the apo form (Finton et al., 2013). While the former allows simultaneous accommodation of the phospholipid head-group moieties and the epitope peptide, the latter assumes the requirement of large conformational changes in the antibody paratope for peptide binding. Structural, thermodynamic and kinetic evidences gathered from three different versions of the CDR-H3 (WT, delta-loop and WDWD; see chapter 2) were essentially indistinguishable among the three constructs examined, therefore discarding mayor conformational changes of the combining site of the antibody after binding. Besides, the crystal structure of the ligand-free version of 4E10 was consistent with the classical view postulating a limited flexibility for the paratope of mature antibodies. Specifically, the structure of the unbound antibody is in agreement with a mechanism in which gains of affinity are the consequence of the regular BCR maturation process, and supports simultaneous lipid and peptide binding.

Mutational and biophysical analyses described in chapter 7 revealed the less obvious role of non-specific electrostatic interactions with the lipid membrane. Although non-specific, a mutational characterization of surface-charge Fab variants performed in that chapter revealed that several positively charged residues in the proximity of the antibody-binding site play a role in the neutralization mechanism of 4E10.

The data in chapter 7 further suggest that the positively charged surface of the 4E10 antibody may have evolved during antibody maturation as a tool to accelerate the binding kinetics to the epitope in the short time interval of fusion. We speculate that the long-range electrostatic interactions between the paratope surface of the antibody and anionic lipids of the viral membrane may favor the capture of the transiently exposed epitope by increasing the association constant rate (k_{on}) of the process (FIG 61) and, consequently, enhance the overall affinity (decrease K_D). Thus, in the absence of such

electrostatic interactions, a slower association to gp41 might result in a less efficient neutralization by the antibody.

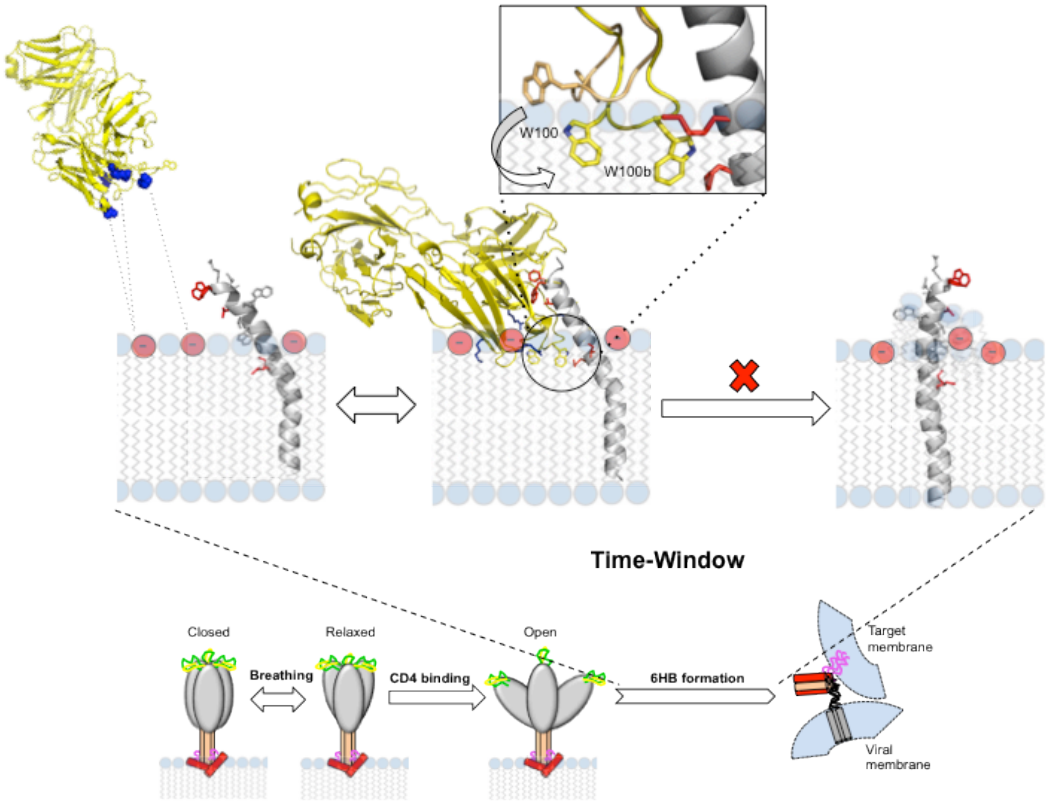

FIG 61. Proposed mechanism for MPER helix engagement by 4E10 at the membrane interface. 4E10-MPER binding occurs in a narrow time-window, after activation of the fusion process and before 6-HB formation. Electrostatic interactions (dashed lines) take place between basic residues on the paratope surface (blue spheres) and acidic lipids in the viral membrane (red). Antibody binding induces the conformational change of the CDR-H3 loop leading to membrane penetration of the apex residues. $Trp100b_{HC}$ sits close to I686 and M687 (in red) of the gp41 TMD (in gray), stabilizing a 4E10-gp41 complex after binding. Fixation of the MPER/TMD region inhibits phospholipid extraction and therefore fusion with the target membrane.

8.1. MODEL PROPOSED FOR ANTIBODY 10E8 DOCKING TO THE MPER/TMD HELIX

In comparison to other anti-MPER antibodies, the mAb 10E8 accesses its epitope more efficiently in the native Env trimer (Huang et al., 2012).

Although 10E8 can engage pre-activated virions (FIG 62), it has been proposed that 10E8 neutralizes HIV-1 in large part by binding to fusion intermediates that arise after receptor engagement (Kim et al., 2014). The 10E8 antibody shows no direct membrane binding through electrostatic interactions since it lacks a localized net charge on the antibody surface. Consequently, 10E8 cannot beneficiate from long distance interactions to maximize binding to the short-lived pre-hairpin intermediate that is formed during the fusion step.

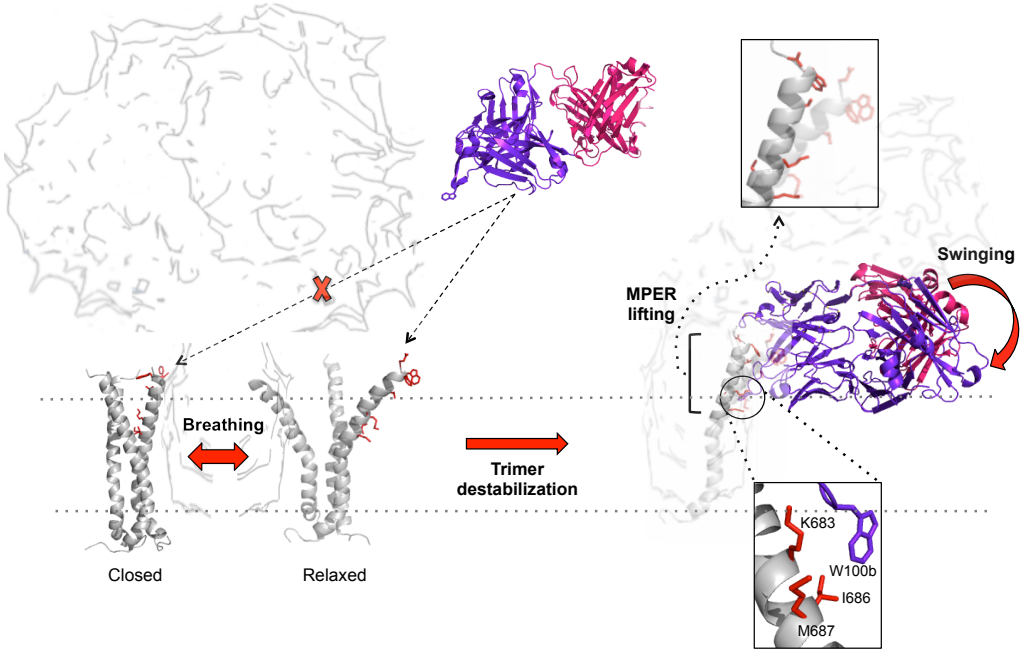

FIG 62. Proposed mechanism for MPER helix engagement by 10E8 at the membrane interface. Env breathing alternatively may alternatively 10E8 key binding residues occluded inside the trimeric-TMD structure (close), or a more exposed orientation (relaxed). The relaxed Env pre-fusion state can be targeted by 10E8. This antibody gains access to MPER by bending its constant region towards the membrane in a way that the entire base of the antibody sits parallel to the surface of the membrane. 10E8-gp41 binding includes specific interactions of the $Trp100b_{HC}$ residue (purple) with residues I686 and M687 (red) of the TMD inside the membrane. 10E8 binding stabilizes MPER/TMD in a lifted position, thus interfering with the subsequent structural transitions required for fusion.

However, 10E8 interaction surface might also involve elements besides the linear MPER and the lipid membrane. Additional contacts between the antibody and gp120 or with the C-terminus of the FP from a neighbor gp41 has been recently suggested (Lee et al., 2016). Supporting the interaction of 10E8

with such surfaces, glycans N88 and N625, located at the base of the trimer, sterically obstructed the binding of the antibody to MPER (Kim et al., 2014; Lee et al., 2016). Hence, cross-reactivity of 10E8, which permits simultaneous binding to gp41 and gp120, could represent an additional mechanism employed by the 10E8 antibody to exert viral neutralization. Establishment of these additional interactions might require specific adaptations to recognize the epitope in the membrane millieu. In this regard, the unusually large "swinging-like" movement of the constant domain relative to the variable domain, reported in chapter 5, might facilitate access to the MPER epitope in the native Env trimer (FIG 62). Hence, the higher neutralization potency reported for the antibody 10E8 may be explained, at least in part, by a higher accessibility to the epitope in the native trimeric Env. Interestingly, the conformation resulting from the swinging movement defines a surface plane at the base of the antibody where the crystal structure revealed several phosphate ion groups. This observation suggests a possible orientation of the Fab with respect to the surface of the viral membrane when bound to native Env trimers (FIG 62).

8.1. RELEVANCE OF THE INTERACTIONS BETWEEN A TRP RESIDUE AND THE MPER/TMD FOR HIV NEUTRALIZATION.

Despite of the several differences encountered between the 4E10 and the 10E8 antibodies, the neutralization potency of both antibodies relies on Trp residues located at the apex of their CDR-H3 loops (Alam et al., 2009; Apellaniz et al., 2014b; Huang et al., 2012; Scherer et al., 2010). As proposed by the mechanisms outlined in FIG 61 and 62 the apex residues of the CDR-H3 loops of 4E10 and 10E8 antibodies would increase the binding affinity to their membrane-embedded epitopes through the establishment of direct interactions with the TMD. Hence, it is reasonable to think that these interactions increase the epitope-binding affinity in a membrane context by decreasing the dissociation constant rate (k_{off}). Formation of a stable antibody-peptide-lipid complex may block MPER-induced decrease in membrane surface hydration and electrostatic repulsion, which is required for initial lipid mixing in the fusion

event and also, interrupt the conformational changes required for 6-HB completion.

Moreover, tight interaction with an MPER/TMD protomer would likely interfere with the trimeric conformation of the TMD. Amino acid modification in the gp41 MPER/TMD region was argued to alter the neutralization sensitivity of the mutated PsV to anti-gp120 antibodies inferring important implications of this region in the overall trimeric conformation of the Env glycoprotein (Bradley et al., 2016; Dev et al., 2016). Residues I686 and M687 are located within the TMD residues that form the coiled-coil motif holding the trimeric architecture of the native gp160. Env breathing between a close and a slightly more open conformation might probably increase exposure of key epitope residues for antibody engagement, including M687. We propose that M687 binding is further stabilized by I686 resulting in a more open trimer conformation of Env. The formation of such stable complex would halt the cell infection process by either interfering with the membrane structural transition required for fusion or by disrupting the labile gp41-gp120 subunit association, resulting in slow irreversible gp120 shedding (Kim et al., 2014; Ruprecht et al., 2011). Collectively, these mechanisms would strengthen the neutralization potency of the antibody.

8.2. CONCLUDING REMARKS

Structural, kinetic and sequence-based properties of 4E10 and 10E8 antibodies determine the distinct MPER binding rates and accessibilities, explaining, at least in part, the neutralization mechanism of each antibody. The data presented in this thesis, however, underscore a common trend: the importance of preserving a continuous α-helical MPER/TMD junction for efficient 4E10/10E8 antibody binding. We believe that formation of a tight complex involving: i) the aromatic residue Trp100b$_{HC}$ at the apex of the CDR-H3; ii) residues of the gp41 TMD; and iii) viral membrane lipids, is instrumental for neutralization by both antibodies. In that context, stabilization of the

protomer would interrupt the progression of fusion and hence, cell infection inhibition. Impediments in designing successful immunogens for elicitation of anti-MPER-like antibodies are partly attributed to an incomplete understanding of the structural and binding characteristics of this class of antibodies. All in all, the findings presented in this thesis might contribute to the development of more efficient vaccines against HIV infection. Furthermore, they may help delineate the functional elements that should be preserved in efficient immunotherapeutic agents.

APPENDICES

MPER peptide	*Sequence*
(656-683)	NEQELLELDKWASLWNWFNITNWLWYIK-amide
(656-683)R	RRR-NEQELLELDKWASLWNWFDITNWLWYIR-RRR-amide
(671-683)	NWFDITNWLWYIK-KKK-amide
(671-683)R	NWFDITNWLWYIR-RRR-amide
(671-686)	KKK-NWFDITNWLWYIKLFI-KKK-amide
(671-690)	NWFNITNWFNITNWLWYIKLFIMIVG-KKKKK-amide
$(664\text{-}690)_{sol}$	KKKK-DKWASLWNWFNITNWLWYIKLFIMIVG-KKKKK-amide
$(664\text{-}690)_{insol}$	KK-DKWASLWNWFNITNWLWYIKLFIMIVGKKK-amide
(671-693)	KKK-NWFDITNWLWYIKLFIMIVGGLV-KK-amide
(671-693)/W672A-F673A	KKK-NAADITNWLWYIKLFIMIVGGLV-KK-amide

4E10 Antibody	CDR-H3	MPER	K_D (nM)	ΔG° (kcal mol^{-1})	ΔH° (kcal mol^{-1})	-TΔS° (kcal mol^{-1})[a]	n[b]	T_m (°C)	ΔT_m (°C)	ΔH (kcal mol^{-1})	HXB2- IC_{50} (μg/mL)	JRCSF- IC_{50} (μg/mL)
		(656-683)	119 ± 9	-9.4 ± 0.1	-19.2 ± 0.2	9.8	0.9 ± 0.1	n.d.		n.d.		
		(671-683)	167 ± 21	-9.2 ± 0.1	-15.9 ± 0.3	6	0.8 ± 0.1	69.9	0.1	-339		
		(671-686)	48 ± 4	-10.0 ± 0.1	-17.9 ± 0.1	7.9	0.8 ± 0.1	n.d.		n.d.		
4E10_WT	EGTTGWGWLGKPIG	(671-690)	4.8 ± 0.5	11.3 ± 0.1	-14. 3 ± 0.1	3.0	1.1 ± 0.1	n.d.		n.d.	0.21 ± 0.02	1.3 ± 0.1
		(664-690)	4.6 ± 1.5	-11.4 ± 0.2	-15.1 ± 0.2	3.7	1.0 ± 0.1	73.2	2.5	-427		
		(671-693)	22 ± 2	-10.4 ± 0.1	-12.4 ± 0.1	1.9	1.3 ± 0.1	n.d.		n.d.		
		-						69.8	n.a.	-362		
		(671-683)	45 ± 5	10.0 ± 0.1	-20.9 ± 0.2	10.8	1.0 ± 0.1	73.1	0.8	-362		
4E10_Δloop	EGTTGSGGKPIG	(664-690)	7.1 ± 1.2	-11.1 ± 0.1	-15.0 ± 0.1	3.8	1.2 ± 0.1	74.3	2.0	-392	> 100	> 100
		(671-693)	31 ± 4	-10.2 ± 0.1	-10.9 ± 0.1	0.7	1.3 ± 0.1	n.d.		n.d.		
		-						72.3	n.a.	-325		
		(671-683)	96 ± 6	-9. 6 ± 0.1	-18.2 ± 0.1	8.6	1.2 ± 0.1	72.9	0.5	-337		
W/D-W/D	EGTTGDGDLGKPIG	(664-690)	13.9 ± 2.2	-10.7 ± 0.1	-12.6 ± 0.1	1.9	1.1 ± 0.1	74.1	1.7	-384	> 100	> 100
		-						72.4	n.a.	-334		
3W	EGTTGWGWWGKPIG	(664-690)	10.0 ± 1.4	-10.9 ± 0.1	-11.8 ± 0.1	0.89	1.1 ± 0.1	73.0	4	-360	0.47 ± 0.02	2.9 ± 0.4
		-						69.0	n.a.	-269		
W/Y-W/Y	EGTTGYGYLGKPIG	(664-690)	6.3 ± 0.9	-11.2 ± 0.1	-14.2 ± 0.1	3.0	1.1 ± 0.1	73.1	2.8	-319	10.1 ± 3.6	19.8 ± 2.9
		-						70.3	n.a.	-300		
Scr-1	EGTTGLGWWGKPIG	(664-690)	3.6 ± 0.5	-11.5 ± 0.1	-13.1 ± 0.1	1.6	1.1 ± 0.1	72.2	3.1	-387	3.3 ± 0.6	7.0 ± 0.3
		-						69.1	n.a.	-277		
Scr-2	EGTTGGWWLGKPIG	(664-690)	5.3 ± 0.9	-11.3 ± 0.1	-15.2 ± 0.1	3.9	1.1 ± 0.1	73.1	4.8	-377	0.81 ± 0.04	6.3 ± 0.6
		-						68.3	n.a.	-282		
2F5loop	EGTTGLFGVGKPIG	(664-690)	12.5 ± 2.6	-10.8 ± 0.1	-11.9 ± 0.1	1.1	1.1 ± 0.1	72.9	2.7	-361	18.4 ± 7.8	36 ± 14
		-						70.2	n.a.	-230		
N_prol	EGTTPPGWGWLGKPIG	(664-690)	6.2 ± 1.3	-11.2 ± 0.1	-12.8 ± 0.1	1.6	1.1 ± 0.1	73.9	5.3	-376	0.30 ± 0.08	6.5 ± 1.6
		-						68.6	n.a.	-288		
C_prol	EGTTGWGWLGPPKPIG	(664-690)	6.9 ± 1.5	-11.1 ± 0.1	-15.2 ± 0.2	4.0	1.0 ± 0.1	72.9	5.4	-350	6.4 ± 1.4	17.1 ± 4.3
		-						67.5	n.a.	-245		
W_{100}/C	EGTTGCGWLGKPIG	-						n.d.		n.d.	5.9 ± 1.0	48 ± 39
W_{100b}/C	EGTTGWGCLGKPIG	-						n.d.		n.d.	4.6 ± 0.6	15.1 ± 2.0

4E10 Antibody	CDRH3	Additional mutation	MPER	K_D (nM)	ΔG° (kcal mol^{-1})	ΔH° (kcal mol^{-1})	-TΔS° (kcal mol^{-1})[a]	n[b]	HXB2- IC_{50} (μg/mL)	JRCSF- IC_{50} (μg/mL)
BS	EGTTGWGWLGKPIG	$S28_{LC}$/A $S30_{LC}$/A	(664-690)	12.2 ± 2.5	-10.8 ± 0.1	-11.7 ± 0.1	0.9	1.3 ± 0.	0.38 ± 0.03	1.59 ± 0.27
R73E	EGTTGWGWLGKPIG	$R73_{LC}$/E	(671-693)	12.8 ± 3.5	-10.8 ± 0.1	-14.7 ± 0.2	3.9	1.1 ± 0.1	5.3 ± 0.4	13.2 ± 3.5
K100eE	EGTTGWGWLGKPIG	$K100e_{LC}$/E	(671-693)	91 ± 14	-9.6 ± 0.2	-10.4 ± 0.2	0.7	1.4 ± 0.1	2.5 ± 0.3	12.7 ± 4.0
Δloop_K100eE	EGTTGSGGKPIG	$K100e_{LC}$/E	(664-690)	44 ± 11	10.0 ± 0.2	-17.5 ± 0.4	7.5	1.1 ± 0.1	> 100	> 100

10E8 Antibody	CDR-H3	(MPER)	K_D (nM)	ΔG° (kcal mol^{-1})	ΔH° (kcal mol^{-1})	-TΔS° (kcal mol^{-1})[a]	n[b]	T_m (°C)	$ΔT_m$ (°C)	ΔH (kcal mol^{-1})	HXB2- IC_{50} (μg/mL)	JRCSF- IC_{50} (μg/mL)
10E8_WT	GKYYDFWSGYPPGEE	(656-683)	93 ± 13	9.6 ± 0.1	-5.4 ± 0.1	-4.2	0.9 ± 0.1	65.8	4.3	-118	0.27 ± 0.01	0.29 ± 0.02
		(671-683)	746 ± 307	-8.3 ± 0.3	-3.3 ± 0.3	-5.0	0.9 ± 0.1	62.1	0.6	-76		
		(671-686)	369 ± 84	-8.7 ± 0.1	-9.6 ± 0.5	0.9	0.9 ± 0.1	n.d.		n.d.		
		(671-690)	10 ± 1.6	-10.9 ± 0.1	-8.4 ± 0.1	-2.5	0.8 ± 0.1	68.2	6.7	-216		
		(664-690)	9.6 ± 1.0	-10.9 ± 0.1	-9.6 ± 0.1	-1.3	1.0 ± 0.1	69.2	7.7	-303		
		(671-693)	9.4 ± 2.0	-10.9 ± 0.1	-9.0 ± 0.1	-1.9	1.3 ± 0.1	n.d.		n.d.		
		-						61.5	n.a.	-78		
10E8_P/A	GKYYDFWSGYAPGEE	(656-683)	n.a.	n.a.	n.a.	n.a.	n.a.	61.1	0.7	-57	8.6 ± 4.2	0.68 ± 0.06
		(664-690)	161 ± 22	-9.2 ± 0.1	-11.1 ± 0.2	1.9 ± 0.3	0.8 ± 0.1	62.4	2.0	-58		
		-						60.4	n.a.	-67		
10E8_W/Y	GKYYDFYSGYPPGEE	(656-683)	277 ± 39	-8.9 ± 0.1	-8.7 ± 0.3	-0.25	0.7 ± 0.1	63.2	1.7	-88	8.1 ± 0.9	7.0 ± 0.5
		(664-690)	52 ± 12	-9.9 ± 0.1	-8.9 ± 0.1	-1.0 ± 0.2	1.1 ± 0.1	65.0	3.5	-82		
		-						61.5	n.a.	-101		
10E8_W/A	GKYYDFASGYPPGEE	(656-683)	568 ± 139	8.5 ± 0.1	-6.2 ± 0.1	-2.28	0.8 ± 0.1	63.2	1.1	-88	> 100	19.5 ± 6.9
		(664-690)	361 ± 82	-8.8 ± 0.1	-10.0 ± 0.5	1.2	1.0 ± 0.1	63.7	1.6	-82		
		-						62.1	n.a.	-75		
10E8_W/D	GKYYDFDSGYPPGEE	(656-683)	376 ± 76	-8.7 ± 0.2	-4.6 ± 0.2	-4.1	1.2 ± 0.1	63.7	0.6	-124	> 100	> 100
		(664-690)	375 ± 66	-8.7 ± 0.1	-6.5 ± 0.3	-2.2	1.0 ± 0.1	64.0	0.9	-33		
		-						63.1	n.a.	-43		

[a] Temperature was 298 K.
[b] ***n*** refers to the molar ratio peptide/protein

REFERENCES

Abe, R., Caaveiro, J.M., Kozuka-Hata, H., Oyama, M., and Tsumoto, K. (2012). Mapping ultra-weak protein-protein interactions between heme transporters of Staphylococcus aureus. The Journal of biological chemistry *287*, 16477-16487.

Adams, P.D., Afonine, P.V., Bunkoczi, G., Chen, V.B., Davis, I.W., Echols, N., Headd, J.J., Hung, L.W., Kapral, G.J., Grosse-Kunstleve, R.W.*, et al.* (2010). PHENIX: A comprehensive Python-based system for macromolecular structure solution. Acta Crystallogr D *66*, 213-221.

Alam, S.M., McAdams, M., Boren, D., Rak, M., Scearce, R.M., Gao, F., Camacho, Z.T., Gewirth, D., Kelsoe, G., Chen, P.*, et al.* (2007). The role of antibody polyspecificity and lipid reactivity in binding of broadly neutralizing anti-HIV-1 envelope human monoclonal antibodies 2F5 and 4E10 to glycoprotein 41 membrane proximal envelope epitopes. Journal of immunology *178*, 4424-4435.

Alam, S.M., Morelli, M., Dennison, S.M., Liao, H.X., Zhang, R., Xia, S.M., Rits-Volloch, S., Sun, L., Harrison, S.C., Haynes, B.F.*, et al.* (2009). Role of HIV membrane in neutralization by two broadly neutralizing antibodies. Proceedings of the National Academy of Sciences of the United States of America *106*, 20234-20239.

Alving, C.R., Rao, M., Steers, N.J., Matyas, G.R., and Mayorov, A.V. (2012). Liposomes containing lipid A: an effective, safe, generic adjuvant system for synthetic vaccines. Expert review of vaccines *11*, 733-744.

Apellaniz, B., Huarte, N., Largo, E., and Nieva, J.L. (2014a). The three lives of viral fusion peptides. Chem Phys Lipids *181*, 40-55.

Apellaniz, B., Ivankin, A., Nir, S., Gidalevitz, D., and Nieva, J.L. (2011). Membrane-proximal external HIV-1 gp41 motif adapted for destabilizing the highly rigid viral envelope. Biophys J *101*, 2426-2435.

Apellaniz, B., Rujas, E., Carravilla, P., Requejo-Isidro, J., Huarte, N., Domene, C., and Nieva, J.L. (2014b). Cholesterol-dependent membrane fusion induced by the gp41 membrane-proximal external region-transmembrane domain connection suggests a mechanism for broad HIV-1 neutralization. J Virol *88*, 13367-13377.

Apellaniz, B., Rujas, E., Serrano, S., Morante, K., Tsumoto, K., Caaveiro, J.M., Jimenez, M.A., and Nieva, J.L. (2015). The Atomic Structure of the HIV-1 gp41 Transmembrane Domain and Its Connection to the Immunogenic Membrane-proximal External Region. J Biol Chem *290*, 12999-13015.

Arbuzova, A., Wang, J., Murray, D., Jacob, J., Cafiso, D.S., and McLaughlin, S. (1997). Kinetics of interaction of the myristoylated alanine-rich C kinase substrate, membranes, and calmodulin. The Journal of biological chemistry *272*, 27167-27177.

Aslund, F., and Beckwith, J. (1999). The thioredoxin superfamily: redundancy, specificity, and gray-area genomics. J Bacteriol *181*, 1375-1379.

Asokan, M., Rudicell, R.S., Louder, M., McKee, K., O'Dell, S., Stewart-Jones, G., Wang, K., Xu, L., Chen, X., Choe, M.*, et al.* (2015). Bispecific Antibodies Targeting Different Epitopes on the HIV-1 Envelope Exhibit Broad and Potent Neutralization. Journal of virology *89*, 12501-12512.

Balazs, A.B., Chen, J., Hong, C.M., Rao, D.S., Yang, L., and Baltimore, D. (2012). Antibody-based protection against HIV infection by vectored immunoprophylaxis. Nature *481*, 81-84.

Barbas, C.F., 3rd, Bjorling, E., Chiodi, F., Dunlop, N., Cababa, D., Jones, T.M., Zebedee, S.L., Persson, M.A., Nara, P.L., Norrby, E.*, et al.* (1992). Recombinant human Fab fragments neutralize human type 1 immunodeficiency virus in vitro. Proceedings of the National Academy of Sciences of the United States of America *89*, 9339-9343.

Barbas, C.F., 3rd, Kang, A.S., Lerner, R.A., and Benkovic, S.J. (1991). Assembly of combinatorial antibody libraries on phage surfaces: the gene III site. Proceedings of the National Academy of Sciences of the United States of America *88*, 7978-7982.

Barbian, H.J., Decker, J.M., Bibollet-Ruche, F., Galimidi, R.P., West, A.P., Jr., Learn, G.H., Parrish, N.F., Iyer, S.S., Li, Y., Pace, C.S.*, et al.* (2015). Neutralization properties of simian immunodeficiency viruses infecting chimpanzees and gorillas. mBio *6*.

Barouch, D.H., Whitney, J.B., Moldt, B., Klein, F., Oliveira, T.Y., Liu, J., Stephenson, K.E., Chang, H.W., Shekhar, K., Gupta, S.*, et al.* (2013). Therapeutic efficacy of potent neutralizing HIV-1-specific monoclonal antibodies in SHIV-infected rhesus monkeys. Nature *503*, 224-228.

Barre-Sinoussi, F., Chermann, J.C., Rey, F., Nugeyre, M.T., Chamaret, S., Gruest, J., Dauguet, C., Axler-Blin, C., Vezinet-Brun, F., Rouzioux, C.*, et al.* (1983). Isolation of a T-lymphotropic retrovirus from a patient at risk for acquired immune deficiency syndrome (AIDS). Science *220*, 868-871.

Batista, F.D., and Harwood, N.E. (2009). The who, how and where of antigen presentation to B cells. Nat Rev Immunol *9*, 15-27.

Besenicar, M., Macek, P., Lakey, J.H., and Anderluh, G. (2006). Surface plasmon resonance in protein-membrane interactions. Chemistry and physics of lipids *141*, 169-178.

Bessette, P.H., Aslund, F., Beckwith, J., and Georgiou, G. (1999). Efficient folding of proteins with multiple disulfide bonds in the Escherichia coli cytoplasm. Proceedings of the National Academy of Sciences of the United States of America *96*, 13703-13708.

Binley, J.M., Cayanan, C.S., Wiley, C., Schulke, N., Olson, W.C., and Burton, D.R. (2003). Redox-triggered infection by disulfide-shackled human immunodeficiency virus type 1 pseudovirions. Journal of virology *77*, 5678-5684.

Binley, J.M., Sanders, R.W., Clas, B., Schuelke, N., Master, A., Guo, Y., Kajumo, F., Anselma, D.J., Maddon, P.J., Olson, W.C.*, et al.* (2000). A recombinant human immunodeficiency virus type 1 envelope glycoprotein complex stabilized by an intermolecular disulfide bond between the gp120 and gp41 subunits is an antigenic mimic of the trimeric virion-associated structure. Journal of virology *74*, 627-643.

Binley, J.M., Wrin, T., Korber, B., Zwick, M.B., Wang, M., Chappey, C., Stiegler, G., Kunert, R., Zolla-Pazner, S., Katinger, H.*, et al.* (2004). Comprehensive cross-clade neutralization analysis of a panel of anti-human immunodeficiency virus type 1 monoclonal antibodies. Journal of virology *78*, 13232-13252.

Bird, G.H., Irimia, A., Ofek, G., Kwong, P.D., Wilson, I.A., and Walensky, L.D. (2014). Stapled HIV-1 peptides recapitulate antigenic structures and engage broadly neutralizing antibodies. Nature structural & molecular biology *21*, 1058-1067.

Blattner, C., Lee, J.H., Sliepen, K., Derking, R., Falkowska, E., de la Pena, A.T., Cupo, A., Julien, J.P., van Gils, M., Lee, P.S.*, et al.* (2014). Structural delineation of a quaternary, cleavage-dependent epitope at the gp41-gp120 interface on intact HIV-1 Env trimers. Immunity *40*, 669-680.

Blumenthal, R., Durell, S., and Viard, M. (2012). HIV entry and envelope glycoprotein-mediated fusion. The Journal of biological chemistry *287*, 40841-40849.

Bonomelli, C., Doores, K.J., Dunlop, D.C., Thaney, V., Dwek, R.A., Burton, D.R., Crispin, M., and Scanlan, C.N. (2011). The glycan shield of HIV is predominantly oligomannose independently of production system or viral clade. PLoS One *6*, e23521.

Bonsignori, M., Zhou, T., Sheng, Z., Chen, L., Gao, F., Joyce, M.G., Ozorowski, G., Chuang, G.Y., Schramm, C.A., Wiehe, K.*, et al.* (2016). Maturation Pathway from Germline to Broad HIV-1 Neutralizer of a CD4-Mimic Antibody. Cell *165*, 449-463.

Bradley, T., Trama, A., Tumba, N., Gray, E., Lu, X., Madani, N., Jahanbakhsh, F., Eaton, A., Xia, S.M., Parks, R.*, et al.* (2016). Amino Acid Changes in the HIV-1 gp41 Membrane Proximal Region Control Virus Neutralization Sensitivity. EBioMedicine.

Breden, F., Lepik, C., Longo, N.S., Montero, M., Lipsky, P.E., and Scott, J.K. (2011). Comparison of antibody repertoires produced by HIV-1 infection, other chronic and acute infections, and systemic autoimmune disease. PLoS One *6*, e16857.

Briney, B.S., Willis, J.R., and Crowe, J.E., Jr. (2012). Human peripheral blood antibodies with long HCDR3s are established primarily at original recombination using a limited subset of germline genes. PLoS One *7*, e36750.

Brunel, F.M., Zwick, M.B., Cardoso, R.M.F., Nelson, J.D., Wilson, I.A., Burton, D.R., and Dawson, P.E. (2006). Structure-Function Analysis of the Epitope for 4E10, a Broadly Neutralizing Human Immunodeficiency Virus Type 1 Antibody. Journal of virology *80*, 1680-1687.

Buchacher, A., Predl, R., Strutzenberger, K., Steinfellner, W., Trkola, A., Purtscher, M., Gruber, G., Tauer, C., Steindl, F., Jungbauer, A.*, et al.* (1994). Generation of human monoclonal antibodies against HIV-1 proteins; electrofusion and Epstein-Barr virus transformation for peripheral blood lymphocyte immortalization. AIDS Res Hum Retroviruses *10*, 359-369.

Burton, D.R., Ahmed, R., Barouch, D.H., Butera, S.T., Crotty, S., Godzik, A., Kaufmann, D.E., McElrath, M.J., Nussenzweig, M.C., Pulendran, B.*, et al.* (2012). A Blueprint for HIV Vaccine Discovery. Cell host & microbe *12*, 396-407.

Burton, D.R., Desrosiers, R.C., Doms, R.W., Koff, W.C., Kwong, P.D., Moore, J.P., Nabel, G.J., Sodroski, J., Wilson, I.A., and Wyatt, R.T. (2004). HIV vaccine design and the neutralizing antibody problem. Nature immunology *5*, 233-236.

Burton, D.R., and Hangartner, L. (2016). Broadly Neutralizing Antibodies to HIV and Their Role in Vaccine Design. Annu Rev Immunol *34*, 635-659.

Burton, D.R., and Mascola, J.R. (2015). Antibody responses to envelope glycoproteins in HIV-1 infection. Nature immunology *16*, 571-576.

Burton, D.R., Pyati, J., Koduri, R., Sharp, S.J., Thornton, G.B., Parren, P.W., Sawyer, L.S., Hendry, R.M., Dunlop, N., Nara, P.L.*, et al.* (1994). Efficient neutralization of primary isolates of HIV-1 by a recombinant human monoclonal antibody. Science *266*, 1024-1027.

Buzon, V., Natrajan, G., Schibli, D., Campelo, F., Kozlov, M.M., and Weissenhorn, W. (2010). Crystal structure of HIV-1 gp41 including both fusion peptide and membrane proximal external regions. PLoS Pathog *6*, e1000880.

Calarese, D.A., Scanlan, C.N., Zwick, M.B., Deechongkit, S., Mimura, Y., Kunert, R., Zhu, P., Wormald, M.R., Stanfield, R.L., Roux, K.H.*, et al.* (2003). Antibody domain exchange is an immunological solution to carbohydrate cluster recognition. Science *300*, 2065-2071.

Cardoso, R.M., Brunel, F.M., Ferguson, S., Zwick, M., Burton, D.R., Dawson, P.E., and Wilson, I.A. (2007). Structural basis of enhanced binding of extended and helically constrained peptide epitopes of the broadly neutralizing HIV-1 antibody 4E10. Journal of molecular biology *365*, 1533-1544.

Cardoso, R.M., Zwick, M.B., Stanfield, R.L., Kunert, R., Binley, J.M., Katinger, H., Burton, D.R., and Wilson, I.A. (2005). Broadly neutralizing anti-HIV antibody 4E10 recognizes a helical conformation of a highly conserved fusion-associated motif in gp41. Immunity *22*, 163-173.

Caskey, M., Klein, F., Lorenzi, J.C., Seaman, M.S., West, A.P., Jr., Buckley, N., Kremer, G., Nogueira, L., Braunschweig, M., Scheid, J.F.*, et al.* (2015). Viraemia suppressed in HIV-1-infected humans by broadly neutralizing antibody 3BNC117. Nature *522*, 487-491.

Chakrabarti, B.K., Walker, L.M., Guenaga, J.F., Ghobbeh, A., Poignard, P., Burton, D.R., and Wyatt, R.T. (2011). Direct antibody access to the HIV-1 membrane-proximal external region positively correlates with neutralization sensitivity. Journal of virology *85*, 8217-8226.

Chen, J., Frey, G., Peng, H., Rits-Volloch, S., Garrity, J., Seaman, M.S., and Chen, B. (2014). Mechanism of HIV-1 neutralization by antibodies targeting a membrane-proximal region of gp41. Journal of virology *88*, 1249-1258.

Chernomordik, L.V., and Kozlov, M.M. (2003). Protein-lipid interplay in fusion and fission of biological membranes. Annu Rev Biochem *72*, 175-207.

Cleland, W.W., and Northrop, D.B. (1999). Energetics of substrate binding, catalysis, and product release. Methods Enzymol *308*, 3-27.

Coffin, J., Haase, A., Levy, J.A., Montagnier, L., Oroszlan, S., Teich, N., Temin, H., Toyoshima, K., Varmus, H., Vogt, P.*, et al.* (1986). What to call the AIDS virus? Nature *321*, 10.

Conley, A.J., Kessler, J.A., 2nd, Boots, L.J., Tung, J.S., Arnold, B.A., Keller, P.M., Shaw, A.R., and Emini, E.A. (1994). Neutralization of divergent human immunodeficiency virus type 1 variants and primary isolates by IAM-41-2F5, an anti-gp41 human monoclonal antibody. Proceedings of the National Academy of Sciences of the United States of America *91*, 3348-3352.

Correia, B.E., Ban, Y.E., Holmes, M.A., Xu, H., Ellingson, K., Kraft, Z., Carrico, C., Boni, E., Sather, D.N., Zenobia, C.*, et al.* (2010). Computational design of epitope-scaffolds allows induction of antibodies specific for a poorly immunogenic HIV vaccine epitope. Structure *18*, 1116-1126.

Daghestani, H.N., and Day, B.W. (2010). Theory and applications of surface plasmon resonance, resonant mirror, resonant waveguide grating, and dual polarization interferometry biosensors. Sensors *10*, 9630-9646.

Damian, L. (2013). Isothermal Titration Calorimetry for Studying Protein-Protein Interactions.

Deng, H., Liu, R., Ellmeier, W., Choe, S., Unutmaz, D., Burkhart, M., Di Marzio, P., Marmon, S., Sutton, R.E., Hill, C.M.*, et al.* (1996). Identification of a major co-receptor for primary isolates of HIV-1. Nature *381*, 661-666.

Dennison, S.M., Stewart, S.M., Stempel, K.C., Liao, H.X., Haynes, B.F., and Alam, S.M. (2009). Stable docking of neutralizing human immunodeficiency virus type 1 gp41 membrane-proximal external region monoclonal antibodies 2F5 and 4E10 is dependent on the membrane immersion depth of their epitope regions. Journal of virology *83*, 10211-10223.

Dennison, S.M., Sutherland, L.L., Jaeger, F.H., Anasti, K.M., Parks, R., Stewart, S., Bowman, C., Xia, S.M., Zhang, R., Shen, X.*, et al.* (2011). Induction of antibodies in rhesus macaques that recognize a fusion-intermediate conformation of HIV-1 gp41. PloS one *6*, e27824.

Dev, J., Park, D., Fu, Q., Chen, J., Ha, H.J., Ghantous, F., Herrmann, T., Chang, W., Liu, Z., Frey, G.*, et al.* (2016). Structural basis for membrane anchoring of HIV-1 envelope spike. Science *353*, 172-175.

Dimitrov, A.S., Jacobs, A., Finnegan, C.M., Stiegler, G., Katinger, H., and Blumenthal, R. (2007). Exposure of the membrane-proximal external region of HIV-1 gp41 in the course of HIV-1 envelope glycoprotein-mediated fusion. Biochemistry *46*, 1398-1401.

Diskin, R., Scheid, J.F., Marcovecchio, P.M., West, A.P., Jr., Klein, F., Gao, H., Gnanapragasam, P.N., Abadir, A., Seaman, M.S., Nussenzweig, M.C.*, et al.* (2011). Increasing the potency and breadth of an HIV antibody by using structure-based rational design. Science *334*, 1289-1293.

Doores, K.J., Bonomelli, C., Harvey, D.J., Vasiljevic, S., Dwek, R.A., Burton, D.R., Crispin, M., and Scanlan, C.N. (2010). Envelope glycans of immunodeficiency virions are almost entirely oligomannose antigens. Proceedings of the National Academy of Sciences of the United States of America *107*, 13800-13805.

Doria-Rose, N.A., Klein, R.M., Manion, M.M., O'Dell, S., Phogat, A., Chakrabarti, B., Hallahan, C.W., Migueles, S.A., Wrammert, J., Ahmed, R.*, et al.* (2009). Frequency and phenotype of human

immunodeficiency virus envelope-specific B cells from patients with broadly cross-neutralizing antibodies. Journal of virology *83*, 188-199.

Doria-Rose, N.A., Schramm, C.A., Gorman, J., Moore, P.L., Bhiman, J.N., DeKosky, B.J., Ernandes, M.J., Georgiev, I.S., Kim, H.J., Pancera, M.*, et al.* (2014). Developmental pathway for potent V1V2-directed HIV-neutralizing antibodies. Nature *509*, 55-62.

Doyle, J.E.L.a.M.L. (2004). Biocalorimetry 2: Applications of Calorimetry in the Biological Sciences.

Doyle-Cooper, C., Hudson, K.E., Cooper, A.B., Ota, T., Skog, P., Dawson, P.E., Zwick, M.B., Schief, W.R., Burton, D.R., and Nemazee, D. (2013). Immune tolerance negatively regulates B cells in knock-in mice expressing broadly neutralizing HIV antibody 4E10. Journal of immunology *191*, 3186-3191.

Earl, P.L., Doms, R.W., and Moss, B. (1990). Oligomeric structure of the human immunodeficiency virus type 1 envelope glycoprotein. Proceedings of the National Academy of Sciences of the United States of America *87*, 648-652.

Emsley, P., Lohkamp, B., Scott, W.G., and Cowtan, K. (2010). Features and development of Coot. Acta Crystallogr D *66*, 486-501.

Evans, P. (2006). Scaling and assessment of data quality. Acta Crystallogr D *62*, 72-82.

Falkowska, E., Le, K.M., Ramos, A., Doores, K.J., Lee, J.H., Blattner, C., Ramirez, A., Derking, R., van Gils, M.J., Liang, C.H.*, et al.* (2014). Broadly neutralizing HIV antibodies define a glycan-dependent epitope on the prefusion conformation of gp41 on cleaved envelope trimers. Immunity *40*, 657-668.

Feng, Y., Broder, C.C., Kennedy, P.E., and Berger, E.A. (1996). HIV-1 entry cofactor: functional cDNA cloning of a seven-transmembrane, G protein-coupled receptor. Science *272*, 872-877.

Finton, K.A., Friend, D., Jaffe, J., Gewe, M., Holmes, M.A., Larman, H.B., Stuart, A., Larimore, K., Greenberg, P.D., Elledge, S.J.*, et al.* (2014). Ontogeny of Recognition Specificity and Functionality for the Broadly Neutralizing Anti-HIV Antibody 4E10. PLoS pathogens *10*, e1004403.

Finton, K.A., Larimore, K., Larman, H.B., Friend, D., Correnti, C., Rupert, P.B., Elledge, S.J., Greenberg, P.D., and Strong, R.K. (2013). Autoreactivity and exceptional CDR plasticity (but not unusual polyspecificity) hinder elicitation of the anti-HIV antibody 4E10. PLoS pathogens *9*, e1003639.

Freed, E.O. (2015). HIV-1 assembly, release and maturation. Nat Rev Microbiol *13*, 484-496.

Frey, G., Peng, H., Rits-Volloch, S., Morelli, M., Cheng, Y., and Chen, B. (2008). A fusion-intermediate state of HIV-1 gp41 targeted by broadly neutralizing antibodies. Proceedings of the National Academy of Sciences of the United States of America *105*, 3739-3744.

Gallo, R.C., Salahuddin, S.Z., Popovic, M., Shearer, G.M., Kaplan, M., Haynes, B.F., Palker, T.J., Redfield, R., Oleske, J., Safai, B.*, et al.* (1984). Frequent detection and isolation of cytopathic retroviruses (HTLV-III) from patients with AIDS and at risk for AIDS. Science *224*, 500-503.

Gaschen, B., Taylor, J., Yusim, K., Foley, B., Gao, F., Lang, D., Novitsky, V., Haynes, B., Hahn, B.H., Bhattacharya, T.*, et al.* (2002). Diversity considerations in HIV-1 vaccine selection. Science *296*, 2354-2360.

Gelb, M.H., Cho, W., and Wilton, D.C. (1999). Interfacial binding of secreted phospholipases A(2): more than electrostatics and a major role for tryptophan. Curr Opin Struct Biol *9*, 428-432.

Gorman, J., Soto, C., Yang, M.M., Davenport, T.M., Guttman, M., Bailer, R.T., Chambers, M., Chuang, G.Y., DeKosky, B.J., Doria-Rose, N.A.*, et al.* (2016). Structures of HIV-1 Env V1V2 with broadly

neutralizing antibodies reveal commonalities that enable vaccine design. Nat Struct Mol Biol *23*, 81-90.

Gray, E.S., Madiga, M.C., Hermanus, T., Moore, P.L., Wibmer, C.K., Tumba, N.L., Werner, L., Mlisana, K., Sibeko, S., Williamson, C.*, et al.* (2011). The neutralization breadth of HIV-1 develops incrementally over four years and is associated with CD4+ T cell decline and high viral load during acute infection. Journal of virology *85*, 4828-4840.

Gruell, H., Bournazos, S., Ravetch, J.V., Ploss, A., Nussenzweig, M.C., and Pietzsch, J. (2013). Antibody and antiretroviral preexposure prophylaxis prevent cervicovaginal HIV-1 infection in a transgenic mouse model. Journal of virology *87*, 8535-8544.

Gustchina, E., Bewley, C.A., and Clore, G.M. (2008). Sequestering of the prehairpin intermediate of gp41 by peptide N36Mut(e,g) potentiates the human immunodeficiency virus type 1 neutralizing activity of monoclonal antibodies directed against the N-terminal helical repeat of gp41. Journal of virology *82*, 10032-10041.

Hallenberger, S., Bosch, V., Angliker, H., Shaw, E., Klenk, H.D., and Garten, W. (1992). Inhibition of furin-mediated cleavage activation of HIV-1 glycoprotein gp160. Nature *360*, 358-361.

Halper-Stromberg, A., Lu, C.L., Klein, F., Horwitz, J.A., Bournazos, S., Nogueira, L., Eisenreich, T.R., Liu, C., Gazumyan, A., Schaefer, U.*, et al.* (2014). Broadly neutralizing antibodies and viral inducers decrease rebound from HIV-1 latent reservoirs in humanized mice. Cell *158*, 989-999.

Haynes, B.F., Fleming, J., St Clair, E.W., Katinger, H., Stiegler, G., Kunert, R., Robinson, J., Scearce, R.M., Plonk, K., Staats, H.F.*, et al.* (2005). Cardiolipin polyspecific autoreactivity in two broadly neutralizing HIV-1 antibodies. Science *308*, 1906-1908.

Haynes, B.F., Gilbert, P.B., McElrath, M.J., Zolla-Pazner, S., Tomaras, G.D., Alam, S.M., Evans, D.T., Montefiori, D.C., Karnasuta, C., Sutthent, R.*, et al.* (2012a). Immune-correlates analysis of an HIV-1 vaccine efficacy trial. N Engl J Med *366*, 1275-1286.

Haynes, B.F., Kelsoe, G., Harrison, S.C., and Kepler, T.B. (2012b). B-cell-lineage immunogen design in vaccine development with HIV-1 as a case study. Nat Biotechnol *30*, 423-433.

Haynes, B.F., Nicely, N.I., and Alam, S.M. (2010). HIV-1 autoreactive antibodies: are they good or bad for HIV-1 prevention? Nature structural & molecular biology *17*, 543-545.

Heesters, B.A., Myers, R.C., and Carroll, M.C. (2014). Follicular dendritic cells: dynamic antigen libraries. Nature reviews Immunology *14*, 495-504.

Heuck, A.P., Hotze, E.M., Tweten, R.K., and Johnson, A.E. (2000). Mechanism of membrane insertion of a multimeric beta-barrel protein: perfringolysin O creates a pore using ordered and coupled conformational changes. Molecular cell *6*, 1233-1242.

Holdgate, G.A., and Ward, W.H. (2005). Measurements of binding thermodynamics in drug discovery. Drug Discov Today *10*, 1543-1550.

Homola, J. (2003). Present and future of surface plasmon resonance biosensors. Analytical and bioanalytical chemistry *377*, 528-539.

Huang, J., Kang, B.H., Pancera, M., Lee, J.H., Tong, T., Feng, Y., Imamichi, H., Georgiev, I.S., Chuang, G.Y., Druz, A.*, et al.* (2014). Broad and potent HIV-1 neutralization by a human antibody that binds the gp41-gp120 interface. Nature *515*, 138-142.

Huang, J., Ofek, G., Laub, L., Louder, M.K., Doria-Rose, N.A., Longo, N.S., Imamichi, H., Bailer, R.T., Chakrabarti, B., Sharma, S.K.*, et al.* (2012). Broad and potent neutralization of HIV-1 by a gp41-specific human antibody. Nature *491*, 406-412.

Huarte, N., Carravilla, P., Cruz, A., Lorizate, M., Nieto-Garai, J.A., Krausslich, H.G., Perez-Gil, J., Requejo-Isidro, J., and Nieva, J.L. (2016). Functional organization of the HIV lipid envelope. Scientific reports *6*, 34190.

Huarte, N., Lorizate, M., Maeso, R., Kunert, R., Arranz, R., Valpuesta, J.M., and Nieva, J.L. (2008). The broadly neutralizing anti-human immunodeficiency virus type 1 4E10 monoclonal antibody is better adapted to membrane-bound epitope recognition and blocking than 2F5. Journal of virology *82*, 8986-8996.

Inaba, K., Murakami, S., Suzuki, M., Nakagawa, A., Yamashita, E., Okada, K., and Ito, K. (2006). Crystal structure of the DsbB-DsbA complex reveals a mechanism of disulfide bond generation. Cell *127*, 789-801.

Irimia, A., Sarkar, A., Stanfield, R.L., and Wilson, I.A. (2016). Crystallographic Identification of Lipid as an Integral Component of the Epitope of HIV Broadly Neutralizing Antibody 4E10. Immunity *44*, 21-31.

Ito, K. (2010). Editing disulphide bonds: error correction using redox currencies. Mol Microbiol *75*, 1-5.

Johnson, W.E., and Desrosiers, R.C. (2002). Viral persistence: HIV's strategies of immune system evasion. Annu Rev Med *53*, 499-518.

Jones, T.A., Zou, J.Y., Cowan, S.W., and Kjeldgaard, M. (1991). Improved methods for building protein models in electron-density maps and the location of errors in these models. Acta Crystallogr A *47*, 110-119.

Julien, J.P., Bryson, S., Nieva, J.L., and Pai, E.F. (2008). Structural details of HIV-1 recognition by the broadly neutralizing monoclonal antibody 2F5: epitope conformation, antigen-recognition loop mobility, and anion-binding site. Journal of molecular biology *384*, 377-392.

Julien, J.P., Cupo, A., Sok, D., Stanfield, R.L., Lyumkis, D., Deller, M.C., Klasse, P.J., Burton, D.R., Sanders, R.W., Moore, J.P.*, et al.* (2013). Crystal structure of a soluble cleaved HIV-1 envelope trimer. Science *342*, 1477-1483.

Julien, J.P., Huarte, N., Maeso, R., Taneva, S.G., Cunningham, A., Nieva, J.L., and Pai, E.F. (2010). Ablation of the complementarity-determining region H3 apex of the anti-HIV-1 broadly neutralizing antibody 2F5 abrogates neutralizing capacity without affecting core epitope binding. Journal of virology *84*, 4136-4147.

Karlsson Hedestam, G.B., Fouchier, R.A., Phogat, S., Burton, D.R., Sodroski, J., and Wyatt, R.T. (2008). The challenges of eliciting neutralizing antibodies to HIV-1 and to influenza virus. Nature reviews Microbiology *6*, 143-155.

Kim, A.S., Leaman, D.P., and Zwick, M.B. (2014). Antibody to gp41 MPER alters functional properties of HIV-1 Env without complete neutralization. PLoS pathogens *10*, e1004271.

Kim, M., Song, L., Moon, J., Sun, Z.Y., Bershteyn, A., Hanson, M., Cain, D., Goka, S., Kelsoe, G., Wagner, G.*, et al.* (2013). Immunogenicity of membrane-bound HIV-1 gp41 membrane-proximal external region (MPER) segments is dominated by residue accessibility and modulated by stereochemistry. The Journal of biological chemistry *288*, 31888-31901.

Kimball, R.A., Martin, L., and Saier, M.H., Jr. (2003). Reversing transmembrane electron flow: the DsbD and DsbB protein families. J Mol Microbiol Biotechnol *5*, 133-149.

Kiyoshi, M., Caaveiro, J.M., Miura, E., Nagatoishi, S., Nakakido, M., Soga, S., Shirai, H., Kawabata, S., and Tsumoto, K. (2014). Affinity improvement of a therapeutic antibody by structure-based computational design: generation of electrostatic interactions in the transition state stabilizes the antibody-antigen complex. PloS one *9*, e87099.

Kiyoshi, M., Caaveiro, J.M.M., Kawai, T., Tashiro, S., Ide, T., Asaoka, Y., Hatayama, K., and Tsumoto, K. (2015). Structural basis for binding of human IgG1 to its high-affinity human receptor Fc[gamma]RI. Nat Commun *6*.

Klatzmann, D., Champagne, E., Chamaret, S., Gruest, J., Guetard, D., Hercend, T., Gluckman, J.C., and Montagnier, L. (1984). T-lymphocyte T4 molecule behaves as the receptor for human retrovirus LAV. Nature *312*, 767-768.

Klein, F., Diskin, R., Scheid, J.F., Gaebler, C., Mouquet, H., Georgiev, I.S., Pancera, M., Zhou, T., Incesu, R.B., Fu, B.Z.*, et al.* (2013a). Somatic mutations of the immunoglobulin framework are generally required for broad and potent HIV-1 neutralization. Cell *153*, 126-138.

Klein, F., Gaebler, C., Mouquet, H., Sather, D.N., Lehmann, C., Scheid, J.F., Kraft, Z., Liu, Y., Pietzsch, J., Hurley, A.*, et al.* (2012a). Broad neutralization by a combination of antibodies recognizing the CD4 binding site and a new conformational epitope on the HIV-1 envelope protein. J Exp Med *209*, 1469-1479.

Klein, F., Halper-Stromberg, A., Horwitz, J.A., Gruell, H., Scheid, J.F., Bournazos, S., Mouquet, H., Spatz, L.A., Diskin, R., Abadir, A.*, et al.* (2012b). HIV therapy by a combination of broadly neutralizing antibodies in humanized mice. Nature *492*, 118-122.

Klein, F., Mouquet, H., Dosenovic, P., Scheid, J.F., Scharf, L., and Nussenzweig, M.C. (2013b). Antibodies in HIV-1 vaccine development and therapy. Science *341*, 1199-1204.

Klein, J.S., Gnanapragasam, P.N.P., Galimidi, R.P., Foglesong, C.P., West, A.P., and Bjorkman, P.J. (2009). Examination of the contributions of size and avidity to the neutralization mechanisms of the anti-HIV antibodies b12 and 4E10. Proc Natl Acad Sci U S A *106*, 7385-7390.

Kohler, G., and Milstein, C. (1975). Continuous cultures of fused cells secreting antibody of predefined specificity. Nature *256*, 495-497.

Kong, L., Lee, J.H., Doores, K.J., Murin, C.D., Julien, J.P., McBride, R., Liu, Y., Marozsan, A., Cupo, A., Klasse, P.J.*, et al.* (2013). Supersite of immune vulnerability on the glycosylated face of HIV-1 envelope glycoprotein gp120. Nat Struct Mol Biol *20*, 796-803.

Kong, R., Xu, K., Zhou, T., Acharya, P., Lemmin, T., Liu, K., Ozorowski, G., Soto, C., Taft, J.D., Bailer, R.T.*, et al.* (2016). Fusion peptide of HIV-1 as a site of vulnerability to neutralizing antibody. Science *352*, 828-833.

Kozlov, M.M., McMahon, H.T., and Chernomordik, L.V. (2010). Protein-driven membrane stresses in fusion and fission. Trends Biochem Sci *35*, 699-706.

Krissinel, E., and Henrick, K. (2007). Inference of macromolecular assemblies from crystalline state. J Mol Biol *372*, 774-797.

Kunert, R., Ruker, F., and Katinger, H. (1998). Molecular characterization of five neutralizing anti-HIV type 1 antibodies: Identification of nonconventional D segments in the human monoclonal antibodies 2G12 and 2F5. AIDS Res Hum Retroviruses *14*, 1115-1128.

Kwon, Y.D., Georgiev, I.S., Ofek, G., Zhang, B., Asokan, M., Bailer, R.T., Bao, A., Caruso, W., Chen, X., Choe, M.*, et al.* (2016a). Optimization of the Solubility of HIV-1-Neutralizing Antibody 10E8 through Somatic Variation and Structure-Based Design. Journal of virology.

Kwon, Y.D., Georgiev, I.S., Ofek, G., Zhang, B., Asokan, M., Bailer, R.T., Bao, A., Caruso, W., Chen, X., Choe, M.*, et al.* (2016b). Optimization of the Solubility of HIV-1-Neutralizing Antibody 10E8 through Somatic Variation and Structure-Based Design. Journal of virology *90*, 5899-5914.

Kwon, Y.D., Pancera, M., Acharya, P., Georgiev, I.S., Crooks, E.T., Gorman, J., Joyce, M.G., Guttman, M., Ma, X., Narpala, S.*, et al.* (2015). Crystal structure, conformational fixation and entry-related interactions of mature ligand-free HIV-1 Env. Nature structural & molecular biology *22*, 522-531.

Kwong, P.D., and Mascola, J.R. (2012). Human antibodies that neutralize HIV-1: identification, structures, and B cell ontogenies. Immunity *37*, 412-425.

Ladokhin, A.S., Jayasinghe, S., and White, S.H. (2000). How to measure and analyze tryptophan fluorescence in membranes properly, and why bother? Anal Biochem *285*, 235-245.

Lakowicz, J.R. (2006). Principles of Fluorescence Spectroscopy.

Lanzavecchia, A., Corti, D., and Sallusto, F. (2007). Human monoclonal antibodies by immortalization of memory B cells. Curr Opin Biotechnol *18*, 523-528.

Laskowski, R.A., MacArthur, M.W., Moss, D.S., and Thornton, J.M. (1993). PROCHECK - a program to check the stereochemical quality of protein structures. J Appl Crystallogr *26*, 283-291.

Lawrence, M.C., and Colman, P.M. (1993). Shape complementarity at protein-protein interfaces. J Mol Biol *234*, 946-950.

Leaman, D.P., Lee, J.H., Ward, A.B., and Zwick, M.B. (2015). Immunogenic display of purified chemically cross-linked HIV-1 spikes. J Virol *89*, 6725-6745.

Lee, J.H., Ozorowski, G., and Ward, A.B. (2016). Cryo-EM structure of a native, fully glycosylated, cleaved HIV-1 envelope trimer. Science *351*, 1043-1048.

Levy, J.A., Hoffman, A.D., Kramer, S.M., Landis, J.A., Shimabukuro, J.M., and Oshiro, L.S. (1984). Isolation of lymphocytopathic retroviruses from San Francisco patients with AIDS. Science *225*, 840-842.

Li, Y., Thompson, H., Hemphill, C., Hong, F., Forrester, J., Johnson, R.H., Zhang, W., and Meldrum, D.R. (2010). An improved one-tube RT-PCR protocol for analyzing single-cell gene expression in individual mammalian cells. Anal Bioanal Chem *397*, 1853-1859.

Liao, H.X., Lynch, R., Zhou, T., Gao, F., Alam, S.M., Boyd, S.D., Fire, A.Z., Roskin, K.M., Schramm, C.A., Zhang, Z.*, et al.* (2013). Co-evolution of a broadly neutralizing HIV-1 antibody and founder virus. Nature *496*, 469-476.

Liu, M., Yang, G., Wiehe, K., Nicely, N.I., Vandergrift, N.A., Rountree, W., Bonsignori, M., Alam, S.M., Gao, J., Haynes, B.F.*, et al.* (2015). Polyreactivity and autoreactivity among HIV-1 antibodies. Journal of virology *89*, 784-798.

Lobstein, J., Emrich, C.A., Jeans, C., Faulkner, M., Riggs, P., and Berkmen, M. (2012). SHuffle, a novel Escherichia coli protein expression strain capable of correctly folding disulfide bonded proteins in its cytoplasm. Microb Cell Fact *11*, 56.

Lorizate, M., Cruz, A., Huarte, N., Kunert, R., Perez-Gil, J., and Nieva, J.L. (2006). Recognition and blocking of HIV-1 gp41 pre-transmembrane sequence by monoclonal 4E10 antibody in a Raft-like membrane environment. The Journal of biological chemistry *281*, 39598-39606.

Lyumkis, D., Julien, J.P., de Val, N., Cupo, A., Potter, C.S., Klasse, P.J., Burton, D.R., Sanders, R.W., Moore, J.P., Carragher, B.*, et al.* (2013). Cryo-EM structure of a fully glycosylated soluble cleaved HIV-1 envelope trimer. Science *342*, 1484-1490.

MacLennan, I.C. (1994). Germinal centers. Annu Rev Immunol *12*, 117-139.

Maeso, R., Huarte, N., Julien, J.P., Kunert, R., Pai, E.F., and Nieva, J.L. (2011). Interaction of anti-HIV type 1 antibody 2F5 with phospholipid bilayers and its relevance for the mechanism of virus neutralization. AIDS research and human retroviruses *27*, 863-876.

Makrides, S.C. (1996). Strategies for achieving high-level expression of genes in Escherichia coli. Microbiol Rev *60*, 512-538.

Matyas, G.R., Beck, Z., Karasavvas, N., and Alving, C.R. (2009). Lipid binding properties of 4E10, 2F5, and WR304 monoclonal antibodies that neutralize HIV-1. Biochimica et biophysica acta *1788*, 660-665.

Mayer, L.D., Hope, M.J., and Cullis, P.R. (1986). Vesicles of variable sizes produced by a rapid extrusion procedure. Biochim Biophys Acta *858*, 161-168.

McCafferty, J., Griffiths, A.D., Winter, G., and Chiswell, D.J. (1990). Phage antibodies: filamentous phage displaying antibody variable domains. Nature *348*, 552-554.

McCarthy, A.A., Haebel, P.W., Torronen, A., Rybin, V., Baker, E.N., and Metcalf, P. (2000). Crystal structure of the protein disulfide bond isomerase, DsbC, from Escherichia coli. Nat Struct Biol *7*, 196-199.

McCoy, A.J., Grosse-Kunstleve, R.W., Adams, P.D., Winn, M.D., Storoni, L.C., and Read, R.J. (2007). Phaser crystallographic software. J Appl Crystallogr *40*, 658-674.

McDonald, S.K., and Fleming, K.G. (2016). Aromatic side chain water-to-lipid transfer free energies show a depth-dependence across the membrane normal. Journal of the American Chemical Society.

McLaughlin, S. (1989). The electrostatic properties of membranes. Annual review of biophysics and biophysical chemistry *18*, 113-136.

McLaughlin, S., and Aderem, A. (1995). The myristoyl-electrostatic switch: a modulator of reversible protein-membrane interactions. Trends in biochemical sciences *20*, 272-276.

McLellan, J.S., Chen, M., Joyce, M.G., Sastry, M., Stewart-Jones, G.B., Yang, Y., Zhang, B., Chen, L., Srivatsan, S., Zheng, A.*, et al.* (2013). Structure-based design of a fusion glycoprotein vaccine for respiratory syncytial virus. Science *342*, 592-598.

McLellan, J.S., Pancera, M., Carrico, C., Gorman, J., Julien, J.P., Khayat, R., Louder, R., Pejchal, R., Sastry, M., Dai, K.*, et al.* (2011). Structure of HIV-1 gp120 V1/V2 domain with broadly neutralizing antibody PG9. Nature *480*, 336-343.

Melikyan, G.B. (2008). Common principles and intermediates of viral protein-mediated fusion: the HIV-1 paradigm. Retrovirology *5*, 111.

Melikyan, G.B. (2011). Membrane fusion mediated by human immunodeficiency virus envelope glycoprotein. Curr Top Membr *68*, 81-106.

Mirassou, Y., Santiveri, C.M., Perez de Vega, M.J., Gonzalez-Muniz, R., and Jimenez, M.A. (2009). Disulfide bonds versus TrpTrp pairs in irregular beta-hairpins: NMR structure of vammin loop 3-derived peptides as a case study. Chembiochem : a European journal of chemical biology *10*, 902-910.

Moldt, B., Rakasz, E.G., Schultz, N., Chan-Hui, P.Y., Swiderek, K., Weisgrau, K.L., Piaskowski, S.M., Bergman, Z., Watkins, D.I., Poignard, P.*, et al.* (2012). Highly potent HIV-specific antibody neutralization in vitro translates into effective protection against mucosal SHIV challenge in vivo. Proceedings of the National Academy of Sciences of the United States of America *109*, 18921-18925.

Montefiori, D.C. (2009). Measuring HIV neutralization in a luciferase reporter gene assay. Methods Mol Biol *485*, 395-405.

Montero, M., Gulzar, N., Klaric, K.A., Donald, J.E., Lepik, C., Wu, S., Tsai, S., Julien, J.P., Hessell, A.J., Wang, S.*, et al.* (2012). Neutralizing epitopes in the membrane-proximal external region of HIV-1 gp41 are influenced by the transmembrane domain and the plasma membrane. Journal of virology *86*, 2930-2941.

Montero, M., van Houten, N.E., Wang, X., and Scott, J.K. (2008). The membrane-proximal external region of the human immunodeficiency virus type 1 envelope: dominant site of antibody neutralization and target for vaccine design. Microbiol Mol Biol Rev *72*, 54-84, table of contents.

Moore, P.L., Crooks, E.T., Porter, L., Zhu, P., Cayanan, C.S., Grise, H., Corcoran, P., Zwick, M.B., Franti, M., Morris, L.*, et al.* (2006). Nature of nonfunctional envelope proteins on the surface of human immunodeficiency virus type 1. Journal of virology *80*, 2515-2528.

Mouquet, H., and Nussenzweig, M.C. (2012). Polyreactive antibodies in adaptive immune responses to viruses. Cell Mol Life Sci *69*, 1435-1445.

Mouquet, H., Scharf, L., Euler, Z., Liu, Y., Eden, C., Scheid, J.F., Halper-Stromberg, A., Gnanapragasam, P.N., Spencer, D.I., Seaman, M.S.*, et al.* (2012). Complex-type N-glycan recognition by potent broadly neutralizing HIV antibodies. Proceedings of the National Academy of Sciences of the United States of America *109*, E3268-3277.

Mouquet, H., Scheid, J.F., Zoller, M.J., Krogsgaard, M., Ott, R.G., Shukair, S., Artyomov, M.N., Pietzsch, J., Connors, M., Pereyra, F.*, et al.* (2010). Polyreactivity increases the apparent affinity of anti-HIV antibodies by heteroligation. Nature *467*, 591-595.

Mulgrew-Nesbitt, A., Diraviyam, K., Wang, J., Singh, S., Murray, P., Li, Z., Rogers, L., Mirkovic, N., and Murray, D. (2006). The role of electrostatics in protein-membrane interactions. Biochimica et biophysica acta *1761*, 812-826.

Murshudov, G.N., Vagin, A.A., and Dodson, E.J. (1997). Refinement of macromolecular structures by the maximum-likelihood method. Acta Crystallogr D *53*, 240-255.

Muster, T., Guinea, R., Trkola, A., Purtscher, M., Klima, A., Steindl, F., Palese, P., and Katinger, H. (1994). Cross-neutralizing activity against divergent human immunodeficiency virus type 1 isolates induced by the gp41 sequence ELDKWAS. Journal of virology *68*, 4031-4034.

Muster, T., Steindl, F., Purtscher, M., Trkola, A., Klima, A., Himmler, G., Ruker, F., and Katinger, H. (1993). A conserved neutralizing epitope on gp41 of human immunodeficiency virus type 1. J Virol *67*, 6642-6647.

Nakamoto, H., and Bardwell, J.C. (2004). Catalysis of disulfide bond formation and isomerization in the Escherichia coli periplasm. Biochim Biophys Acta *1694*, 111-119.

Nelson, J.D., Brunel, F.M., Jensen, R., Crooks, E.T., Cardoso, R.M., Wang, M., Hessell, A., Wilson, I.A., Binley, J.M., Dawson, P.E.*, et al.* (2007). An affinity-enhanced neutralizing antibody against the membrane-proximal external region of human immunodeficiency virus type 1 gp41 recognizes an epitope between those of 2F5 and 4E10. Journal of virology *81*, 4033-4043.

Nieva, J.L., Apellaniz, B., Huarte, N., and Lorizate, M. (2011). A new paradigm in molecular recognition? Specific antibody binding to membrane-inserted HIV-1 epitopes. Journal of molecular recognition : JMR *24*, 642-646.

Ofek, G., McKee, K., Yang, Y.P., Yang, Z.Y., Skinner, J., Guenaga, F.J., Wyatt, R., Zwick, M.B., Nabel, G.J., Mascola, J.R.*, et al.* (2010). Relationship between antibody 2F5 neutralization of HIV-1 and hydrophobicity of its heavy chain third complementarity-determining region. J Virol *84*, 2955-2962.

Ofek, G., Tang, M., Sambor, A., Katinger, H., Mascola, J.R., Wyatt, R., and Kwong, P.D. (2004). Structure and mechanistic analysis of the anti-human immunodeficiency virus type 1 antibody 2F5 in complex with its gp41 epitope. Journal of virology *78*, 10724-10737.

Ota, T., Doyle-Cooper, C., Cooper, A.B., Huber, M., Falkowska, E., Doores, K.J., Hangartner, L., Le, K., Sok, D., Jardine, J.*, et al.* (2012). Anti-HIV B Cell lines as candidate vaccine biosensors. J Immunol *189*, 4816-4824.

Palella, F.J., Jr., Delaney, K.M., Moorman, A.C., Loveless, M.O., Fuhrer, J., Satten, G.A., Aschman, D.J., and Holmberg, S.D. (1998). Declining morbidity and mortality among patients with advanced human immunodeficiency virus infection. HIV Outpatient Study Investigators. N Engl J Med *338*, 853-860.

Pancera, M., Lebowitz, J., Schon, A., Zhu, P., Freire, E., Kwong, P.D., Roux, K.H., Sodroski, J., and Wyatt, R. (2005). Soluble mimetics of human immunodeficiency virus type 1 viral spikes produced by replacement of the native trimerization domain with a heterologous trimerization motif: characterization and ligand binding analysis. Journal of virology *79*, 9954-9969.

Pancera, M., Zhou, T., Druz, A., Georgiev, I.S., Soto, C., Gorman, J., Huang, J., Acharya, P., Chuang, G.Y., Ofek, G.*, et al.* (2014). Structure and immune recognition of trimeric pre-fusion HIV-1 Env. Nature *514*, 455-461.

Parker, D.C. (1993). T cell-dependent B cell activation. Annu Rev Immunol *11*, 331-360.

Parvin, J.D., Moscona, A., Pan, W.T., Leider, J.M., and Palese, P. (1986). Measurement of the mutation rates of animal viruses: influenza A virus and poliovirus type 1. Journal of virology *59*, 377-383.

Patching, S.G. (2014). Surface plasmon resonance spectroscopy for characterisation of membrane protein-ligand interactions and its potential for drug discovery. Biochimica et biophysica acta *1838*, 43-55.

Pegu, A., Yang, Z.Y., Boyington, J.C., Wu, L., Ko, S.Y., Schmidt, S.D., McKee, K., Kong, W.P., Shi, W., Chen, X.*, et al.* (2014). Neutralizing antibodies to HIV-1 envelope protect more effectively in vivo than those to the CD4 receptor. Science translational medicine *6*, 243ra288.

Pettersen, E.F., Goddard, T.D., Huang, C.C., Couch, G.S., Greenblatt, D.M., Meng, E.C., and Ferrin, T.E. (2004). UCSF Chimera--a visualization system for exploratory research and analysis. J Comput Chem *25*, 1605-1612.

Pritchard, L.K., Vasiljevic, S., Ozorowski, G., Seabright, G.E., Cupo, A., Ringe, R., Kim, H.J., Sanders, R.W., Doores, K.J., Burton, D.R.*, et al.* (2015). Structural Constraints Determine the Glycosylation of HIV-1 Envelope Trimers. Cell Rep *11*, 1604-1613.

Purtscher, M., Trkola, A., Gruber, G., Buchacher, A., Predl, R., Steindl, F., Tauer, C., Berger, R., Barrett, N., Jungbauer, A.*, et al.* (1994). A broadly neutralizing human monoclonal antibody against gp41 of human immunodeficiency virus type 1. AIDS research and human retroviruses *10*, 1651-1658.

Rajewsky, K. (1996). Clonal selection and learning in the antibody system. Nature *381*, 751-758.

Reardon, P.N., Sage, H., Dennison, S.M., Martin, J.W., Donald, B.R., Alam, S.M., Haynes, B.F., and Spicer, L.D. (2014). Structure of an HIV-1-neutralizing antibody target, the lipid-bound gp41 envelope membrane proximal region trimer. Proceedings of the National Academy of Sciences of the United States of America *111*, 1391-1396.

Rerks-Ngarm, S., Pitisuttithum, P., Nitayaphan, S., Kaewkungwal, J., Chiu, J., Paris, R., Premsri, N., Namwat, C., de Souza, M., Adams, E.*, et al.* (2009). Vaccination with ALVAC and AIDSVAX to prevent HIV-1 infection in Thailand. N Engl J Med *361*, 2209-2220.

Ringe, R.P., Sanders, R.W., Yasmeen, A., Kim, H.J., Lee, J.H., Cupo, A., Korzun, J., Derking, R., van Montfort, T., Julien, J.P.*, et al.* (2013). Cleavage strongly influences whether soluble HIV-1 envelope glycoprotein trimers adopt a native-like conformation. Proceedings of the National Academy of Sciences of the United States of America *110*, 18256-18261.

Rupp, B. (2009). Bimolecular crystallography.

Ruprecht, C.R., Krarup, A., Reynell, L., Mann, A.M., Brandenberg, O.F., Berlinger, L., Abela, I.A., Regoes, R.R., Gunthard, H.F., Rusert, P.*, et al.* (2011). MPER-specific antibodies induce gp120 shedding and irreversibly neutralize HIV-1. The Journal of experimental medicine *208*, 439-454.

Ryu, S.E., and Hendrickson, W.A. (2012). Structure and design of broadly-neutralizing antibodies against HIV. Mol Cells *34*, 231-237.

Saez-Cirion, A., Arrondo, J.L., Gomara, M.J., Lorizate, M., Iloro, I., Melikyan, G., and Nieva, J.L. (2003). Structural and functional roles of HIV-1 gp41 pretransmembrane sequence segmentation. Biophysical journal *85*, 3769-3780.

Saez-Cirion, A., Nir, S., Lorizate, M., Agirre, A., Cruz, A., Perez-Gil, J., and Nieva, J.L. (2002). Sphingomyelin and cholesterol promote HIV-1 gp41 pretransmembrane sequence surface aggregation and membrane restructuring. The Journal of biological chemistry *277*, 21776-21785.

Sakamoto, S., Caaveiro, J.M.M., Sano, E., Tanaka, Y., Kudou, M., and Tsumoto, K. (2009). Contributions of Interfacial Residues of Human Interleukin15 to the Specificity and Affinity for Its Private α-Receptor. Journal of molecular biology *389*, 880-894.

Salamon, Z., Macleod, H.A., and Tollin, G. (1997). Surface plasmon resonance spectroscopy as a tool for investigating the biochemical and biophysical properties of membrane protein systems. I: Theoretical principles. Biochimica et biophysica acta *1331*, 117-129.

Salzwedel, K., West, J.T., and Hunter, E. (1999). A conserved tryptophan-rich motif in the membrane-proximal region of the human immunodeficiency virus type 1 gp41 ectodomain is important for Env-mediated fusion and virus infectivity. J Virol *73*, 2469-2480.

Sanchez-Martinez, S., Lorizate, M., Hermann, K., Kunert, R., Basanez, G., and Nieva, J.L. (2006a). Specific phospholipid recognition by human immunodeficiency virus type-1 neutralizing anti-gp41 2F5 antibody. FEBS Lett *580*, 2395-2399.

Sanchez-Martinez, S., Lorizate, M., Katinger, H., Kunert, R., and Nieva, J.L. (2006b). Membrane association and epitope recognition by HIV-1 neutralizing anti-gp41 2F5 and 4E10 antibodies. AIDS Res Hum Retroviruses *22*, 998-1006.

Sanders, R.W., Vesanen, M., Schuelke, N., Master, A., Schiffner, L., Kalyanaraman, R., Paluch, M., Berkhout, B., Maddon, P.J., Olson, W.C.*, et al.* (2002). Stabilization of the soluble, cleaved, trimeric form of the envelope glycoprotein complex of human immunodeficiency virus type 1. Journal of virology *76*, 8875-8889.

Sattentau, Q.J. (2014). Immunogen design to focus the B-cell repertoire. Curr Opin HIV AIDS *9*, 217-223.

Scharf, L., Scheid, J.F., Lee, J.H., West, A.P., Jr., Chen, C., Gao, H., Gnanapragasam, P.N., Mares, R., Seaman, M.S., Ward, A.B.*, et al.* (2014). Antibody 8ANC195 reveals a site of broad vulnerability on the HIV-1 envelope spike. Cell Rep *7*, 785-795.

Schawaller, M., Smith, G.E., Skehel, J.J., and Wiley, D.C. (1989). Studies with crosslinking reagents on the oligomeric structure of the env glycoprotein of HIV. Virology *172*, 367-369.

Scheid, J.F., Horwitz, J.A., Bar-On, Y., Kreider, E.F., Lu, C.L., Lorenzi, J.C., Feldmann, A., Braunschweig, M., Nogueira, L., Oliveira, T.*, et al.* (2016). HIV-1 antibody 3BNC117 suppresses viral rebound in humans during treatment interruption. Nature *535*, 556-560.

Scheid, J.F., Mouquet, H., Feldhahn, N., Walker, B.D., Pereyra, F., Cutrell, E., Seaman, M.S., Mascola, J.R., Wyatt, R.T., Wardemann, H.*, et al.* (2009). A method for identification of HIV gp140 binding memory B cells in human blood. J Immunol Methods *343*, 65-67.

Scherer, E.M., Leaman, D.P., Zwick, M.B., McMichael, A.J., and Burton, D.R. (2010). Aromatic residues at the edge of the antibody combining site facilitate viral glycoprotein recognition through membrane interactions. Proceedings of the National Academy of Sciences of the United States of America *107*, 1529-1534.

Schibli, D.J., Montelaro, R.C., and Vogel, H.J. (2001). The membrane-proximal tryptophan-rich region of the HIV glycoprotein, gp41, forms a well-defined helix in dodecylphosphocholine micelles. Biochemistry *40*, 9570-9578.

Schofield, D.J., Pope, A.R., Clementel, V., Buckell, J., Chapple, S., Clarke, K.F., Conquer, J.S., Crofts, A.M., Crowther, S.R., Dyson, M.R*., et al.* (2007). Application of phage display to high throughput antibody generation and characterization. Genome Biol *8*, R254.

Seaman, M.S., Janes, H., Hawkins, N., Grandpre, L.E., Devoy, C., Giri, A., Coffey, R.T., Harris, L., Wood, B., Daniels, M.G*., et al.* (2010). Tiered categorization of a diverse panel of HIV-1 Env pseudoviruses for assessment of neutralizing antibodies. Journal of virology *84*, 1439-1452.

Serrano, S., Araujo, A., Apellaniz, B., Bryson, S., Carravilla, P., de la Arada, I., Huarte, N., Rujas, E., Pai, E.F., Arrondo, J.L*., et al.* (2014). Structure and immunogenicity of a peptide vaccine, including the complete HIV-1 gp41 2F5 epitope: implications for antibody recognition mechanism and immunogen design. J Biol Chem *289*, 6565-6580.

Shepard, L.A., Heuck, A.P., Hamman, B.D., Rossjohn, J., Parker, M.W., Ryan, K.R., Johnson, A.E., and Tweten, R.K. (1998). Identification of a membrane-spanning domain of the thiol-activated pore-forming toxin Clostridium perfringens perfringolysin O: an alpha-helical to beta-sheet transition identified by fluorescence spectroscopy. Biochemistry *37*, 14563-14574.

Shingai, M., Nishimura, Y., Klein, F., Mouquet, H., Donau, O.K., Plishka, R., Buckler-White, A., Seaman, M., Piatak, M., Jr., Lifson, J.D*., et al.* (2013). Antibody-mediated immunotherapy of macaques chronically infected with SHIV suppresses viraemia. Nature *503*, 277-280.

Simek, M.D., Rida, W., Priddy, F.H., Pung, P., Carrow, E., Laufer, D.S., Lehrman, J.K., Boaz, M., Tarragona-Fiol, T., Miiro, G*., et al.* (2009). Human immunodeficiency virus type 1 elite neutralizers: individuals with broad and potent neutralizing activity identified by using a high-throughput neutralization assay together with an analytical selection algorithm. Journal of virology *83*, 7337-7348.

Smith, K., Garman, L., Wrammert, J., Zheng, N.Y., Capra, J.D., Ahmed, R., and Wilson, P.C. (2009). Rapid generation of fully human monoclonal antibodies specific to a vaccinating antigen. Nat Protoc *4*, 372-384.

Sok, D., van Gils, M.J., Pauthner, M., Julien, J.P., Saye-Francisco, K.L., Hsueh, J., Briney, B., Lee, J.H., Le, K.M., Lee, P.S*., et al.* (2014). Recombinant HIV envelope trimer selects for quaternary-dependent antibodies targeting the trimer apex. Proceedings of the National Academy of Sciences of the United States of America *111*, 17624-17629.

Song, L., Sun, Z.Y., Coleman, K.E., Zwick, M.B., Gach, J.S., Wang, J.H., Reinherz, E.L., Wagner, G., and Kim, M. (2009). Broadly neutralizing anti-HIV-1 antibodies disrupt a hinge-related function of gp41 at the membrane interface. Proceedings of the National Academy of Sciences of the United States of America *106*, 9057-9062.

Sorensen, H.P., and Mortensen, K.K. (2005). Advanced genetic strategies for recombinant protein expression in Escherichia coli. J Biotechnol *115*, 113-128.

Soto, C., Ofek, G., Joyce, M.G., Zhang, B., McKee, K., Longo, N.S., Yang, Y., Huang, J., Parks, R., Eudailey, J*., et al.* (2016). Developmental Pathway of the MPER-Directed HIV-1-Neutralizing Antibody 10E8. PloS one *11*, e0157409.

Stamatatos, L., Morris, L., Burton, D.R., and Mascola, J.R. (2009). Neutralizing antibodies generated during natural HIV-1 infection: good news for an HIV-1 vaccine? Nature medicine *15*, 866-870.

Stanfield, R.L., Zemla, A., Wilson, I.A., and Rupp, B. (2006). Antibody elbow angles are influenced by their light chain class. J Mol Biol *357*, 1566-1574.

Steinitz, M., Klein, G., Koskimies, S., and Makel, O. (1977). EB virus-induced B lymphocyte cell lines producing specific antibody. Nature *269*, 420-422.

Stiegler, G., Kunert, R., Purtscher, M., Wolbank, S., Voglauer, R., Steindl, F., and Katinger, H. (2001). A potent cross-clade neutralizing human monoclonal antibody against a novel epitope on gp41 of human immunodeficiency virus type 1. AIDS research and human retroviruses *17*, 1757-1765.

Suarez, T., Gallaher, W.R., Agirre, A., Goni, F.M., and Nieva, J.L. (2000). Membrane interface-interacting sequences within the ectodomain of the human immunodeficiency virus type 1 envelope glycoprotein: putative role during viral fusion. Journal of virology *74*, 8038-8047.

Sun, Z.Y., Oh, K.J., Kim, M., Yu, J., Brusic, V., Song, L., Qiao, Z., Wang, J.H., Wagner, G., and Reinherz, E.L. (2008). HIV-1 broadly neutralizing antibody extracts its epitope from a kinked gp41 ectodomain region on the viral membrane. Immunity *28*, 52-63.

Tiller, T., Meffre, E., Yurasov, S., Tsuiji, M., Nussenzweig, M.C., and Wardemann, H. (2008). Efficient generation of monoclonal antibodies from single human B cells by single cell RT-PCR and expression vector cloning. J Immunol Methods *329*, 112-124.

Tiller, T., Tsuiji, M., Yurasov, S., Velinzon, K., Nussenzweig, M.C., and Wardemann, H. (2007). Autoreactivity in human IgG+ memory B cells. Immunity *26*, 205-213.

Trkola, A., Purtscher, M., Muster, T., Ballaun, C., Buchacher, A., Sullivan, N., Srinivasan, K., Sodroski, J., Moore, J.P., and Katinger, H. (1996). Human monoclonal antibody 2G12 defines a distinctive neutralization epitope on the gp120 glycoprotein of human immunodeficiency virus type 1. Journal of virology *70*, 1100-1108.

van den Bedem, H., Bhabha, G., Yang, K., Wright, P.E., and Fraser, J.S. (2013). Automated identification of functional dynamic contact networks from X-ray crystallography. Nat Methods *10*, 896-U110.

van Gils, M.J., and Sanders, R.W. (2014). In vivo protection by broadly neutralizing HIV antibodies. Trends in microbiology *22*, 550-551.

Venditto, V.J., Watson, D.S., Motion, M., Montefiori, D., and Szoka, F.C., Jr. (2013). Rational design of membrane proximal external region lipopeptides containing chemical modifications for HIV-1 vaccination. Clinical and vaccine immunology : CVI *20*, 39-45.

Verkoczy, L., and Diaz, M. (2014). Autoreactivity in HIV-1 broadly neutralizing antibodies: implications for their function and induction by vaccination. Curr Opin HIV AIDS *9*, 224-234.

Verkoczy, L., Kelsoe, G., and Haynes, B.F. (2014). HIV-1 envelope gp41 broadly neutralizing antibodies: hurdles for vaccine development. PLoS Pathog *10*, e1004073.

Veselinovic, M., Neff, C.P., Mulder, L.R., and Akkina, R. (2012). Topical gel formulation of broadly neutralizing anti-HIV-1 monoclonal antibody VRC01 confers protection against HIV-1 vaginal challenge in a humanized mouse model. Virology *432*, 505-510.

Vishwanathan, S.A., and Hunter, E. (2008). Importance of the membrane-perturbing properties of the membrane-proximal external region of human immunodeficiency virus type 1 gp41 to viral fusion. Journal of virology *82*, 5118-5126.

Walker, L.M., Huber, M., Doores, K.J., Falkowska, E., Pejchal, R., Julien, J.P., Wang, S.K., Ramos, A., Chan-Hui, P.Y., Moyle, M.*, et al.* (2011). Broad neutralization coverage of HIV by multiple highly potent antibodies. Nature *477*, 466-470.

Walker, L.M., Phogat, S.K., Chan-Hui, P.Y., Wagner, D., Phung, P., Goss, J.L., Wrin, T., Simek, M.D., Fling, S., Mitcham, J.L.*, et al.* (2009). Broad and potent neutralizing antibodies from an African donor reveal a new HIV-1 vaccine target. Science *326*, 285-289.

Wallace, A.C., Laskowski, R.A., and Thornton, J.M. (1995). Ligplot - a program to generate schematic diagrams of protein ligand interactions. Prot Eng *8*, 127-134.

Ward, A.B., and Wilson, I.A. (2015). Insights into the trimeric HIV-1 envelope glycoprotein structure. Trends in biochemical sciences *40*, 101-107.

Wardemann, H., Yurasov, S., Schaefer, A., Young, J.W., Meffre, E., and Nussenzweig, M.C. (2003). Predominant autoantibody production by early human B cell precursors. Science *301*, 1374-1377.

West, A.P., Jr., Scharf, L., Scheid, J.F., Klein, F., Bjorkman, P.J., and Nussenzweig, M.C. (2014). Structural insights on the role of antibodies in HIV-1 vaccine and therapy. Cell *156*, 633-648.

White, S.H., Ladokhin, A.S., Jayasinghe, S., and Hristova, K. (2001). How membranes shape protein structure. The Journal of biological chemistry *276*, 32395-32398.

White, S.H., and Wimley, W.C. (1999). Membrane protein folding and stability: physical principles. Annu Rev Biophys Biomol Struct *28*, 319-365.

Wimley, W.C., and White, S.H. (1996). Experimentally determined hydrophobicity scale for proteins at membrane interfaces. Nature structural biology *3*, 842-848.

Wu, X., Yang, Z.Y., Li, Y., Hogerkorp, C.M., Schief, W.R., Seaman, M.S., Zhou, T., Schmidt, S.D., Wu, L., Xu, L.*, et al.* (2010). Rational design of envelope identifies broadly neutralizing human monoclonal antibodies to HIV-1. Science *329*, 856-861.

Wu, X., Zhou, T., Zhu, J., Zhang, B., Georgiev, I., Wang, C., Chen, X., Longo, N.S., Louder, M., McKee, K.*, et al.* (2011). Focused evolution of HIV-1 neutralizing antibodies revealed by structures and deep sequencing. Science *333*, 1593-1602.

Wyatt, R., and Sodroski, J. (1998). The HIV-1 envelope glycoproteins: fusogens, antigens, and immunogens. Science *280*, 1884-1888.

Xiao, X., Chen, W., Feng, Y., Zhu, Z., Prabakaran, P., Wang, Y., Zhang, M.Y., Longo, N.S., and Dimitrov, D.S. (2009). Germline-like predecessors of broadly neutralizing antibodies lack measurable binding to HIV-1 envelope glycoproteins: implications for evasion of immune responses and design of vaccine immunogens. Biochem Biophys Res Commun *390*, 404-409.

Xu, H.Y., Song, L.K., Kim, M., Holmes, M.A., Kraft, Z., Sellhorn, G., Reinherz, E.L., Stamatatos, L., and Strong, R.K. (2010). Interactions between lipids and human anti-HIV antibody 4E10 can be reduced without ablating neutralizing activity. J Virol *84*, 1076-1088.

Xu, Z., Zan, H., Pal, Z., and Casali, P. (2007). DNA replication to aid somatic hypermutation. Adv Exp Med Biol *596*, 111-127.

Yang, X., Lee, J., Mahony, E.M., Kwong, P.D., Wyatt, R., and Sodroski, J. (2002). Highly stable trimers formed by human immunodeficiency virus type 1 envelope glycoproteins fused with the trimeric motif of T4 bacteriophage fibritin. Journal of virology *76*, 4634-4642.

Yethon, J.A., Epand, R.F., Leber, B., Epand, R.M., and Andrews, D.W. (2003). Interaction with a membrane surface triggers a reversible conformational change in Bax normally associated with induction of apoptosis. The Journal of biological chemistry *278*, 48935-48941.

Young, T.S., Ahmad, I., Yin, J.A., and Schultz, P.G. (2010). An enhanced system for unnatural amino acid mutagenesis in E. coli. Journal of molecular biology *395*, 361-374.

Zanetti, G., Briggs, J.A., Grunewald, K., Sattentau, Q.J., and Fuller, S.D. (2006). Cryo-electron tomographic structure of an immunodeficiency virus envelope complex in situ. PLoS Pathog *2*, e83.

Zhu, P., Liu, J., Bess, J., Jr., Chertova, E., Lifson, J.D., Grise, H., Ofek, G.A., Taylor, K.A., and Roux, K.H. (2006). Distribution and three-dimensional structure of AIDS virus envelope spikes. Nature *441*, 847-852.

Zhu, Z., Qin, H.R., Chen, W., Zhao, Q., Shen, X., Schutte, R., Wang, Y., Ofek, G., Streaker, E., Prabakaran, P.*, et al.* (2011). Cross-reactive HIV-1-neutralizing human monoclonal antibodies identified from a patient with 2F5-like antibodies. Journal of virology *85*, 11401-11408.

Zwick, M.B. (2005). The membrane-proximal external region of HIV-1 gp41: a vaccine target worth exploring. Aids *19*, 1725-1737.

Zwick, M.B., Labrijn, A.F., Wang, M., Spenlehauer, C., Saphire, E.O., Binley, J.M., Moore, J.P., Stiegler, G., Katinger, H., Burton, D.R.*, et al.* (2001). Broadly neutralizing antibodies targeted to the membrane-proximal external region of human immunodeficiency virus type 1 glycoprotein gp41. Journal of virology *75*, 10892-10905.